Data driven reduced order modelling of transonic buffet

Using invariant manifolds

ME55035: ME-EFPT MSc Thesis

Rahul Jayaraj

Delft University of Technology

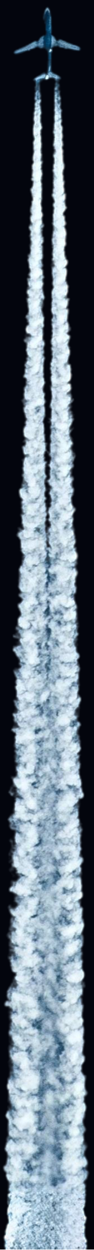

TUDelft

Data driven reduced order modelling of transonic buffet

Using invariant manifolds

by

Rahul Jayaraj

Student number:	5935156
Supervisor TU Delft:	Dr. Abel-John Buchner
Supervisor DLR:	Dr. David Quero Martin
Exam committee:	Dr. Abel-John Buchner Dr. David Quero Martin Dr. Dimitris Boskos Ms. Tea Vojković
Institution:	Delft University of Technology
Faculty:	Faculty of Mechanical Engineering, Delft
Project Duration:	December 2024 - September 2025

The thesis was carried out in collaboration with the German Aerospace Center/Deutsches Zentrum für Luft- und Raumfahrt e.V. (DLR).

"Somewhere, something incredible is waiting to be known."

— Carl Sagan

Preface

This thesis is the culmination of my Master's degree in Mechanical Engineering: Energy, Flow and Process technology, at Delft University of Technology and reflects a deep engagement with the complex dynamics of transonic buffet phenomena. Conducted in collaboration with the German Aerospace Center/Deutsches Zentrum für Luft- und Raumfahrt (DLR), the work explores an emerging and powerful approach to reduced order modelling using Spectral Submanifold (SSM) theory, using the method of spectra submanifold embedding. The objective was to develop a non-linear, data-driven, reduced order model that can accurately capture the unsteady flow dynamics characteristic of transonic buffet, a phenomena that continues to challenge both researchers and practitioners in the aerospace field.

The inspiration for this research arose from the recognition that conventional linear models fall short in describing the non-linearities and the growth of the non-linearities associated with buffet onset and progression, governed by Hopf bifurcations. This limitation presents a bottleneck in designing effective control strategies for mitigating buffeting and extending aircraft operational envelopes. Motivated by the need for physically consistent, yet computationally efficient models, SSM-based reduced order modelling methods were chosen as the means to create reduced order models for describing the phenomena. SSM-based methods have been investigated and used to describe the dynamics of various nonlinearizable phenomena with great success and possess a potential to capture the essential dynamics of transonic flow within a compact representation.

The work presented here has required a good mix of theoretical understanding and practical application conducted through the use of governing equations of compressible flow, turbulence modelling, invariant manifold theory and data regression techniques. Bridging these domains has not only broadened my academic perspective but also deepened my appreciation for the interplay between physics-based modelling and modern dynamical systems theory.

This research journey has been both intellectually rigorous and personally transformative. It is my hope that the insights offered by this thesis contribute meaningfully to the field of reduced order modelling, and that they encourage further exploration into modelling of more nonlinearizable systems using the SSM embedding methodology.

Rahul Jayaraj
Delft, September 2025

Acknowledgement

Looking back at the journey that this thesis has took me through, I find myself reflecting over the struggles and learnings I received. It was a long and arduous journey, and I could not have done it by myself. I had the support of so many talented and brilliant individuals who taught me, corrected me and have challenged me along the way, to have what I believe is, the culmination of my efforts. In the spirit of the timeless carnatic composition "*Entarō Mahanubhavulu... Andariki vandanamulu*", by Saint Thyagaraja which reveres the presence of great souls and offers salutations to all who walk the path of wisdom, I extend my heartfelt thanks to the many *mahanubhavulu* who have made this journey possible.

First and foremost, I would like to express my sincere gratitude to my academic supervisors, Dr. Abel-John Buchner at TU Delft and Dr. David Quero Martin at DLR. Their mentorship, expertise, and thoughtful insights not only guided the technical direction of this work but also challenged me to grow as a researcher. Their belief in scientific rigour and clarity of thought has left a lasting impact on my academic development.

I am grateful to Ms. Tea Vojković, who was my daily supervisor, for her support through each step of the way of this thesis. This thesis would not have been possible without her advice, mentorship and efforts.

I am equally grateful to the members of the thesis examination committee for their time and review, which have helped refine the final outcome of this thesis. I also wish to thank the researchers and staff at the German Aerospace Center (DLR) especially Mr. Cristoph Kaiser and Mr. Kristopher-Marc Davies who provided their immense support and expertise which paved the way to completeion of this work. The access to computational resources provided by them and the many technical discussions we had were invaluable in overcoming the challenges posed by this complex subject.

To my parents and sister, this would never be possible without your unwavering support, patience, and quiet strength. Even though you are a continent away, you were always up whenever I needed you.

To my friends and fellow students, thank you for the camaraderie, encouragement, and occasional distractions that helped keep this journey balanced and fulfilling.

To my dear girlfriend Rosmi, thank you for being my noot, my rock and for worrying over me. I would never have kept my sanity when things got chaotic, if not for you.

Finally, I dedicate this work to all those who seek knowledge not merely for its utility but for the joy of understanding. To all the mentors, collaborators, and kind souls I encountered along the way—*andariki vandanamulu*.

Abstract

On aircraft wings operating in the transonic regime, self-sustained shock oscillations brought on by shock wave–boundary layer interactions give rise to the phenomenon known as transonic buffet. The operational flying envelope is limited by the ensuing unstable aerodynamic loads, which, if unchecked, may cause structural fatigue or even catastrophic failure. The non-linear dynamics of Hopf bifurcations and limit cycle oscillations, which control buffet start and progression, are not sufficiently captured by traditional linear reduced-order models (ROMs), despite the fact that they have been used with varying level of success for buffet suppression, with the use of controllers. The current thesis builds a data-driven, non-linear, reduced order modelling framework for describing the transonic buffet dynamics, based on spectral submanifold (SSM) embedding, in order to get over this restriction.

The methodology implements the use of unsteady Reynolds-averaged Navier–Stokes (URANS) simulations, which simulate an n-dimensional dynamical system, combined with the use of an invariant manifold in n-dimensions, to construct compact and data-driven ROMs. First, steady and unsteady flow simulations are performed for a supercritical aerofoil across different Mach number–angle of attack combinations to identify the buffet onset boundary. Linear (eigenmode) analysis and Proper Orthogonal Decomposition (POD) are applied to extract eigenmodes and POD modes from the flow field, which are used to define a two-dimensional tangent space, to the n-dimensional manifold. The n-dimensional system dynamics, stored as flowfield data, can be projected onto this tangent space, creating a set of reduced coordinates through an encoder function. The dynamics of the system in the reduced coordinates are then captured with the help of an ordinary differential equation, obtained via polynomial regression. The pair of encoder function and the ordinary differential equations obtained, results in a reduced order model for the system. Both the linear and non-linear behaviour of the original system are captured and combined with a Taylor series expansion of the reduced coordinates to form a decoder function, which reconstructs the n-dimensional system output in the flowfield form. The identified ordinary differential equation is used to predict the evolution of reduced coordinates in the tangent space, while the decoder function enables the evaluation of the full flow field from the predicted reduced coordinates.

The validation of the obtained ROM is carried out against independent URANS simulations with alternate initialization condition, for each flow condition evaluated. The results show that the SSM-based ROM is capable of accurately reproducing limit cycle oscillations and reconstructing full flowfields with good accuracy. The reduced order model predictions and the reconstructed flowfields obtained from it show good agreement with actual features of the buffet phenomena like shock location at various points in time.

This work establishes the use of spectral submanifold embedding as a promising tool for constructing non-linear ROMs of transonic buffet. The developed framework provides new opportunities for real-time prediction and control of buffet phenomena. Beyond aerospace applications, the methodology has broader potential for analysing other nonlinearizable fluid–structure interaction problems.

Contents

List of Figures

List of Tables

Nomenclature

Abbreviations

Abbreviation	Definition
SWBLI	Shock wave-boundary layer interaction
LCO	Limit cycle oscillation
POD	Proper orthogonal decomposition
SSM	Spectral submanifold
ODE	Ordinary differential equation
URANS eq.	Unsteady Reynold's Average Navier-Stokes equations
CFL no:	Courant–Friedrichs–Lewy number
ROM	Reduced order model

Symbols

Symbol	Definition	Unit
Ma	Mach number	
C_L	Coefficient of lift	
C_p	Coefficient of pressure	
Re	Reynolds number	
α	Angle of attack	[degree]
ω	Complex frequency of eigen mode	[s^{-1}]
γ_0	Growth rate of eigen mode	[s^{-1}]
ω_0	Frequency of eigen mode	[s^{-1}]
ρ	Density	[$\mathrm{kg/m^3}$]
T	Absolute temperature	[K]
ρu	Momentum in x direction	[kg.m/s]
ρw	Momentum in z direction	[kg.m/s]
ρE	Energy density	[kg.m/s]
$\rho\tilde{\nu}$	Eddy viscosity	[kg/m.s]

1

Introduction

Since its introduction to society more than a century ago, air travel has reshaped history and revolutionized mobility. The global aviation industry is projected to have 5 billion passengers in 2025; a 6.7% increase from the previous year. Due to the nature of mobility, safety has always been of paramount importance in the aviation industry. Those aeroplanes whose propulsion is provided by jet engines, have an operating speed between Mach numbers (Ma) 0.6 – 1.2. In this operation range, known as the transonic region, regions of subsonic and supersonic airflow maybe present around the air plane wing/the aerofoil cross-section of the wing. When an aeroplane hits the speed of sound and it overtakes the pressure disturbances produced due to its motion through the air, the air in front gets no warning. The aircraft then generates a shock wave as it forces through the air, causing the air's temperature, density, and pressure to rise suddenly and sharply across the shock. Due to the presence of shock waves in the supersonic regions in the transonic regime, large scale flow separation may occur downstream of the shock on the aerofoil. These shock waves, can impinge onto an aerofoil surface and interact with separated boundary layer creating a shock wave-boundary layer interaction (SWBLI). Frequently, these SWBLI's give rise to flow unsteadiness. This unsteadiness results in large amplitude self-sustained oscillations of the shock, known as buffeting. The oscillation frequency of the shock front is called buffet frequency. The buffet phenomena occurring over a supercritical aerofoil is represented in figure 1.1, taken from Scharnowski et al. [62]. In this image, the start of the buffet phenomena can be seen, when the shock causes an adverse pressure gradient to form, which results in flow separation of the boundary layer downstream of the shock, represented by the top-left image of figure 1.1. This flow separation causes the shock to incline and move upstream as shown in the top-right image of figure 1.1. The further the shock moves upstream towards the leading edge of the aerofoil, the higher the pre-shock Mach numbers become, causing pressure to increase across the shock, and hence the shock strength too. The most upstream position of the shock is represented in the bottom-right image of figure 1.1. At this point, the boundary layer separation collapses and it reattaches to the surface of the aerofoil, causing the shock to move downstream, until the boundary layer separation occurs again, repeating the cycle, represented by the bottom-left image of figure 1.1. The mechanism behind the boundary layer reattachment and the shock oscillation has been investigated in detail by various people including Lee et al. [42], who reasoned the shock oscillation occur due to acoustic wave propagation from trailing edge and its interaction with the shock resulting in the shock oscillation. Another proposed mechanism involves the instability of the global mode of the flow, which results in a phase locked motion of the shock, as explained by Crouch et al. [17]. Other explanations which involve a separation bubble formation, expansion and collapse which causes the shock oscillation were investigated by Raghunathan et al. [58]. The model proposed by Crouch, has found a excellent agreement against the experimental investigations done by McDevitt & Okuno [47] and is widely accepted.

The mechanics of buffeting, as introduced by Crouch et al. [17], involve a supercritical Hopf bifurcation. A supercritical Hopf bifurcation occurs when a stable system slowly changes as a control parameter is varied, causing the stable state to become unstable, which results in a stable oscillation, which grows

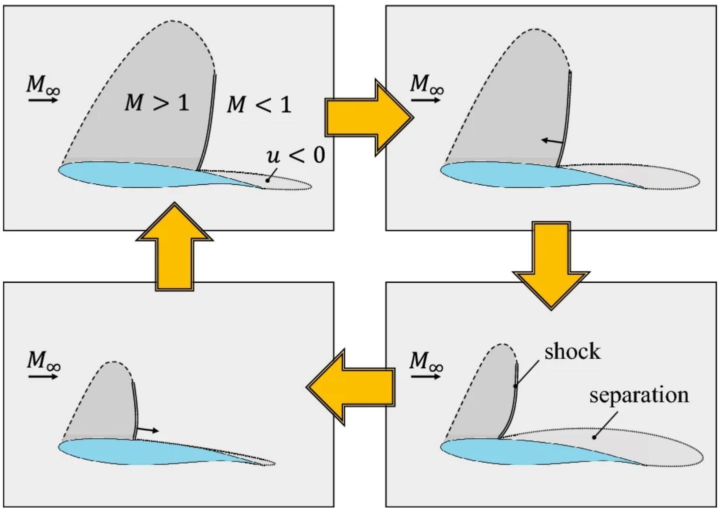

Figure 1.1: A typical shock wave–boundary layer interaction (SWBLI) on a transonic wing causing buffeting as represented in Scharnowski et al. [62]. The buffet cycle is represented in sequence as follows:- Top-left: Shock causes flow separation, top-right: flow separation causes shock incline and upstream travel, bottom-right: Shock strength and pressure increases causing separated boundary layer to reattach, bottom-left: the shock moves downstream again.

gradually into to fixed amplitude oscillation (called a limit cycle) appearing around the old stable point. For an aerofoil, on increasing the angle of attack (α) above a critical angle of attack value (α_c), at a constant free stream Mach number, an instability can been seen being produced in the system, which results in the gradual growth of oscillation of the shock boundary, into a limit cycle oscillation behaviour, indicating a supercritical Hopf bifurcation beyond that critical angle of attack. It had been observed that any perturbations introduced to such an unsteady system consisting of oscillations of the flow field (as what is seen in buffeting), will grow in a weakly non-linear manner before settling into an unsteady, oscillating system as stated in Crouch et al.[16]. Such an evolution of the system indicates the non-linear nature of shock buffeting phenomena too.

Comparing a 2D aerofoil and 3D wing, it was described in Paladini et al. [53] that buffeting appears in span wise-discrete areas or "buffet cells" with shocks that ripple and travel along the span of the 3D wing. For this study only 2D aerofoil profiles are considered, where buffeting results in periodic variation of the aerodynamic loads acting on it. These varying aerodynamic loads, due to its interaction with the structure of the wing, could result in failure due to fatigue, as stated in D'Aguano et al. [19] and Giannelis et al. [29]. The aeroelastic vibrations resulting from the varying aerodynamic loads, could damage the wing by weakening its structural integrity and in extreme cases, failure. To avoid such critical structural failures and to increase the safety of the passengers, buffeting needs to be reduced/suppressed. Buffet control is critical for ensuring aircraft safety, as buffeting can restrict the flight envelope and jeopardize wing structural integrity. Methods for controlling buffet fall into two main categories: passive and active. Passive control techniques, as outlined by Gao et al. [25], utilize devices like mechanical vortex generators and shock control bumps to modify the wing's geometry. These modifications help delay the onset of buffet but are generally effective only at specific operational points and are unable to eliminate buffeting entirely.

Active control approaches, in contrast, use external energy sources to dynamically adjust boundary layer conditions and suppress buffet. Illustrative examples include actuators for trailing-edge devices, as discussed by Gao et al. [26], and fluidic vortex generators, demonstrated by Dandois et al. [20]. Active strategies can be implemented using either open-loop or closed-loop control systems, with closed-loop controllers being particularly advantageous. Closed-loop controllers constantly adapt their inputs in response to real-time feedback, making them well-suited to managing flow instabilities that characterize buffeting. These controllers can be further classified as model-based or model-free. Model-based controllers depend on mathematical or data-driven models of the flow, while model-free approaches do not require explicit models. For real-time control applications, low-dimensional reduced-order models are often preferred in model-based control because they offer a favourable balance between computational efficiency and the ability to capture essential physical behaviours.

Within the scope of closed-loop buffet control, model-based approaches draw on several types of flow models. These include high-fidelity models, which are based on discretized Navier-Stokes equations; low-dimensional reduced-order models, which approximate the key physics of the system; and input-output models, such as those utilizing neural networks [73]. While high-fidelity models offer high accuracy, their significant computational demands make them impractical for real-time control of the complex dynamics involved in buffeting. Input-output models, although flexible, typically lack a direct connection to the underlying physics, which can limit their effectiveness and robustness when designing control laws. Reduced-order models are therefore generally the preferred choice, as they effectively reduce computational requirements while retaining important physical insights, enabling the development of reliable and efficient real-time buffet control strategies [26].

As previously stated, the growth of the perturbation in an unsteady system follow a weakly non-linear trend, where disturbances are small but non-linear effects start to curb the linear exponential growth and set a finite amplitude. The non-linear growths of perturbations in the flow field can be modelled by Stuart-Landau like equations. These equations are based on a global weakly non-linear analysis of the flow, which are governed by the evolution of the most dominant global mode. The dominant global mode, captures the spatial structure of the instability along with its complex eigenvalue that sets growth rate and frequency. Evolution of global mode in time, paired with Stuart-Landau like equations were used in Thompson et al. [69] and in Sipp et al. [64] to create a model, used to describe the oscillatory behaviour of Von Karman vortex shedding, beyond a critical Reynold's number, indicating that the oscillatory vortex shedding is a case of supercritical Hopf bifurcation. The model developed by Sipp et al. [64] was then extended to include an external forcing parameter used for controlling the vortex shedding seen in the wake of the cylinder, making it suitable for closed loop control as shown in Vojković et al. [73]. There have been attempts to model the non-linear growth of parameters like the coefficient of lift (C_L) using Stuart-Landau equation, as seen in Crouch et. al.[16], but this methodology fails to properly implement weakly non-linear analysis using the amplitude evolution of the dominant global mode and instead uses the magnitude of coefficient of lift (C_L). Efforts to create a reduced order model using SINDy technique (Sparse Identification of Non-linear Dynamics, which learns parsimonious governing equations from time-series data by selecting terms from a candidate function library), coupled with the use of DMD modes (Dynamic Mode Decomposition, a data-driven spectral decomposition that extracts coherent spatio-temporal modes with associated growth rates and frequencies from snapshot data) to capture the dynamics as investigated by Sansica et. al. [60], failed to capture and predict the non-linear growth of instabilities. Other attempts include the previously mentioned controllers developed by Gao et al. [26], Dandois et al. [20] which are based on linear control laws, also fail to capture the non-linear growth of instabilities and are only applicable in the limit cycle oscillation region of the buffet. Since these current models for control, fails to account for this non-linear behaviour of the growth of the instability in the flow field, a new model is required to accurately describe the unsteadiness and its growth. The most promising technique would have been the use of weakly non-linear analysis using the time evolution of the amplitude of the global mode, to generate a Stuart-Landau like reduced order model for buffeting, but due to a lack of a well-developed closed form equation governing the flow in a Hopf bifurcation for a transonic buffet case, alternatives means/methods are to be investigated.

An alternative method for producing a reduced order model was described by Haller and Cendese [32, 14], where non-linear dynamical systems like vortex shedding for flow past a cylinder, fluid sloshing in a tank etc were considered. These non-linear systems cannot be linearized without losing out on some defining dynamics and are also called non-linearizable systems. The method implemented by Haller and Cendese [32, 14], involves the use of Spectral submanifold embedding, which utilizes spectral sub manifolds (SSM, an n-dimensional topological space), by reducing the n-dimensional system which defines the non-linearizable case considered, onto a lower two (or d) dimensional tangent plane, where the complete reduced dynamics of the full system can be captured for all time t. SSM embedding has thus been used to generate a low dimensional reduced coordinates, using an encoder function, which are used to define a higher dimensional system dynamics. These reduced coordinates which capture the evolution of the dynamics of the higher dimensional system are used to reconstruct the higher dimensional system using Taylor series expansions of the reduced coordinates, which acts as a decoder function. A mapping function or an ordinary differential equation (ODE) is defined to describe the evolution of the reduced order coordinates in the spectral sub manifold. The combination of the encoder function and the map/ODE produce a reduced order model, and used to predict the dynamics in the reduced coordinates. These predicted reduced coordinates can be used with the decoder function defined, to reconstruct and predict the higher dimensional dynamic system. This has been implemented to great success, for various cases in [14].

The aim of this master's thesis is thus to generate a non-linear reduced order model for flow around an aerofoil in transonic buffet region of operation (at a particular Ma-AOA combination), based on a data driven modelling procedure using the spectral submanifold embedding, to obtain the time evolution of reduced coordinates as well as the time evolution of the full state variables using the mapping function obtained.

2

Investigation of the problem, its details and current solutions

2.1. Transonic shock buffeting: A brief overview

Within a narrow band of transonic-flight conditions between the Mach numbers (Ma) of $0.6 - 1.2$, both subsonic and supersonic airflow can exist around the aircraft's wings or the aerofoil cross-section. As an aeroplane approaches the speed of sound, it begins to overtake the pressure disturbances it creates while moving through the air. Consequently, the air ahead receives no advance warning, and the aircraft must force its way through, generating a shock wave. This shock wave causes a sudden and significant increase in the air's temperature, density, and pressure.

Within the transonic regime, shock waves may form in the supersonic regions around the aerofoil, often leading to large-scale flow separation downstream of the shock. At certain combinations of Mach numbers and angles of attack (α) these shock waves impinge on the aerofoil surface and interact with the intermittently separated boundary layer, a phenomenon known as shock wave–boundary layer interaction (SWBLI) occurs. Such interactions frequently induce flow unsteadiness, resulting in large-amplitude, self-sustained oscillations of the shock—an effect known as buffeting. During buffeting, the shock front is seen to oscillate about a mean position, on the suction side and sometimes the pressure side of the aerofoil. This oscillation occurs at a certain frequency referred to as the buffet frequency. Buffeting reduces the flight envelope i.e. safe operational range of airspeeds, load factors etc. due to it being detrimental to the structural integrity of the aircraft wings due to the production of dynamic loads leading to fatigue failure. Thus buffeting can be stated as a limiting factor to aircraft performance and leads to lowered handling capabilities and fatigue life [29] [19].

The shock buffet cycle visualization is given in figure 2.1, where the shock starts from the most upstream position given in (a) indicated by the horizontal white arrow pointing to the same, and moves until the most downstream position in (b), before moving back to the upstream position. Figure figure 2.1(a) shows a typical lambda-shaped region associated with transonic shock wave/boundary-layer interaction. The white area represents a boundary layer that develops along the slip line originating from the shock foot region. The separated boundary layer above the profile, also indicated by a vertical white arrow, located behind the shock and depicted in black, is also visible. As the shock wave moves upstream, its strength increases (corresponding to higher local pre-shock Mach numbers), resulting in greater flow separation.

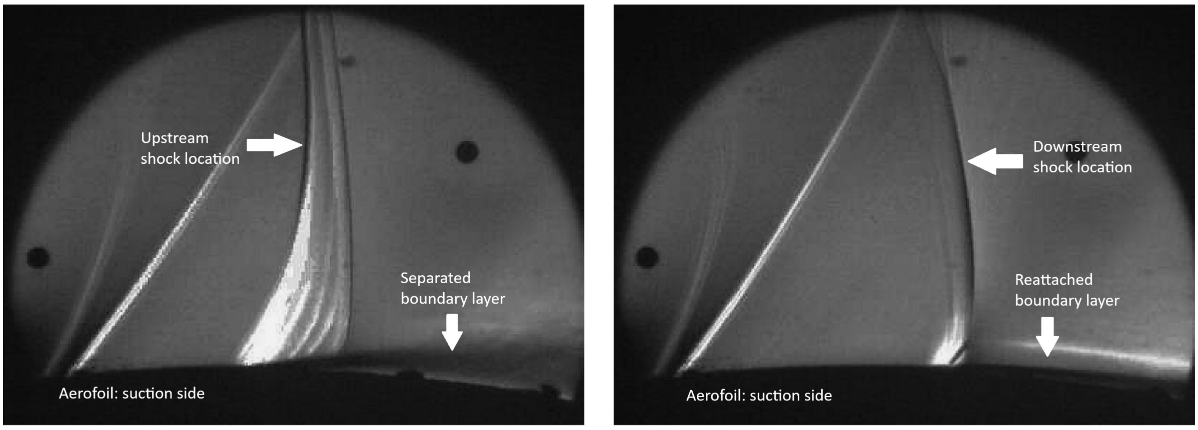

a) Shock at the most upstream location **b) Shock at the most downstream location**

Figure 2.1: Instantaneous schlieren images of OAT15A for Ma= 0.73, α = 3.5° from [35]. (a) represents the shock position at the most upstream location during oscillation and (b) represents the shock position at the most downstream location during oscillation. The bottom of the image beneath the shock foot, shows the suction side of the aerofoil. The white area represents boundary layer that develops from the foot of the sock and the separated boundary layer is represented in black, found above the aerofoil boundary. A pair of horizontal white arrows represent and name the extreme positions of the shock during its motion, while a pair of vertical white arrows indicate state of the boundary layer for the extreme positions of shock motion.

2.2. Non-linear dynamics involved in transonic buffeting

The mechanism behind transonic buffeting involves the growth of an instability, eventually reaching a self sustained oscillatory behaviour which are governed by non-linearities. The details of the mechanism and how it is connected to non-linear dynamics are described in detail in the upcoming sections of this chapter. To understand those relations some elementary knowledge on non-linear dynamics, bifurcation theory etc., are needed. These include concepts like limit cycles, bifurcations, Hopf bifurcations, Stuart-Landau equations, invariance and invariant manifolds, which are discussed in detail in the next part.

2.2.1. Limit cycles

A limit cycle is an isolated closed trajectory or an isolated periodic solution towards which neighbouring states might tend towards, when stable. Limit cycles are inherently non-linear phenomena, i.e. they cannot occur in a linear system. A limit cycle thus models systems that exhibit self-sustained oscillations. If any trajectory near the limit cycle (and not on it), approaches the limit cycle, then the limit cycle is stated to be stable or attracting. If the trajectory repels away from the limit cycle, it is an unstable limit cycle. The various types of limit cycles are depicted in figure 2.2.

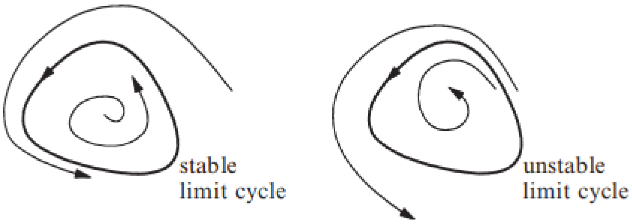

Figure 2.2: Different types of limit cycle as given in [65]. A stable and unstable limit cycle is represented respectively.

2.2.2. Bifurcations

For a system where the dynamics of the vector field associated with it is dependent on parameters, when the parameters are varied, the qualitative structure of the vector field itself is changed. More specifically, fixed points can be created or destroyed in the system for a one-dimensional system, and closed orbits can be created, destroyed or destabilized for two-dimensional systems. The qualitative structural changes in the vector field which occur in the system due to change in parameter values are called bifurcations, and the parameter values at which it occurs are called bifurcation points. Bifurcations are defined in all dimensions, but all the action is confined to a one-dimensional subspace along which the bifurcations occur, while in the extra dimensions the flow is either simple repulsion or attraction from that one-dimensional subspace [65]. For the purpose of considering the transonic flow around a 2D aerofoil, the bifurcations defined in the system having two-dimensional subspace is considered.

Hopf bifurcation

Consider a two-dimensional linear system dependent on a parameter μ, having the following form,

$$\begin{aligned}\dot{x} &= f_\mu(x, y)\\ \dot{y} &= f_\mu(x, y)\end{aligned} \tag{2.1}$$

where μ is a parameter. Suppose it has a fixed point$(x, y) = (x_0, y_0)$, which may depend on μ. The eigenvalues of the Jacobian of this system, at its fixed point, is the key to determining when the system loses its stability as the parameter μ varies. If the fixed point remains stable, then both the eigenvalues λ_1 & λ_2 need to lie on the left half plane of the Re(λ)-Im(λ) plane or Re(λ)< 0. Since the λ's satisfy a quadratic equation with real coefficients, there are two possible situations: either both the eigenvalues are both real and negative or they are a complex conjugate pair as shown in figure 2.3.

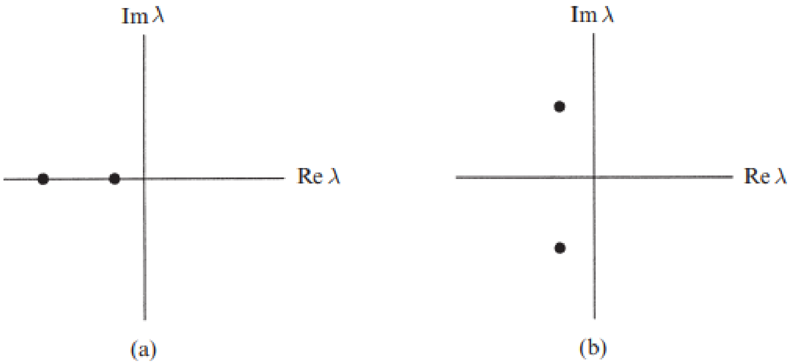

Figure 2.3: Types of eigenvalues in Hopf bifurcation as given in [65]. (a) Shows the pair of eigenvalues being both real and negative and (b) shows the pair of eigenvalues being a complex conjugate pair.

To destabilize the fixed point, one or both the eigenvalues have to cross into the right half-plane by varying, μ i.e. Re(λ)> 0. This can lead to two types of Hopf bifurcation to form:

1. Supercritical Hopf bifurcation: where, the physical system whose decay rate depends on the parameter μ and has an equilibrium state, will lose the equilibrium state at $\mu = \mu_c$. Small disturbances in the system will thus dampen out when $\mu < \mu_c$ and will grow when $\mu > \mu_c$. It can also be described as occurring when a stable spiral changes into an unstable spiral surrounded by a small, nearly elliptical limit cycle (near the critical parameter region). The effect of parameter in a supercritical Hopf bifurcation is shown in figure 2.4 and figure 2.6.

2. Subcritical Hopf bifurcation: where after the bifurcation or when the parameter $\mu > \mu_c$, the trajectories of the system jump to a distant attractor, which is a limit cycle, making the system destabilizing. When $\mu < 0$ there are two attractors: a stable limit cycle and a stable fixed point. These two attractors are separated by an unstable limit cycle. The unstable cycle shrinks to zero

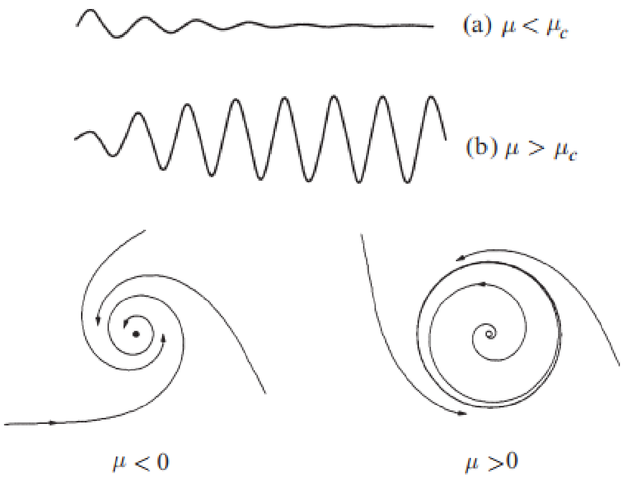

Figure 2.4: Effect on disturbances with change in parameters and impact of parameters in limit cycles, in supercritical Hopf bifurcation as given in [65]. The top image (a) represents the decay of instability when $\mu < \mu_c$ and (b) represents the growth of instability when $\mu > \mu_c$. The bottom image represents the settling on system to a stable fixed point when $\mu < \mu_c$ and the growth of the system to a limit cycle when $\mu > \mu_c$.

amplitude and engulfs the fixed point at $\mu = \mu_c$ and for $\mu > \mu_c$ the system switches to a large amplitude limit cycle, as shown in figure 2.5 and figure 2.6.

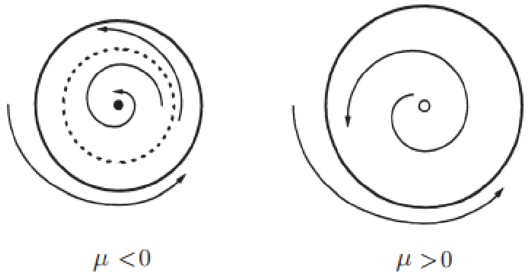

Figure 2.5: Impact on limit cycles due to parameters in subcritical Hopf bifurcation as given in [65]. The image represents two systems, where the left system represents when $\mu < 0$, and has two attractors: a stable limit cycle and a stable fixed point, separated by an unstable limit cycle. The right image represents the system where $\mu > \mu_c$, which causes a switch to a larger amplitude limit cycle.

2.2.3. Invariance and Invariant Manifolds

A subset $\mathcal{M}$ of the state space of a dynamical system is said to be *invariant* if every trajectory that starts in $\mathcal{M}$ remains in $\mathcal{M}$ for all future (and past) times. Invariance is a key requirement for any reduced model to faithfully replicate the system's dynamics. A manifold is a topological space that, around every point, resembles Euclidean space of a fixed dimension. This means that although a manifold may have a complex global structure, such as having a curvature, holes, or even twisting locally (in a sufficiently small neighbourhood of any point) but a local region on the manifold can be mapped in a one-to-one, continuous, and invertible way to standard flat space ($\mathbb{R}^n$). An *invariant manifold* is a differentiable submanifold of the phase space that is invariant under the dynamics. Formally, if $\phi_t(x)$ is the flow map of the system, then a manifold $\mathcal{W}$ is invariant if $\phi_t(x) \in \mathcal{W}$ for all $x \in \mathcal{W}$ and $t \in \mathbb{R}$ (or $t \geq 0$ in dissipative cases).

It has been previously discussed on how a Hopf bifurcation arises when a pair of complex conjugate eigenvalues of the Jacobian at an equilibrium crosses the imaginary axis as a parameter varies, leading to the birth of a small-amplitude periodic orbit (limit cycle) as the equilibrium loses or gains stability.

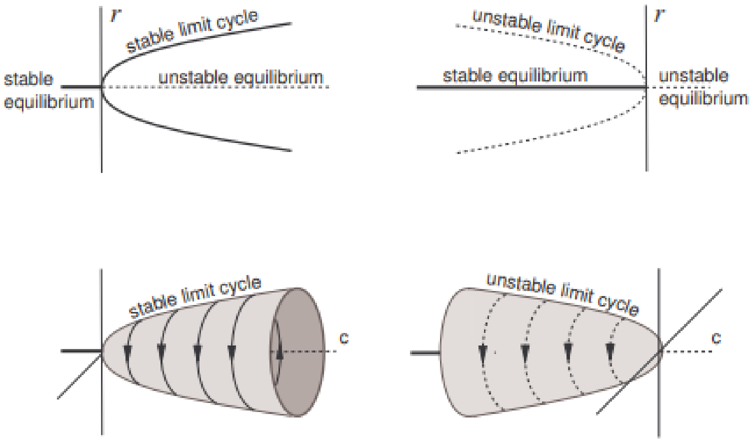

Supercritical (a<0) Subcritical (a>0)

Figure 2.6: A bifurcation diagram indicating a supercritical Hopf bifurcation on the right side images and a subcritical Hopf bifurcation on the left side images, from [34]. Here $a = \mu$, which represents the control parameter. The supercritical Hopf bifurcation diagram shows how the dynamics move from a stable equilibrium to a stable limit cycle behaviour on change of control parameters, while the subcritical Hopf bifurcation diagram shows how the system switches to a large amplitude unstable limit cycle on change of control parameters

Near such a bifurcation, the dynamics of the full system are governed by a two-dimensional centre subspace associated with the purely imaginary eigenvalues. According to the centre manifold theorem as discussed in Yuri et al.[40], there exists a smooth two-dimensional invariant manifold W^c, tangent to this subspace at the equilibrium. All nearby trajectories rapidly contract onto W^c, except possibly along unstable directions, meaning that the essential non-linear dynamics of the bifurcation are captured by the behaviour on this low-dimensional manifold. This indicates how the Hopf bifurcation and invariant manifolds are closely connected, and how together they form a powerful framework for reduced-order modelling of oscillatory dynamics.

The reduction to W^c allows the full n-dimensional system $\dot{x} = f(x, \alpha)$ to be represented by a two-dimensional complex normal form, which describes the amplitude and phase evolution of oscillations. On W^c, the dynamics can be expressed in a simplified form, typically

$$\dot{z} = (\mu + i\omega_0)z + l_1 z|z|^2 + O(|z|^4) \tag{2.2}$$

where $z \in \mathbb{C}$ is a reduced coordinate, μ is the bifurcation parameter, and l_1 is the first Lyapunov coefficient that determines whether the bifurcation is supercritical (stable limit cycle) or subcritical (unstable limit cycle). This reduced normal form captures all qualitative features of the Hopf bifurcation, including the emergence and stability of the limit cycle, while discarding irrelevant higher-dimensional dynamics.

Invariant manifolds, and particularly centre manifolds, are therefore a natural tool for reduced-order modelling. Since all bifurcation phenomena are confined to W^c, constructing a reduced system on this manifold is sufficient to understand the behaviour near the critical point.

2.3. Shock buffet, its mechanics and associated models describing the mechanics

2.3.1. Types of shock buffets, the physics involved and need for buffet control

Types of shock buffets

There are two distinct types of shock buffet that were identified to occur on 2D aerofoils.

1. **Type I buffet**: typically occurs at zero incidence on biconvex sections and encompasses shock oscillations on both the pressure and suction surfaces of an aerofoil. Shock wave-Boundary layer interactions (SWBLI's) happen on either side of the aerofoil, and it initiates a phase-locked oscillations in opposite directions. Through the investigation of Mabey [45] and Gibb [30], a working model of type I buffet has already been developed which involves the weakening of the shock on the suction side as it moves upstream. The shock motion on the lower surfaces occurs in an identical manner, with a 180° phase shift. These pair-of-shock-motions yield a self-sustained shock buffet cycle.
2. **Type II shock buffet**: is characteristic of modern supercritical aerofoils and involves upper surface shock oscillations at non-zero angles of attack. Many categorizations were made for type II shock. Some of these include classifications made by,
    (a) Pearcey & Holder: [54],[55],[56]: Two models of phenomena were identified for type II shock buffet according to Pearcey & Holder:
        i. Model A- consisting only of a shock-induced separation bubble: the bubble bursting by extending to the trailing edge through divergence of trailing edge pressure was studied.
        ii. Model B- for which trailing edge separation is either additionally present or incipient, with:
            - Rear separation provoked by the formation of a bubble
            - Rear separation provoked by the shock
            - Rear separation is present from the outset

        These models proposed by Tijdeman is represented in figure 2.7. In this image, the time evolution of the bubble growth and eventual collapse in model A is represented in under the title of original model A, from plots 0-VI. The various mechanisms for model B is represented under the titles rear separation, rear separation provoked by the shock and rear separation already present respectively. The time evolution for each of these mechanisms are also given vertically below one another.

    (b) Tijdeman [71]: Tijdeman characterized three distinct modes of shock through his experimental investigations of NACA 64A006 aerofoil. These include:
        i. Type A shock motion: which is represented by near sinusoidal shock oscillations on the suction side of the aerofoil, where the shock strength varies throughout the buffet cycle. The maximum strength of shock is achieved in the upstream excursion of the shock. Type A shock motion was described by Lee's model in [42], through an acoustic wave-propagation mechanism, and Crouch's model in [17], using global instability analysis, both of which are described in detail in section 2.3.1.
        ii. Type B shock motion: which resembles type A, but the magnitude of shock strength variation is much larger. This means that the shock disappears on its travel downstream and reappears when moving upstream. A mechanism for type B was proposed by Raghunathan et al. [58], which proposes an unstable shock-wave/separation bubble interaction. The shock must be strong enough to create a separation bubble, whose appearance initiates the periodic motion of shock. The shock oscillation is sustained through the alternating expansion and collapse of the bubble on the upper aerofoil surface. The trailing edge is crucial in communicating flow states between the suction

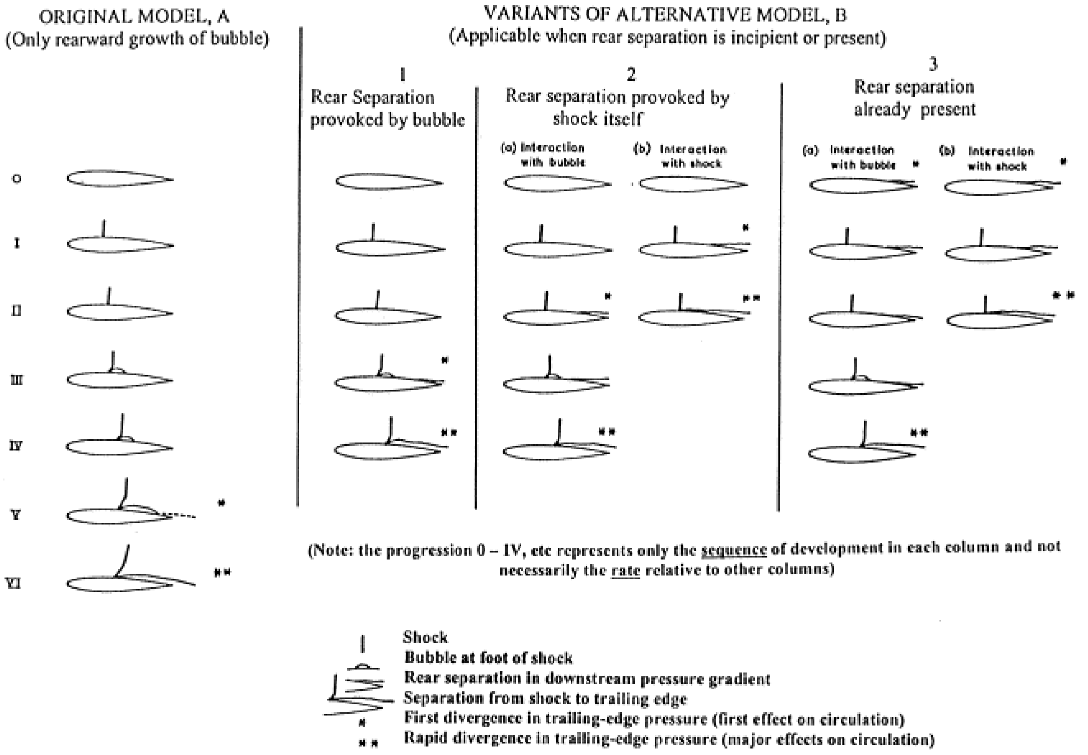

Figure 2.7: Model A and Model B flow separation according to Pearcey et al. [31]. Model A section shows the evolution of the bubble bursting mechanism and Model B section shows how three separate phenomena involving the (1) rear separation provoked by bubble formation, (2) rear separation due to shock formation and (3) rear separation being already present from the outset

and pressure surfaces, and the varied extent of the separated zone alters the aerofoil's effective camber throughout the cycle.

iii. Type C shock motion: Here, the shock travels upstream, initially strengthening and then weakening, but continuing to move forward, eventually propagating forward into the oncoming flow as a free shock-wave. A mechanism for type C shock buffet was proposed in Lee et al. [43]. This proposed mechanism involves the weak compression waves coalesce to form a shock which moves upstream into the flow. After exiting from the leading edge of the aerofoil, weak compression waves are formed again and the process repeats itself.

The Tijdeman shock types are represented in figure 2.8.

Since the mechanism for biconvex aerofoils was already researched and defined in Mabey [45] and Gibb [30], the focus of all further investigations for the past couple of decades has been to the type II shock buffets occurring in super critical aerofoils. Hence, all further studies in this investigation will be done for type II shock buffets, occurring on a supercritical aerofoil. Since the governing models proposed for explaining the behaviour of type II shock buffets, in literature including Lee[42], Crouch et al.[17], Crouch et al.[18], investigate the behaviour of the Tijdeman type A shock motion, the same has been considered for all investigations herein.

Governing physics proposed for type II-Tijdeman type A transonic buffet

There are many prevailing theories that propose various methods of onset of type II-Tijdeman type A shock buffet, which are seen in transonic flow conditions around a supercritical aerofoil. The dominant and widely accepted theories regarding the same, as per Giannelis et al.[29], are stated below:

Model 1: Lee's model The model proposed by Lee [42] establishes that the periodic oscillations of the shock waves due to the SWBLI is caused by a feedback loop involving acoustic wave propagation. This

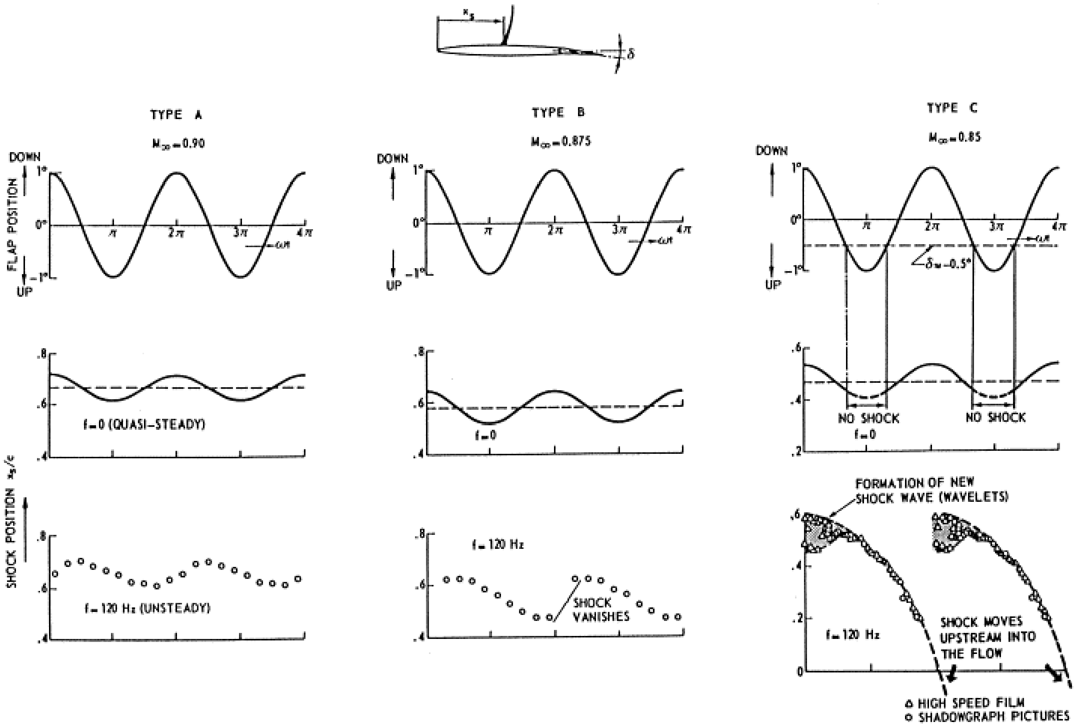

Figure 2.8: Types of periodic shock wave motion represented in Tijdeman et al. [71]. Type A represents a shock which oscillates with a nearly sinusoidally varying frequency and varying shock strength. Type B represents a shock motion where it periodically disappears during its downstream excursion. type C represents the shock motion where upstream propagation periodically occurs.

model enabled the prediction of shock oscillation frequency of the Tijdeman type A shock motions. The disturbances arising from the SWBLI, generated at the shock, are advected downstream and grow in their amplitude on the way through the separated boundary layer. These disturbances then trigger upstream pressure waves at the trailing edge, satisfying the unsteady Kutta condition, thus closing the feedback loop. One of the key features of a shock buffet is the oscillation frequency for the shock or its inverse, the time period taken for a shock oscillation cycle to complete. The shock cycle period is calculated as the sum of the total propagation time of the shock upstream and downstream. i.e. for an aerofoil with a chord length of c, where the mean shock location occurs at a length of x_s,

$$\tau = \int_{x_s}^{c} \frac{1}{a_p} dx - \int_{c}^{x_s} \frac{1}{a_u} dx \tag{2.3}$$

where τ is the period of buffet cycle, a_u is the stream propagation velocity and a_p is the velocity of the downstream propagating pressure waves.

The problem with Lee's model[42] is that the model underestimated the buffet frequency, found through the inverse of time period obtained from equation (2.3) through the use of LES simulations , by approximately 60% when compared to the experimental data obtained from [36], for the OAT15A aerofoil by Garnier & Deck [28]. To accommodate for this, a modified model was proposed that accounts for upstream propagating pressure waves travelling not only along the upper surface but also along the lower surface and around the leading edge. Although it did improve buffet frequency predictions to 36% of deviation compared to the LES data, it suggested that there was a fundamental lack of robustness in the original model proposed by Lee [42].

Model 2: Crouch's model The model proposed by Crouch [15],[17],[18] states that the mechanism dealing with the shock buffet involves the instability of a global aerodynamic mode. A global mode decomposition of the steady transonic flow field under pre-buffet conditions identifies a marginally

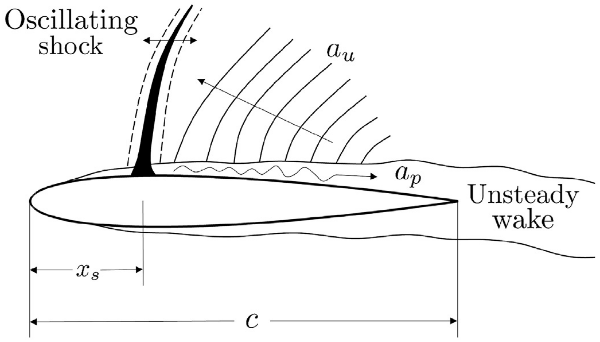

Figure 2.9: Model of self-sustained shock oscillation (adapted from Lee[42]).The shock buffeting occurs due to feedback from acoustic waves propagated from trailing edge. Here, a_u is the stream propagation velocity and a_p is the velocity of the downstream propagating pressure waves. The aerofoil has a chord length of c, where the mean shock location occurs at a length of x_s.

stable eigenvalue associated with the flowfield components. As the angle of incidence increases, a Hopf bifurcation causes this eigenvalue to cross into the unstable regime, leading to phase-locked oscillations of the shock and the separated boundary layer. To understand this model, a brief review of non linear dynamics, bifurcation theory, and the mathematical framework for global stability analysis is required, which has been done in section 2.2. The model is described in detail in upcoming sections.

Other models: The qualitative flow characteristics outlined by Crouch et al. [18] are exactly included in the improved wave propagation model put out by Jacquin et al. [35]. Nitzsche [48] discovered that a natural resonance in the steady transonic flow field might be the cause of shock oscillations in a linear sense.

2.3.2. A detailed look into Crouch's model and its validation

A moderately stable eigenvalue associated with the flowfield components is obtained by global mode decomposition (using global stability analysis), of the steady transonic flow field under pre-buffet conditions. This eigenvalue crosses the stability limit with increasing angle of incidence as a result of a Hopf bifurcation, which results in phase-locked shock motion and a separated boundary layer.

Global stability analysis used in Crouch's model

Global stability analysis methodology was performed by Crouch et al. [17] for evaluating the global modes of an aerofoil. As per the evaluation done in Crouch et al. [17], two-dimensional, viscous, compressible flows were considered, where the chord Reynold's number of the aerofoil is $Re_c \approx O(10^{6-7})$. For these high Reynold's numbers, the boundary layer on the aerofoil is turbulent. At these conditions, the time scales of interest (of the buffet oscillations) is much smaller than the characteristic eddy time scales. Thus, Unsteady Reynold's Average Navier-Stokes (URANS) equations were chosen as defined in section 3.1.2, with the effect of turbulence of the boundary layer was modelled to provide closure to the Reynold's stresses in the URANS, by a turbulence model. The turbulence model chosen by Crouch et al. [17] was a single-equation, eddy-viscosity based model called Spalart-Allmaras (S-A) model, with compressibility correction to account for the discontinuity faced in the shock region. The URANS and the closure equations, can also be expressed in the terms of the following state vector, as stated in Crouch et al. [17]:

$$q = \{\rho, u, v, T, \tilde{\nu}\} \tag{2.4}$$

where the ρ represent the density, u and v are the stream wise and transverse velocities respectively, T is temperature and $\tilde{\nu}$, the modified viscosity.

This state vector can be decomposed into the mean ($\overline{q}$) flow and a fluctuating (q') component, such that:

$$q = \overline{q} + q' \tag{2.5}$$

On assuming the linearization of the governing URANS equations, it is then assumed that the fluctuations in the mean flow (q') behaves like small perturbations. The complete set of equations can thus be expressed in the simplified operator form.

$$\frac{\partial}{\partial t}A[q'] + B_{\overline{q}}[q'] = 0 \tag{2.6}$$

where A is a linear operator consisting of the time derivatives of the URANS equations, while $B_{\overline{q}}$ is a linear operator that includes the linear terms of URANS as well the non-linear coupling terms present due tot the interaction between $\overline{q}$ and q'. These perturbations to the mean flow field $\overline{q}$ may be described by time-harmonic aerodynamic modes:

$$q'(x, y, t) = \hat{q}(x, y) \cdot e^{-i\omega t} \tag{2.7}$$

where $\hat{q}$ is the eigenfunction representing the mode shape while ω is the frequency. Conditioning this result using a matrix (W), as defined in Crouch et al. [17] the following is obtained,

$$-i\omega\hat{q} + L(\overline{q}) \cdot \hat{q} = 0 \tag{2.8}$$

Where L is a second-order differential operator.

Equations equation (2.8) , describes an eigenvalue problem which are solved to find the complex frequency ω and the aerodynamic mode shape $\hat{q}$. The complex frequency obtained can be written as,

$$\omega = \gamma_0 + i\omega_0 \tag{2.9}$$

Here, the real part of the complex frequency ω (γ_0), represents the growth rate of the mode, while the imaginary part (ω_0) represents the frequency of the mode.

Crouch's model

As previously discussed, transonic buffeting occurs under certain combinations of Mach numbers and angle of attacks of the aerofoil (α). The identification of the buffet onset with these combinations is done through observing the level of unsteadiness, measured by the real component or the growth rate of the extracted global mode (γ_0), following the global stability analysis in Crouch et al. [18]. These instability are observed to increase as α increases, at a fixed Mach number. The instability occurs when the prescribed growth rate of the mode (γ_0) becomes positive i.e. $\gamma_0 > 0$. The onset of the instability is characterized by a Hopf bifurcation, which leads to a limit cycle behaviour of the shock or shock oscillations. These shock oscillations can be visualized by observing the evolution of the coefficient of lift (C_L) as seen in figure 2.10. (a) in figure 2.10 shows the time evolution of the lift coefficient for the buffet-onset configuration and (b) presents the same plot but for higher angles of attack: both (a) and (b) are plotted for OAT15A supercritical aerofoil at a Mach number (Ma) = 0.73 and a chord Reynold's number (Re_c) = 3×10^6.

Here, the increase of unsteadiness due to the onset and increase of instability can be observed with the inception and increase of the C_L oscillation over time. The C_L oscillations, after a certain amount of time, can also be seen settling into a particular amplitude and frequency of oscillation, which represents the limit cycle oscillation (LCO) behaviour of the shock. Crouch et al. [18] had suggested that the near the buffet onset, the instability growth rate ($\gamma_0 > 0$) of the dominant mode is observed to exhibit a non-linear variation with the angle of attack (α) which are consistent with a supercritical bifurcation from a weakly non-linear theory.

The variation of growth rate and frequency with the variation in α for aerofoil OAT15A, at Ma=0.72, 0.73 and 0.74 are represented in figure 2.11, as taken from [16].

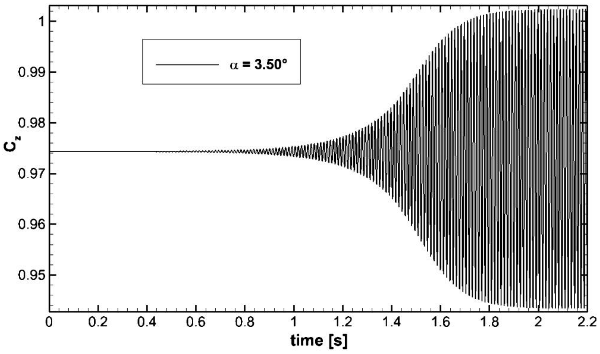

a) Buffet-onset condition (α = 3.5°)

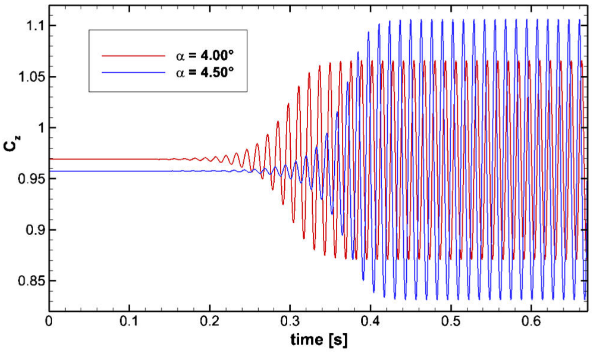

b) Higher angles of attack

Figure 2.10: Evolution of coefficient of lift (C_L or here C_z) for OAT15A at Ma = 0.73, and $Re_c = 3 \times 10^6$. Adapted from Sartor et al. [61]. (a) Represents the growth of lift coefficient at an angle of attack of 3.5° and (b) represents the growth of lift coefficient at angles of attack of 4.0° and 4.5°.

Validation of Crouch's model

The validation of Crouch's model was done by comparing the buffet onset boundary by Crouch et. al. [17, 18], which comprises of the combination of Mach number vs angle of attack where shock buffeting is observed to be at, against experimental data obtained in McDevitt & Okuno [47]. This comparison done for a NACA0012 aerofoil at Reynold's number (Re) = 10×10^6, is shown in figure 2.12. It can be seen that the unsteady URANS simulations match the buffet onset boundary observed through experimental data.

The buffet onset region for various Mach number-α combination is represented for two aerofoils NACA0012 and OAT15A in figure 2.13.

The theory was also validated numerically in Crouch et al. [17] for a NACA0012 aerofoil at Reynolds number (Re)=10 $\times 10^6$ Mach number (Ma) = 0.73 and angle of attack (α) = 3.0°, 3.1° and 3.2°, represented in figure 2.14, where the least stable eigenvalue measured crosses into the real plane causing the buffet onset can be seen.

The unstable/most dominant global mode ($\hat{q}$) associated with growth rate (γ_0)>0 of the eigenvalue, as described in section 2.3.2, is then represented through the unstable u-velocity component of the dominant mode, where the magnitude and phase of the u-velocity component are represented in figure 2.15, as found in Crouch et al. [17]. From figure 2.15 in the magnitude plot (a), it is evident that the unsteadiness is concentrated at the shock location and downstream at the boundary layer, and the phase plot (b) indicates the phase locked motion between the shock wave and the separated boundary layer, i.e. how the boundary layer thins when the shock moves downstream and how it thickens when the shock moves upstream.

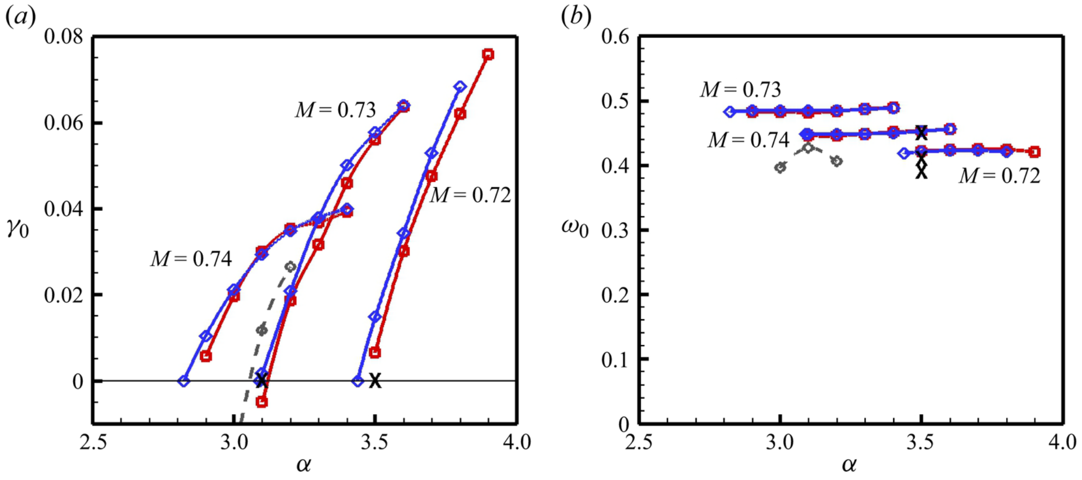

Figure 2.11: (a)Growth rate (γ_0) and (b) frequency (ω_0) determined as per stability analysis (blue diamonds), unsteady simulations (red squares), approach by Crouch et al. in 2009 ([18]) and experiments conducted by Jacquin et al.(×) in 2009 ([35]) for OAT15A aerofoil at Mach numbers of 0.72, 0.73 and 0.74 from [16]

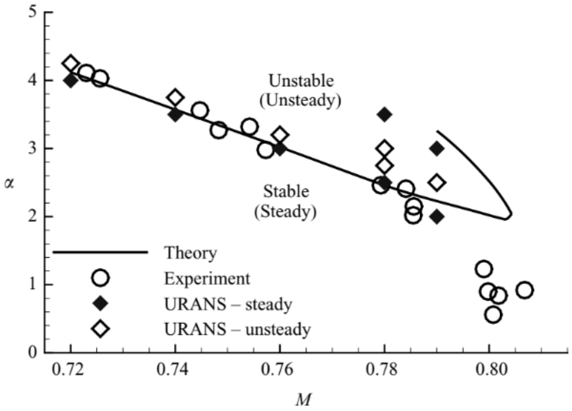

Figure 2.12: Buffet onset boundary measured in NACA0012 aerofoil at $(Re) = 10 \times 10^6$ as given in Crouch et al. [18]. The buffet boundary is marked by theoretical global stability analysis, marked as theory, experimental results observed, marked as experiment and URANS steady and URANS unsteady results obtained.

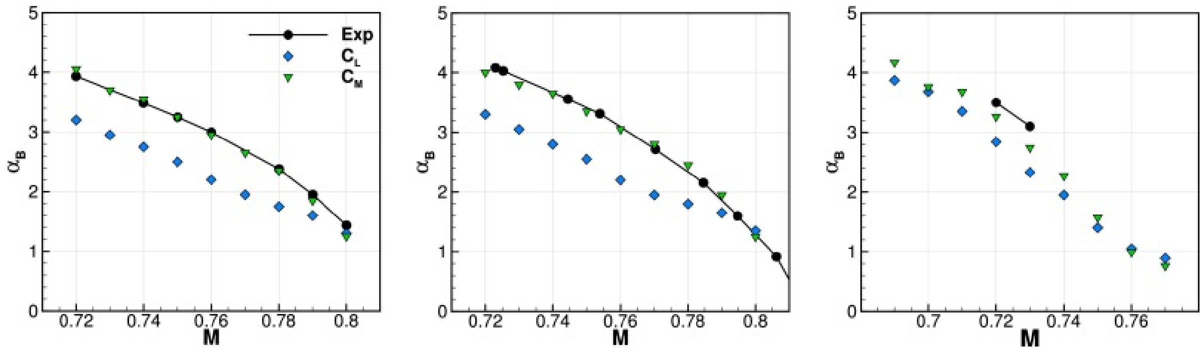

Figure 2.13: Buffet onset obtained from RANS based criteria for NACA0012 (left) at Re = 6.0 $\times 10^6$; NACA0012 (centre) at Re = 10.0 $\times 10^6$; OAT15A (right) at Re = 3.0 $\times 10^6$ (adapted from Petrocchi[9]).

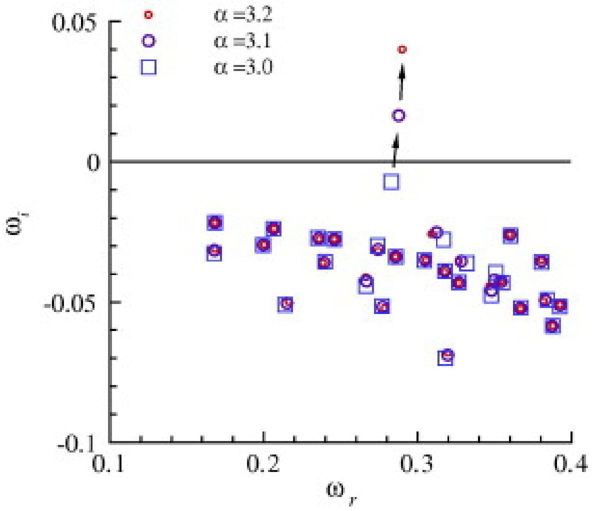

Figure 2.14: Buffet onset in NACA0012 aerofoil at Ma=0.72 as given in [17], which denotes the crossing of an eigenvalue from imaginary value to a real value i.e. from being stable to being unstable.

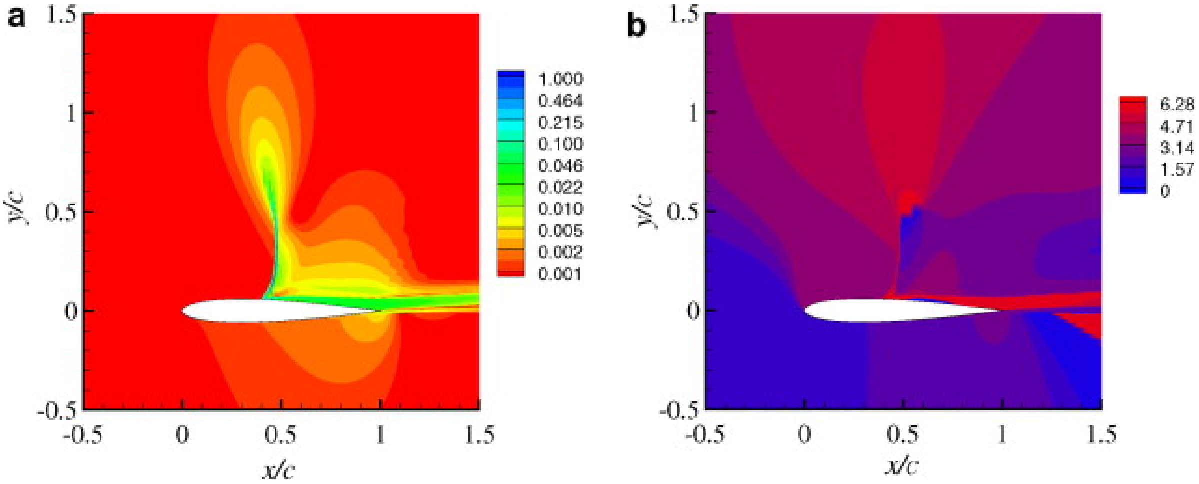

Figure 2.15: (a)u-velocity magnitude, which represents the unsteadiness being concentrated at shock location and (b) phase plot, which indicates the phase locked motion of the shock and the separated boundary layer, in NACA0012 aerofoil at Ma=0.72 as given in [17]

Model selection for describing transonic buffet

Crouch et al. [18] describe shock motion in a way that contrasts with the transonic buffet model proposed by Lee [42]. The model by Crouch et al. [17] indicates that pressure disturbances originate at the shock foot and primarily propagate in the wall-normal direction along the shock, with lower intensity through the boundary layer, rather than being confined to the boundary layer, even though both models emphasize phase-locked modulation of the separated boundary layer and shock position. The pressure variations seen during the shock cycle, shown in figure 2.16 for a Mach number of 0.76 with an angle of attack = 3.2° at a Reynold's number (Re) = 10^7, show how these disturbances advance and dissipate into the incoming airflow as they approach the top of the shock indicated by the position of the green arrows. The shock cycle is defined with eight steps, where the total time period of one oscillation (T) is divided as t/T = 0, 1/8, 2/8, 3/8, 4/8, 5/8, 6/8 and 7/8. Furthermore, these disturbances follow the shock downstream, indicated by the position of the red arrows, intensifying before producing acoustic waves that flow upstream along the bottom surface and across the trailing edge.

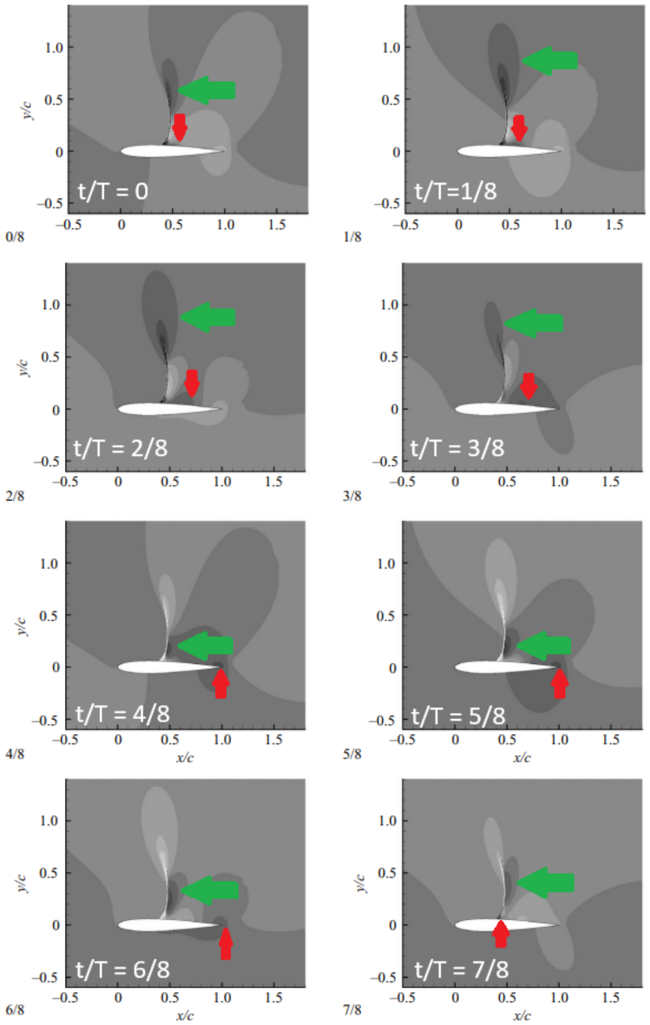

Figure 2.16: Contours of the pressure fluctuation at eight steps during the oscillation cycle (Crouch et al. [18]). Starting from top left marked 0/8, through 1/8, 2/8 ... 7/8 the images represent the eight steps within the total time period of shock oscillation (T).

Comparing transverse velocity components from global mode simulations with Laser Doppler Velocimetry (LDV) measurements for the OAT15A aerofoil done in Crouch et al. [15] reveals excellent agreement, supporting the validity of these findings. The unstable global mode mechanism is further validated by Sartor et al. [61] through the eigenvalue decomposition of the global Jacobian matrix. Due to current acceptance and experimental validation, henceforth all further investigations and research done for the purpose of this master's thesis would be based on Crouch's model.

2.4. Buffet control, its needs and the currently available solutions

2.4.1. Buffet control

Buffet control is a critical aspect of ensuring aircraft operational safety, as aerodynamic buffeting imposes constraints on the flight envelope and poses risks to the structural integrity of the wings. As previously discussed in chapter 1, control methods are divided into passive and active approaches. Passive techniques as seen in Gao et al. [25], such as mechanical vortex generators and shock control bumps, alter wing geometry to delay buffet onset but only work at specific operational points and cannot fully eliminate buffeting. Active controllers, including actuators for trailing-edge devices as given in Gao et al. [26], and fluidic vortex generators, use external energy to adapt boundary layer conditions and suppress buffet as shown in Dandois et al. [20], and are suitable for both open and closed-loop control systems. Closed-loop controllers, which adjust input based on real-time feedback, are preferred for managing flow instabilities over the open-loop controllers, which does not consider any real-time feedback to adjust the input. The closed-loop controllers can be model-based or model-free; model-based approaches rely on flow models, and low-dimensional reduced-order models are favoured for real-time control due to their balance of accuracy and computational efficiency.

In the context of closed-loop buffet control, model-based approaches utilize various types of flow models: high-fidelity models (based on discretized Navier-Stokes equations), low-dimensional reduced-order models (approximating essential system physics), and input-output models (such as neural networks). High-fidelity models, while accurate, are computationally expensive and impractical for real-time control of complex phenomena like buffeting. Input-output models lack direct ties to physical principles, limiting their robustness for control law design. Reduced-order models, on the other hand, are preferred because they significantly lower computational demands while retaining key physical insights, making them well-suited for designing reliable and efficient real-time control strategies.

2.4.2. Reduced order modelling

Problems associated with the need of flow control, once discretized by CFD (Computational fluid dynamics) techniques usually result in a system of order $O(10^{5-8})$. For the purpose flow control, where the controller design are relatively of lower order $O(10^1)$, for the sake of computational efficiency for real-time operation, the system has to be reduced to a lower order as a whole before the design of a closed loop controller. There are different approaches to achieving this according to [41]:

1. Design-then-reduce: where a full dimensional system is constructed as a higher order model, capturing all features of the system, which is then approximated by a reduced-order controller.
2. Reduce-then-design: where an order reduction by capturing essential features of the system, is carried out on the large scale model and a reduced order controller is then designed based on the reduced order model produced.

The 'reduce-then-design' approach has been successfully employed in many cases, as mentioned in [26]. The reduction of the full dimensional system to a reduced order model (ROM) can be carried out in the following ways as per Gao et al.[26]:

1. Proper orthogonal decomposition (POD) approach: Where the Galerkin projection of the equation describing the system, here the Navier-stokes equation, onto a space spanned by POD modes. The modes from the POD give a method of reconstructing the flow field, which then helps the interpretation of the effect of the controller used in modifying the flow. The modes, however, often do not represent the flow field fully, which is a disadvantage of this method.
2. Dynamic mode decomposition (DMD) approach: DMD is a spatio-temporal decomposition technique that extracts coherent structures along with their temporal evolution. DMD is similar to POD in the aspect of extraction of modes from a system but, unlike POD, DMD identifies modes that oscillate at specific frequencies, making it useful for analysing unsteady flows.
3. System identification approach: Where information collected from sensors and actuators or outputs and inputs respectively are used to determine the model without any a priori knowledge of the governing equations. Methods like eigensystem realization method (ERA) and autoregressive method (ARX) are some ways in which the model is constructed.

The creation of a ROM is followed by the design of an active control law, which is used to control the buffeting phenomena.

2.4.3. Currently available reduced order models for and drawbacks

The currently available reduced order models include ones made by ARX (autoregressive with external input) technique to model a flow characterized by an oscillating shock in Gao et al. [24] and Gao et al. [27]. These reduced order models lack any physical interpretations due to the use of ARX for model building, since the ARX can only model linear relationships between inputs and outputs which are not based on any underlying physics. Models based on dynamic mode decomposition (DMD) techniques, to identify flow structures and to describe the underlying physics, as in Gao et al. [26] are also available. Both these model types are linear and fail to capture the non-linearity involved in an unstable flow. So, using these methods the buffeting is controlled only after its settling onto a limit cycle oscillation (LCO). Two methods which has been successful to some degree in modelling non linearity are,

- By using the fit of coefficient of lift variation (C_L) to a Stuart-Landau equation as done in Crouch et al. [16].
- By using the Sparse Identification of Nonlinear Dynamics (SINDy) technique to extract a parametrized, interpretable, and minimal-order description of the dynamics of transonic buffet by modelling a simple parametrized Stuart-Landau oscillator as done in Sansica et al. [60].

Both these methods are discussed in detail below.

ROM modelling through fit of C_L variation to a Stuart-Landau equation

The onset of transonic buffet on aerofoils can be understood within the framework of global stability analysis, which provides the linear foundation for studying flow instabilities. For transonic buffet, the global stability analysis reveals the existence of an oscillatory mode whose growth rate changes sign at a critical angle of attack or Mach number, signalling a Hopf bifurcation, as previously discussed in section 2.3.2. Near this critical point, the flow transitions from a steady state to self-sustained oscillations, and the linear analysis predicts the onset of instability through the growth rate γ_0 and the oscillation frequency ω_0.

To capture the post-critical behaviour, linear theory is insufficient because non-linear effects become significant once the perturbation amplitude grows beyond the linear regime. Due to the non-linear nature of the dominant mode close to the critical point, as stated by Crouch et al. [18][16], it was stated that the behaviour of the buffet follows a Stuart-Landau equation, which assumes that the oscillation amplitude of the mode remains small but evolves on a slow timescale due to non-linear interactions. The solution is expanded in terms of a small parameter representing the amplitude of oscillation which leads to an amplitude evolution equation, where the linear growth predicted by the global analysis is balanced by cubic non-linear saturation. In this framework, the oscillation amplitude $A(t)$ evolves in the form,

$$\frac{\partial A}{\partial t} = \gamma_0 A + \gamma_1 A^3, \tag{2.10}$$

where γ_0 is the linear growth rate obtained from global stability analysis, and γ_1 (the Landau constant or first Lyapunov coefficient) quantifies the leading-order non-linear correction. For a supercritical Hopf bifurcation, which is the case for transonic buffet, $\gamma_1 < 0$, ensuring that the amplitude saturates to a finite value instead of growing unboundedly. Here, the amplitude A is defined directly from the lift fluctuations as

$$A = \frac{1}{2}\,\mathrm{pp}\left(C_L'(t)\right), \tag{2.11}$$

where $C_L'(t) = \frac{C_L(t) - C_L^{(B)}}{C_L^{(B)}}$ is the normalized lift coefficient fluctuation, $C_L(t)$ is the instantaneous lift coefficient, $C_L^{(B)}$ is the steady-state lift coefficient of the base flow, and $\mathrm{pp}(\cdot)$ denotes the peak-to-peak value. This definition directly links the amplitude A to a physically observable quantity, enabling the determination of buffet boundaries based on lift oscillations. But this interpretation of the oscillation amplitude evolution through the lift coefficient does not help in the creation of an generalized flowfield equation, using weakly non-linear analysis, as seen in Vojković et al. [73] where the vortex shedding in the wake region of a cylinder is investigated. It also tries to replace the amplitude of the most dominant mode which evolves in time, which is characterized by the Stuart-Landau equation, by coefficient of lift (C_L), which may behave in the same way, but does not deal with modes as a whole directly. This requires the use of the evolution of the amplitude of global mode in time, which can then be used to describe an asymptotic expansion of the flowfield using the methodology followed in Vojković et al. [73]. The development of such a flowfield definition also requires a bifurcation parameter (ϵ), whose value indicates whether the flow is in a pre or post critical state. The bifurcation parameter in the case of the aerofoil at a constant Mach number would be $\epsilon = f(\alpha_c, \alpha)$, where α represents the angle of attack of the aerofoil, and α_c a critical angle of attack beyond which bifurcation occurs. This asymptotic equation when paired with the governing Navier-Stokes equation results in a set of linear equations, which when solved gives us the evolution of various modes and their interactions in time. The solution of one of these equations results in the amplitude evolution of the global mode, which is governed by the Stuart-Landau equation. But, due to the dependence on multiple parameters, there is lack of a well defined bifurcation parameter expression, due to its complexity. Since the asymptotic expansion of the flowfield requires the bifurcation parameter there is a lack of a the closed form model governing the flowfield. Because of the lack of a closed form model, the weakly non-linear analysis, even though promising, cannot be pursued as a viable method for describing the non-linear nature of the transonic shock-buffet.

ROM modelling through data riven methodology using SINDy and DMD

The study by Sansica et al. [60] presents a data-driven methodology for constructing reduced-order models (ROMs) that are capable of predicting the unsteady dynamics of transonic buffet. The starting point is a set of time series of the lift coefficient, $C_L(t)$, obtained from unsteady Reynolds-averaged Navier–Stokes (URANS) simulations at various angles of attack (AOA). Despite the high-dimensionality of the turbulent flowfield, it was demonstrated that the essential buffet dynamics can be accurately captured using a low-dimensional state representation.

The methodology begins with a *time-delay embedding* of the scalar lift signal using the Broomhead–King algorithm, which transforms $C_L(t)$ into a latent space of dimension two. This is motivated by Takens' embedding theorem, which guarantees that the dynamics of a non-linear system can be reconstructed from time-delayed measurements of a single observable. The resulting Hankel matrix of the lift coefficient is decomposed via singular value decomposition (SVD), revealing that the dynamics are predominantly rank-2, corresponding to amplitude and phase dynamics of the buffet oscillations. To identify a governing dynamical system in this latent space, the authors employ the Sparse Identification of Non-linear Dynamics (SINDy) algorithm [7]. SINDy constructs a library of candidate non-linear terms (up to cubic polynomials) and solves a sparse regression problem to identify the active terms that govern the evolution of the latent variables. The resulting system is found to be equivalent to a Stuart–Landau oscillator, which captures the self-sustained oscillations through a minimal set of non-linear terms. For full-state prediction of the flowfield, the ROM couples the identified Stuart–Landau dynamics with a *Dynamic Mode Decomposition* (DMD) representation of the flow. The high-dimensional flow state $q(x, t)$ is approximated by a Galerkin expansion over a small number of DMD modes $\phi_i(x)$ with time-dependent complex amplitudes $s_i(t)$. A Kalman filter is then used to estimate these amplitudes from the predicted lift coefficient, enabling reconstruction of the full flowfield around the aerofoil. The low-dimensional linear DMD model, combined with interpolation of the DMD operator across different AOAs, enables efficient generalization to untrained flow conditions.

While the ROM approach offers significant computational savings, reducing predictions from hundreds of URANS core hours to seconds, is not without its limitations. The reliance on 2D URANS data means that three-dimensional buffet mechanisms, which are known to be relevant for real wings, are not captured. Furthermore, the accuracy of the DMD-based reconstruction is limited by the finite number of modes used, which can lead to Gibbs-like oscillations near sharp gradients, such as shocks [60]. The non-linear model includes only up to quadratic terms, and thus higher-order harmonics in the power spectral density of the lift signal are not reproduced. Another drawback is the model's dependence on the quality and range of the training data. The interpolation of system parameters (e.g., the SINDy coefficients and DMD operators) is only reliable within the convex hull of the AOAs used for training. Extrapolation to untrained conditions may result in inaccurate predictions. Additionally, because the identified system operates in a latent space, it requires an accurate measurement model to map back to physical observables, which can introduce errors if the latent representation is not well-calibrated.

Overall, the approach demonstrates the power of combining system identification techniques such as SINDy with modal decomposition methods like DMD for capturing essential buffet dynamics in a computationally efficient way. However, its reduced complexity and data-driven nature necessitate careful validation, especially when extending the model to high-fidelity 3D scenarios or control-oriented applications.

Though successful to various degrees, both these techniques fail to capture the nonlinearity completely because of dependence on closed forms and need for multiple modes to define the system. Thus, the exists need of a robust reduced order model, able to capture the nonlinearity seen during the time evolution of transonic buffeting and which can accurately predict untrained conditions.

2.5. Observations, problem statement and research objective

2.5.1. Observations

As stated previously in section 2.3.1 - section 2.3.2, Crouch et al. [18] had suggested that the near the buffet onset, the instability growth rate of the dominant mode is observed to exhibit a non-linear variation with the angle of attack (α) which are consistent with a supercritical bifurcation supported by a weakly non-linear theory. Currently, the proposed models available are linear in nature similar to given in C. Gao et al.[25][26], Sansica et. al. [60], Crouch et al. [16] etc. These models do not fully describe the time evolution of the amplitude of the critical/dominant global mode of the flow, which would be described by a Stuart-Landau model, and hence the non-linear evolution of the flow. The validity of such linear models are restricted to the vicinity of the linearization point and hence has limitations in fully representing the system. Because of this, buffet control implemented based on such models have not been completely successful in eliminating buffeting as a whole and returning the flow field to a steady flow.

Description of the time evolution of the amplitude of the critical global mode requires a closed form equation, defining the evolution of the flow and its dependence on the bifurcation parameter which is defined as the parameter which when changed causes bifurcation. A similar equation was developed for the case of evaluating the bifurcation phenomena observed in vortex shedding in a cylinder as shown in Vojković et al. [73]. The closed form equation for a case of transonic buffeting, whose bifurcation depends on two parameters; Mach number (Ma) and angle of attack (α), is more complex and is not yet developed and is more complex to define. There has also been investigations into creation of a reduced order model through a data-driven manner using SINDy and DMD modes by Sansica et. al. [60], which fails to predict the dynamics for untrained conditions.

Thus, there exists a need for a robust reduced order model which can capture and predict the non-linear dynamics well enough and which can be used for control purposes of transonic buffet.

2.5.2. Problem statement and research objective

The observations stated in section 2.5.1 gives rise to the formulation of the goal of this research: **To generate a non-linear reduced order model for flow around an aerofoil in transonic buffet region of operation (evaluated for selected Ma-α combination) which captures the non-linear nature of the time evolution of the conservative variables which include, density, x-momentum, z-momentum, energy density and eddy viscosity, which are used to define the flow. The reduced order model developed, should be able to capture and predict the dynamics of the flow in terms of the time evolution of conservative variables, as well as be suitable for control purposes.** Here, the problem will be considered for an aerofoil with no external forcing acting from the aerofoil to the flow.

3

Governing equations and solvers used

In this section, the governing equations (Navier-Stokes equation with turbulence closure model) and their RANS form, the details of the solvers and methods used for the RANS and unsteady RANS simulations, extraction of the eigenmodes and POD modes are discussed in detail.

3.1. Governing equations

As discussed in the last chapter, the transonic buffet is a complex, self-sustained aerodynamic instability that occurs on aerofoils and wings operating within the transonic regime, typically characterized by the intermittent oscillation of shock waves and the boundary layer. To investigate the underlying physics of transonic buffet in two dimensions (for a 2D aerofoil), the present study employs the compressible Navier-Stokes equations, which govern the conservation of mass, momentum, and energy in a fluid. These equations are implemented in simulation using the Reynold's Averaged Navier Stokes equation (RANS) form. Given the inherently turbulent nature of the flow in this regime, the RANS equations are complemented by a suitable turbulence closure model, enabling the simulation to capture the flow behaviour with the effects of turbulent fluctuations. The resulting set of equations provides a robust framework for analysing unsteady shock-boundary layer interactions and the onset of buffet in transonic flows. The governing equations are as follows,

3.1.1. Continuity and conservation equations

Here, for a two dimensional compressible flow occurring on the x-z plane is considered. The Navier-stokes equation is then written in terms of the primitive variables, $q = \{\rho, u, w, T, \tilde{\nu}\}$ in the conservative form. Here, ρ represents the density, u represents the velocity along the x-axis, v represents the velocity along the z-axis, T represents the absolute temperature and $\tilde{\nu}$ represents the turbulent viscosity component which provides closure. The governing equations are thus written as follows:

Continuity equation:

$$\frac{\partial \rho}{\partial t} + \frac{\partial(\rho u)}{\partial x} + \frac{\partial(\rho w)}{\partial z} = 0 \tag{3.1a}$$

Conservation of momentum in the x direction:

$$\frac{\partial(\rho u)}{\partial t} + \frac{\partial(\rho u^2)}{\partial x} + \frac{\partial(\rho u w)}{\partial z} = -\frac{\partial p}{\partial x} + \frac{\partial}{\partial x}(t_{xx}) + \frac{\partial}{\partial z}(t_{xz}) \tag{3.1b}$$

Conservation of momentum in the z direction:

$$\frac{\partial(\rho w)}{\partial t} + \frac{\partial(\rho w u)}{\partial x} + \frac{\partial(\rho w^2)}{\partial z} = -\frac{\partial p}{\partial z} + \frac{\partial}{\partial x}(t_{zx}) + \frac{\partial}{\partial z}(t_{zz}) \tag{3.1c}$$

Conservation of energy:

$$\frac{\partial}{\partial t}\Big(\rho(e+\frac{1}{2}\left(u^2+w^2\right)\Big)+\frac{\partial}{\partial x}\left[\rho u\left(h+\tfrac{1}{2}(u^2+w^2)\right)\right]+\frac{\partial}{\partial z}\left[\rho w\left(h+\tfrac{1}{2}(u^2+w^2)\right)\right]= \\ \frac{\partial}{\partial x}(ut_{xx}+wt_{zx})+\frac{\partial}{\partial z}(ut_{xz}+wt_{zz})-\left(\frac{\partial q_x}{\partial x}+\frac{\partial q_z}{\partial z}\right) \tag{3.1d}$$

Here, $p = \rho RT$ by the ideal gas law where, ρ is the density, T is the temperature. Also, u, w are the velocities in x & z directions respectively, R is the specific gas constant, e represents the specific internal energy and $h = e + \frac{p}{\rho}$ the specific enthalpy. The heat flux q is defined as $q_x = -\lambda_{eff}\frac{\partial T}{\partial x}, \quad q_z = -\lambda_{eff}\frac{\partial T}{\partial z}$. The viscous stress tensors t are defined as

$$\begin{aligned} t_{xx} &= 2\mu_{\text{eff}}\frac{\partial u}{\partial x}-\frac{2}{3}\mu_{\text{eff}}\left(\frac{\partial u}{\partial x}+\frac{\partial w}{\partial z}\right), \quad t_{xz} = \mu_{\text{eff}}\left(\frac{\partial u}{\partial z}+\frac{\partial w}{\partial x}\right), \\ t_{zz} &= 2\mu_{\text{eff}}\frac{\partial w}{\partial z}-\frac{2}{3}\mu_{\text{eff}}\left(\frac{\partial u}{\partial x}+\frac{\partial w}{\partial z}\right) \end{aligned} \tag{3.2}$$

where the effective dynamic viscosity μ_{eff} and effective heat conductivity λ_{eff} are defined as,

$$\mu_{\text{eff}} = \mu(T)+\rho\tilde{v}, \quad \lambda_{\text{eff}} = \frac{\mu(T)}{Pr}+\frac{\rho\tilde{v}}{Pr_t} \tag{3.3}$$

Here $\mu = \mu(T)$ is the dynamic viscosity, $\tilde{v}$ represents the turbulent viscosity, Pr and Pr_t are the Prandtl number and the turbulent Prandtl number, respectively.

3.1.2. Governing equations in Reynold's averaged form

Reynold's decomposition is a technique used to separate any flow variable into a mean (ensemble averaged) component and a fluctuating (perturbation) component. This is fundamental in turbulence modelling and forms the basis of Reynolds-Averaged Navier-Stokes (RANS) equations.

Reynolds averaging for a component γ can thus be described as:

$$\gamma = \bar{\gamma}+\gamma' \tag{3.4}$$

where $\bar{\gamma}$ represents the mean component of γ, while γ' represents the fluctuating component. Here,

$$\bar{\gamma} = \lim_{N\to\infty}\frac{1}{N}\sum_{j=1}^{N}\gamma^{(\alpha)} \tag{3.5}$$

and, by definition,

$$\bar{\gamma'} = 0 \tag{3.6}$$

Here, N are the number of samples considered for the component.

The full state vector describing the flow can be decomposed into a mean flow (steady-state) component and a perturbation (unsteady/fluctuating) component using Reynolds averaging.

$$q = \bar{q}+q' \tag{3.7}$$

where

$$\bar{q} = \{\bar{\rho},\bar{u},\bar{w},\bar{T},\bar{v}\} \tag{3.8}$$

$$q' = \{\rho',u',w',T',v'\} \tag{3.9}$$

For flows close to steady state, the fluctuating component q' can be considered to be small when compared to the mean flow $\bar{q}$ i.e. $q' \ll \bar{q}$. By substituting $q = \bar{q} + q'$ into the governing equations, subtracting the equations for the mean flow, a set of equations for the perturbations is obtained.

RANS equations for perturbations in the xz-plane:
Continuity equation:

$$\frac{\partial \bar{\rho}}{\partial t} + \frac{\partial(\bar{\rho}\tilde{u})}{\partial x} + \frac{\partial(\bar{\rho}\tilde{w})}{\partial z} = 0. \tag{3.10a}$$

Conservation of momentum in the x direction:

$$\frac{\partial(\bar{\rho}\tilde{u})}{\partial t} + \frac{\partial(\bar{\rho}\tilde{u}^2)}{\partial x} + \frac{\partial(\bar{\rho}\tilde{u}\tilde{w})}{\partial z} = -\frac{\partial \bar{p}}{\partial x} + \frac{\partial}{\partial x}\left(\bar{t}_{xx} - \bar{\rho}\overline{u'u'}\right) + \frac{\partial}{\partial z}\left(\bar{t}_{xz} - \bar{\rho}\overline{u'w'}\right). \tag{3.10b}$$

Conservation of momentum in the z direction:

$$\frac{\partial(\bar{\rho}\tilde{w})}{\partial t} + \frac{\partial(\bar{\rho}\tilde{w}\tilde{u})}{\partial x} + \frac{\partial(\bar{\rho}\tilde{w}^2)}{\partial z} = -\frac{\partial \bar{p}}{\partial z} + \frac{\partial}{\partial x}\left(\bar{t}_{zx} - \bar{\rho}\overline{w'u'}\right) + \frac{\partial}{\partial z}\left(\bar{t}_{zz} - \bar{\rho}\overline{w'w'}\right). \tag{3.10c}$$

Conservation of energy:

$$\begin{aligned}
&\frac{\partial}{\partial t}\left[\bar{\rho}\left(\tilde{e} + \tfrac{1}{2}(\tilde{u}^2 + \tilde{w}^2)\right) + \frac{1}{2}\left(\overline{\rho u'^2} + \overline{\rho w'^2}\right)\right] + \frac{\partial}{\partial x}\left[\bar{\rho}\tilde{u}\left(\tilde{h} + \tfrac{1}{2}(\tilde{u}^2 + \tilde{w}^2)\right) + \tilde{u}\,\frac{1}{2}\left(\overline{\rho u'^2} + \overline{\rho w'^2}\right)\right] \\
&+\frac{\partial}{\partial z}\left[\bar{\rho}\tilde{w}\left(\tilde{h} + \tfrac{1}{2}(\tilde{u}^2 + \tilde{w}^2)\right) + \tilde{w}\,\frac{1}{2}\left(\overline{\rho u'^2} + \overline{\rho w'^2}\right)\right] = \frac{\partial}{\partial x}\Big[- \bar{q}_x - \overline{\rho u'h'} + \bar{t}_{xx}\tilde{u} + \bar{t}_{zx}\tilde{w} - \overline{\rho u'\tfrac{1}{2}(u'^2 + w'^2)}\Big] + \\
&\frac{\partial}{\partial z}\Big[- \bar{q}_z - \overline{\rho w'h'} + \bar{t}_{xz}\tilde{u} + \bar{t}_{zz}\tilde{w} - \overline{\rho w'\tfrac{1}{2}(u'^2 + w'^2)}\Big] + \frac{\partial}{\partial x}\Big[\tilde{u}(\bar{t}_{xx} - \overline{\rho u'u'}) + \tilde{w}(\bar{t}_{xz} - \overline{\rho u'w'})\Big] \\
&+\frac{\partial}{\partial z}\Big[\tilde{u}(\bar{t}_{zx} - \overline{\rho w'u'}) + \tilde{w}(\bar{t}_{zz} - \overline{\rho w'w'})\Big]
\end{aligned} \tag{3.10d}$$

where,

$$\begin{aligned}
t'_{xx} &= 2\bar{\mu}_{\text{eff}}\left[\frac{\partial u'}{\partial x} - \frac{1}{3}\left(\frac{\partial u'}{\partial x} + \frac{\partial w'}{\partial z}\right)\right] + 2\mu'_{\text{eff}}\left[\frac{\partial \bar{u}}{\partial x} - \frac{1}{3}\left(\frac{\partial \bar{u}}{\partial x} + \frac{\partial \bar{w}}{\partial z}\right)\right], \\
t'_{xz} &= \bar{\mu}_{\text{eff}}\left(\frac{\partial u'}{\partial z} + \frac{\partial w'}{\partial x}\right) + \mu'_{\text{eff}}\left(\frac{\partial \bar{u}}{\partial z} + \frac{\partial \bar{w}}{\partial x}\right), \\
t'_{zz} &= 2\bar{\mu}_{\text{eff}}\left[\frac{\partial w'}{\partial z} - \frac{1}{3}\left(\frac{\partial u'}{\partial x} + \frac{\partial w'}{\partial z}\right)\right] + 2\mu'_{\text{eff}}\left[\frac{\partial \bar{w}}{\partial z} - \frac{1}{3}\left(\frac{\partial \bar{u}}{\partial x} + \frac{\partial \bar{w}}{\partial z}\right)\right], \\
q_x &= \overline{\rho u''h''}, \qquad q_z = \overline{\rho w''h''}
\end{aligned} \tag{3.11}$$

and

$$\mu'_{\text{eff}} = \rho'\bar{\nu}_t + \bar{\rho}\nu'_t, \qquad \lambda'_{\text{eff}} = \frac{\mu'_{\text{eff}}}{\text{Pr}_t} \tag{3.12}$$

3.1.3. Turbulence model and equation used

The turbulent viscosity component used to provide closure to the conservation equation, depends on the turbulence model used. Generally, for a single equation model they can be written as

$$\rho\nu = f(\phi) \tag{3.13}$$

where $f(\phi)$ is a function specific to the model used. Due to inherent limitations of the types of turbulence models which could be used at DLR for the methodology followed in this study, the choice of model selection is restricted to the Spalart-Allmaras single equation turbulence model and its modifications. The SA-neg model [2] is a modification of the original Spalart-Allmaras one-equation model designed to handle negative values of the working variable of eddy viscosity ($\tilde{\nu}$), which can occur due to numerical errors. When $\tilde{\nu} < 0$, the transport equation is modified to maintain stability and avoid non-physical behaviour.

Governing Equation for $\tilde{\nu} < 0$:

$$\frac{\partial \tilde{\nu}}{\partial t} + u_j \frac{\partial \tilde{\nu}}{\partial x_j} = c_{b1}(1 - c_{t3})\Omega\tilde{\nu} + c_{w1}\left(\frac{\tilde{\nu}}{d}\right)^2 + \frac{1}{\sigma}\left[\frac{\partial}{\partial x_j}\left((\nu + \tilde{\nu} f_n)\nabla\tilde{\nu}\right) + c_{b2}\frac{\partial \tilde{\nu}}{\partial x_i}\frac{\partial \tilde{\nu}}{\partial x_i}\right] \tag{3.14}$$

Here, where Ω describes the vorticity magnitude. The turbulent eddy viscosity ($\mu_t = \nu_t \rho$) relation is given by:

$$\mu_t = \begin{cases} \rho\tilde{\nu} f_{v1}, & \tilde{\nu} \geq 0 \\ 0, & \tilde{\nu} < 0 \end{cases} \tag{3.15}$$

The correction terms used here are:

$$\chi = \frac{\tilde{\nu}}{\nu}, \quad f_n = \frac{c_{n1} + \chi^3}{c_{n1} - \chi^3} \tag{3.16}$$

The constants used in the model are:

- $c_{b1} = 0.1355$ (production term coefficient)
- $c_{b2} = 0.622$ (cross-diffusion coefficient)
- $\kappa = 0.41$ (von Kármán constant)
- $\sigma = \frac{2}{3}$ (diffusion coefficient)
- $c_{t3} = 1.2$ (negative damping factor)
- $c_{n1} = 16$ (correction function constant)
- $c_{w1} = \dfrac{c_{b1}}{\kappa^2} + \dfrac{1 + c_{b2}}{\sigma}$ (wall destruction term)

The SA-neg model ensures that no turbulent viscosity is generated when $\tilde{\nu} < 0$, and the governing equation in this regime is constructed to smoothly return $\tilde{\nu}$ to a physically valid positive value. The production term is damped using the factor $(1 - c_{t3})$, and diffusion is modified using the function f_n to maintain numerical stability. For $\tilde{\nu} \geq 0$, the model reverts to the original Spalart–Allmaras formulation.

3.2. Solvers and methods used

The RANS simulations are done on the DLR cluster CARO, using the the in-house CFD simulation software known as TAU. TAU is used to generate numerical solutions of compressible flow equations on unstructured and hybrid computational meshes, with common physical flow and turbulence models, and numerical algorithms for efficient steady-state and time-accurate simulations (e.g. multi-grid, dual time-stepping method). All further simulations were carried out in TAU and the solvers and methods used for the same are described here.

3.2.1. Time-linearized Navier–Stokes solver for RANS simulation

TAU implements a time-linearized Navier-Stokes solver for implementing RANS simulations. The governing equations used here are the mass-weighted (Favre-averaged) three-dimensional, time-dependent Navier-Stokes equations or RANS equations [70]. The equations apply to an open domain $\Omega(t) \subset \mathbb{R}^3$ with a smooth boundary $\partial\Omega(t)$, described by the time-dependent coordinates:

$$\mathbf{x}(t) = [x(t),\, y(t),\, z(t)]^T \tag{3.17}$$

The velocity field is defined as:

$$\mathbf{U}[\mathbf{x}(t), t] = [u(x,t),\ v(x,t),\ w(x,t)]^T \tag{3.18}$$

These equations are expressed in a non-dimensionalized, integral strong conservation form as follows:

$$\begin{aligned} \frac{d}{dt}\int_{\Omega(t)} \mathbf{Q}\, d|\Omega| + \int_{\partial\Omega(t)} (\mathbf{f}_c \cdot \mathbf{n} - \mathbf{f}_v \cdot \mathbf{n} - \mathbf{W}\dot{\mathbf{x}} \cdot\ \mathbf{n})\, d|\partial\Omega| \\ = \int_{\Omega(t)} \mathbf{Q}\, d|\Omega| \end{aligned} \tag{3.19}$$

where $|\Omega|$ is the volume of the domain Ω and $|\partial\Omega|$ is the surface area of its boundary $\partial\Omega$.

Here

- $\mathbf{W} = (\rho, \rho u, \rho v, \rho w, \rho E, \rho\tilde{\nu})^T$ is the state vector of conservative variables, where ρ denotes the density, E is the specific total energy, and $\tilde{\nu}$ is the primitive variable of the S-A turbulence model.
- $\dot{\mathbf{x}}$ is the grid velocity.
- $\mathbf{Q}$ is turbulence source term containing the production, destruction, diffusion of $\tilde{\nu}$.
- $\mathbf{f}_c$ is the convective flux vector, $\mathbf{f}_v$ is the viscous flux vector, along the face normal vector $\mathbf{n}$. They are defined as,

  $$\mathbf{f}_c \cdot \mathbf{n} = \begin{bmatrix} \dot{m} \\ \dot{m}\,\mathbf{U} + p\mathbf{n} \\ \dot{m}H \\ \dot{m}\tilde{\nu} \end{bmatrix}, \quad \mathbf{f}_v \cdot \mathbf{n} = \begin{bmatrix} 0 \\ \boldsymbol{\tau} \cdot \mathbf{n} \\ \boldsymbol{\Theta} \cdot \mathbf{n} \\ \tau_\nu \cdot \mathbf{n} \end{bmatrix} \tag{3.20}$$

  where $\dot{m} = \rho(\mathbf{U} \cdot \mathbf{n})$ is the mass flux through the surface $\partial\Omega$. Here, $\mathbf{U}$ is the velocity vector, p is the static pressure, H is the specific total enthalpy, $\tilde{\nu}$ is the S–A turbulence working variable, $\boldsymbol{\tau}$ is the viscous stress tensor, $\boldsymbol{\Theta}$ represents the heat flux, and τ_ν is the diffusion term associated with $\tilde{\nu}$. For a calorically perfect gas, the relation between static pressure p and temperature T is given by the equation of state $p/\rho = T$.

By applying the finite volume method and isolating the time derivative of equation (3.19), the governing equations can be reformulated as:

$$\frac{d}{dt}\int_{\Omega(t)} \mathbf{W}\, d|\Omega| = -\mathbf{R}(\mathbf{W}, \mathbf{x}, \dot{\mathbf{x}}) \tag{3.21}$$

where the residual $\mathbf{R}$ is defined by

$$\mathbf{R}(\mathbf{W}, \mathbf{x}, \dot{\mathbf{x}}) := \int_{\partial\Omega(t)} (\mathbf{f}_c \cdot \mathbf{n} - \mathbf{f}_v \cdot \mathbf{n} - \mathbf{W}\,\dot{\mathbf{x}} \cdot \mathbf{n})\, d|\partial\Omega| - \int_{\Omega(t)} \mathbf{Q}\, d|\Omega| \tag{3.22}$$

Discretizing in space with a finite volume approach, equation (3.21) can be reformulated in semi discrete form as

$$\frac{d(\mathbf{MW})}{dt} + \mathbf{R}(\mathbf{W}, \mathbf{x}, \dot{\mathbf{x}}) = 0 \tag{3.23}$$

where $\mathbf{W} := \mathbf{W}(\mathbf{x}, \dot{\mathbf{x}})$, and the mass matrix $\mathbf{M}$ is given by

$$\mathbf{M} := \mathbf{M}(\mathbf{x}) = \operatorname{diag}(|\Omega_i(t)|), \quad i = 1, \ldots, N \tag{3.24}$$

with N denoting the total number of discrete control volumes. For temporal discretization, the unsteady RANS equations are solved using dual-time stepping with an implicit backward difference formula (BDF). At each physical time step, the residual is marched to a pseudo-steady-state using a multigrid solver.

Linearization of $\mathbf{W}$ using Taylor series expansion results in

$$\mathbf{W}(t) \approx \bar{\mathbf{W}}(\bar{\mathbf{x}}) + \bar{\mathbf{W}}(\bar{\mathbf{x}}, \bar{\mathbf{x}}), \quad \mathbf{x}(t) \approx \bar{\mathbf{x}} + \bar{\mathbf{x}}(t), \quad \mathbf{x}(t) \approx \dot{\bar{\mathbf{x}}} + \dot{\bar{\mathbf{x}}}(t) = \dot{\bar{\mathbf{x}}}(t) \tag{3.25}$$

For small harmonic perturbations the following is assumed,

$$\mathbf{W}(t) = \bar{\mathbf{W}} + \hat{\mathbf{W}}e^{i\omega t}, \quad \mathbf{x}(t) = \bar{\mathbf{x}} + \hat{\mathbf{x}}e^{i\omega t} \tag{3.26}$$

Substituting into the semi-discrete RANS form and linearizing yields:

$$\left(i\omega\bar{\mathbf{M}}(\bar{\mathbf{x}}) + \left.\frac{\partial \mathbf{R}}{\partial \mathbf{W}}\right|_{\bar{\mathbf{W}},\bar{\mathbf{x}},\dot{\bar{\mathbf{x}}}} \right) \hat{\mathbf{W}} = \mathbf{b} \tag{3.27}$$

The right-hand side $\mathbf{b}$ accounts for mesh motion and deformation via finite differences. Separating into real and imaginary parts, it can then be written as a linear system of equations defined by

$$\mathbf{A}\mathbf{W} = \mathbf{b} \tag{3.28}$$

where,

$$\mathbf{A} := \begin{bmatrix} \frac{\partial \mathbf{R}}{\partial \mathbf{W}}\Big|_{\bar{\mathbf{W}},\bar{\mathbf{x}},\dot{\bar{\mathbf{x}}}} & -\omega\bar{\mathbf{M}}(\bar{\mathbf{x}}) \\ \omega\bar{\mathbf{M}}(\bar{\mathbf{x}}) & \frac{\partial \mathbf{R}}{\partial \mathbf{W}}\Big|_{\bar{\mathbf{W}},\bar{\mathbf{x}},\dot{\bar{\mathbf{x}}}} \end{bmatrix}, \quad \mathbf{b} := -\begin{bmatrix} \frac{\partial \mathbf{R}}{\partial \mathbf{x}}\Big|_{\bar{\mathbf{W}},\bar{\mathbf{x}},\dot{\bar{\mathbf{x}}}} & -\omega\left(\frac{\partial \mathbf{R}}{\partial \dot{\mathbf{x}}} + \bar{\mathbf{W}}(\bar{\mathbf{x}})\frac{\partial \mathbf{M}}{\partial \mathbf{x}}\Big|_{\bar{\mathbf{x}}}\right) \\ \omega\left(\frac{\partial \mathbf{R}}{\partial \dot{\mathbf{x}}} + \bar{\mathbf{W}}(\bar{\mathbf{x}})\frac{\partial \mathbf{M}}{\partial \mathbf{x}}\Big|_{\bar{\mathbf{x}}}\right) & \frac{\partial \mathbf{R}}{\partial \mathbf{x}}\Big|_{\bar{\mathbf{W}},\bar{\mathbf{x}},\dot{\bar{\mathbf{x}}}} \end{bmatrix}\hat{\mathbf{x}} \tag{35}$$

where, $\mathbf{M}$ is of the same dimension as the flux Jacobian $\frac{\partial \mathbf{R}}{\partial \mathbf{W}}$.The system is then solved to obtain $\mathbf{W}$ and is then post processed to gain quantities of interest like the lift force ($\hat{C}_L$). The solver thus constructs the flowfield solutions as $\mathbf{W}$ and the post processed quantities of interest, which are later used for the construction of reduced order models as discussed in chapter 4.

3.2.2. Linear analysis and eigenmode extraction

Investigation of buffeting phenomena, based on Crouch's model, involves the extraction and study the dominant eigenmode as well as its corresponding eigenvalues for the case of Ma-α considered. These extractions are carried out for the steady flowfield results in terms of conservative variable, obtained from the RANS simulation using the solver discussed in section 3.2.1. For the extraction of eigenmodes, the evolution of a small-amplitude perturbation is defined and analyzed, denoted by $\epsilon w'$, superimposed on a steady base flow $\bar{w}$. The total flow is expressed as:

$$w = \bar{w} + \epsilon w', \quad \epsilon \ll 1$$

By linearizing the discretized Navier–Stokes equations to first order in ϵ, the governing equation for the perturbation is obtained:

$$\frac{dw'}{dt} = Jw' \tag{4}$$

Here, $J \in \mathbb{R}^{N\times N}$ is the Jacobian matrix of the discrete Navier–Stokes residual operator $\mathcal{R}$, evaluated at the base flow $\bar{w}$:

$$J_{ij} = \left.\frac{\partial \mathcal{R}_i}{\partial w_j}\right|_{w=\bar{w}} \tag{5}$$

The term $\mathcal{R}_i$ denotes the i-th component of the residual vector, which depends on all unknowns w_j across the computational mesh. Since J involves spatial derivatives, it is a sparse matrix. Notably, this framework allows for spatial inhomogeneity in the base flow and applies to global (as opposed to local) linear stability analysis.

For two-dimensional (2-D) flows, it is assumed that the flow and perturbations are homogeneous in the third dimension. The stability of the base flow is determined by analyzing the eigenvalue spectrum of J. Perturbations are assumed to take the form of normal modes:

$$w' = \hat{w}e^{\lambda t}$$

Substituting into Eq. (4) yields the eigenvalue problem:

$$J\hat{w} = \lambda\hat{w} \tag{6}$$

The real part of the eigenvalue λ corresponds to the growth rate σ. If any λ has a positive real part, the base flow $\bar{w}$ is unstable. In such cases, the associated eigenmodes grow in time and dominate the flow dynamics. Conversely, if all modes are damped (i.e., the flow is globally stable), then external forcing is required to sustain unsteadiness.

To numerically compute the Jacobian matrix J, a finite difference approximation is employed. For an arbitrary perturbation vector u, the product Ju can be estimated using residual evaluations as:

$$Ju = \frac{1}{\epsilon}\left[\mathcal{R}(\bar{w} + \epsilon u) - \mathcal{R}(\bar{w})\right] \tag{7}$$

where ϵ is a small constant. By applying this expression to a set of well-chosen perturbation vectors u, the entire Jacobian matrix J can be constructed.

Once the matrix J is assembled, the eigenvalue problem in Eq. (6) is solved using Krylov subspace methods. These methods allow targeting of the least stable (least-damped) eigenvalues via shift-invert techniques. Although the shift-invert method incurs significant memory costs (typically about 50 times the matrix size), it is highly effective for resolving the desired part of the spectrum.

3.2.3. Proper Orthogonal Decomposition (POD)

Proper Orthogonal Decomposition (POD) [38] is a statistical technique used to extract dominant spatial structures (modes) from high-dimensional data, such as those encountered in fluid dynamics, structural vibrations, or any spatio-temporal system. It achieves model order reduction by projecting the original high-dimensional dynamics onto a low-dimensional subspace spanned by the most energetic modes. POD modes can be used to visualize the most energetic modes in an unsteady system, which here would be extracted from the Unsteady RANS (URANS) flowfields extracted using the TAU solver as discussed in section 3.2.1. The method of extraction of these modes is described as follows:

Let $\theta(x,t)$ be a random spatio-temporal field defined on a domain Ω over time t. The field is decomposed into a mean $\mu(x)$ and a time-varying part $\vartheta(x,t)$:

$$\theta(x,t) = \mu(x) + \vartheta(x,t) \tag{3.29}$$

At discrete time instances t_k, the system state is represented as a snapshot:

$$\vartheta^k(x) = \vartheta(x,t_k) \tag{3.30}$$

POD seeks to find an orthonormal spatial basis function $\phi(x)$ that maximizes the average projection (or "energy") of the fluctuation field onto that basis:

$$\max_{\|\phi\|=1} \left\langle \left| \left(\vartheta^k, \phi \right) \right|^2 \right\rangle \tag{3.31}$$

Here,

- $(f,g) = \int_\Omega f(x)g(x)\,dx$ is the inner product in Ω,
- $\|\phi\|^2 = (\phi,\phi)$ is the L^2 norm,
- $\langle\cdot\rangle$ denotes averaging over snapshots.

Using a Lagrange multiplier formulation, the above optimization leads to the following eigenvalue problem:

$$\int_\Omega \left\langle \vartheta^k(x)\vartheta^k(x') \right\rangle \phi(x')\,dx' = \lambda\phi(x) \tag{3.32}$$

The kernel $\langle\vartheta(x)\vartheta(x')\rangle$ is the averaged auto-correlation function. The eigenfunctions $\phi_i(x)$ are the Proper Orthogonal Modes (POMs) or POD modes, and the corresponding eigenvalues λ_i ($\lambda_i > 0$) are the Proper Orthogonal Values (POVs), indicating the energy captured by each mode.

The fluctuation field can be reconstructed as an expansion over the POMs:

$$\vartheta(x,t) = \sum_{i=1}^{\infty} a_i(t)\,\phi_i(x) \tag{3.33}$$

where

$$a_i(t) = \big(\vartheta(x,t), \phi_i(x)\big) \tag{3.34}$$

The coefficients $a_i(t)$ are uncorrelated in time:

$$\big\langle a_i(t) a_j(t) \big\rangle = \delta_{ij}\lambda_i \tag{3.35}$$

Discrete POD Using Data Matrices

Suppose there are n snapshots $\mathbf{x}_1, \ldots, \mathbf{x}_n \in \mathbb{R}^m$ (i.e., n observations of a m-dimensional vector $\mathbf{x}$), forming the response matrix:

$$\mathbf{X} = [\mathbf{x}_1\ \mathbf{x}_2\ \cdots\ \mathbf{x}_n] \in \mathbb{R}^{m\times n} \tag{3.36}$$

Assuming zero mean, the sample covariance matrix is:

$$\Sigma_S = \frac{1}{n}\mathbf{X}\mathbf{X}^T \tag{3.37}$$

The eigenvalue problem becomes:

$$\Sigma_S \mathbf{u}_i = \lambda_i \mathbf{u}_i \tag{3.38}$$

The vectors $\mathbf{u}_i$ are the discrete POMs and λ_i are the corresponding POVs.

Alternative Computation via SVD

An alternative and numerically stable approach is to use Singular Value Decomposition (SVD):

$$\mathbf{X} = \mathbf{U}\mathbf{S}\mathbf{V}^T \tag{3.39}$$

- $\mathbf{U} \in \mathbb{R}^{m\times m}$ is an orthonormal matrix, containing the left singular vectors (POMs),
- $\mathbf{S} \in \mathbb{R}^{m\times n}$ is a pseudo-diagonal and semi-positive definite matrix with diagonal entries containing the singular values σ_i,
- $\mathbf{V} \in \mathbb{R}^{n\times n}$ is an orthonormal matrix containing the right singular vectors.

Energy Content

The eigenvalues of the covariance matrix relate to the singular values via:

$$\lambda_i = \frac{\sigma_i^2}{n} \tag{3.40}$$

The total energy in the data is:

$$\varepsilon = \sum_{i=1}^{n} \lambda_i \tag{3.41}$$

The percentage of energy captured by the ith mode is:

$$\frac{\lambda_i}{\sum_{j=1}^{n} \lambda_j} \tag{3.42}$$

This allows selection of a reduced number of modes capturing, for instance, 99% of the system's energy.

POD provides an optimal linear basis (in the L^2 sense) for representing high-dimensional data by minimizing the average reconstruction error. The extracted POD modes can be used to reconstruct the dominant dynamics of the system with drastically reduced dimensionality. This makes POD highly valuable in reduced-order modelling and system identification.

4

Proposed technique for ROM creation, case selection and methodology

Through this chapter, a technique called spectral submanifold embedding which can be used to derive a ROM will be discussed first. Then, the cases chosen and evaluated, along with the methodologies implemented in the thesis are also described in detail. Along with that, a detailed discussion on the aerodynamic model chosen for the study, along with details on the simulation setup are also discussed. The reasoning of the choices taken are also discussed.

4.1. Spectral sub manifold theory

Many physical systems exhibit high-dimensional non-linear dynamics, which has been proven difficult to produce a reduced order model for, as discussed in the previous sections. These reduced order models are indispensable not only for reducing computational cost, but also for enabling deeper physical understanding, facilitating design optimization, and supporting real-time control. Despite this clear demand, a general, robust methodology for deriving such models from data, which captures the full dynamics of the system, has not been achieved. A widely used approach for reducing non-linear systems is the Proper Orthogonal Decomposition (POD) followed by a Galerkin projection, which identifies the most energetic modes of a system and projects the dynamics onto a low-dimensional linear subspace as seen in [4, 44]. However, this approach has significant limitations. POD focuses on linear modal content and neglects essential non-linear interactions that are often critical for correctly capturing the long-term behaviour of complex systems. Other methods which involve the use of machine learning using neural networks and sparse regression models, as a data-driven alternative has also been implemented to various degrees of success, for some systems, as seen in [7, 21] etc. Although these methods show promise, they tend to act as black-box models that offer little in terms of physical interpretability. They require large datasets and careful tuning and often struggle to generalize outside the training regime. As a result, machine learning models tend to be either overly complex or insufficiently robust, particularly when extrapolating beyond the regime of training data. Use of Dynamic mode decomposition (DMD) and its various extensions as seen in [8, 5], has also been used to try and fit a linear model to the evolution of observable quantities, thereby offering a data-driven approach to identify coherent structures in the dynamics. But the methods using DMD are only valid near fixed points in the dynamics, and fail to capture the entire dynamics of a non-linear system. These observations were discussed and evaluated in detail in [14], where it was summarized that most real-world systems are not globally linearizable. The presence of multiple attractors, such as fixed points, limit cycles, or chaotic sets, precludes the possibility of any global linear coordinate transformation that can capture the dynamics faithfully. Linearization-based methods, such as DMD or Koopman operator approaches, are intrinsically incapable of resolving systems that exhibit phenomena such as bifurcations, multi stability, or chaos.

Given that many systems of interest are fundamentally non-linearizable, constructing a low dimensional reduced order model requires a new methodology. The theory of Spectral Submanifolds (SSMs) proves to be a compelling alternative for this requirement. SSMs provide a mathematically rigorous framework for model reduction in non-linear dynamical systems. It was previously discussed in section 2.2.3 on how invariant manifolds, particularly the centre manifolds capture the qualitative features of a Hopf bifurcation. In essence, an SSM is the smoothest invariant manifold that acts as a non-linear continuation of a spectral subspace, which is defined as a direct sum of selected modal subspaces, of the linearized system. Whereas linear modal analysis focuses on eigenspaces of the linearized Jacobian matrix, the SSM extends those eigenspaces into the non-linear regime, yielding invariant manifolds that retain key geometric and dynamical properties even under the influence of non-linear terms. Unlike projection-based methods, SSMs do not require knowledge of the governing equations; they can be extracted purely from data. Furthermore, SSMs are robust: they persist under small perturbations and are uniquely defined when certain non-resonance conditions are met. The manifold geometry provides a natural coordinate system for describing the dynamics, and the reduced dynamics on the SSM can be described using polynomial normal forms, resulting in explicit, interpretable, and sparse models. Importantly, the SSM-based model is not merely a local linear approximation. Methodology using SSM, for data driven modelling and using the reduced order model produced for the prediction of non-linearizable dynamics has been implemented in [14].

4.1.1. History and inception of SSM theory

History of SSM theory

The development of SSM theory started of from Linear Spectral theory. Linear spectral theory [22] is a well-established tool for analysing linear and linearizable dynamical systems. When a system can be brought into linear form via appropriate coordinate transformations, its behaviour can be effectively described through spectral analysis. Linear spectral theory consists of linearization of non-linear systems, spectral decomposition and modal analysis, which are explained below,

Linearization of Non-linear Systems: For a general non-linear system of the form

$$\dot{x} = f(x), \quad x \in \mathbb{R}^n,$$

the behavior near an equilibrium point x^* (where $f(x^*) = 0$) is often approximated by a linear model. This is achieved by expanding $f(x)$ in a Taylor series around x^* and retaining only the linear terms:

$$\dot{x} \approx A(x - x^*), \quad \text{where } A = Df(x^*) \text{ is the Jacobian matrix.}$$

This yields a linear system that approximates the original system near the equilibrium.

Spectral Decomposition: The solution to the linear system $\dot{x} = Ax$ can be expressed in terms of the eigenvalues and eigenvectors of A. The eigenvalues determine the stability and timescales of the modes:

- Eigenvalues with negative real parts correspond to decaying modes.
- Eigenvalues with zero real part indicate marginal stability.
- Eigenvalues with positive real parts correspond to unstable growth.

Each eigenvector defines a direction in phase space along which the solution evolves exponentially in time.

Modal Analysis: The state space can be decomposed into invariant subspaces (modal subspaces) associated with groups of eigenvalues. Projecting the dynamics onto these subspaces allows one to analyze and interpret the contributions of different modes independently. This forms the basis for modal reduction and motivates the search for non-linear analogues, especially in the presence of weak nonlinearity or damping.

However, systems that are inherently non-linear require more advanced techniques, as the superposition principle no longer applies. While linear modal analysis provides a solid foundation for understanding local dynamics near equilibria, many real-world systems exhibit non-linear effects that invalidate the assumptions of linearity. To address this, researchers have extended the idea of linear modes to non-linear settings, leading to the development of *non-linear normal modes* (NNMs). In his seminal work, Rosenberg [59] defined NNMs for conservative systems as families of synchronous periodic motions in which all generalized coordinates reach their maximum and minimum values simultaneously. These motions represent the simplest form of invariant oscillations in conservative multi-degree-of-freedom systems. These synchronous motions lie on one or higher-dimensional invariant manifolds in the system's phase space. These manifolds are tangent to the linear modal subspaces at the equilibrium and capture non-linear deformations of linear normal modes. To generalize the concept of NNMs to dissipative systems, Shaw and Pierre [63] introduced the idea of *non-linear invariant manifolds*. These manifolds are low-dimensional surfaces in the phase space that are tangent to selected eigenspaces of the linearized system and invariant under the full non-linear dynamics. They serve as non-linear continuations of the spectral subspaces and enable the study of energy exchange between modes.

However, this construction faced limitations:

- Such manifolds are typically not unique: infinitely many invariant manifolds may satisfy the tangency condition at an equilibrium point.
- Their smoothness and analyticity are not generally guaranteed.
- Their local nature restricts their domain of validity.

Lyapunov Subcenter Manifold Theorem: In conservative systems with purely imaginary eigenvalues and under nonresonance conditions, the Lyapunov subcenter manifold theorem [3, 37] ensures the existence of a unique, analytic invariant manifold that contains small-amplitude periodic orbits. This result lays the mathematical foundation for Rosenberg's original concept of NNMs in conservative settings.

The limitations of NNMs in the dissipative case motivated the search for a more robust, rigorous framework for non-linear model reduction—a quest that led to the development of Spectral Submanifolds (SSMs).

To address the ambiguity in NNMs, Haller and Ponsioen [32] introduced Spectral Submanifolds (SSMs) as:

> *"The unique smoothest invariant manifolds that act as non-linear extensions of non-resonant eigenspaces from the linearization of the system at a stationary point."*

This definition relies on spectral quotients derived from the ratio of real parts of eigenvalues and is supported by the parameterization method of Cabr'e, de la Llave, and Fontich [11, 13, 12], and geometric invariant theory from Haro and de la Llave [33].

SSM theory has since been applied to various settings: in forced vibration analysis [67, 6], finite element models [23], automated computation [57], data-driven modelling [14], and direct parametrization of invariant manifolds [72, 52]. Most of these developments concern finite-dimensional systems. Only limited work addresses SSMs in infinite-dimensional systems, including PDE models [39] and fluid dynamics [10].

4.1.2. Spectral submanifolds and its use in creating a reduced order model

According to the result of research done on dynamical systems as stated in [14], all eigenspaces or spectral subspaces of linearized systems, under well-defined mathematical conditions, possess unique non-linear continuations. Amongst these subspaces, as discussed, spectral submanifolds are the unique smoothest invariant manifolds that act as non-linear extensions of non-resonant eigenspaces from the linearization of the system at a stationary point. For a non autonomous n-dimensional dynamical system of the form

$$\dot{\mathbf{x}} = \mathbf{A}\mathbf{x} + \mathbf{f_0}(\mathbf{x}) + \epsilon \mathbf{f_1}(\mathbf{x}, \mathbf{\Omega}t; \epsilon), \qquad \mathbf{f_0}(x) = O(|\mathbf{x}|^2), \qquad 0 \leq \epsilon \ll 1, \tag{4.1}$$

where $\mathbf{A} \in \mathbb{R}^{n \times n}$ is a constant matrix defining the linearized system. $\mathbf{f_0}$ is the autonomous nonlinearity of at least quadratic order. $\mathbf{f_1}$ is time-dependent (e.g., quasiperiodic) forcing, where $\mathbf{\Omega} \in \mathbb{R}^l$ which denotes the rationally independent components of the frequency vector, where ϵ denotes a small parameter for external forcing strength.

The linear part of equation (4.1), i.e: $\dot{\mathbf{x}} = \mathbf{A}\mathbf{x}$ has eigenvalues given as $\lambda_j = \alpha_j + i\omega_j$, which are ordered as

$$Re(\lambda_j) \leq Re(\lambda_{j-1}) \cdots \leq Re(\lambda) \tag{4.2}$$

The corresponding real modal subspaces or eigenspaces of these eigenvalues are defined as $\mathbf{E_j} \subset \mathbb{R}^n$, and are spanned by the real and imaginary components of the corresponding eigenvectors and generalized eigenvectors of $\mathbf{A}$. Thus the system is assumed to be hyperbolic (no center modes): all eigenvalues of $\mathbf{A}$ have non-zero real parts, i.e: $Re(\lambda_j) = \alpha_j \neq 0$ holds for all eigenvalues, i.e., $x = 0$ is a hyperbolic fixed point for $\epsilon = 0$.

Spectral subspace A spectral subspace $\mathbf{E_{j1,\cdots,j_q}}$ is defined as the direct sum of selected modal subspaces associated with a subset of eigenvalues, which here would be defined as,

$$\mathbf{E_{j_1,\cdots,j_q}} = \mathbf{E_{j_1}} \oplus \mathbf{E_{j_2}} \oplus \cdots \oplus \mathbf{E_{j_q}} \tag{4.3}$$

The spectral subspace is thus an arbitrary collection of model subspaces which is always an invariant subspace of of the linear part of equation (4.1). The unstable subspace formed by the eigenvalues with $Re(\lambda_j) > 0$ is an example of one such spectral subspace. Projections of the linearized system onto slow spectral subspaces, which are under a nested hierarchy as defined by,

$$E^1 \subset E^2 \subset E^3 \cdots, \qquad E^k = E_{1,\cdots,k}, \qquad k = 1, \cdots, n \tag{4.4}$$

These projections provide the exact reduced order model of the linearized dynamics defined by the equation (4.1), over an increasing number of timescales as k increases.

Invariant manifold An invariant manifold [23] for a dynamical system, as previously discussed in section 2.2.3, is the subset of phase space such that any trajectory starting on the manifold, remains on the manifold for all future and past time. For a chosen specific spectral subspace $E = E_{j_1,\cdots,j_q}$ there exists infinitely many invariant manifolds tangent to E at a fixed point, here $\epsilon = 0$. Out of these infinitely many manifolds, there exists one unique, smoothest invariant manifold, called the spectral submanifold (SSM) of E denoted by $W(E, \mathbf{\Omega}t; \epsilon)$.

If the dynamical system defined in equation (4.1) is analytic, i.e. r=a, then as per [23], the reduced dynamics on a slow SSM, where the slowest decaying modes of the linearized system exists (E^k), can be approximated with arbitrarily high accuracy using arbitrarily high-order Taylor expansions, without ever increasing the dimension of E^k. The reduced models generated out of projection-based procedures can only be improved by increasing their dimension, thus proving the advantage of using an SSM based reduced order model generation. This advantage of the use of spectral submanifold over conventional methods like DMD, which produces a linear reduced order model through Galerkin projection is represented in figure 4.1

Embedding of an SSM The embedding of a Spectral Submanifold (SSM) is a mathematical process that constructs a smooth, non-linear, low-dimensional invariant surface within the high-dimensional phase space of a dynamical system. This surface is tangent to a chosen spectral subspace at an equilibrium (or a periodic/quasiperiodic orbit), and it captures the long-term dynamics of the full system near that reference state. Embedding is done to map the low-dimensional reduced coordinates (on the SSM) to full-state coordinates in the high-dimensional space. This makes the reduced dynamics physically interpretable in terms of full-state variables and the full dynamics can be reconstructed using the reduced coordinates. Taken's delay embedding theorem [68], has been extended and generalized to be used to embed a a compact d-dimensional subset of a Spectral Submanifold (SSM), denoted $C \subset W(E, \Omega t, \varepsilon)$, n the delay-coordinate space of an observable $s(t)$, forming a manifold $\mathcal{M}(\Omega t)$, for almost all choices of

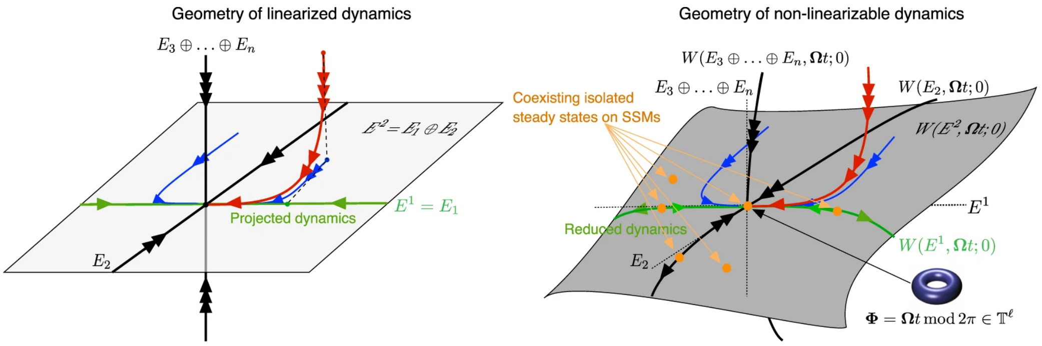

(a) (b)

Figure 4.1: (a) *Linear model reduction via Galerkin projection.* The slowest spectral subspace E_1 (green), together with another modal subspace E_2 (black), spans the second-slowest spectral subspace, $E_2 = E_1 \oplus E_2$. Projecting the full system dynamics (red trajectory) onto E_1 yields a reduced model that captures only the slow dynamics, excluding transients. Projection onto E_2 (blue trajectory) retains both the slow dynamics and the slowest decaying transient. Faster-decaying transients can be included by projecting onto higher-dimensional subspaces E_k, for $k > 2$. (b) *Reduction of non-linearizable dynamics via spectral submanifolds (SSMs).* In the unforced limit $\epsilon = 0$, a spectral submanifold $W(E, \Omega t; 0)$ provides the unique, smoothest non-linear continuation of a nonresonant spectral subspace E, even under quasiperiodic forcing with ℓ frequencies. In particular, the slowest SSM $W(E_k, \Omega t; 0)$ (green) extends the slowest subspace E_k into a non-linear invariant manifold. The system exhibits non-linearizable behaviour if isolated stationary states (e.g., fixed points or limit cycles) coexist on at least one such SSM. The image and description is taken from [14]

$s(t)$. This is subjective to the condition that the number of delays p satisfies $p > 2(d + \ell)$, and certain generic conditions on the periodic trajectories of $\mathcal{M}(\Omega t)$ hold. Following a suitable coordinate shift, the trivial fixed point of the autonomous limit of system represented in equation (4.1) can be placed at the origin $\mathbf{y} = 0$ in the observable space. To identify an embedded d-dimensional SSM $\mathcal{M}_0 \subset \mathbb{R}^p$ anchored at this origin for $\epsilon = 0$ in equation (4.1), the regions of the observable space where $\mathcal{M}_0$ are considered and can be represented as a graph over its tangent space $\mathcal{T}_0\mathcal{M}_0$ at $y = 0$. Such regions always exist and are typically large enough to encompass the non-linear features of the dynamics in most applications. Importantly, the tangent space $\mathcal{T}_0\mathcal{M}_0$ corresponds to the image of the spectral subspace E under the observable mapping. The mapping obtained between the high and low dimensional space can be used to create a set of reduced coordinates in the low dimensional tangent space $\mathcal{T}_0\mathcal{M}_0$ at $y = 0$, whose time evolution in that space corresponds to the dynamics observed for the higher dimensional system. Therefore if the dynamics in the lower dimensional system can be defined by using a normal form equation or ODE representing the time evolution of the reduced coordinates, the dynamics of the higher dimensional system can be reconstructed by reverse mapping from the low to high dimensional systems.

The mapping function between the higher to lower dimension along with the normal form equation/ODE capturing the reduced coordinate dynamics can then be used to generate a reduced order model for the full dynamics, such that the reduced order model can both track some features of the data over time and predict them into the future, assuring ROM invariance [66]. A very important feature of using spectral submanifold embedding for creating a reduced order model is that, since all of the involved dynamics of a non-linearizable system is said to be captured / lie on the manifold, it is non-dependant on the initial conditions of the system. This means that for a non-linearizable system operating in a particular condition/ set of defining parameters, regardless of the initial conditions, the dynamics will lie on the same manifold. Hence by defining the reduced dynamics on the tangent space for one initialization condition, the evolution of the dynamics can be predicted for any other initialization condition for the same set of defining parameters. The method of implementation of this technique will be discussed in detail in the upcoming sections.

4.2. Case selection and description

OAT15A, developed by ONERA (Office National d'Études et de Recherches Aérospatiales), is the aerofoil selected for this study, which is represented in figure 4.2. For this selected aerofoil, the transonic buffet region present is evaluated for a selected Reynold's number, for various Ma-α conditions. For this non-linearizable phenomena of buffeting, spectral submanifold embedding of the system is implemented and linear regression of the reduced coordinates thus obtained will be performed, which will be then used to construct low-dimensional/reduced order models from data sets, as shown in [14]. Due to the limitations in the using of the different types of turbulence models because of the availability of existing and developed code for TAU, SA-neg turbulence model was chosen. The usage of SA-neg turbulence model results in a range of Mach numbers (Ma) and angle of attack (α) combinations, where buffeting is observed, which are atypical from the range of Ma-α seen in the commonly available research on transonic buffeting such as Giannelis et. al, Couch et.al, Accorinti et. al etc [29, 18, 1]. This could be due to the choice of turbulence model, which results in creation of the shock wave-boundary layer interaction for the same case of Ma-α considered to be different, for different turbulence model. The onset of instability bought on by the shift of the growth rate (γ_0) of the global mode to positive as discussed in section 2.3.2, would thus happen at different $\alpha_{critical}$ or α_c for each turbulence model chosen. According to [50], for the same aerofoil, using the same turbulence model, the investigation done over a Mach number range of 0.64-0.76, showed a result where buffeting was only observed between Ma=0.64-0.72. The angles of attack used for the same study ranged in between $4° - 9°$. The combinations of $Ma - \alpha$ checked, to identify the transonic buffet onset/offset boundary in [50], is represented in figure 4.3.

The image figure 4.3 consists of subplots that show variation of coefficient of lift (C_L) with time, for each combination of $Ma - \alpha$ considered. The lines in red represent the region/combinations of $Ma - \alpha$ where buffeting was observed. The lines in blue represent the region/combinations of $Ma - \alpha$ where no buffeting was observed. For the range of Mach number investigated in [50], it can be seen in figure 4.3 that buffeting does not seem to occur beyond a Ma=0.71. This could be because of the potential shock location stabilization at higher Mach numbers, closer to the leading edge, which reduces the interaction with the boundary layer. It could also be due to the fact that because of higher local Mach numbers the flow disturbances that propagate upstream to interact with the shock, are instead swept away downstream.

For the thesis, two Mach numbers, 0.69 and 0.71 from the the case considered in [50], which matches the current chosen aerofoil and simulation setup, are selected for investigation. The transonic buffet onset and offset boundary represented in figure 4.3, will be validated beforehand for comparison. The identification methodology for the transonic buffet onset region is discussed in detail in section 4.4.2. For the selected Mach numbers, the spectral submanifold embedding methodology would be implemented to generate reduced order models.

Figure 4.2: OAT15A profile with a shock wave present on the suction side, from [46]

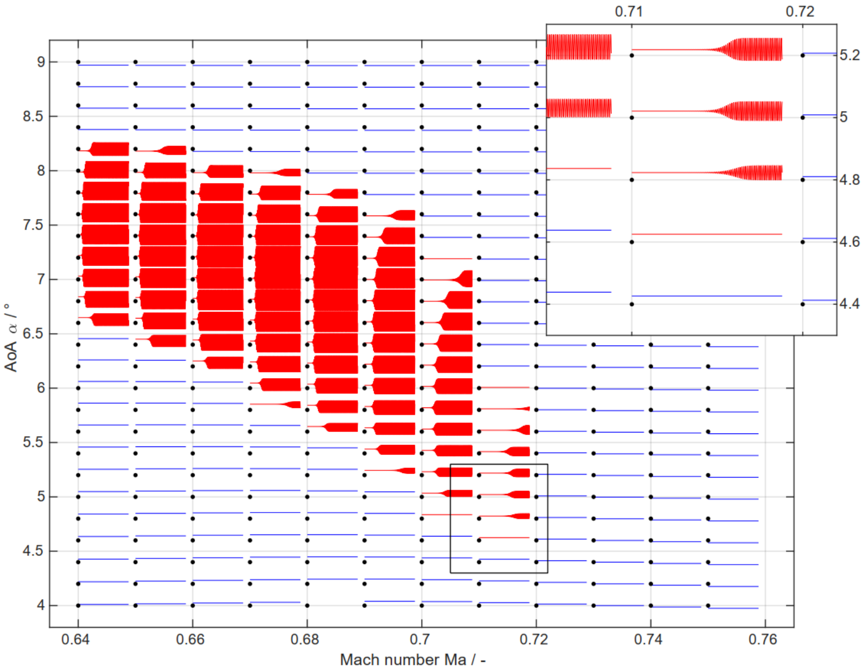

Figure 4.3: The transonic buffet onset and offset boundary investigated for OAT15A, for SA-neg turbulence model as given in Nitzsche et. al.[50]. The lines in red represent the region/combinations of $Ma - \alpha$ where buffeting was observed. The lines in blue represent the region/combinations of $Ma - \alpha$ where no buffeting was observed.

4.3. Numerical setup

4.3.1. Aerodynamic model used

As previously discussed, DLR's unstructured-mesh RANS solver TAU is employed to solve the RANS equations and obtain the flowfield solutions. The spatial and temporal discretization schemes are selected based on established experience, reflecting a compromise between accuracy and computational cost.

Mesh used and spatial discretization

The mesh used in the study, represented in figure 4.4 is the same one available based on [49] for OAT15A and has been extensively used at DLR. The non-dimensional chord length of the aerofoil used has been kept as $c = 1$. The number of grid points amounts to 120 thousand and the number of elements being 161 thousand. In the outer (separated) boundary layer and wake regions, an approximately isotropic cell spacing of $\Delta x \approx 0.5\%$ is maintained. Near the wall region, the cell spacing is kept at $\Delta x \approx 0.035\%$. The stretching of cells in both the wall-tangent and wall-normal directions does not exceed a factor of 1.2 anywhere in the domain. To minimize the influence of numerical reflections, the far-field boundary is placed 100 chord lengths away from the aerofoil. The chord Reynold's number of the flow surrounding the aerofoil has been fixed at $Re_c = 3 \times 10^6$, same as the cases found in [16],[61]. The ideal gas constant has been set at 287 J/kg.K with the gas constant/heat capacity ratio at (γ) 1.4 at a reference temperature of $T_0 = 273.15K$.

A second order central Jameson-Schmidt-Turkel scheme with matrix dissipation in space is employed, in a dual-grid setup, along with the use of multi-grid methodology as an acceleration technique. Along with this, a first order Roe scheme has been used to model the central convective turbulence flux. These settings were chosen to match the ones used in Nitzsche et. al. [50] where the same aerofoil and mesh was used for the study of buffet phenomena for a range of Ma-α, to validate and replicate the results.

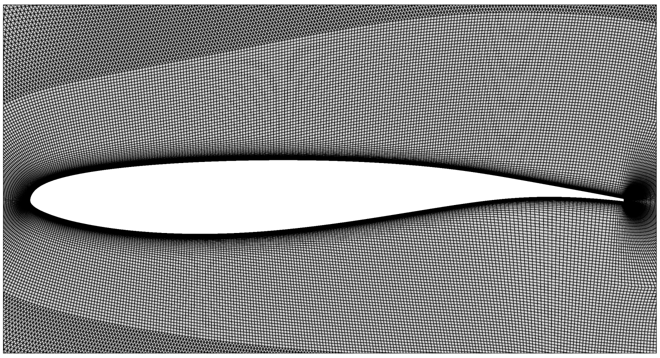

(a) Unstructured mesh near the aerofoil

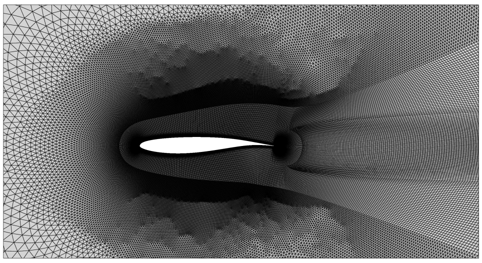

(b) Unstructured mesh around the aerofoil: view 1

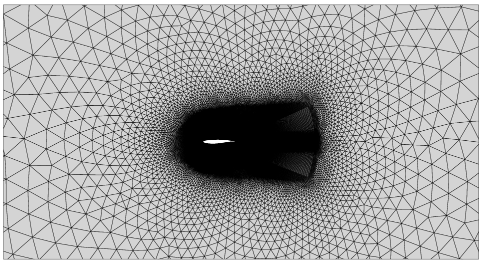

(c) Unstructured mesh around the aerofoil: view 2

Figure 4.4: Unstructured mesh considered for RANS simulation, for OAT15A aerofoil. (a) shows the mesh near the aerofoil, while (b) and (c) show different views of the mesh around the aerofoil.

Temporal discretization

A dual-time stepping approach is employed in the present study to perform unsteady flow simulations. This technique is implemented using a fully implicit second order backward Euler scheme (BDF2) for temporal discretization in the physical (outer) time, and the resulting non-linear system at each physical time step is solved iteratively using the LU-SGS (Lower-Upper Symmetric Gauss-Seidel) algorithm.

The simulation proceeds over a specified number of oscillation periods, with the physical time step size Δt determined based on four user-defined parameters encoded in the TAU CFD solver:

- the maximum reduced frequency w, whose default value is kept as 1.
- the number of oscillation periods **N** over which the simulation is conducted,
- the number of time steps per period n, and
- the number of inner iterations per physical time step t_{inner}, which controls how accurately the numerical solution converges at each physical time step when using dual-time stepping.

The reduced frequency w, a dimensionless parameter characterizing the unsteadiness of the flow, is defined as:

$$w = \frac{2\pi f}{U_\infty}$$

where f is the physical oscillation frequency, and U_∞ is a reference free-stream velocity. This reference velocity is derived from the chord-based Reynolds number, defined by:

$$Re_c = \frac{U_\infty c}{\nu}$$

where c is the chord length and ν is the kinematic viscosity of air. Given Re_c and ν, the reference velocity U_∞ can be determined.

Rewriting the reduced frequency equation, the physical oscillation frequency f is:

$$f = \frac{wU_\infty}{2\pi}$$

The corresponding period of oscillation T is the inverse of the frequency:

$$T = \frac{1}{f} = \frac{2\pi}{wU_\infty}$$

To resolve one period of oscillation using n discrete time steps, the physical time step size dt is computed as:

$$\Delta t = \frac{T}{n} = \frac{2\pi}{wU_\infty n} \tag{4.5}$$

This time step is used to advance the simulation in physical time, while convergence at each time step is enforced via t_{inner} pseudo-time iterations using the LU-SGS solver.

For instance, when the maximum reduced frequency $w = 1$, $\mathbf{N} = 1000$ periods, a number of time step per period chosen as $n = 64$ for a $U_\infty = 225.275$ m/s, a time step of $\Delta t = 4.5 \times 10^{-4}$ s is obtained.

This approach ensures that the unsteady dynamics corresponding to the chosen reduced frequency w are resolved accurately over the specified number of oscillation periods. At the same time, the use of implicit time integration and inner pseudo-time iterations guarantees stability and convergence of the numerical scheme.

4.4. Methodology

In this section, a walk-through of the methodology implemented is discussed sequentially, in detail. It includes a detailed description on how the steady simulations for the base flows were done through RANS simulations and how the unsteady simulations though URANS simulations. It also includes details on how linear analysis and eigenmode extraction are carried out, how POD modes are extracted and finally how spectral submanifold embedding and reduced order model for the system is produced.

4.4.1. Steady simulations for base flows (RANS)

The general evaluation principle of the RANS simulations done for this study is to use a CFL number i.e. Courant–Friedrichs–Lewy number, of 10 and a maximum iteration of 100000 to reach the minimum residual value of 10^{-10}, such that all steady simulations converge. A set of monitoring values are evaluated to check the rate of convergence with increase in iteration, which include density residual(Res_{rho}), coefficient of lift (C_{lift} or C_L), coefficient of drag (C_{drag} or C_D) etc. Two separate set of steady simulations were done for this thesis. They are as follows:

Steady simulations for transonic buffet onset boundary evaluation

An important part of working with transonic buffets is to identify the transonic buffet onset conditions, which occur at unique combinations of Ma and $\alpha_{critical}$, where beyond $\alpha_{critical}$ i.e. $\alpha > \alpha_{critical}$, buffeting phenomena for a particular Ma is observed. Based on [50], the Ma range of evaluation between 0.68-0.72 is selected, with a step size of $\Delta Ma = 0.01$ between the range of Ma chosen. Here steady simulations are initially performed between a span of α between $4° - 6°$, with a step size of $\Delta\alpha_{step} = 0.25°$ for each of the Ma chosen. The chord Reynold's number ($Re_c = 3 \times 10^6$) was kept as a constant for all cases. The converged steady simulation results serve as the initialization conditions for further unsteady simulations. Thus 9 cases of α for each case of Ma were selected. The combinations of Ma-α evaluated are depicted in table 4.1.

Mach \ α°	4.00	4.25	4.50	4.75	5.00	5.25	5.50	5.75	6.00
0.68	✓	✓	✓	✓	✓	✓	✓	✓	✓
0.69	✓	✓	✓	✓	✓	✓	✓	✓	✓
0.70	✓	✓	✓	✓	✓	✓	✓	✓	✓
0.71	✓	✓	✓	✓	✓	✓	✓	✓	✓
0.72	✓	✓	✓	✓	✓	✓	✓	✓	✓

Table 4.1: Ma-α cases evaluated for transonic buffet onset evaluation.

Steady simulations for detailed investigation into selected Mach numbers

For the thesis, 2 Mach numbers of operation for detailed investigation and for reduced order modelling were selected: 0.69 and 0.71. The chord Reynold's number ($Re_c = 3 \times 10^6$) was kept as a constant for both the cases of Mach numbers. Now, based on the results observed in [50], for the same turbulence model selected, (SA- neg model), the shock buffet region was observed to lie between the angle of attack (α°) $5° - 8°$ for $Ma = 0.69$ and between $4.5° - 6°$ for $Ma = 0.71$. For the sake of identifying the transonic buffet onset and offset boundary for both the Mach numbers, a span of angles of attack between $4° - 6°$ for $Ma = 0.71$ and $4° - 8°$ for $Ma = 0.69$, was selected for further study.

For identification of the onset boundary, which is of more interest in this section of the study, the span of α selected for both Mach numbers were divided. To do this investigation of the span using two distinct step size of α or $\Delta\alpha$ is done. To accurately identify the region of onset, $\Delta\alpha_{fine} = 0.05°$ is used, and to investigate the rest of the span, $\Delta\alpha_{coarse} = 0.25°$ is used.

Based on the onset region identified in [50], for Ma=0.69, $\Delta\alpha_{fine} = 0.05°$ was used to check between $4.6° - 4.9°$ and for Ma=0.71, $\Delta\alpha_{fine} = 0.05°$ was used to check between $4° - 4.5°$. Thus, for Ma= 0.69, the rest of the span of α i.e. $4° - 4.6°$ & $4.9° - 8°$, and for Ma=0.71, the rest of the span of $4.5° - 6°$ use the $\Delta\alpha_{coarse} = 0.25°$ for investigation. This is depicted in the table table 4.2

	Span of α using $\Delta\alpha_{fine}$ =0.05°	Span of α using $\Delta\alpha_{coarse}$ =0.25°
$Ma = 0.69$	4.6°–4.9°	4°–4.6°& 4.9°–8°
$Ma = 0.71$	4°–4.5°	4.5°–6°

Table 4.2: Range values corresponding to different Mach numbers and $\Delta\alpha$ values.

Thus 23 cases for Ma = 0.69 and 17 cases for Ma = 0.71 were chosen to be investigated. The steady simulations of all these cases were carried out until there was convergence.

4.4.2. Unsteady simulations (URANS)

The URANS simulations are initialized using the converged RANS solutions, with fixed CFL number of 20. According to [61], at a fixed Mach number when the angle of attack is small and below the transonic buffet onset boundary point i.e. i.e. $\alpha < \alpha_{critical}$, URANS computations converge toward a steady solution, and no unsteady phenomena is observed. On further increasing the angle of attack, URANS simulations indicate an unsteady behaviour as soon as the transonic buffet onset boundary point ($\alpha_{critical}$) is reached i.e $\alpha \geq \alpha_{critical}$. At and beyond this point, the shock wave present over the aerofoil begins to oscillate back and forth with a periodic motion, which is known as limit cycle oscillations (LCO), which has been described in detail in section 2.1. Identification of the transonic buffet onset boundary is important in recognizing the region of Ma-α where the buffeting phenomena is observed. This requires setting up of URANS simulations for various Ma-α cases with the converged steady solutions obtained as the result of section 4.4.1. But, before running the URANS simulation, the setup for the URANS simulation including modifying its initial conditions and choosing a time step for the URANS simulation need to be carried out. These are carried out through conducting a perturbation study, which determines the additional initialization condition needed for conducting a URANS simulation with lesser computational resources, and through a time step evaluation, which determines the optimum time step which could be implemented for all the URANS simulations.

Perturbation study

Due to how the DLR TAU operates, the unsteady simulations initialized by the converged RANS solutions, have some numerical "bridging" error which serves as the initial disturbance which could either grow into a LCO or converge back into the steady solution. The growth into an LCO or converging back into the steady solution, depends on which α for a specific Ma, the URANS simulation is done for. The evolution of the solution in time is observed and evaluated through studying the evolution of the coefficient of lift (C_L) in time. For a chosen Ma, if $\alpha < \alpha_{critical}$, the initial numerical disturbance converges back to the steady solution, and if $\alpha > \alpha_{critical}$ the initial disturbance grows into an LCO at some time "t".

But these numerical errors are very weak and very small in nature ($O(\sim 10^{-14})$). When the URANS simulations are initialized with only the converged solution of the steady simulation, for cases of $\alpha = \alpha_{critical}$ or very slightly greater than $\alpha_{critical}$, the evolution of the flow to LCO behaviour, takes a very long time. Due to the γ_0 of the eigenmodes being ≈ 0, or very slightly greater than 0 for these cases as discussed in section 2.3.2, which indicates the onset of unsteadiness but with a very small growth rate of the unsteadiness, the time taken to reach LCO behaviour in the URANS simulation is high and thus is computationally expensive to evaluate. To remedy this, additional disturbances are provided along with the the initialization condition of using the converged steady state solution. This is done with the help of FS Forced motion (FSFM), a tool used at DLR to provide dynamic motion to aerofoils/wings while in URANS simulation. The dynamic motion can be a pitching motion, a heaving motion or a rolling motion (if a 3D wing is considered). These motions are initiated by specifying the following factors,

- Type of motion: whether the intended motion is a pitch, a roll or a heave.
- The amplitude factor/strength of pulse: which determines what would be the angle of motion i.e pitch, roll or heave about an axis. This corresponds to the strength of the disturbance introduced in the flow. The amplitude factor is specified in degree angle (°).
- Shape of the motion: which decides on what sort of a shape the perturbation takes. FSFM contains many shapes including a pulse shape (Gaussian curve), sinusoidal shape etc.
- Steps per pulse: which determines the total duration taken for the motion to occur, undergoing the specified shape.
- Axis and location of pivot: the axis of intended motion and the location about which the motion occurs can be specified.

Since the case at hand considers a 2D aerofoil, pitching and heaving motion were considered as potential methods of perturbation to be used with the converged steady state solution initialization. To evaluate the superior method for providing perturbation, which results in the quickest evolution to LCO for a case where $\alpha > \alpha_{critical}$, a URANS simulation case where an equal strength pitch and heave were used were initially compared, with conditions: Ma = 0.71, and $\alpha = 4.5°$, which was selected as per details from [50]. The strength of heave can be matched with the pitching degree by the following equation,

$$h_c = (1 - x)c\theta \tag{4.6}$$

where c is the chord length of the aerofoil, which is considered 1 as per out simulation setup ($c = 1$). The location of pivot measured from the leading edge of the aerofoil is x, with the pitch motion in radians is represented by θ. For instance, a pitching strength of 0.001°, a corresponding heave strength of 1.31×10^{-5} radians is obtained, when the pitch point is 0.25 units measured from the leading edge of the aerofoil. The pitching motion was found to result in a quicker evolution to LCO for the α considered, which is discussed in detail in the section 5.1.2. Multiple pitching strengths were then evaluated to find the optimum pitching strength which can be used for the initialization of the URANS simulation, paired up with the converged steady state solution. The various perturbation conditions evaluated are as follows:

- No perturbation
- Pitching perturbation of strength = $(1 \times 10^{-5})^{\circ}$
- Pitching perturbation of strength = $(1 \times 10^{-4})^{\circ}$
- Pitching perturbation of strength = $(1 \times 10^{-3})^{\circ}$
- Heaving perturbation of strength = (1.31×10^{-5}) units, which matches the pitching strength of $(1 \times 10^{-3})^{\circ}$
- Pitching perturbation of strength = $(5 \times 10^{-3})^{\circ}$
- Pitching perturbation of strength = $(1 \times 10^{-2)^{\circ}}$
- Pitching perturbation of strength = $(1 \times 10^{-1})^{\circ}$

Time step evaluation

The time step size used for the URANS simulation, calculated as per equation (4.5), is evaluated for its impact on the evolution of the unsteadiness in the flow into LCO for $\alpha > \alpha_{critical}$. This was done to select an appropriately small enough time step to evaluate the flow behaviour, all the while minimizing the computational effort required. The study was done for the case: $Ma = 0.68$ and $\alpha = 5.5°$. The time steps considered were:

- $\Delta t = 1 \times 10^{-3} s$
- $\Delta t = 3 \times 10^{-4} s$
- $\Delta t = 3.5 \times 10^{-4} s$
- $\Delta t = 4 \times 10^{-4} s$
- $\Delta t = 4.4 \times 10^{-4} s$
- $\Delta t = 4.5 \times 10^{-4} s$
- $\Delta t = 5 \times 10^{-3} s$
- $\Delta t = 5 \times 10^{-4} s$

The time step was successively reduced from an initial value of (5×10^{-3}s), with each run using a smaller step, until further refinement produced no discernible change in the solution. The investigation and results of comparison of different time steps are compared and evaluated in section 5.1.2.

Transonic buffet onset boundary evaluation

The perturbation evaluation and the time step evaluation conducted to setup the initialization condition and the time step for URANS simulation respectively, results in a setup with the minimum amount of computational resources and effort for all URANS simulation needed to be done for the thesis. This setup is then utilized for evaluating the transonic buffet boundary, by initializing the URANS simulations for the range of $Ma - \alpha$ selected as per section 4.4.1, with the converged steady simulation results obtained from section 4.4.1, along with a perturbation finalized from section 4.4.2. The time step selected for the URANS simulation is taken from the results of section 4.4.2. The evaluation of the variation of coefficient of lift (C_L) against time is done to observe whether any LCO behaviour is reached or the case considered or whether the perturbation dies down to the steady solution. Thus, for evaluation, all cases discussed in detail in table 4.1 and table 4.2 are considered as steady initialization condition to do URANS simulation with the corresponding Ma-α combination.

4.4.3. Linear Analysis

To find the "n" most dominant eigen modes in a system of unique $Ma - \alpha$ combination, an in-house DLR TAU + Python code is used, modified to analyse the converged steady solution obtained for the chosen $Ma - \alpha$ combination, where the number of modes that need to be extracted is specified. The underlying principle behind the process is as described in section 3.2.2, involving shift-invert techniques. The eigen modes extracted will be represented in the conservative variables form, i.e. each eigen mode will have corresponding components, both real and imaginary parts for the conservative variables: $[\rho, \rho u, \rho w, \rho E, \rho\tilde{\nu}]$, where,

- ρ is the density of the flow,
- ρu is the momentum in the x direction or x-momentum of the flow,
- ρw is the momentum in the z direction or z-momentum of the flow,
- ρE is the energy density measured for the flow,
- $\rho\tilde{\nu}$ is the eddy viscosity of the flow.

The adjoint of the eigenmodes can also be extracted using the TAU code. The eigenvalues corresponding to each of the extracted eigen modes are represented in the form $\omega = \gamma_0 + i\omega_0$, where the real part of the complex eigenvalue ω (γ_0) represents the growth rate of the mode and the imaginary part (ω_0) represents the frequency of the mode. As discussed in section 2.3.2, those eigenmodes are of interest, whose eigenvalues have a positive real component, i.e. $\gamma_0 > 0$. From the extracted eigenvalues obtained for each $Ma - \alpha$ combination for the selected Ma, an eigenvalue spectrum is plotted on a $Re - Im$ plane, for the entire span of α investigated. From the eigenvalue spectrum, the eigenvalues whose real part cross the real axis are noted. Those α with real part of the eigenvalue having the least positive (lowest) and most positive (highest) are noted. This gives us 3 α:

- α_1, which is the angle of attack whose real part of the eigenvalue, crosses the real axis first, in the span of α tested,
- α_2 which is the angle of attack which has the highest real part of the eigenvalue,
- α_3 which is the angle of attack which has the last positive real part of the eigenvalue.

These eigenvalues for each of the eigenmodes for all $Ma - \alpha$ combinations, discussed in table 4.1 and section 4.4.1, for Ma=0.69 and Ma=0.71 are investigated to observe a clearer picture of when the transonic buffet onset occurs.

4.4.4. URANS flow field data recording

After evaluation of the transonic boundary 2 Mach numbers 0.69 and 0.71 are selected, as stated in section 4.2. For the selected Ma, URANS simulations are initialized with the converged steady simulation results obtained from section 4.4.1, along with a perturbation finalized from section 4.4.2 with the time step selected from the results of section 4.4.2. For the selected cases, the flow field data for the conservative variables $[\rho, \rho u, \rho w, \rho E, \rho\tilde{\nu}]$ are to be recorded at each time step. This flow field data recorded is to be referred to as *training data*. Another set of flow field recording was also done for the same $Ma - \alpha$ combinations and the time step, but for the secondary perturbation chosen, which could later be used for validation/testing purposes for any reduced order model obtained. This secondary set of flow field recording was to be referred as *validation/test data*. The perturbations chosen for the same are discussed in section 5.1.2.

4.4.5. POD mode extraction

To extract the "n" most dominant POD modes in a system of unique $Ma - \alpha$ combination, the URANS flow field *training data* recorded at a time interval dt is used, as per section 4.4.4. The evaluation of the coefficient of lift (C_L) with time is checked for each of the cases to note the points in time where the flow reaches limit cycle oscillation behaviour. The points of time at which the first cycle of LCO starts and ends are noted and the same is repeated for second and third cycles of LCO. Using the SVD methodology discussed in the section 3.2.3, the required dominant POD modes are extracted using the flow field data of first, second and third LCO cycles. As per standard practices followed in DLR, encouraging the use of approximately 300-500 fully developed flowfield recording of time instances to find POD from, three cycles of LCO which contains $\tilde{4}71$ time instance recording were chosen. The SVD method is implemented in python using the *flowtorch* module [74], whose built-in functions are then used to extract the dominant POD modes.

4.4.6. Spectral submanifold embedding

Since transonic buffet at its core, is a bifurcation phenomena as previously discussed in section 2.3.2 and is a higher dimensional non-linear and non-linearizable system as per the definition seen in [14], the embedding process of an SSM can be implemented in the current problem of producing a reduced order model for the purpose of transonic buffet control. This may be carried out in the following manner:

The spectral submanifold (SSM) attached to the fixed point $\mathbf{w}_b$, is defined as two-dimensional ($d = 2$). To embed this SSM, denoted $\mathcal{M}_0 \subset \mathbb{R}^n$, the regions of the observable space where $\mathcal{M}_0$ can be represented as a graph over its tangent space $\mathcal{T}_0\mathcal{M}_0$ at the origin $\mathbf{w}' = \mathbf{0}$ were focused on. This tangent space $\mathcal{T}_0\mathcal{M}_0$ corresponds to the image of the unstable spectral subspace $\mathbf{E}_u$ (which is two-dimensional) under the observable map. Such graph-based domains exist in general and are typically large enough to capture the essential non-linear, non-linearizable features of the dynamics, unless $\mathcal{M}_0$ develops a fold over $\mathcal{T}_0\mathcal{M}_0$. Cendese et al.[14] tackles the problem of fold of $\mathcal{M}_0$, over $\mathcal{T}_0\mathcal{M}_0$, for a case of time-periodic vortex shedding for the flow past a cylinder, by defining the tangent plane using the two most dominant POD modes extracted from the flow.

After the embedding, an encoder function ($\mathbf{U}$) is obtained, which connects the full-state coordinates in the high-dimensional space to the low-dimensional reduced coordinates (on the SSM) as per [66]. The encoder function along with a map $\mathbf{S}$, which can be used for predicting the data in the low-dimensional space, constitutes the ingredients of a reduced order model. The map $\mathbf{S}$, can be obtained through linear regression of the low-dimensional reduced coordinates, producing a pair of ordinary differential equations (ODE's) which can be used to capture the evolution of the reduced coordinates and hence the reduced dynamics.

After implementing predictions in the reduced order coordinates with the help of ODE's, a decoder function ($\mathbf{W}$) can be used to construct the high-dimensional space from the lower dimensional predictions. The methodology discussed in [14] has already been implemented for a case of Hopf bifurcation: vortex shedding for a flow past a cylinder. Due to the nature of very good prediction results obtained using the reduced order model obtained with SSM embedding compared to other conventional methods used to model such phenomena, which has been compared in [14], for the case of transonic shock buffeting over an aerofoil, the same methodology with appropriate modifications is implemented, to obtain a reduced order model. A depiction of the algorithm implemented in this study is shown in figure 4.5.

For a case of transonic buffeting for an aerofoil, the dynamics are assumed to lie on an n-dimensional space, $\mathbb{R}^{n\times n}$. A procedure based on the theory discussed in section 4.1 is established. Here, in the setting chosen, the full phase space of the discretized RANS simulation as the observable space is taken. i.e. If p flow field recordings are present, as per section 4.4.4, then $n = p$. To learn the graph parametrization of $\mathcal{M}_0$ from data, a matrix $\mathbf{U}_1 \in \mathbb{R}^{n\times 2}$ is defined, whose columns are orthonormal vectors and span the tangent space $\mathcal{T}_0\mathcal{M}_0$. After the definition of the orthonormal vectors, the unsteady components of the URANS data recorded is projected onto the orthonormal basis to produce a pair of reduced coordinates on $\mathcal{T}_0\mathcal{M}_0$ that capture the dynamics of the n-dimensional system. The dynamics of the system are then captured into a pair of matrices which comprises of linear and non-linear coefficients which are used with a Taylor expansion of the reduced coordinate monomials. These matrices are then used along with the reduced coordinate monomials formed to reconstruct the n-dimensional system. This process of embedding the dynamics on a spectral submanifold and the reconstruction of the higher dimensional system are described in the upcoming parts of the section in detail, and is depicted as a flowchart in figure 4.6.

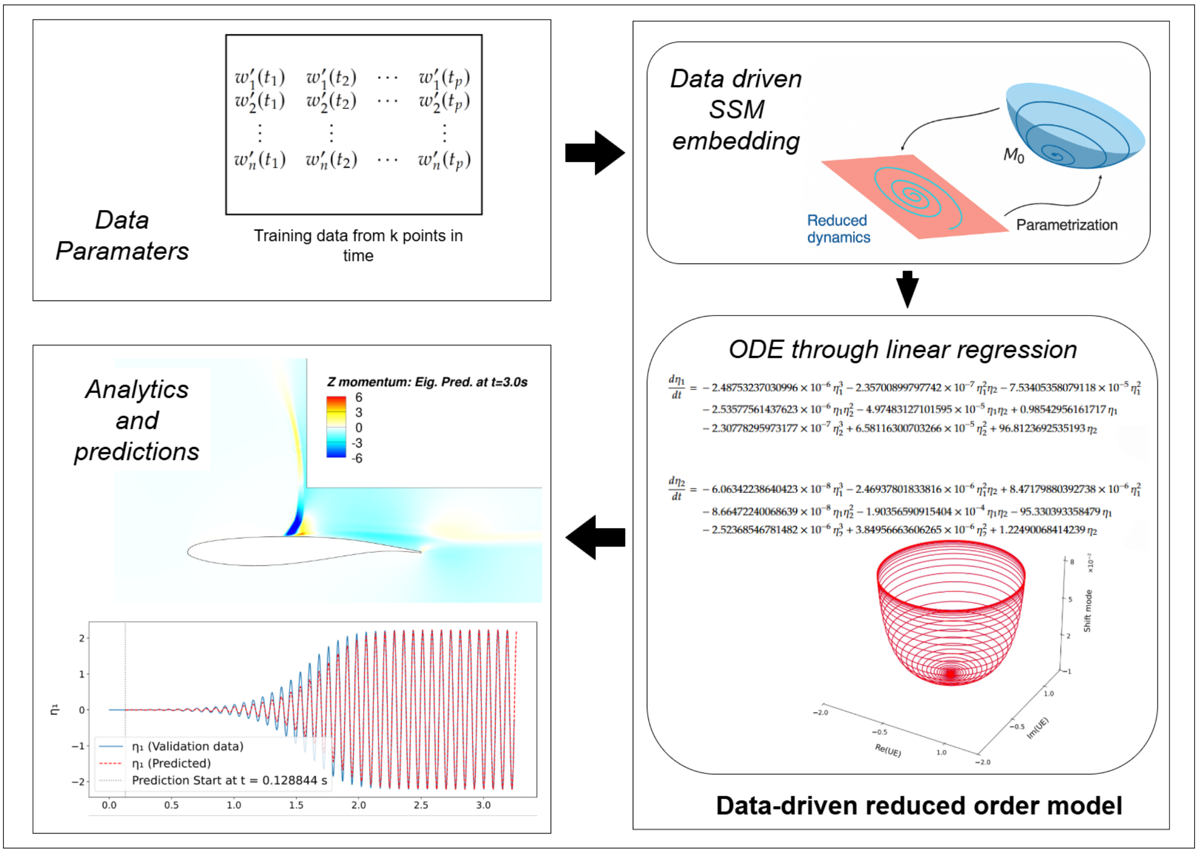

Figure 4.5: This image represents an algorithm of the SSM embedding methodology used for data driven reduced order model generation and use of the reduced order model for prediction. Initially a set of data parameters, recorded as time series data of field is considered. Next these training data recorded are embedded onto the SSM. Through linear regression, ODE's are generated that describe the dynamics of the reduced coordinates obtained through SSM embedding. Finally, the algorithm uses this model to predict individual unforced trajectories for alternate initialization conditions and is then used to reconstruct flowfields for these new trajectories. The image is inspired by the algorithm represented in Fig.3 of [14].

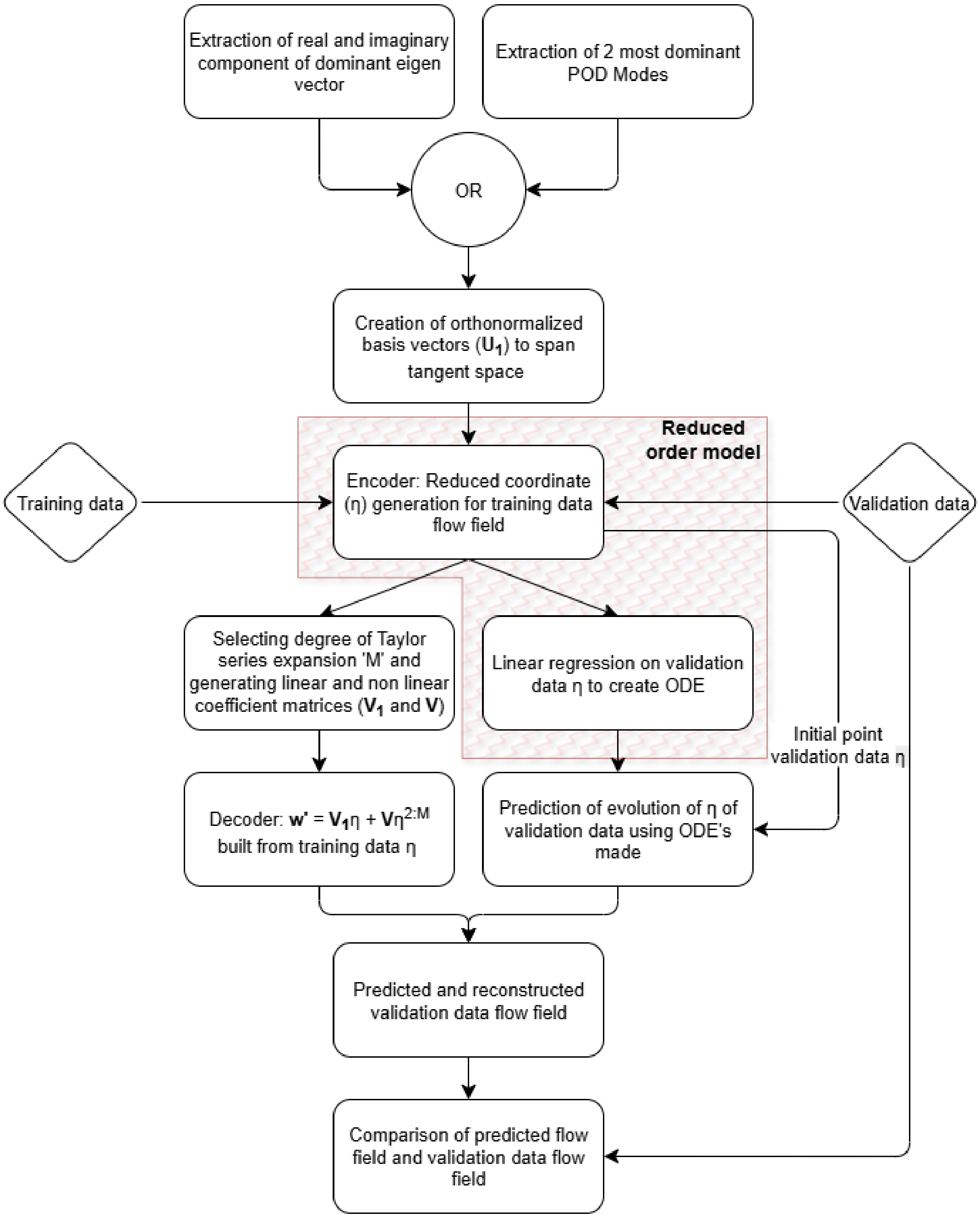

Figure 4.6: A flowchart representing the sequence of steps involved in reduced order modelling using spectral submanifold embedding. The process starts with selecting either the most dominant eigen mode and orthonormalizing its components or 2 most dominant POD modes and orthonormalizing them. These orthonormalized vectors are used to create reduced coordinates (η) of *training data* (functioning as an encoder), which are used to capture the linear and non-linear coefficient matrices $\mathbf{V_1}$ and $\mathbf{V}$ respectively, suing Taylor series expansion of degree M. A linear regression over the reduced coordinates result in pair of ODE's which are used to predict evolution of reduced coordinates of *validation data*. The predicted reduced coordinates are then converted back to full flowfield state using a decoder function which uses $\mathbf{V_1}$ and $\mathbf{V}$. The encoder and the ODE created together forms a reduced order model, marked by the red boundary.

Creation of orthonormal basis for spanning $\mathcal{T}_0\mathcal{M}_0$
The orthonormal vectors used to span $\mathcal{T}_0\mathcal{M}_0$ can be created in two ways,

- Using the real and imaginary component of the most dominant eigenvector, extracted as per section 4.4.3.
- Using the most dominant and second most dominant POD modes (POD_1 and POD_2) extracted as per section 4.4.5.

These components are then multiplied by the volume of the cells in the mesh used to obtain a weighted vectors, to consider the impact of the mesh considered and its density. These orthonormal vectors are created using Gram–Schmidt orthonormalization process, which can be described as follows:

Given a set of linearly independent vectors $\{\mathbf{v}_1, \mathbf{v}_2, \ldots, \mathbf{v}_n\}$ in an inner product space, the Gram-Schmidt process constructs an orthonormal set $\{\mathbf{u}_1, \mathbf{u}_2, \ldots, \mathbf{u}_n\}$ as follows:

1. Set the first orthogonal vector:
$$\mathbf{w}_1 = \mathbf{v}_1 \tag{4.7}$$
2. For $k = 2, 3, \ldots, n$, set
$$\mathbf{w}_k = \mathbf{v}_k - \sum_{j=1}^{k-1} \frac{\langle \mathbf{v}_k, \mathbf{w}_j \rangle}{\langle \mathbf{w}_j, \mathbf{w}_j \rangle} \mathbf{w}_j \tag{4.8}$$
3. Normalize each vector:
$$\mathbf{u}_k = \frac{\mathbf{w}_k}{\|\mathbf{w}_k\|} \tag{4.9}$$
for $k = 1, 2, \ldots, n$.

Thus, $\{\mathbf{u}_1, \mathbf{u}_2, \ldots, \mathbf{u}_n\}$ is an orthonormal set spanning the same subspace as $\{\mathbf{v}_1, \mathbf{v}_2, \ldots, \mathbf{v}_n\}$.

Creation of reduced coordinates and defining the unsteady dynamics using Taylor expansions
The flow field recorded according to section 4.4.4, is in a form $\mathbf{w} = \bar{\mathbf{w}} + \mathbf{w}'$, where $\bar{\mathbf{w}}$ represents the steady component of the total flow field and $\mathbf{w}'$ represents the unsteady component of the flow field. Subtracting out the steady component or the converged steady solution for the same Ma-α, from the results of steps done in section 4.4.1, the unsteady component of each flow field is obtained, in the conservative variables $[\rho, \rho u, \rho w, \rho E, \rho\tilde{v}]$. The volume of the mesh used, is multiplied with the flowfield either before the subtraction process i.e. to both the total flowfield and the steady component or after the subtraction process,i.e, to the unsteady component. This was done for a set of *training data* for the $Ma - \alpha$ chosen for which URANS simulations with flowfield recording was conducted for, as discussed in section 4.4.4. Since the dynamics of the flow lies on the embedded manifold $\mathcal{M}_0$, a pair of reduced coordinates $\boldsymbol{\eta} \in \mathbb{R}^2$ for a point $\mathbf{w}' \in \mathcal{M}_0$ are obtained via orthogonal projection:

$$\boldsymbol{\eta} = \mathbf{U}_1^T \mathbf{w}'. \tag{4.10}$$

This projection function is the encoder function ($\mathbf{U}$), that is used to map between the n-dimensional space and the low (d=2) dimensional space, as discussed in section 4.1. From this projection, the reduced coordinates are obtained as,

$$\boldsymbol{\eta} = [\eta_1, \eta_2]^T \tag{4.11}$$

$\mathcal{M}_0$ near $\boldsymbol{\eta} = \mathbf{0}$ is approximated using a Taylor expansion in terms of monomials $\boldsymbol{\eta}^{2:M}$, where $\boldsymbol{\eta}^{2:M}$ includes all monomials in η_1 and η_2 from degree 2 to M. For example, when $M = 3$,

$$\boldsymbol{\eta}^{2:M} = [\eta_1^2, \eta_1\eta_2, \eta_2^2, \eta_1^3, \eta_1^2\eta_2, \eta_1\eta_2^2, \eta_2^3]^T. \tag{4.12}$$

As a graph over $\mathcal{T}_0\mathcal{M}_0$, the SSM $\mathcal{M}_0$ is approximated by:

$$\mathbf{w}' = \mathbf{V}_1\boldsymbol{\eta} + \mathbf{V}\boldsymbol{\eta}^{2:M}, \tag{4.13}$$

where $\mathbf{V}_1$ and $\mathbf{V}$ contain the linear and non-linear coefficients, respectively. These matrices capture the linear and non-linear dynamics of the system respectively, and are used along with the Taylor expansion of the monomials to describe the higher dimensional system using the reduced coordinates. This description of the reconstructed dynamics seen in equation (4.13), is obtained from [14]. Here the right hand side of this equation constitutes a decoder function ($\mathbf{W}$) used to map between the low dimensional space (d=2) back to the n-dimensional space where the dynamics originally lie.

To obtain these matrices $\mathbf{V}_1$ and $\mathbf{V}$ the following procedure is used:

Given P observations $\{\mathbf{w}'_1, \dots, \mathbf{w}'_P\}$, learning $\mathcal{M}_0$ amounts to solving the following minimization problem:

$$\begin{aligned}(\mathbf{U}_1^*, \mathbf{V}_1^*, \mathbf{V}^*) = \arg \min_{\mathbf{U}_1, \mathbf{V}_1, \mathbf{V}} \sum_{j=1}^{P} \left\| \mathbf{w}'_j - \mathbf{V}_1 \mathbf{U}_1^T \mathbf{w}'_j - \mathbf{V} \left(\mathbf{U}_1^T \mathbf{w}'_j \right)^{2:M} \right\|^2 \\ \text{subject to} \quad \mathbf{U}_1^T \mathbf{U}_1 = \mathbf{I}.\end{aligned} \tag{4.14}$$

From the results of a prior linear stability analysis, the real and imaginary parts of the unstable eigenvector, $\hat{\mathbf{w}}_r$ and $\hat{\mathbf{w}}_i$, are considered for spanning the tangent space $\mathcal{T}_0\mathcal{M}_0$. Normalizing and orthogonalizing these vectors yields the matrix $\mathbf{U}_1$.The tangent space $\mathcal{T}_0\mathcal{M}_0$ can also be spanned by using the POD_1 and POD_2 modes as seen in [14].

Assuming $\mathbf{V}_1 = \mathbf{U}_1$, the only unknown is the non-linear coefficient matrix $\mathbf{V}$, which can be computed by minimizing:

$$\mathbf{V}^* = \arg \min_{\mathbf{V}} \sum_{j=1}^{P} \left\| \mathbf{w}'^{\perp}_j - \mathbf{V} \boldsymbol{\eta}_j^{2:M} \right\|^2, \tag{4.15}$$

where $\mathbf{w}'^{\perp}_j = \mathbf{w}'_j - \mathbf{V}_1 \mathbf{U}_1^T \mathbf{w}'_j$ and $\boldsymbol{\eta}_j^{2:M} = \left(\mathbf{U}_1^T \mathbf{w}'_j\right)^{2:M}$. Here, the $\mathbf{w}'_j$ can be split into its tangential ($\mathbf{w}'^{\parallel}_j = \mathbf{V}_1 \mathbf{U}_1^T \mathbf{w}'_j$) and normal component ($\mathbf{w}'^{\perp}_j$).

The residual vector for each sample can be expressed as:

$$\mathbf{X}_j = \mathbf{w}'^{\perp}_j - \begin{bmatrix} | & & | & & | \\ \mathbf{V}^{20} & \cdots & \mathbf{V}^{m_1 m_2} & \cdots & \mathbf{V}^{M0} \\ | & & | & & | \end{bmatrix} \begin{bmatrix} \eta_{1,j}^2 \\ \vdots \\ \eta_{1,j}^{m_1} \eta_{2,j}^{m_2} \\ \vdots \\ \eta_{2,j}^M \end{bmatrix}. \tag{4.16}$$

This can be rewritten compactly using the Kronecker product:

$$\mathbf{X}_j = \mathbf{w}'^{\perp}_j - \left(\begin{bmatrix} \eta_{1,j}^2 & \cdots & \eta_{1,j}^{m_1} \eta_{2,j}^{m_2} & \cdots & \eta_{2,j}^M \end{bmatrix} \otimes \mathbf{I}^n \right) \begin{bmatrix} \mathbf{V}^{20} \\ \vdots \\ \mathbf{V}^{m_1 m_2} \\ \vdots \\ \mathbf{V}^{M0} \end{bmatrix}. \tag{4.17}$$

Summing over all P samples, the total reconstruction loss becomes:

$$\|\mathbf{X}\|^2 = \sum_{j=1}^{P} \|\mathbf{X}_j\|^2, \tag{4.18}$$

where

$$\mathbf{X} = \begin{bmatrix} \mathbf{w'}_1^{\perp} \\ \vdots \\ \mathbf{w'}_P^{\perp} \end{bmatrix} - \left(\begin{bmatrix} \eta_{1,1}^2 & \cdots & \eta_{1,1}^{m_1}\eta_{2,1}^{m_2} & \cdots & \eta_{2,1}^M \\ \vdots & \ddots & \vdots & \ddots & \vdots \\ \eta_{1,P}^2 & \cdots & \eta_{1,P}^{m_1}\eta_{2,P}^{m_2} & \cdots & \eta_{2,P}^M \end{bmatrix} \otimes \mathbf{I}^n \right) \begin{bmatrix} \mathbf{V}^{20} \\ \vdots \\ \mathbf{V}^{m_1 m_2} \\ \vdots \\ \mathbf{V}^{M0} \end{bmatrix}. \tag{4.19}$$

Finally, the matrix $\mathbf{V}$ minimizing the error is computed using the pseudo-inverse:

$$\begin{bmatrix} \mathbf{V}^{20} \\ \vdots \\ \mathbf{V}^{ik} \\ \vdots \\ \mathbf{V}^{M0} \end{bmatrix} = \underbrace{\begin{bmatrix} \eta_{1,1}^2 & \cdots & \eta_{1,1}^{m_1}\eta_{2,1}^{m_2} & \cdots & \eta_{2,1}^M \\ \vdots & \ddots & \vdots & \ddots & \vdots \\ \eta_{1,P}^2 & \cdots & \eta_{1,P}^{m_1}\eta_{2,P}^{m_2} & \cdots & \eta_{2,P}^M \end{bmatrix}^{\dagger}}_{\mathbf{A}} \otimes \mathbf{I}^n \underbrace{\begin{bmatrix} \mathbf{w'}_1^{\perp} \\ \vdots \\ \mathbf{w'}_P^{\perp} \end{bmatrix}}_{\mathbf{W}} \tag{4.20}$$

which gives,

$$\mathbf{V} = \mathbf{A}^{\dagger} \otimes \mathbf{I}^n \mathbf{W} \tag{4.21}$$

Using the property of Kronecker products involving vectorization, defined for for matrices A, B, and C of dimensions $k \times l$, $l \times m$, and $m \times n$ respectively,

$$\mathbf{vec}(AB) = (I_m \otimes A)\mathbf{vec}(B) = (B^T \otimes I_k)\mathbf{vec}(A) \tag{4.22}$$

It can be thus written that,

$$\mathbf{V} = W(A^{\dagger})^T \tag{4.23}$$

Substituting $\mathbf{V}_1 = \mathbf{U}_1$, and equation (4.23) in equation (4.13), the reduced form of the $\mathbf{w'}$ is constructed. The entire process is repeated to find the ideal degree of of monomial required (M) for fitting the trajectory of the full flow field in the reduced coordinate a time until the end of 1st LCO cycle. By the theory of SSM embedding, when encoder function is used to reduce the n-dimensional system to a two dimensional tangent space $\mathcal{T}_0\mathcal{M}_0$ resulting in reduced coordinates η, the construction $\mathbf{V}$ matrix with a non-linear, Taylor series expansion of the reduced coordinate η will capture the normal component, $\mathbf{w'}_j^{\perp}$, i.e. $\mathbf{V}_1\boldsymbol{\eta}$ would capture the tangential components of the system, while $\mathbf{V}\boldsymbol{\eta}^{2:M}$ would capture the normal components.

Visualization of the embedded spectral submanifold and the reconstructions done in 3D

The visualization of the embedded spectral submanifold can be implemented using a third vector, shift mode: defined as the difference between the mean flow $\mathbf{u}_{\mathrm{m}}(\mathbf{x})$ and the steady flow $\mathbf{u}_{\mathrm{b}}(\mathbf{x})$. When a flow undergoes a supercritical Hopf bifurcation, a single oscillatory global mode becomes unstable, grows, and then saturates because non-linear terms interact and modify the base/steady flow. The shift mode is a simple representation of a missing dynamic mean-field correction, or how much the mean flow is deviating from the steady flow behaviour as described in Noack et al.[51]. The unit vector along the shift mode is described as:

$$\mathbf{u}_{\Delta}(\mathbf{x}) = \frac{\mathbf{u}_{\mathrm{m}}(\mathbf{x}) - \mathbf{u}_{\mathrm{b}}(\mathbf{x})}{||\mathbf{u}_{\mathrm{m}}(\mathbf{x}) - \mathbf{u}_{\mathrm{b}}(\mathbf{x})||} \tag{4.24}$$

Orthonormalizing shift mode vector to the orthonormal vectors that span the tangent plane, a three-dimensional basis can made, which is used for visualizing the n-dimensional space in a reduced coordinate system, through projection to the basis vectors. The trajectories obtained through the projections of the actual flow field from the *training data* ($\mathbf{w'}_{real}$) and the reconstructed-reduced flow field ($\mathbf{w'}_{reduced}$), defined by fitting of the reduced coordinates, can be used to generate enveloping surfaces, to visualize the evolution of the dynamics in three dimensions. The cross section of the $\mathbf{w'}_{real}$ surface and

$\mathbf{w}'_{reduced}$ surface can be used to check for best fitting in 3D by varying degree of monomial used (M), along with a regular check for fit in the reduced dimensions, η. This fitting process for the ideal degree of monomial obtained (M), is repeated for different point in time for during the evolution of the flow from steady state to LCO to check the evolution of fitting at different points of the dynamics.

4.4.7. Linear regression on the reduced coordinates and use of the fitted curve for prediction

After obtaining the $\mathbf{V}_1$ and $\mathbf{V}$ matrices from the *training data* of the $Ma - \alpha$ cases chosen, the process of using linear regression to capture the evolution of the dynamics in the reduced coordinates is started. This is done for the sake of understanding the reduced dynamics as well as using it for the sake of the prediction of reduced dynamics for the same system of $Ma - \alpha$, under different initialization conditions. This methodology of using linear regression to define a set of ordinary differential equations (ODE's) to capture the reduced coordinate evolution, and using it for predicting the reduced coordinate evolution of the same system under a different initialization condition works, because of the dynamics lying on the spectral submanifold, regardless of the initialization conditions, as discussed in section 4.1. The process is begun with the training time series $\{\eta_1(t), \eta_2(t)\}_{t=0}^{T}$ obtained from the original flow field, referred to as *training data* or *training flow field*, as described in section 4.4.6. Additionally, a new partial time series $\{\tilde{\eta}_1(t), \tilde{\eta}_2(t)\}_{t=0}^{t_{\max}}$ is considered from a new flow field, termed *training data*, generated with a different perturbation according to section 4.4.4.

To train a model for the reduced dynamics, the discrete time derivatives of the *training data* using finite differences is computed first. For each time step, the time increment is given by $\Delta t_i = t_{i+1} - t_i$, and the derivatives are calculated as

$$\left.\frac{d\eta_1}{dt}\right|_{t_i} \approx \frac{\eta_1(t_{i+1}) - \eta_1(t_i)}{\Delta t_i}, \qquad \left.\frac{d\eta_2}{dt}\right|_{t_i} \approx \frac{\eta_2(t_{i+1}) - \eta_2(t_i)}{\Delta t_i}. \tag{4.25}$$

The corresponding input features are constructed as $\boldsymbol{\eta}_t = [\eta_1(t), \eta_2(t)]$, while the target outputs are the computed derivatives at each time step.

Next, a polynomial degree $d \in \mathbb{N}$, for example $d = 3$, is selected, and a polynomial feature transformation is applied to each input vector. The feature mapping $\Phi(\boldsymbol{\eta}_t)$ consists of all monomials in η_1 and η_2 up to degree d:

$$\Phi(\boldsymbol{\eta}_t) = \left[\phi_1(\eta_1, \eta_2), \phi_2(\eta_1, \eta_2), \ldots, \phi_M(\eta_1, \eta_2)\right], \tag{4.26}$$

where each ϕ_i denotes a unique monomial basis function.

Polynomial Regression and Model Fitting

The regression process begins with the construction of the input and output datasets from the training time series $\{\eta_1(t), \eta_2(t)\}_{t=0}^{T}$, as outlined previously. For each time step, the input feature vector is given by

$$\boldsymbol{\eta}_t = [\eta_1(t),\ \eta_2(t)], \tag{4.27}$$

and the target outputs are the numerically computed time derivatives,

$$\left.\frac{d\eta_1}{dt}\right|_{t}, \quad \left.\frac{d\eta_2}{dt}\right|_{t}. \tag{4.28}$$

To capture non-linear dependencies, the input features are transformed using a polynomial feature map of degree d, which produces all monomials in η_1 and η_2 up to degree d. Denote the polynomial feature vector as

$$\Phi(\boldsymbol{\eta}_t) = [\phi_1(\eta_1, \eta_2),\ \phi_2(\eta_1, \eta_2),\ \ldots,\ \phi_M(\eta_1, \eta_2)], \tag{4.29}$$

where each ϕ_i is a monomial basis function, and M is the total number of features. For example, when the polynomial degree chosen is d=3, there are M=7 components in the monomial basis function, which are defined as

$$\Phi(\boldsymbol{\eta}_t) = [\eta_1^2, \eta_1\eta_2, \eta_2^2, \eta_1^3, \eta_1^2\eta_2, \eta_1\eta_2^2, \eta_2^3] \tag{4.30}$$

The regression model for each time derivative coordinate is specified as

$$\left.\frac{d\eta_j}{dt}\right|_t \approx f_j(\eta_1(t), \eta_2(t)) = \sum_{i=1}^{M} w_i^{(j)}\, \phi_i(\eta_1(t), \eta_2(t)), \qquad j = 1, 2, \tag{4.31}$$

where $w_i^{(j)}$ are the regression coefficients for the j-th state variable.

Now, let N be the total number of training samples, and let $X_{\text{poly}} \in \mathbb{R}^{N\times M}$ denote the matrix whose rows are the polynomial feature vectors $\Phi(\boldsymbol{\eta}_t)$ for each time step. Let $\mathbf{y}_j \in \mathbb{R}^N$ be the vector of numerically computed derivatives for the j-th state variable.

The coefficients $w_i^{(j)}$ are determined by solving the ordinary least squares (OLS) problem, which minimizes the sum of squared errors between the predicted and actual derivatives:

$$\min_{\mathbf{w}^{(j)}\in\mathbb{R}^M} \left\| X_{\text{poly}}\, \mathbf{w}^{(j)} - \mathbf{y}_j \right\|_2^2 . \tag{4.32}$$

The solution to this minimization problem is given (when $X_{\text{poly}}^T X_{\text{poly}}$ is invertible) by the closed-form normal equations:

$$\mathbf{w}^{(j)} = \left(X_{\text{poly}}^T X_{\text{poly}}\right)^{-1} X_{\text{poly}}^T\, \mathbf{y}_j . \tag{4.33}$$

This process is carried out independently for $j = 1$ and $j = 2$, yielding two sets of regression coefficients.

After fitting, the learned models f_1 and f_2 provide polynomial approximations for the time derivatives of the reduced coordinates or as ODE's, which are subsequently used for integration and flowfield prediction as described below.

Prediction and Reconstruction Phase

Once the ODE' are formed from the *training data*, the prediction and reconstruction phase can be carried out by using the last known state from the *test/validation data*, $\tilde{\eta}(t_{\max}) = [\tilde{\eta}_1(t_{\max}), \tilde{\eta}_2(t_{\max})]$, as the initial condition for forward prediction. For each subsequent time step $t = t_{\max} + 1, \ldots, t_{\max} + N_{\text{pred}}$, the polynomial features $\Phi(\tilde{\eta}(t-1))$ are computed and the time derivatives are predicted using the trained models:

$$\left.\frac{d\tilde{\eta}_j}{dt}\right|_{t-1} = f_j(\tilde{\eta}_1(t-1), \tilde{\eta}_2(t-1)), \qquad j = 1, 2. \tag{4.34}$$

The reduced coordinates are then advanced using the forward Euler method:

$$\tilde{\eta}_j(t) = \tilde{\eta}_j(t-1) + \Delta t \cdot \left.\frac{d\tilde{\eta}_j}{dt}\right|_{t-1} . \tag{4.35}$$

At each predicted time step, the quality of the trajectory can be evaluated by comparing the predicted and actual test data values using the mean squared error or the normalized mean trajectory error (NMTE), defined as following:

Given P observations of the observable vector $\mathbf{y}_j$ and their corresponding model-based reconstructions $\hat{\mathbf{y}}_j$, the NMTE is defined as follows:

$$\text{NMTE} = \frac{1}{\|\mathbf{y}\|} \frac{1}{P} \sum_{j=1}^{P} \|\mathbf{y}_j - \hat{\mathbf{y}}_j\| . \tag{4.36}$$

For each predicted $\tilde{\eta}(t)$, the non-linear polynomial features are computed as

$$\tilde{\eta}^{2:M}(t) = \left[\phi_2(\tilde{\eta}(t)), \ldots, \phi_M(\tilde{\eta}(t))\right] . \tag{4.37}$$

The corresponding reduced flow field is reconstructed using the known coefficient matrices obtained from *training data*: $\mathbf{V}_1$ and $\mathbf{V}$, via

$$\mathbf{w}'(t) = \mathbf{V}_1 \tilde{\eta}(t) + \mathbf{V}\, \tilde{\eta}^{2:M}(t). \tag{4.38}$$

The final output is the predicted reduced flow field $\mathbf{w'}(t)$ for future time steps. Therefore, for any new case where the embedding matrices $\mathbf{V}_1$ and $\mathbf{V}$ are known, the reduced coordinates and associated flow field can be predicted under any initialization by fitting and integrating the polynomial regression models for the time derivatives. These reconstructed flow fields from the *test/validation* data is compared against the actual flowfields recorded from URANS simulation for the same, after dividing out the reconstructed flowfield with the cell volumes of the mesh to "de-weigh" the flowfield. Using the feature of flow property variation across shock, the predicted/ reconstructed flowfields are processed and the URANS flow fields to compare the shock location too.

5

Results

In this section, the results of the methodology proposed as per section 4.4 is discussed in detail. This consists of evaluating the steady RANS simulation results, the unsteady RANS (URANS) simulation results which consists of various sub-studies/investigations for optimizing the methodology, linear analysis or the eigen mode extraction, POD mode extraction, and the process of spectral submanifold embedding for creating a reduced order model. Finally, linear regression to fit a polynomial curve along the reduced order model trajectory obtained and is then used to predict the evolution of flow in reduced coordinates as well as mapping the predicted reduced flow to full flow field of higher dimensions is also discussed.

5.1. Problem evaluation

5.1.1. Steady simulation

As per the methodology discussed in section 4.4.1, the steady RANS simulation of various $Ma - \alpha$ combinations is implemented. Evaluating a set of monitoring values like density residual(Res_{rho} or $Rrho$) or coefficient of lift (C_L or $C - lift$), the rate of convergence with increase in iteration is checked. One such case is represented in figure 5.1, for $Ma = 0.71$ and $\alpha = 4.45°$. Log plot and linear plot of the monitoring values Res_{rho} and C_L respectively, against the number of iterations taken is plotted here. figure 5.1a shows the convergence of energy density residual ($RrhoE$) to a value $\approx 10^{-10}$, and figure 5.1b shows the convergence of the coefficient of lift (C_L or $C - lift$) to a constant value of 1.05, with increase in number of inner iterations. The simulation is stated to have reached convergence when the monitoring values reach a constant state on all further iterations.

On convergence of the solution for the cases evaluated, the flow field data obtained for each of these combinations are obtained. One such set of flow field plot for each of the conservative variables considered i.e. $[\rho, \rho u, \rho w, \rho E, \rho\tilde{\nu}]$ is represented in figure 5.2 for $Ma = 0.71$ and $\alpha = 4.45°$. Here in each of the conservative variable plotted for the flowfield, except the plot for the eddy viscosity, it can also be seen that the presence of shock on the surface of the aerofoil, represented by a zone of distinct colour. Based on the evaluations done in section 4.4.1 and section 4.4.1, multiple steady state simulations are done across combinations of Ma-α, to estimate the transonic buffet onset boundary and for further detailed investigations into those selected $Ma - \alpha$ combinations.

To understand the influence of α on parameters, one of the commonly adopted method as seen in Sansica et. al, Sartor et. al,[60, 61] etc. is to evaluate the distribution of the coefficient of pressure (C_p) around the aerofoil. This has been evaluated in figure 5.3. The set of curves observed here are for $\alpha = 4.0°, 4.5°, 5.0°, 5.5°$ and $6.0°$. The curves have two parts, an upper curve and a lower curve, whose ends are joined at points $x/c = 0.0$ and $x/c = 1.0$. The upper curve represents the C_p distribution of the suction side of the aerofoil, corresponding to the chord coordinates x/c. The sharp drop of the C_p value observed on the suction side denotes the presence of shock wave. It can be seen in figure 5.3, that as the α increases from 4.0° to 6.0°, the position of the shock wave shifts to the leading edge of the aerofoil.

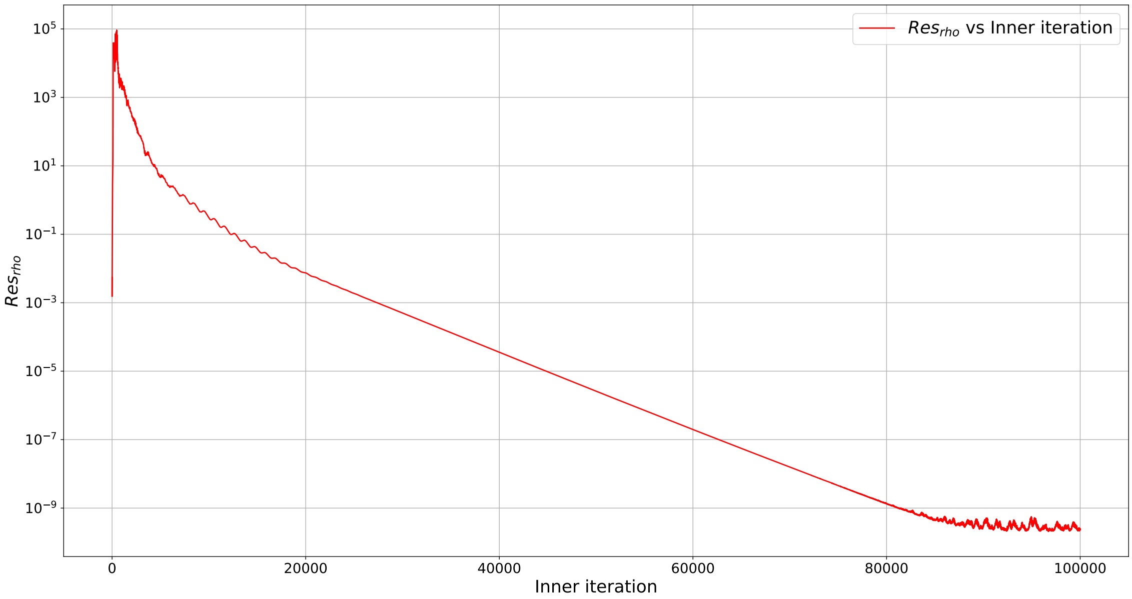

(a) Convergence evaluation of energy density residual (RrhoE), where the y axis is plotted in log scale. The steady simulation is said to be converged if the residual falls below the desired value: here 10^{-10}

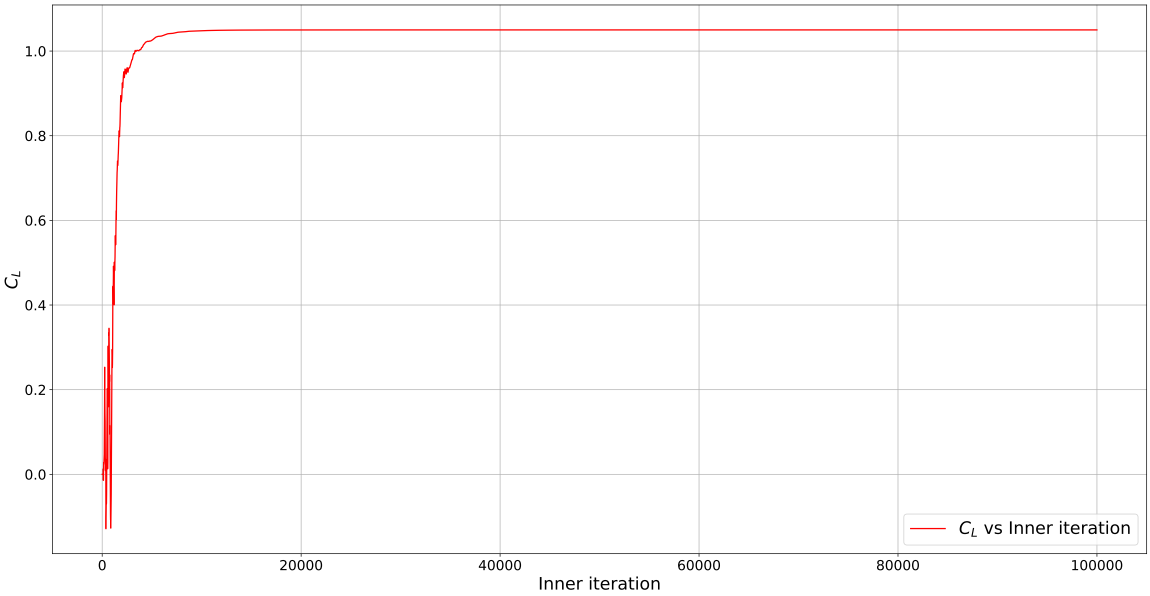

(b) Convergence evaluation of coefficient of lift (C_L) , where the y axis is plotted in linear scale. The steady simulation is said to be converged if the coefficient of lift attains a constant value on further iterations.

Figure 5.1: Convergence evaluation with increase in iteration for steady simulations done for $Ma = 0.71$ and $\alpha = 4.45°$

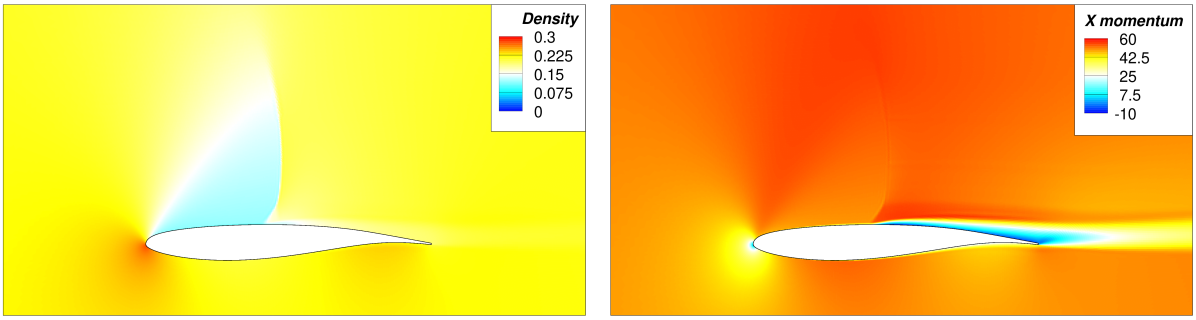

(a) Steady flow plot of density (ρ) for $Ma = 0.71$ and $\alpha = 4.45°$

(b) Steady flow plot of x momentum (ρu) for $Ma = 0.71$ and $\alpha = 4.45°$

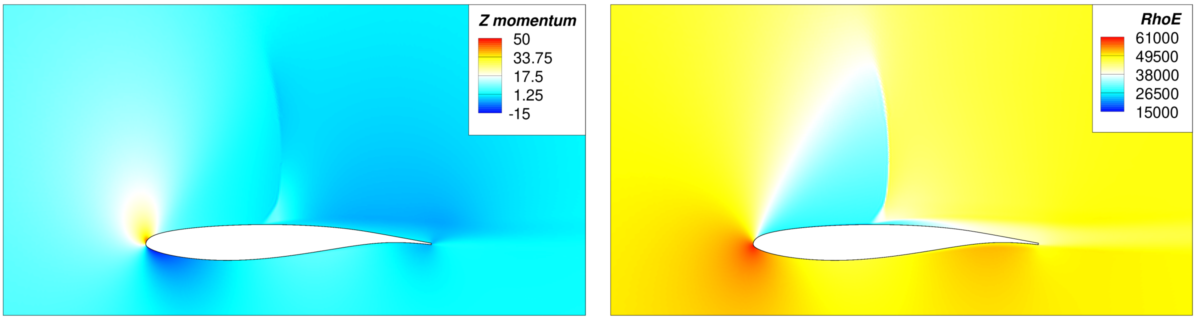

(c) Steady flow plot of z momentum (ρw) for $Ma = 0.71$ and $\alpha = 4.45°$

(d) Steady flow plot of rhoE (ρE) for $Ma = 0.71$ and $\alpha = 4.45°$

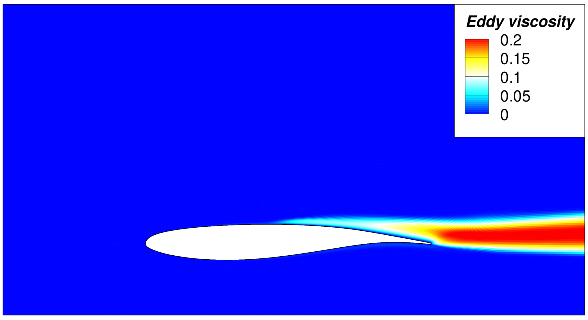

(e) Steady flow plot of eddy viscosity ($\rho\tilde{\nu}$)for $Ma = 0.71$ and $\alpha = 4.45°$

Figure 5.2: Steady simulation flow field plots of conservative variables for $Ma = 0.71$ and $\alpha = 4.45°$

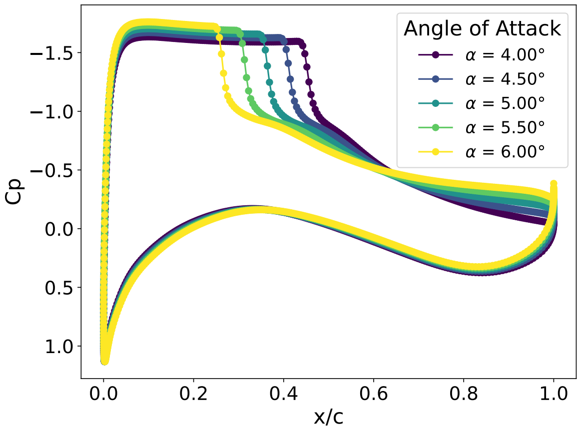

Figure 5.3: Coefficient of pressure (C_p) comparison done for various angles of attack for $Ma = 0.71$. The curve seen can be split in two halves: the lower curve representing the pressure side and the upper curve representing the suction side. The point x/c at which the sharpest gradient of C_p can be seen indicates the location of the shock for the α considered. As α is increased, it can be seen that the shock move towards x/c=0 or towards the the leading edge of the aerofoil.

5.1.2. URANS simulation

Using the converged steady solutions obtained, as seen in section 5.1.1, the URANS simulation is initialized to investigate selected cases of $Ma - \alpha$ combinations. These investigations start with determining an adequate perturbation to allow growth of unsteadiness to an LCO, time step evaluation to determine the most appropriate time step which could be used for the URANS simulation, determining the transonic buffet onset boundary and finally flow field recording and evaluations for selected case on and above the transonic buffet boundary.

Perturbation study

As discussed in section 4.4.2, the impact and difference between various perturbation motions is evaluated, to understand the effect it has on the evolution of the unsteadiness with time. The perturbation evaluation is done for a case of $Ma = 0.71$ at $\alpha = 4.5°$. The evolution of the coefficient of lift (C_L) in time, is plotted and compared for different perturbations conditions which include pitching strengths or amplitude factor of pulse pitch angles in degree (°) angle of $1{\times}10^{-5}, 1{\times}10^{-4}, 1{\times}10^{-3}, 5{\times}10^{-3}, 1{\times}10^{-2}$ and $1{\times}10^{-1}$ and a heaving motion of strength 1.31×10^{-5}, which can be comparable to the pitching strength of 1×10^{-3} as per equation (4.6). Comparing to the case, which is initialized with no perturbation, it can be seen that the stronger the perturbation, the faster the evolution of C_L into an LCO behaviour. For an equal strength pitch vs heave scenario as seen for the cases of pitching strength of 1×10^{-3} and heaving motion of strength of 1.31×10^{-5}, the pitching motion perturbation is seen to grow faster, into an LCO. The pitching strength of 1×10^{-3} and 1×10^{-2} were selected as the initialization condition for the *training data* simulations and *test/validation data* simulations respectively, because of the slower evolution into an LCO compared to the stronger perturbation cases, thus ensuring the data at hand can capture adequate amount of flowfield data, near to the base flow as well as throughout the development into the LCO behaviour.

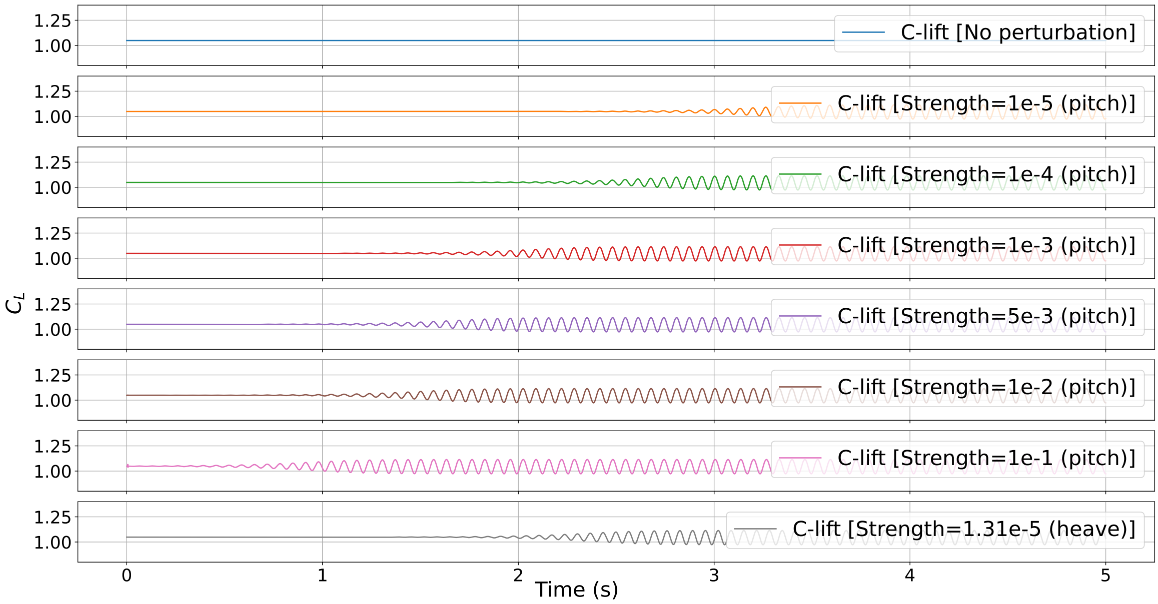

Figure 5.4: Variations of C_L with time for various strengths of perturbations for $Ma = 0.71$ at $\alpha = 4.5°$. It can be seen here, for higher the perturbation strength given during at the start of the URANS simulation through a pitching motion, the faster the evolution into an LCO is reached. On comparing between similar strength pitching and heaving perturbation, it can be seen that the pitching perturbation produces a stronger effect.

Time step valuation

The impact of the time step for the URANS simulation has been assessed for the following time step periods: $1 \times 10^{-3}s$, $3 \times 10^{-4}s$, $3.5 \times 10^{-4}s$, $4 \times 10^{-4}s$, $4.4 \times 10^{-4}s$, $4.5 \times 10^{-4}s$, $5 \times 10^{-3}s$ and $5 \times 10^{-4}s$. The time step period was chosen in an irregular but sequential manner, moving from the larger time step 5×10^{-3} and reducing it after each run such that at some point no further effect in further time step discretization will be observed. This evaluation was done for a case of $Ma = 0.68$ and $\alpha = 5.5°$, which was considered to be a point where $\alpha > \alpha_{critical}$, as per figure 4.3. It can be seen from figure 5.5b that, for all the time steps aside from $\Delta t = 5 \times 10^{-3} s$, LCO behaviour was observed, whose peaks occur within a span of 0.01 s. A time step of $\Delta t = 4.4 \times 10^{-4} s$ was selected as the optimum time step below which the amplitude and phase of the peaks of C_L are overlapping, and above which all time steps with a larger value shows a non overlap condition.

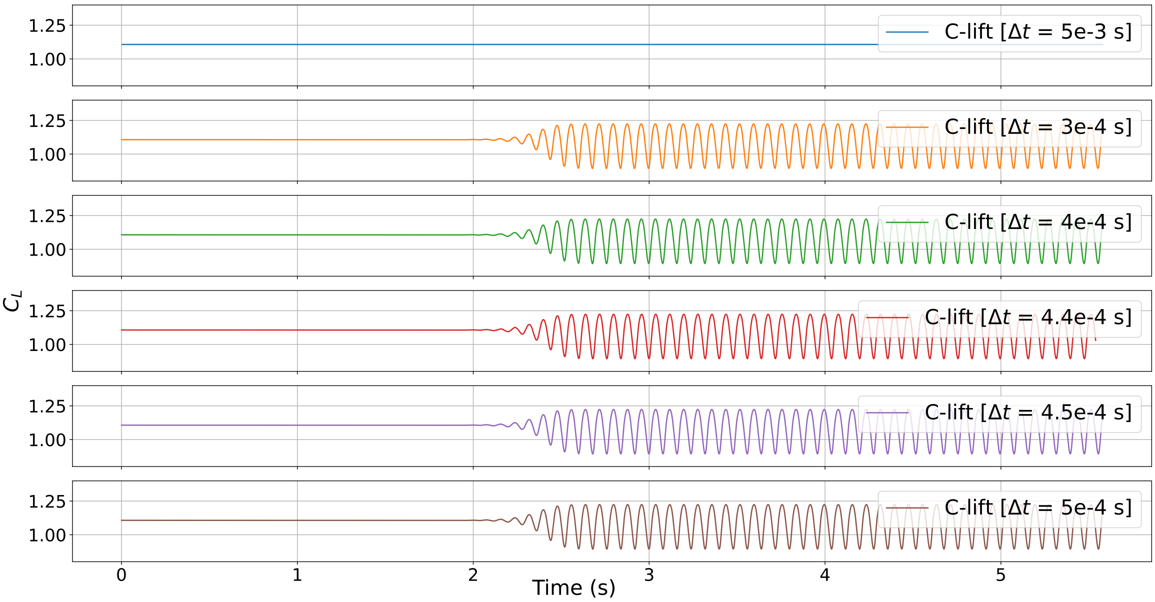

(a) Variations of C_L with time for various time step sizes chosen. Various time step sizes were chosen to study the impact of it and to choose and ideal time step, which would be short enough to evaluate and capture the LCO phenomena, as well as being computationally less intensive.

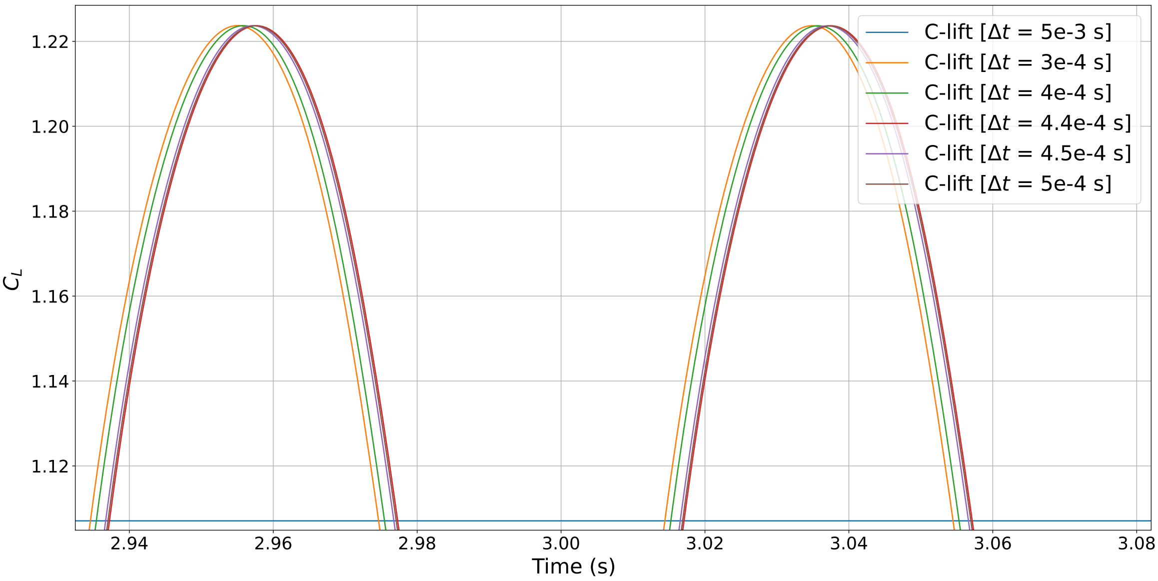

(b) Zoomed view of variations of C_L with time for various time step sizes chosen.

Figure 5.5: Variations of C_L with time for various time step sizes. For the various time step sizes chosen and evaluated, it can be seen that going above a time step size of $5 \times 10^{-3} s$s does not produce a C_L that oscillates with time i.e. no LCO behaviour is observed. Further decreasing the time step size, the oscillations in the C_L with time can be seen, where the peaks of the C_L in the LCO region seem to shift slightly to the right. But on reaching a time step size of $4.4 \times 10^{-4} s$ overlapping peaks can be seen for all time step sizes below it.

Buffet boundary evaluation

The transonic boundary obtained following the methodology discussed in section 4.4.1 and section 4.4.4, is evaluated. Here, a plot consisting of C_L evolutions in time for combinations of $Ma - \alpha$ is constructed based on the methodology and choices mentioned in section 4.4.1. The evaluation of the transonic boundary is done over a Ma range of 0.68-0.72, within an α range of $4° - 6°$. For the URANS simulations done over these Ma-α combinations, the evolution of C_L in time is evaluated. figure 5.6 shows the C_L evolutions in time for the Ma-α evaluated. Here, the C_L curves which are represented in blue colour are cases where no growth in unsteadiness or settling onto the converged steady state is observed. All cases which has a growing unsteadiness, which occurs for $\alpha > \alpha_{critical}$, are represented with red C_L curves. The $\alpha_{critical}$ for each Ma, which is indicated by the first curve in red when moving from the lower α to higher α's, when combined to their respective Ma give us the buffet onset boundary. This is further compared to other available models from literature as shown in figure 5.7. It can be seen that the transonic buffet onset boundary observed between Nitzsche et. al. [50], represented as the orange curve closely matches the URANS simulations done in this study, represented by the green curve. A slight deviation between the buffet onset boundary exists between the two curves due to the step size of α considered for evaluation. It is also evident that, using the SA-neg turbulence model, as done in this study results in a different buffet onset boundary compared to the boundaries obtained using other turbulence models such as SST model in Giannelis et. al. [29] and SA-comp model used in Crouch et. al. [16].

Now, two specific Ma are selected for all further evaluations. From the bifurcation plot observed in figure 5.6, Ma:0.69 and 0.71 are considered. For these Mach numbers, further URANS simulations were conducted as per the methodology described in section 4.4.1. For the selected Ma-α combinations described as given in table 4.2, the URANS simulations are carried out. For each of the URANS simulations done, the evolution of C_L in time is recorded. The maximum value of C_L', where $C_L' = \frac{C_L - C_{L(0)}}{C_{L(0)}}$, and $C_{L(0)}$ represents the value of C_L at time t= 0, is evaluated for various α to show a bifurcation plot indicating onset of Hopf bifurcation and indicating $\alpha_{critical}$ with better clarity. This is represented in the plot figure 5.8, from which it can be seen that for Ma=0.69, it is found that $\alpha_{critical} = 5°$ and for Ma=0.71, $\alpha_{critical} = 4.45°$. This representation is one of the methods followed to find critical angles for buffet cases, in Crouch et. al. [16].

URANS flow field

As discussed in section 4.4.4, two Ma:0.69 and 0.71, were selected for URANS flow field data recording which would be used for all subsequent cases and for the generation of a reduced order model using spectral submanifold embedding. Using an initialization perturbation of 1×10^{-3}, an initial set of flow field recording is captured, referred to as *training data* which would be used for spectral submanifold embedding and reduced order model generation and a second flow field recording with an initialization perturbation of 1×10^{-2}, referred to as *test/validation data*, to be used for prediction of flow evolution using the reduced order model generated.

5.1.3. Linear Analysis

The eigen modes are extracted from the converged steady solution for the combinations of $Ma - \alpha$ discussed in section 4.4.4. Thirty of the most dominant eigenmodes are extracted from the steady solution, where the eigen modes are split into their real and imaginary components for the conservative variables discussed in section 4.4.3. The eigenvalues corresponding to each of the eigen mode extracted is represented in the form $\omega = \gamma_0 + i\omega_0$, where the real part of the complex eigenvalue ω (γ_0) represents the growth rate of the mode and the imaginary part (ω_0) represents the frequency of the mode. These eigen values extracted, for all the α's considered for $Ma = 0.69$ and 0.71 are plotted along a Re-Im axis representation of the eigenvalues in figure 5.10a and figure 5.10b respectively, in a non dimensional form where the real and imaginary part are divided by $\frac{L}{U_\infty}$ where L is the characteristic length or chord length (c) which is 1 in this case and U_∞ is the farfield velocity of the case considered. Here, the most dominant eigen values, represented as triangle indices, are seen to move from having a negative real part to having a positive real part when α is increased. This shift of the value of the real part of the eigen value across the real axis, represented by the dotted black line in figure 5.10a and figure 5.10b, represents the onset of instability, indicating a Hopf bifurcation, as it was previously seen in figure 2.14. The first α which crosses the real axis, is the $\alpha_{critical}$, which confirms the observations seen in section 5.1.2. It can also seen that the corresponding eigen value of the most dominant eigenmode has its growth rate of mode (γ_0) increasing with increase in α. The γ_0 value reaches a maximum at some α and then it decreases on further increase of α. At some α the value of γ_0 crosses the real axis and becomes negative again indicating the buffet offset angle.

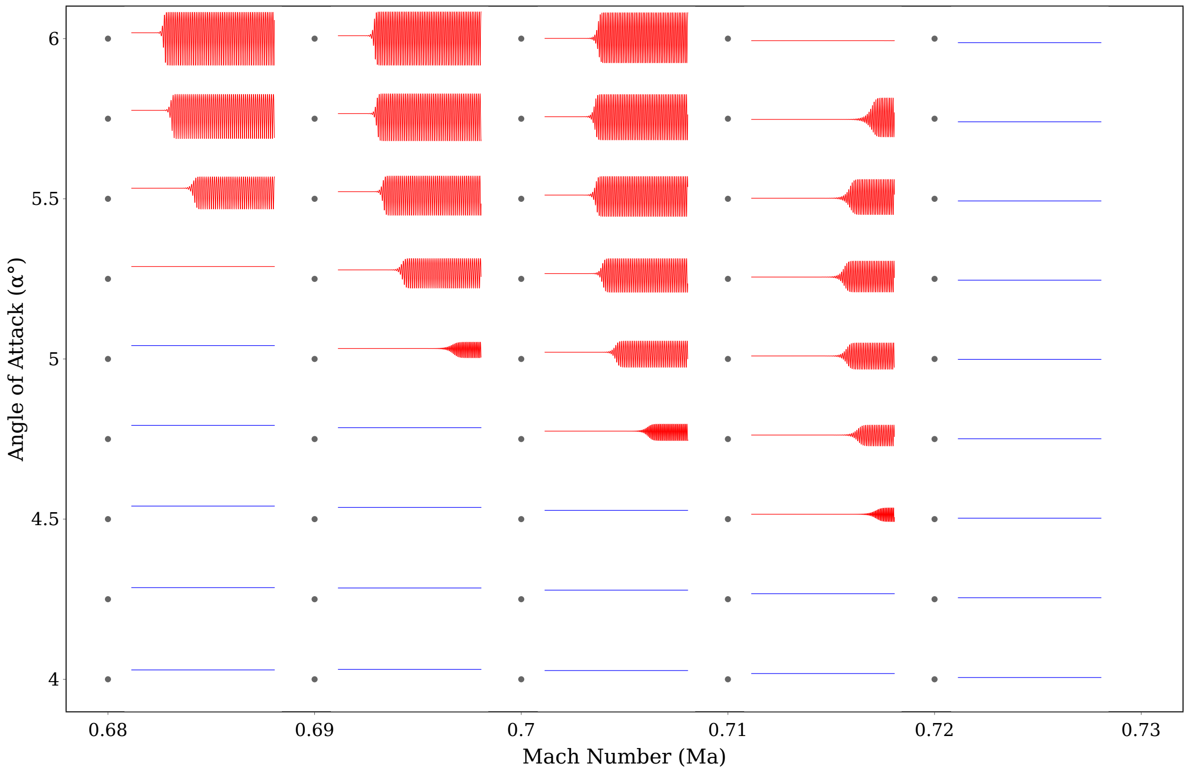

Figure 5.6: Bifurcation plot with subplots of C_L evolution in time for various Ma-α combinations. Here, the each subplot is either blue or red in colour, where cases with blue curves indicate no growth of unsteadiness into an LCO and the red curves indicate the cases where an unsteadiness grows into an LCO behaviour. The cases of α, where the red curves start with for each Ma mark the transonic buffet onset boundary. Some cases with red lines are those with very small growth rate and LCO cycle amplitude, which are not easily visible in this scale.

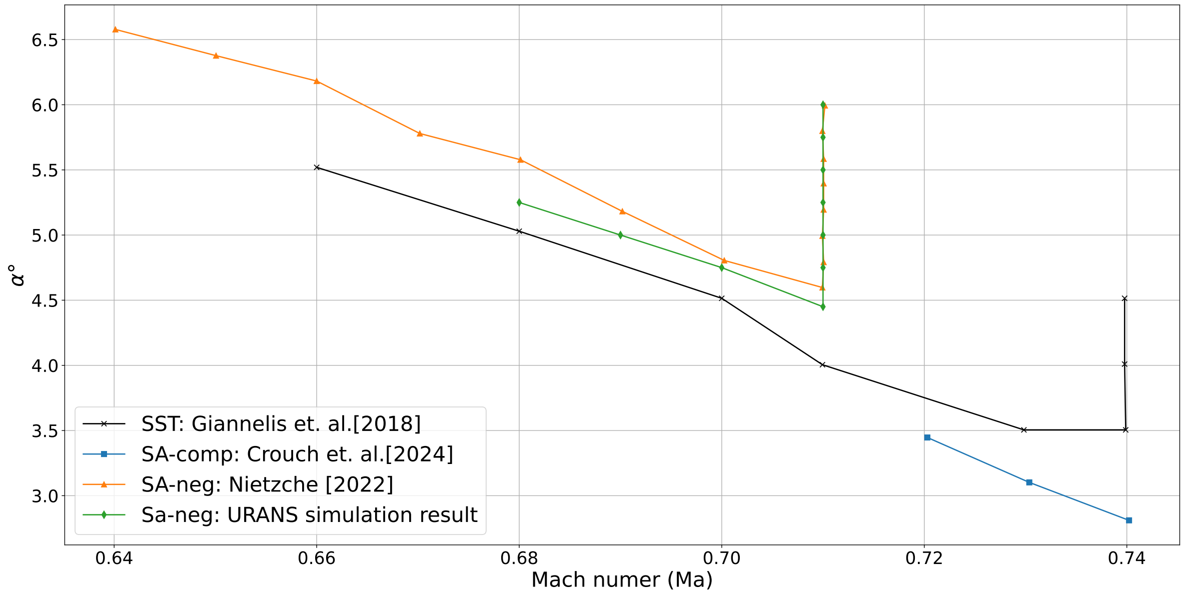

Figure 5.7: Comparison of the bifurcation boundary observed in figure 5.6 with the transonic buffet boundary available in various literature. It can be seen here that boundary nearly matches with the one seen in Nitzsche et. al. [50] and is different because of the difference in steps of α investigated for each Ma. The boundaries obtained from Giannelis et. al [29] and Crouch et. al. [16] are different from the boundary obtained in the current study due to different turbulence closure models chosen.

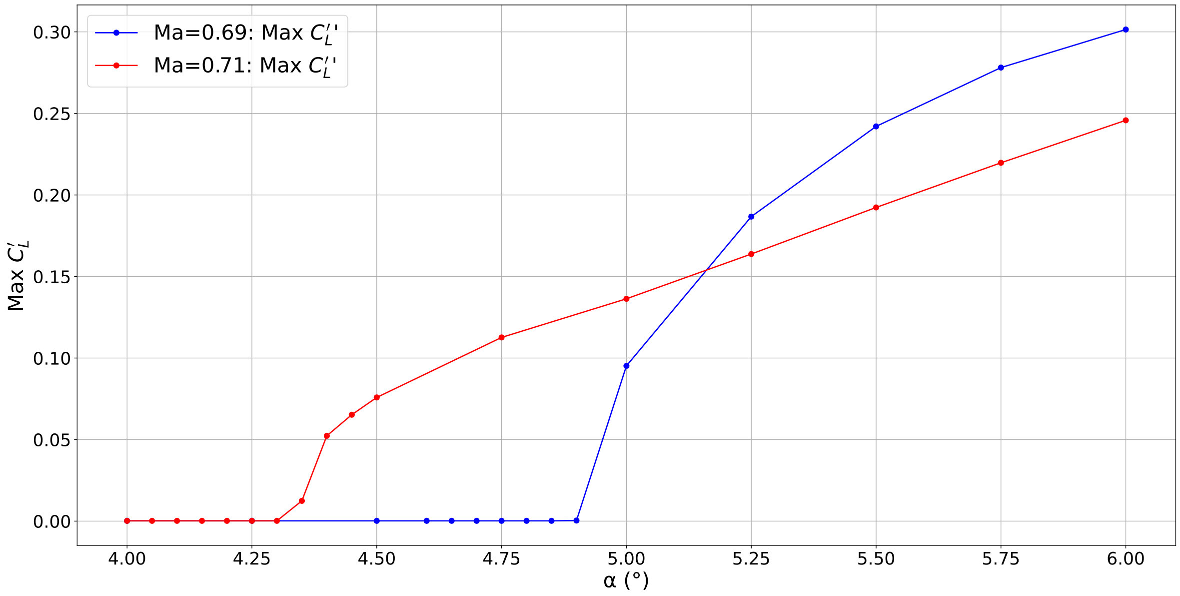

Figure 5.8: C_L' bifurcation plot, where $C_L' = \frac{C_L - C_{L(0)}}{C_{L(0)}}$ is plotted against the α for two Mach numbers 0.69 and 0.71. For each Ma evaluated, it can be seen that at a particular $\alpha = \alpha_{critical}$, an increase and divergence of the C_L' value from 0 can be seen, indicating the position of buffet onset more accurately.

The α at which the minimum values and maximum values of γ_0 is noted in table 5.1. These α represents where the minimum and maximum growth rate of the unsteadiness is observed for the buffet oscillation and for the purpose of reduced order modelling, these are considered as the points of interest.

	Ma = 0.69	Ma = 0.71
α where minimum γ_0 is observed: Buffet onset point	5°	4.45°
α where maximum γ_0 is observed:	6°	5.25°
α where minimum γ_0 is observed: Buffet offset point	7.25°	6°

Table 5.1: Onset and offset points of γ_0 for different Mach numbers. The buffet onset point is indicated by the the lowest α at which the lowest positive value of γ_0 is observed for a Ma, and the buffet offset point is indicated by the highest α at which the lowest positive value of γ_0 is observed for a Ma. The α for which the maximum γ_0 is observed is also noted, which indicates the α of highest growth rate of unsteadiness.

The extracted dominant eigen modes of the flow field data, split into their real and imaginary components for the conservative variables, for an angle of attack of 4.45°for Ma=0.71 is represented in figure 5.9.

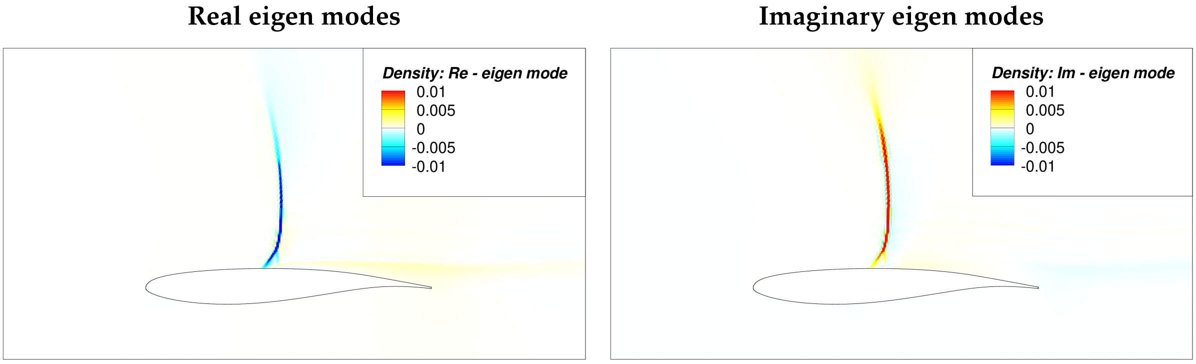

(a) Re-Density

(f) Im-Density

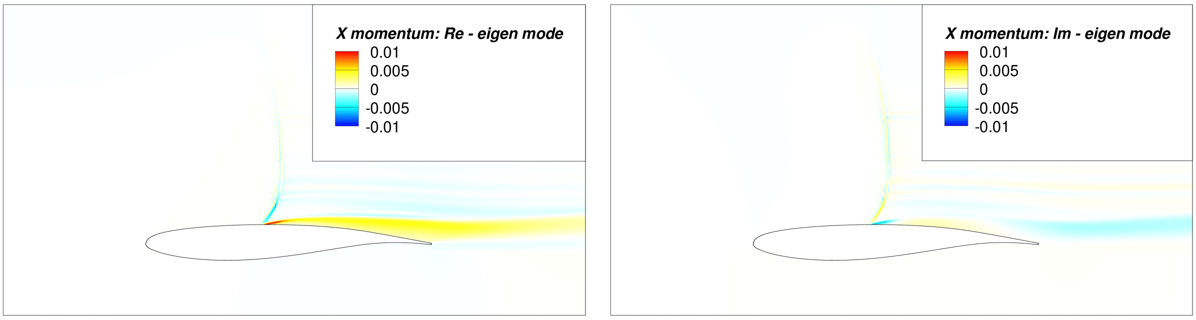

(b) Re-X momentum

(g) Im-X momentum

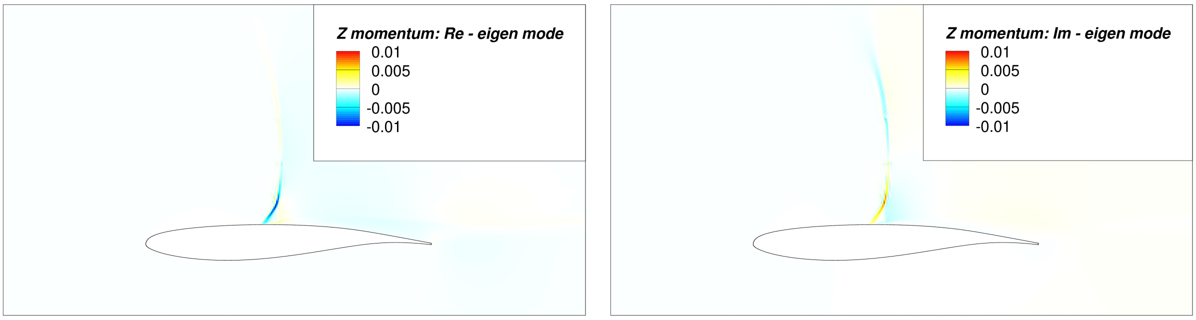

(c) Re-Z momentum

(h) Im-Z momentum

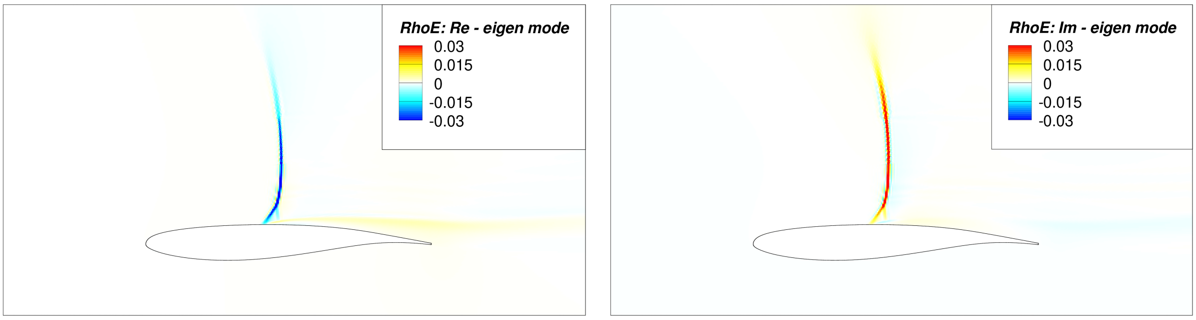

(d) Re-RhoE

(i) Im-RhoE

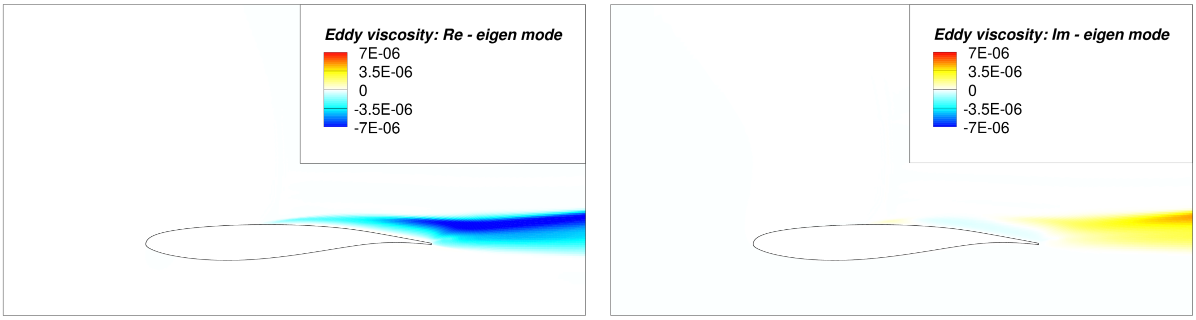

(e) Re-Eddy viscosity

(j) Im-Eddy viscosity

Figure 5.9: Real and Imaginary eigen modes extracted for $Ma = 0.71$ at $\alpha = 4.45°$. The components of the conservative variables of the most dominant eigen mode are split into its real and imaginary components and represented in the right and left columns respectively.

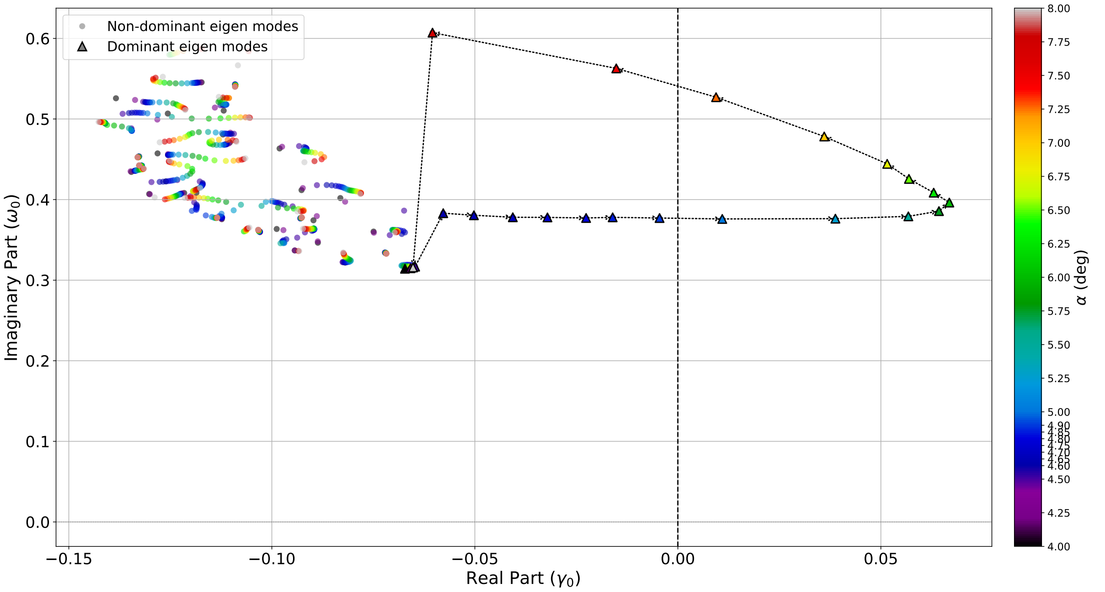

(a) Eigen spectra observed for $Ma = 0.69$

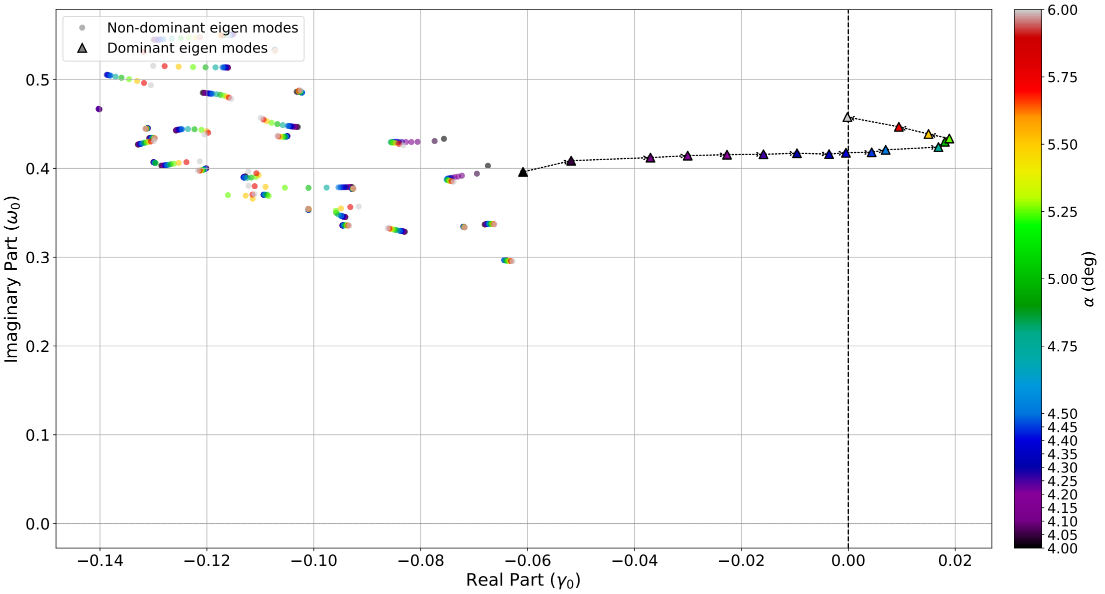

(b) Eigen spectra observed for $Ma = 0.71$

Figure 5.10: Eigen spectra for $Ma = 0.69, 0.71$. The triangles indicate the position of the most unstable/dominant eigenmode while the circles represent the other eigenmodes. The positions are indicated through the reduced damping rate (γ_0) and the reduced frequency (ω_0) in the real and imaginary axis respectively. It can be seen that on increasing the α for a Ma, the most dominant eigenmodes position shifts rightward from a negative γ_0 to a positive one, indicating the onset of instability or the buffet onset point for the Ma considered. On further increase of α the γ_0 reaches a maximum value indicating the maximum instability or growth rate obtained for a Ma. The γ_0 is seen to decrease with further increase in α before becoming a negative value, indicating the buffet offset point for the Ma.

5.1.4. POD modes

Using the *training data* recorded following section 4.4.4, the 2 most dominant POD modes can be extracted using the SVD matrix extraction, provided in the *flowtorch* module in python. Using the same cases for which the eigen modes were extracted for and which falls in the criteria followed in table 5.1, the POD modes are extracted. Evaluating the training data through the evolution of C_L with time, the flow field recordings which show 1st, 2nd and 3rd LCO oscillations were considered from the *training data*, and is used to extract the dominant modes from, following a standard practise of having ≈300–500 mature flowfield recordings for POD. By considering three LCO cycles, 471 time instances corresponding to three complete LCO cycles will be considered for POD mode extraction. The time points which correspond to the start and end of the 1st, 2nd and 3rd LCO oscillation are depicted in figure 5.11. Here, the evolution of C_L with time for a case of Ma=0.71 and $\alpha = 4.45°$ is depicted as the solid line. The dotted black line represents the maximum value of C_L possible in the time evolution of C_L, which is present at the LCO region. The dotted grey line represents the initial C_L value for the case. The vertical red lines indicate the time points at which the 1st, 2nd and 3rd LCO oscillation starts and ends. The points in time chosen are described in detail in table 5.2. The extracted dominant POD modes as flow field data, for an angle of attack of 4.45°for Ma=0.71 is represented in figure 5.12. Only two dominant eigenmodes are extracted and represented here, as for the methodology following SSM embedding as given in Cenedese et. al[14], the two most dominant POD modes are only needed. POD modes are different from eigen modes in the following manner: The POD modes are orthonormal structures extracted by a data-driven manner, which are ranked on how much energy each mode contains, while eigenmodes are solutions to a linearized governing equation of the flow which gives intrinsic linear dynamical structures which dictate how small perturbations evolve. Close to the base flow region of buffeting, the POD modes and eigen modes would appear similar to each other. Beyond the base flow, they differ from each other.

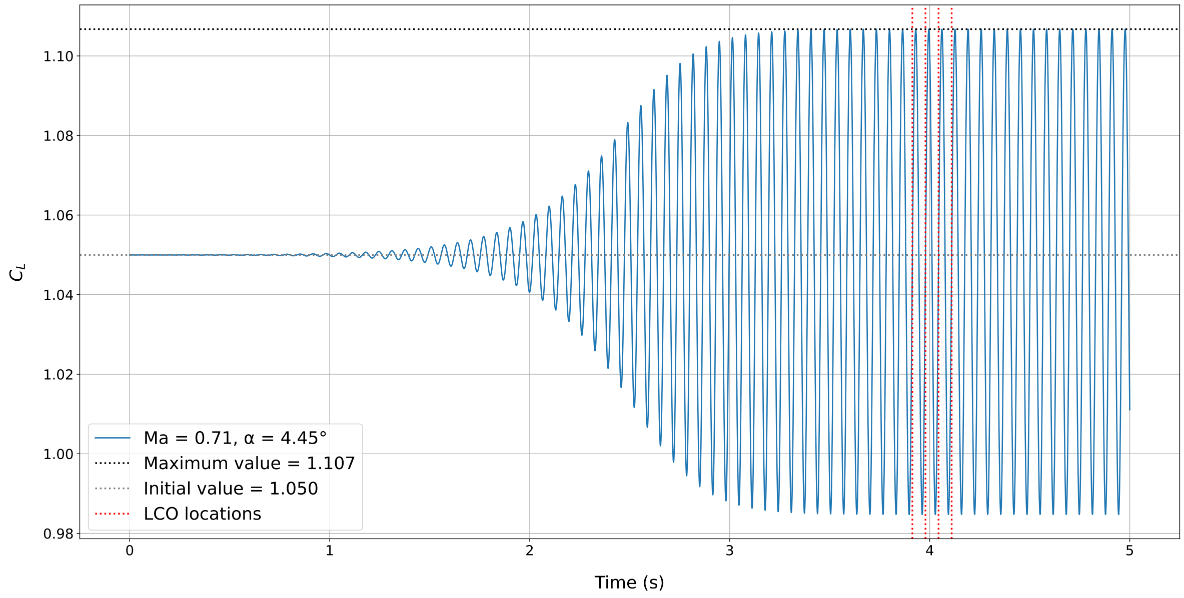

Figure 5.11: Time at which 1st, 2nd and 3rd LCO oscillations are observed in C_L, marked by vertical red lines. These points in time are considered for the evaluation of the POD modes, where 3 cycles in the LCO region were to be taken for the same. The initial value of C_L is marked by a grey dotted line, while the maximum value is marked by a black dotted line.

POD LCO times	t (s)
1st LCO start time (t_0)	3.9138
1st LCO end time and 2nd LCO start time (t_1)	3.9979
2nd LCO end time and 3rd LCO start time (t_2)	4.0443
3rd LCO end time (t_3)	4.1099

Table 5.2: The point of times at which LCO cycles are evaluated at for extracting POD modes.

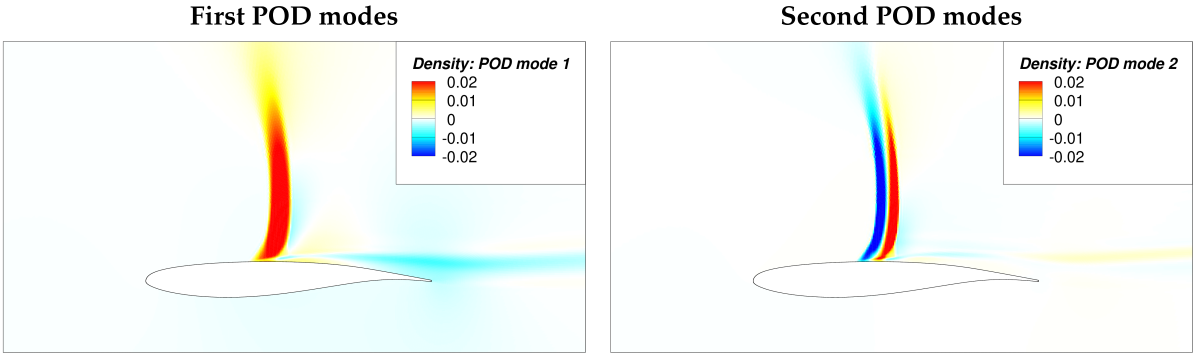

(a) POD 1 - Density **(f)** POD 2 - Density

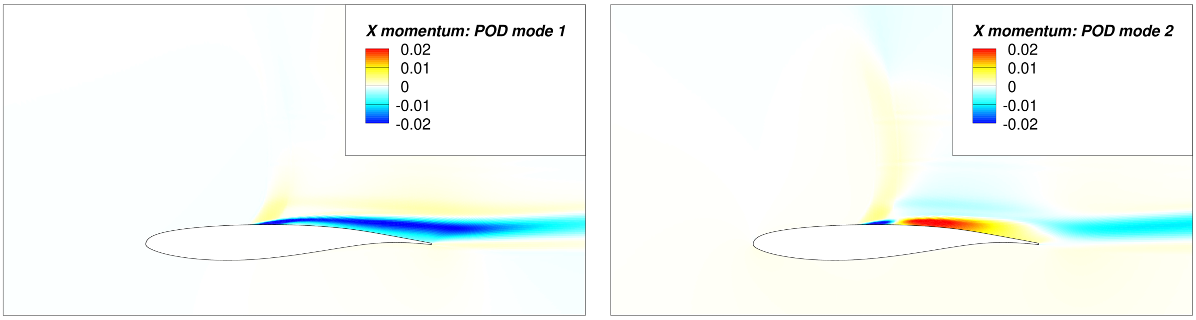

(b) POD 1 - X momentum **(g)** POD 2 - X momentum

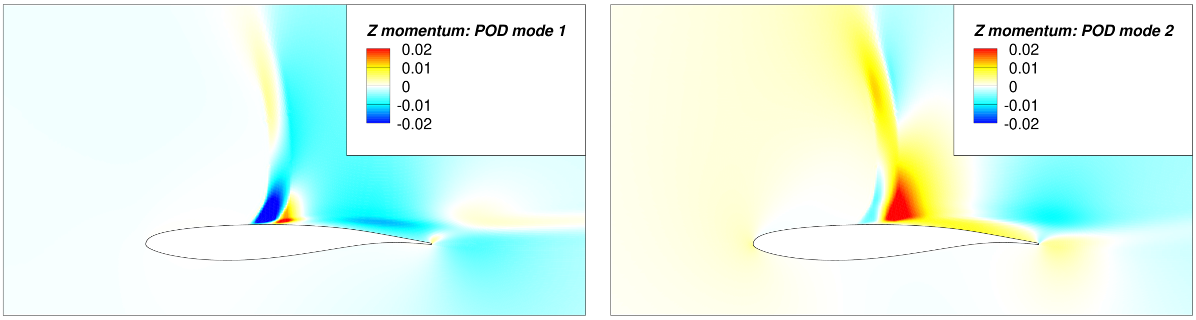

(c) POD 1 - Z momentum **(h)** POD 2 - Z momentum

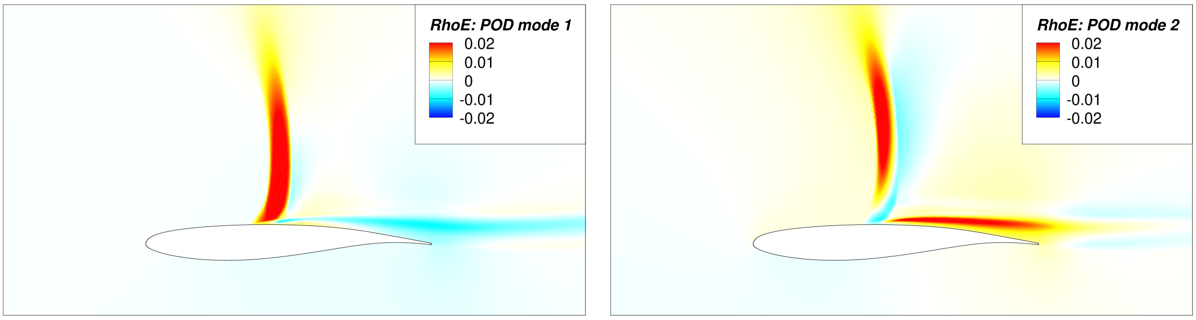

(d) POD 1 - RhoE **(i)** POD 2 - RhoE

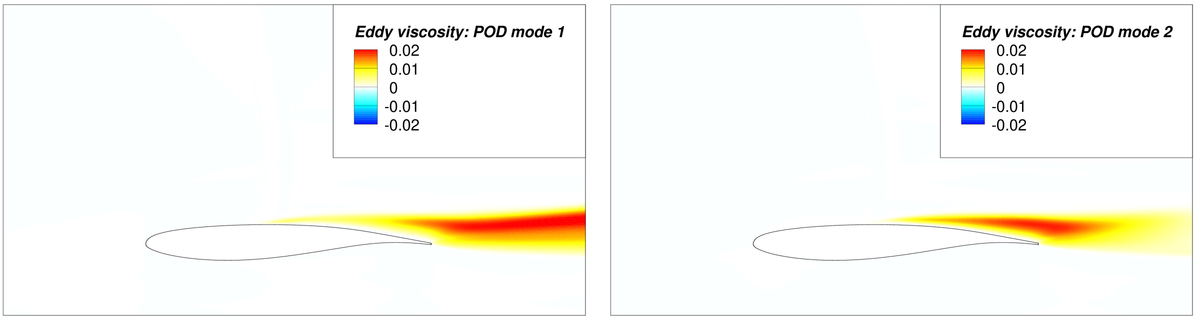

(e) POD 1 - Eddy viscosity **(j)** POD 2 - Eddy viscosity

Figure 5.12: POD modes extracted for $Ma = 0.71$ at $\alpha = 4.45°$. The components of the conservative variables are split into the first most dominant POD modes and the second most dominant POD mode and is represented in the right and left columns respectively.

5.2. Spectral submanifold embedding and reduced order model generation

On extracting the eigen modes and the POD modes, the same are used to describe an orthonormalized basis which spans a tangent space $\mathcal{T}_0\mathcal{M}_0$, which is then used for the embedding of the unsteady dynamics on to it. The embedding of the unsteady dynamics in the tangent space, is obtained through its projection on to the components of the basis, as described in section 4.4.6. This projection acts as an encoder/ map between the higher, n-dimensional space where the dynamics actually lie, and a reduced/low-dimensional space of 2 dimensions. To capture the linear and non-linear components of the unsteady dynamics, a Taylor expansion is carried out, fitting using the monomials constructed out of the reduced coordinates $\boldsymbol{\eta} = [\eta_1, \eta_2]^T$ obtained through projections. These monomials are described between orders of 2 to M, where M is the degree of monomial order chosen to test a fit of dynamics. The unsteady dynamics described by the linear coefficient $\mathbf{V_1}$ and a non-linear coefficient $\mathbf{V}$, is used to reconstruct the flow field, using a decoder function $\mathbf{W}$, described in equation (4.13). To define the linear and non-linear coefficients, proper fitting of the reconstructed flow field to the *training data* is required, as described in section 4.4.6. Here, a reduced order model is created through the embedding of the spectral submanifold on a tangent space $\mathcal{T}_0\mathcal{M}_0$ and defining the dynamics of the reduced coordinates on the tangent space through linear regression as discussed in section 4.4.7. Thus the encoder function ($\boldsymbol{\eta} = [\eta_1, \eta_2]^T$) obtained through the embedding, paired up with the ODE generated by linear regression gives rise to the required reduced order model. To initiate this process, the first step involves appropriately capturing the linear and non-linear dynamics on the tangent space using Taylor expansions, which is discussed in the upcoming section.

5.2.1. Fitting the manifold

To properly capture the linear and non-linear dynamics of the training data into coefficients, $\mathbf{V_1}$ and $\mathbf{V}$, the 3-dimensional reduced representation of the n-dimensional manifold through projection over the orthonormalized basis vectors is checked. These orthonormalized basis could be constructed by two methods

- Basis type A: Consisting of the real and imaginary part of the most unstable eigen vectors of the flow field considered, as well as shift mode. When plotting, the real component axis is represented as Re(UE) and the imaginary component axis as Im(UE), where UE represents the unstable eigenvector. Here the reduced coordinates $[\eta_1, \eta_2]$ are obtained through the projections of the unsteady flow field on to the real and imaginary part of the most unstable eigen vector.
- Basis type B: Consisting of the the most dominant and second most dominant POD modes extracted from the flow field considered, as well as shift mode. When plotting, the first POD mode axis is represented as POD_1 and the second POD mode axis as POD_2. Here the reduced coordinates $[\eta_1, \eta_2]$ are obtained through the projections of the unsteady flow field on to the first and second POD modes.

The three dimensional basis is used only for the sake of representing the n-dimensional manifold in three dimensions. For the sake of embedding of the dynamics and creation of a reduced order model, the components of the basis without the shift mode are considered.

When considering the three dimensional trajectory obtained through the projections of the unsteady part of the URANS *training data* over the total basis including the shift mode, it has to be noted that the trajectory so obtained is said to lie on the surface of a manifold according to theory described in [14], discussed in section 4.1. The theory also states that, for a particular flow condition (here defined by Ma and α), all trajectories, obtained from unsteady flowfields of various initial conditions, would lie on the surface of the same manifold. This has been verified in figure 5.13a, for a case of Ma=0.69, $\alpha = 7.25°$, where the trajectories constructed out of the *test data* and the *validation data* are seen to both lie on the same manifold, with a degree of fit M=5. The selection of degree of fit is discussed in detail in the upcoming sections. It is to be noted that the manifold $\mathcal{M}_0$ represented in 3D in basis type A for this case, is tangential to the plane $\mathcal{T}_0\mathcal{M}_0$ constructed out of the real and imaginary parts of the eigen vectors, in the case of basis type A. For the trajectories, obtained through the projection of the reconstructed flowfields obtained by using equation (4.13) over the basis chosen, through the process of varying the degree of fitting M for the training data, it should match the original *training data* trajectories produced and should lie on the same manifold. These new trajectories obtained through projection of the reconstructed flowfields obtained by using equation (4.13) over the basis chosen will be referred to as reconstructed trajectories here on.

In figure 5.13a, as previously stated, two trajectories built from the *training data* and the *validation data* flowfields over basis type A are seen, lying over the surface of the same manifold $\mathcal{M}_0$. The trajectories start from the tangent plane $\mathcal{T}_0\mathcal{M}_0$, at a point $[\eta_1, \eta_2] = (0, 0)$ indicating the start of the unsteady flowfield at a time t=0, at the base flow. Due to the growth of the unsteadiness owing to Hopf bifurcation, the trajectories seem to grow until reaching the top of the manifold, whose cusp at which the trajectories seem to lie on after a point in time. This cusp of the manifold around which the trajectories lie indicate the LCO region, where the trajectories finally end up on. Since both the trajectories constructed out of *training data* and the *validation data* flowfields lie on the same manifold, it can also be seen that both the trajectories reaching the cusp of the manifold and remaining there during LCO. This can be better understood by visualizing the trajectories over the tangent plane $\mathcal{T}_0\mathcal{M}_0$.

In figure 5.13b, the URANS *training data* trajectories and the *validation data* trajectories are shown to lie on the tangent plane $\mathcal{T}_0\mathcal{M}_0$. From theory discussed in section 4.1, it is known that the reduction of the n-dimensional dynamics to a 2 dimensional system occurs when the higher dimensional system is used to create reduced coordinates, which are $[\eta_1, \eta_2]$. The tangent plane $\mathcal{T}_0\mathcal{M}_0$ coincides with the image of the unstable two dimensional spectral subspace $\mathbf{E}$ under observable mapping, as discussed in section 4.1. This means that the the trajectories seen in three dimensional basis can be used to produce an image on the two dimensional tangent plane $\mathcal{T}_0\mathcal{M}_0$, without any loss of information, unless the three dimensional manifold develops a fold over itself. For the case of Ma=0.69, $\alpha = 7.25°$ represented in figure 5.13, such a fold is not seen, and therefore the two dimensional trajectory obtained as an image of the three dimensional trajectory, captures the higher dimensional dynamics evolution, in a lower dimension. The tangent plane $\mathcal{T}_0\mathcal{M}_0$ is constructed out of the real and imaginary parts of the eigen vectors, over which the *training data* and the *validation data* flowfields were projected to obtain the reduced coordinates $[\eta_1, \eta_2]$. For the trajectories of both *training data* and the *validation data*, the gradual growth from point $[\eta_1, \eta_2] = (0, 0)$, to an outer bound is seen, where the trajectory resides once the flow reaches LCO behaviour. As seen for the manifold $\mathcal{M}_0$ and the three dimensional trajectories lying on it from figure 5.13a, both the trajectories lie on the cusp of the manifold in the LCO region of flow. Looking at the image of the same over the tangent plane shown in figure 5.13b, it can be seen that both the trajectories lie on the same outer bound in the LCO region of flow, which is the image of the cusp of the manifold. Thus it is safe to conclude that for any specific condition of flow, here Ma-α, any and all trajectories made through varying the initial condition would lie on the same manifold and collapse on to the same manifold cusp/outer bound of trajectories.

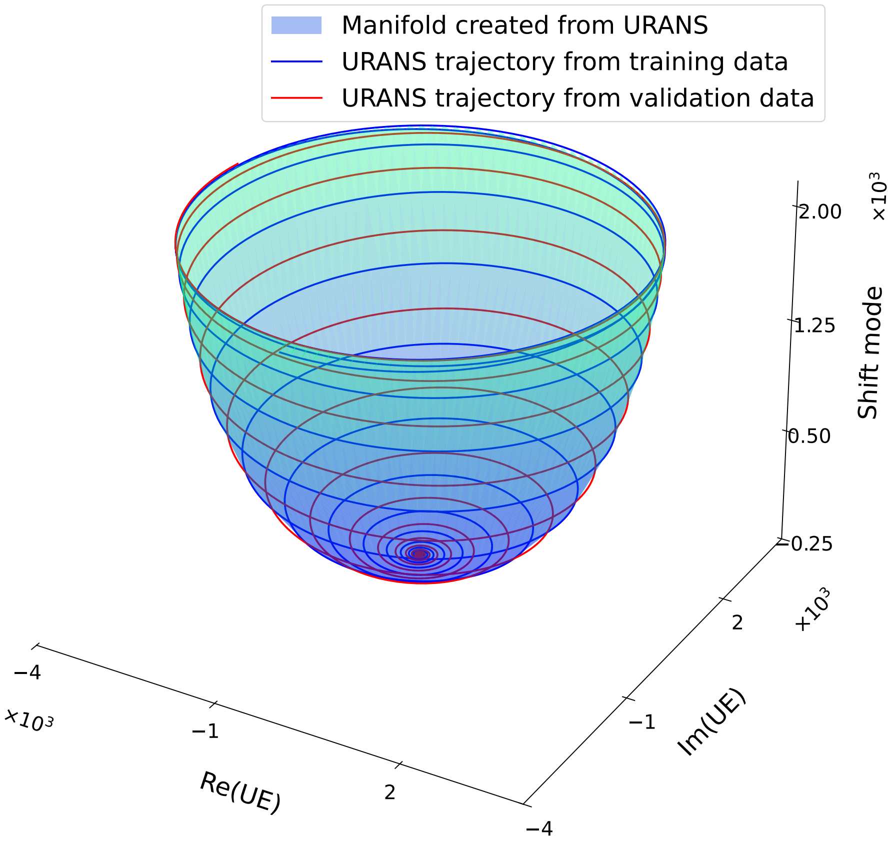

(a) The reduced trajectories of both *training data* and *validation data* of Ma=0.69, $\alpha = 7.25°$, present on the surface of a manifold $\mathcal{M}_0$, representing the n-dimensional dynamics in 3D. The basis used here is basis type A.

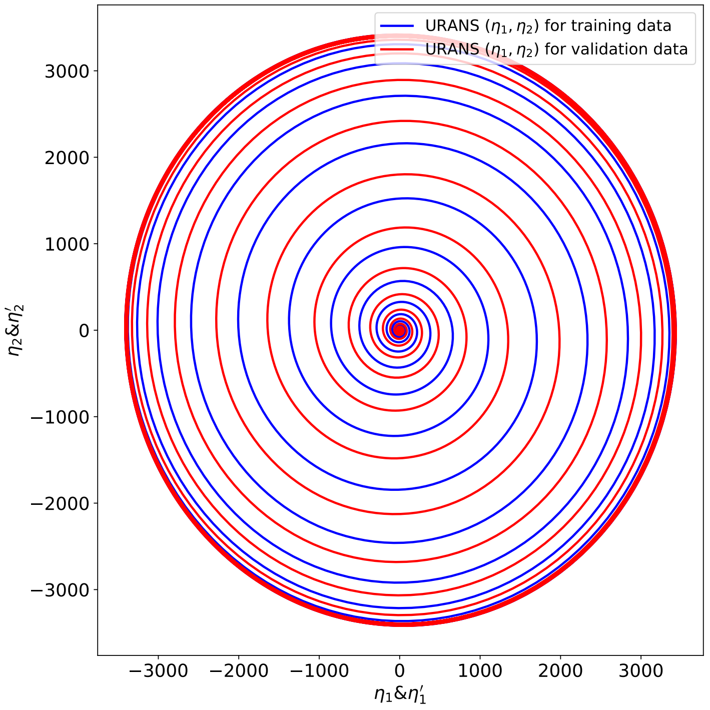

(b) The reduced trajectories of both *training data* and *validation data* of Ma=0.69, $\alpha = 7.25°$, represented on the the tangent surface of $\mathcal{T}_0\mathcal{M}_0$ to the manifold $\mathcal{M}_0$. The basis used to define the tangent surface is the basis type A, where η_1 and η_2 represents the reduced coordinates obtained through projection of dynamics on to the vectors tat define the basis, which are the real and imaginary parts of the eigen vectors in this case.

Figure 5.13: The manifold $\mathcal{M}_0$, of the dynamics of Ma=0.69, $\alpha = 7.25°$, represented in 3 dimensions constructed out of basis type A, along with the trajectories of the *training data* and *validation data* of the same case considered. The trajectories of both the training data as well as the validation data lie on the same manifold, confirming what was seen in the theory discussed in [14]. The tangent plane $\mathcal{T}_0\mathcal{M}_0$ constructed out of the real and imaginary parts of the eigen vectors of the case considered and the dynamics captured on the tangent plane is also represented here.

Evaluating the degree of fitting M

A suitable degree of fitting M, for a case considered can be decided by comparing the manifold on which the reconstructed trajectories lie and the manifold on which the *training data* trajectories lie. This can be implemented by considering the cross-section of the manifolds along a plane parallel to the shift mode. This process is evaluated for all the conservative variables combined, for which there exists a manifolds for each flow condition. One such instance of evaluation of the degree of fitting is represented in figure 5.14a, for a case of the flowfield for Ma=0.69 $\alpha = 7.25°$, which checks the cross sectional fit of the manifold formed by the URANS *training data* and various manifolds formed by changing the degree of fitting M. Here, the training data and the reconstructed flowfield data for various degrees of M are projected onto basis type A of the flowfield, to obtain trajectories in space, which are then used to define a manifold on which the trajectories lie. The cross section of the manifold of the URANS *training data*, represented by the black line and the cross section of manifolds formed by the reconstructed flowfield data for various M, represented by dotted lines of various colours are checked for the best fit. The best degree of fit is evaluated by considering the normalized mean trajectory error (NMTE), which was considered for works on other cases using SSM in [14]. NMTE is defined as follows; Given P observations of the observable vector $\mathbf{y}_j$ and their corresponding model-based reconstructions $\hat{\mathbf{y}}_j$, the NMTE is defined as follows:

$$\text{NMTE} = \frac{1}{\|\mathbf{y}\|}\frac{1}{P}\sum_{j=1}^{P}\|\mathbf{y}_j - \hat{\mathbf{y}}_j\|. \tag{5.1}$$

Here, $\mathbf{y}$ represents a relevant normalization vector, such as the data point with the largest norm. The NMTE error comparison was considered for the full flow, from time $t = 0$ s. Various degrees of fitting (M) were considered as shown in figure 5.14a, the NMTE of which are represented in table 5.3. From figure 5.14a, it can be inferred that M=5 is the best degree of fit for reconstruction of the manifold of the flowfield for a case of Ma=0.69 $\alpha = 7.25°$.

Degree of fitting (M)	NMTE
3	0.1709
4	0.05061
5	0.05008
6	0.05809
10	0.1188
15	0.1756

Table 5.3: Normalized mean-trajectory-error (NMTE) for various degree of fitting (M) for Ma=0.69 α=7.25°. The NMTE error is found to be minimum at M=5.

Evaluating the effect of M at various points in time (t)

The degree of fit obtained from the previous evaluation, is compared to check for fit with the *training data* manifold, at various points in time, until the first LCO oscillation. For the case of Ma=0.69 $\alpha = 7.25°$, discussed in section 5.2.1, it was seen that the best degree of fit was M=5. The cross section of the manifold obtained for the reconstructed flowfield starting from $t = 0$ to for various end times T, at M=5 is compared in figure 5.14b. Here, the end times T vary from 0.3s to 1.3701s. Times at 1.3156s indicate when the limit cycle oscillation is initially observed for this case, which is obtained by checking the variation of lift coefficient in time (C_L). The point of the first limit cyle oscillation (LCO) is obtained as the time at which the maximum value of lift coefficent is observed once the lift coeffient exhibits repeated oscillation of its value in time. The end point of first limit cycle oscillation at T=1.3701s is also considered for comparison. This process was done to evaluate how well the manifold of the reconstructed manifold fits against the URANS *training data* manifold at various points in time. The fit at various points in time can be used to assess how well the reconstructed manifold captures the dynamics of the *training data* at various points in time. Comparing the NMTE between the URANS data as given in table 5.4, a decreasing error trend till the LCO cycle is seen, marking the capture of the dynamics of the *training data* quite well for M=5.

Evaluating various cases of flow and their degree of fit

For evaluation of the degrees of fit, two cases are considered:

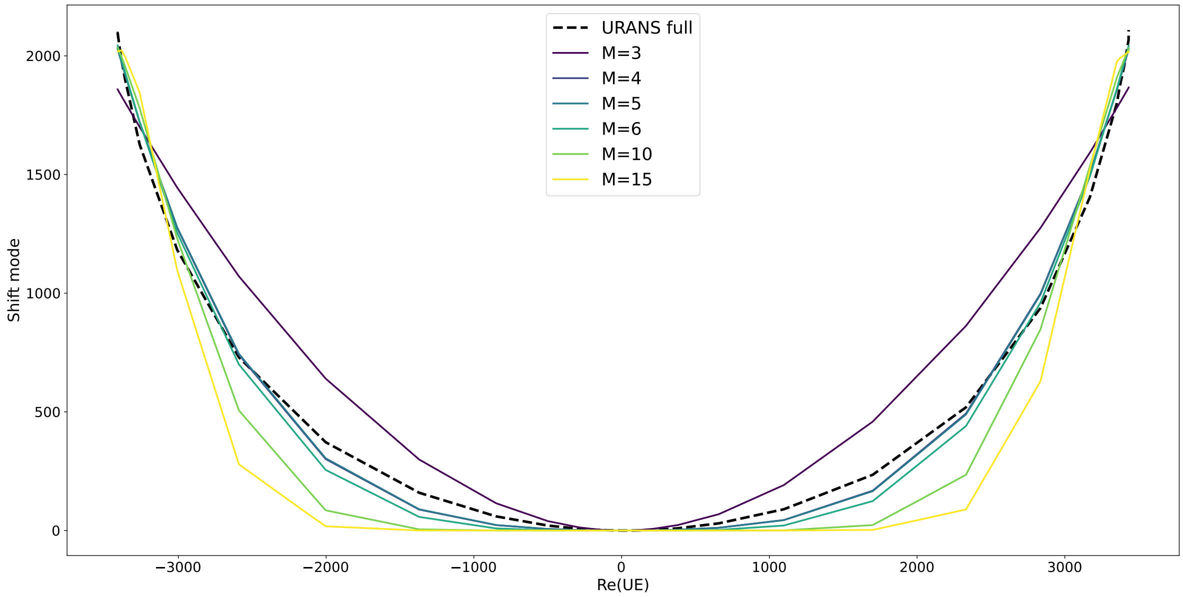

(a) Fit check for various degrees of monomials (M) considered for Ma 0.69, α = 7.25°. It can be seen here that increase in M can only improve fitting to a certain degree, beyond which some level of over fitting is observed. The optimum degree of fitting of the manifold for this case is M = 5.

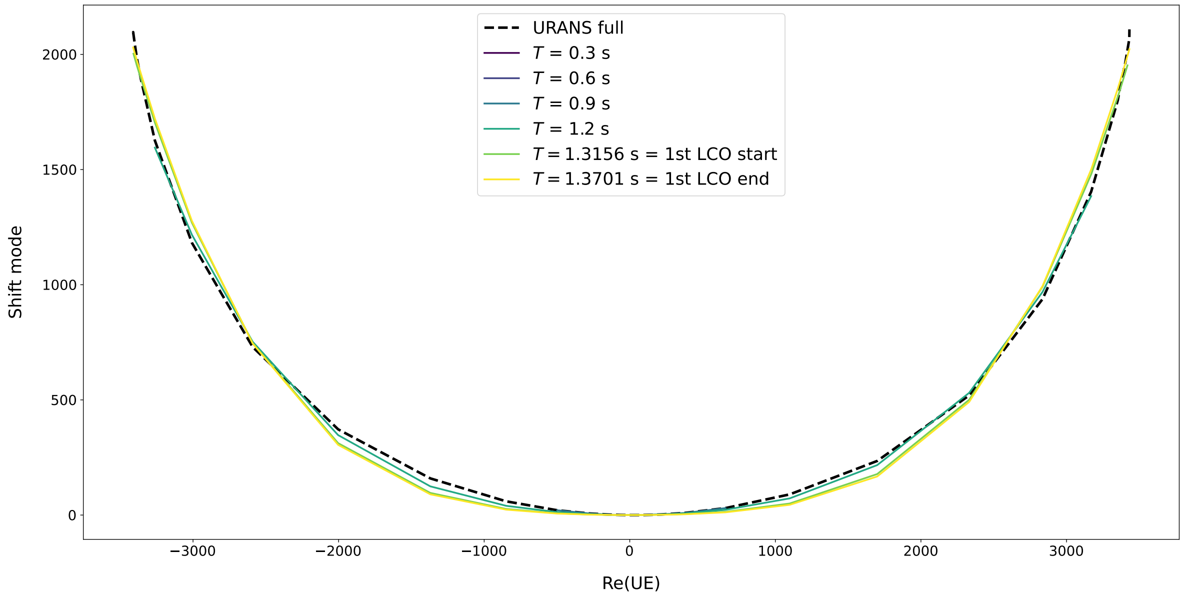

(b) Fit check for a chosen degree of monomial (M = 5) for various points in time, considered for Ma 0.69, α = 7.25°. It can be seen from table 5.9 that there is a good fit close to the base flow, for lower values of T and the fit improves when T is increased to till a value close to the beginning and end of the first LCO cycle.

Figure 5.14: Determination of the degree of monomial used for defining the embedding of the manifold and the fit observed for various points in time. On increasing M to an optimum value,improved fitting can be seen, beyond which an overfitting is also seen. For fitting the manifold for the optimum degree of fitting at various point in time, an improved fitting can be seen when moving from a T close to the base flows to a T at which the first LCO oscillation take place.

Time considered (s)	NMTE
0.3	0.7629
0.6	0.35
0.9	0.0711
1.2	0.0359
1.3156	0.0504
1.3701	0.0521

Table 5.4: Normalized mean-trajectory-error (NMTE) for different times considered. The NMTE errors indicate a good capture of the dynamics from points close to the base flow and points including the LCO region.

- Case 1: A flow condition of Ma = 0.69 at $\alpha = 5°$
- Case 2: A flow condition of Ma = 0.69 at $\alpha = 7.25°$

The cases are further subdivided on the basis which they use to define the reconstructed flowfield. These basis may be defined by the eigen vectors (eigen basis) as basis type A or the basis defined by the POD modes (POD basis) i.e. basis type B. Case 1 is depicted in figure 5.15 and case 2, in figure 5.16.

First consider the case of the embedded manifold of the flowfield for the case of Ma=0.69 and $\alpha = 5°$ or Case 1 in figure 5.15:

- The right column consists of figure 5.15a and figure 5.15b, which comprises of the projection of the unsteady part of URANS *training data* and reconstructed flowfield onto basis type A of this flowfield. This projection results in the creation of a manifold as seen in figure 5.15a of the URANS *training data* over which trajectory of the reconstructed flowfield lies. The degree of fit used here is M=5.
- The left column consists of figure 5.15c and figure 5.15d, which comprises of the projection of the unsteady part of URANS *training data* and reconstructed flowfield onto basis type B of this flowfield. This projection results in the creation of a manifold as seen in figure 5.15c of the URANS *training data* over which trajectory of the reconstructed flowfield lies. The degree of fit uses here is M=5.

In figure 5.16, case 2 is evaluated, where the embedded manifold of the flowfield, for a case of Ma=0.69 and $\alpha = 7.25°$ is observed. Two columns of images are present here,

- The right column consists of figure 5.16a and figure 5.16b, which comprises of the projection of the unsteady part of URANS *training data* and reconstructed flowfield onto basis type A of this flowfield. This projection results in the creation of a manifold as seen in figure 5.16a of the URANS *training data* over which trajectory of the reconstructed flowfield lies. The degree of fit used here is M=5.
- The left column consists of figure 5.16c and figure 5.16d, which comprises of the projection of the unsteady part of URANS *training data* and reconstructed flowfield onto basis type B of this flowfield. This projection results in the creation of a manifold as seen in figure 5.16c of the URANS *training data* over which trajectory of the reconstructed flowfield lies. The degree of fit uses here is M=5.

For both the cases, the NMTE error of the cross section of the manifold formed from the reconstructed flowfield and the unsteady part of URANS *training data* was evaluated, as previously done in section 5.2.1 and section 5.2.1, shown in table 5.5. The comparison of the URANS *training data* flowfield trajectories and the reconstructed flowfield trajectories for the cases considered, over the tangent plane $\mathcal{T}_0\mathcal{M}_0$ is portrayed in figure 5.17. Here η_1 and η_2 are obtained through the projection of the URANS *training data* flowfield over the real and imaginary components of the eigenvectors which make up part of basis type A and over POD1 and POD2 components which make up part of the basis type B. η_1' and η_2' are the projections of the reconstructed flowfields obtained through equation (4.13), over the basis type A and basis type B, both without the shift mode. Comparing between the URANS *training data* flowfield trajectories and the reconstructed flowfield trajectories, a deviation between the two can be seen. The reconstructed flowfield trajectories possess this deviation because of the inability to completely capture linear and non-linear nature of the dynamics using monomial expansions of the reduced coordinates. This results in $\mathbf{V_1}$ and $\mathbf{V}$ matrices to produce imperfect flow reconstructions, and thus imperfect reconstructed flowfield trajectories.

	Ma = 0.69, α = 5°	Ma = 0.69, α = 7.25°
NMTE for **Basis type A**	0.05008	0.0500838
NMTE for **Basis type B**	0.044313	0.044313

Table 5.5: NMTE values between the cross section of the manifolds made through URANS projections and reconstructed flowfield projections onto different basis types and parameter combinations

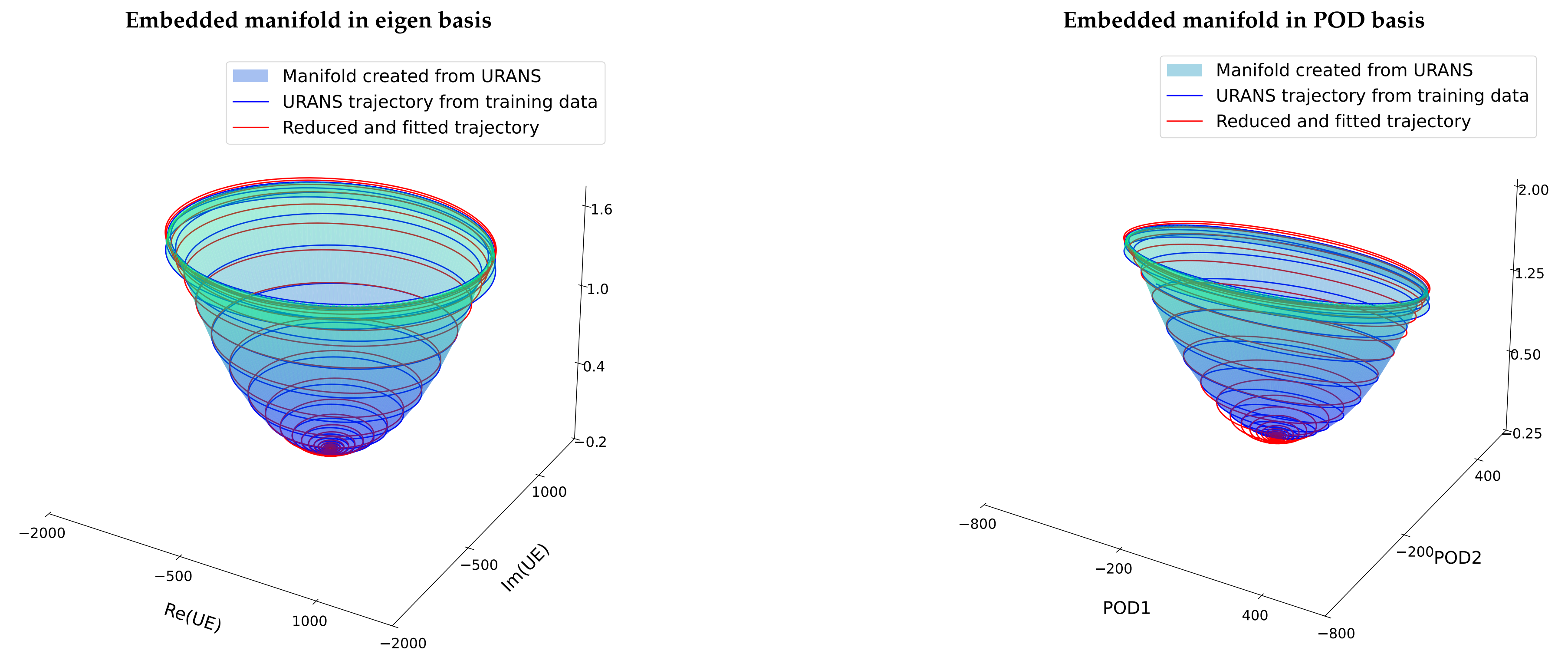

(a) 3D embedded manifold of the URANS *training data* for Ma=0.69 - $\alpha = 5°$ constructed with the eigen basis, with trajectories obtained through projection of the reconstructed flowfield data onto the eigen basis.

(c) 3D embedded manifold of the URANS *training data* for Ma=0.69 - $\alpha = 5°$ constructed with the POD basis, with trajectories obtained through projection of the reconstructed flowfield data onto the POD basis.

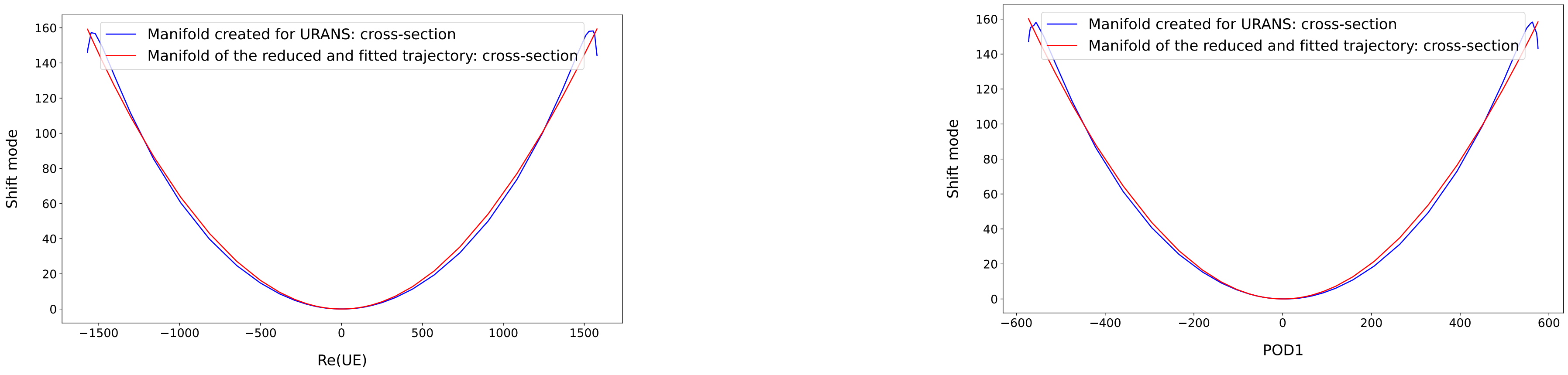

(b) Cross section of the 3D embedded manifold of the URANS *training data* for Ma=0.69 - $\alpha = 5°$ constructed with the eigen basis, with the cross section of the manifold constructed out of the trajectories obtained through projection of the reconstructed flowfield data onto the eigen basis.

(d) Cross section of the 3D embedded manifold of the URANS *training data* for Ma=0.69 - $\alpha = 5°$ constructed with the POD basis, with the cross section of the manifold constructed out of the trajectories obtained through projection of the reconstructed flowfield data onto the POD basis.

Figure 5.15: Embedded manifolds of the URANS *training data* and the trajectories of the reconstructed data constructed using eigen and POD basis, along with comparison of the cross section of their manifolds: $Ma = 0.69$ at $\alpha = 5°$

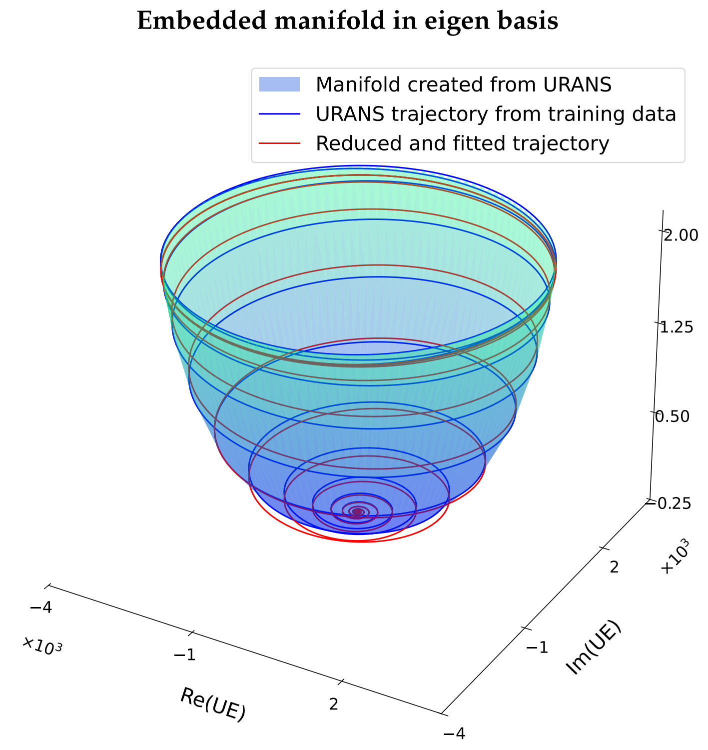

(a) 3D embedded manifold of the URANS *training data* for Ma=0.69 - $\alpha = 7.25°$ constructed with the eigen basis, with trajectories obtained through projection of the reconstructed flowfield data onto the eigen basis.

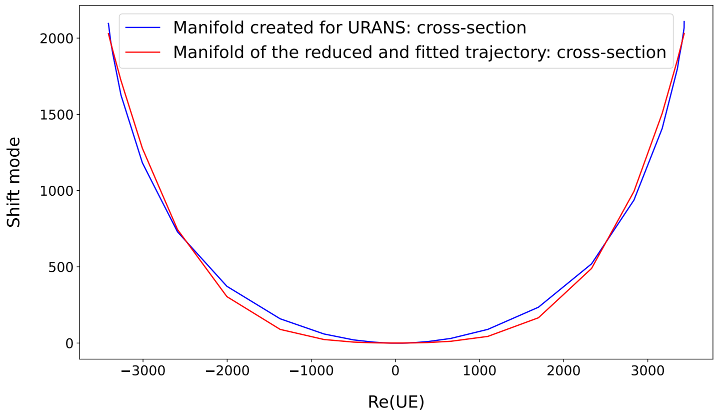

(b) Cross section of the 3D embedded manifold of the URANS *training data* for Ma=0.69 - $\alpha = 7.25°$ constructed with the eigen basis, with the cross section of the manifold constructed out of the trajectories obtained through projection of the reconstructed flowfield data onto the eigen basis.

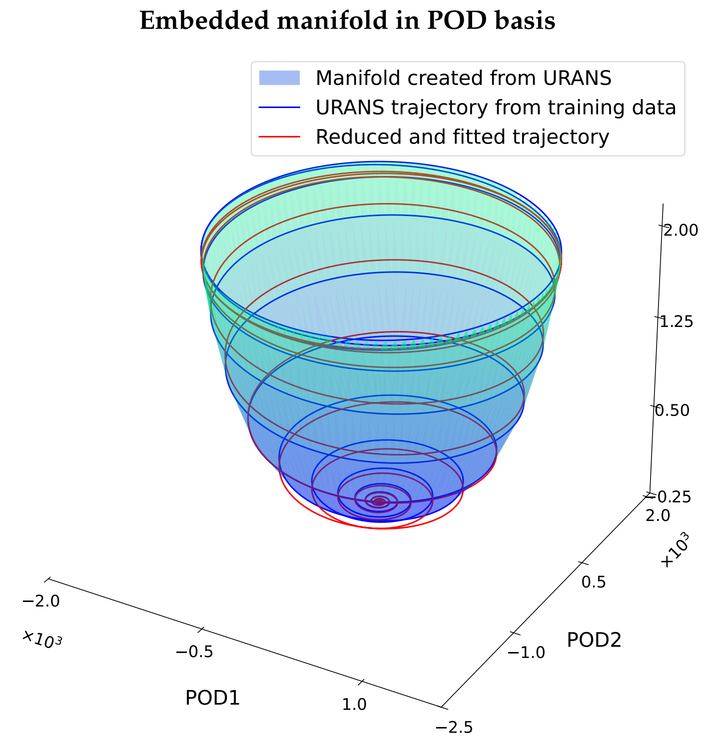

(c) 3D embedded manifold of the URANS *training data* for Ma=0.69 - $\alpha = 7.25°$ constructed with the POD basis, with trajectories obtained through projection of the reconstructed flowfield data onto the POD basis.

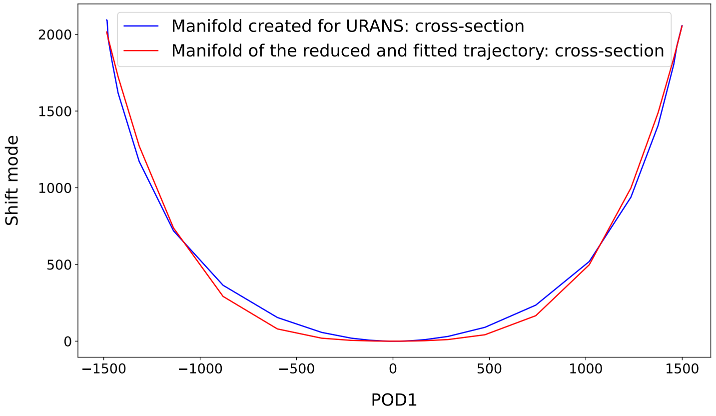

(d) Cross section of the 3D embedded manifold of the URANS *training data* for Ma=0.69 - $\alpha = 7.25°$ constructed with the POD basis, with the cross section of the manifold constructed out of the trajectories obtained through projection of the reconstructed flowfield data onto the POD basis.

Figure 5.16: Embedded manifolds of the URANS *training data* and the trajectories of the reconstructed data constructed using eigen and POD basis, along with comparison of the cross section of their manifolds: $Ma = 0.69$ at $\alpha = 7.75°$

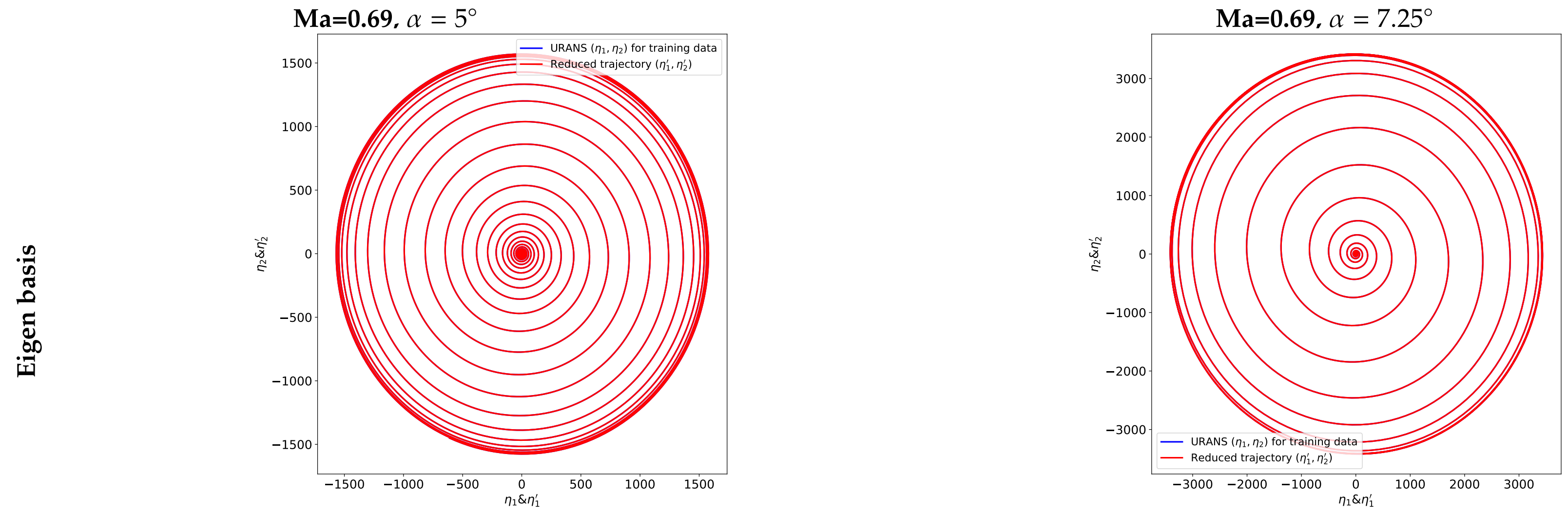

(a) Trajectories of URANS *training data* (η_1 and η_2) and the reduced flowfield projections obtained from equation (4.13) (η_1' and η_2'), made by projection of the URANS field and reconstructed field on basis type A vector components without the shifted mode for: Ma=0.69, α = 5° in the eigen basis

(b) Trajectories of URANS *training data* (η_1 and η_2) and the reduced flowfield projections obtained from equation (4.13) (η_1' and η_2'), made by projection of the URANS field and reconstructed field on basis type A vector components without the shifted mode for: Ma=0.69, α = 7.25° in the eigen basis

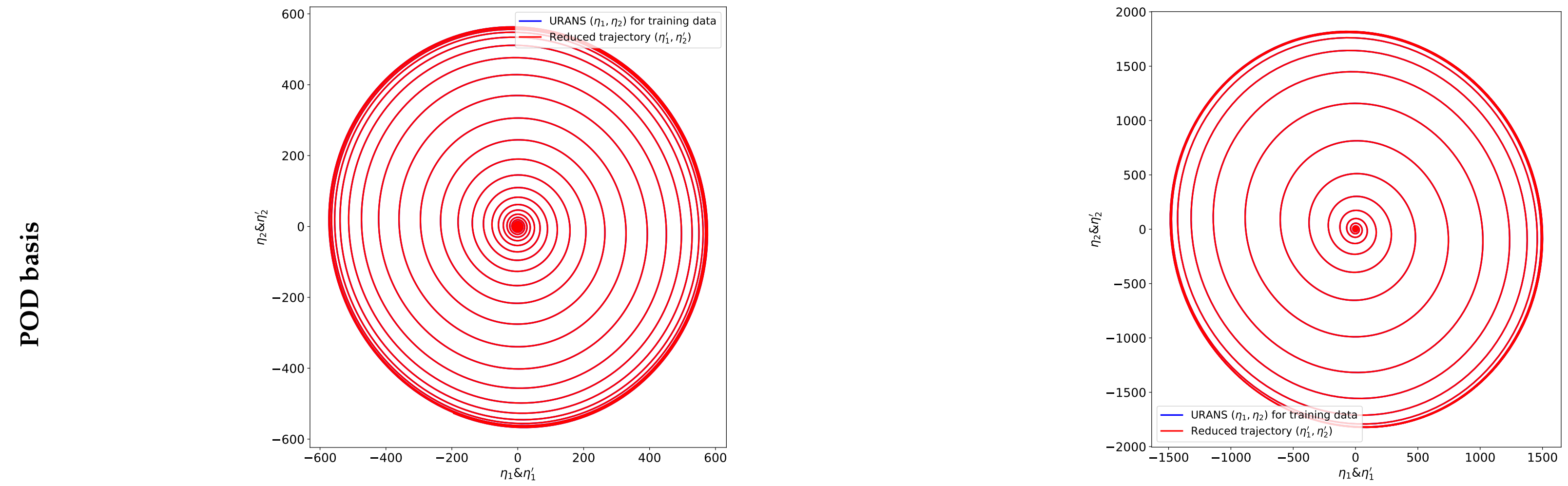

(c) Trajectories of URANS *training data* (η_1 and η_2) and the reduced flowfield projections obtained from equation (4.13) (η_1' and η_2'), made by projection of the URANS field and reconstructed field on basis type B vector components without the shifted mode for: Ma=0.69, α = 5° in the POD basis

(d) Trajectories of URANS *training data* (η_1 and η_2) and the reduced flowfield projections obtained from equation (4.13) (η_1' and η_2'), made by projection of the URANS field and reconstructed field on basis type B vector components without the shifted mode for: Ma=0.69, α = 7.25° in the POD basis

Figure 5.17: Images depicting trajectories of URANS *training data* (η_1 and η_2) and the reduced flowfield projections obtained from equation (4.13) (η_1' and η_2'), made by projection of the URANS field and reconstructed field on basis type A and B vector components without the shifted mode. Columns are Ma-AOA combinations, rows are basis type.

5.2.2. Using fitted manifold for polynomial regression

After fitting of the manifold to reconstruct the conservative variables components of the flowfield, $\mathbf{V_1}$ and $\mathbf{V}$ is obtained for each of the cases of the flowfield (Ma-α), which capture their linear and non-linear nature receptively. For each of the manifold of the different cases of flow fields, the *training data* used for generation of the manifold and original trajectory, is used to create the reduced coordinates η_1 and η_2 by projection onto an orthonormal basis type A or basis type B. While using both basis type A and basis type B for producing reduced coordinates, only two components of it are considered, excluding the shifted mode component. The 3D basis created through basis type A and basis type B were used only to visualize the embedding process and to check whether the degree of fit M use to define the reconstructed flowfield as per equation (4.13) appropriately matches the *training data* flowfield. As per the definition of the decoder function discussed in section 4.4.6 and in section 4.1, since the tangent space on which the imaging is done is described using only the reduced coordinates η_1 and η_2 only parts of the basis are considered for the purposes of linear regression. To reiterate,

- When using basis type A, η_1 is the reduced coordinate obtained by the projection of the *training data* flowfield onto the real component of the eigen vector and η_2 is the reduced coordinate obtained by the projection of the *training data* flowfield onto the imaginary component of the eigen vector.
- When using basis type B, η_1 is the reduced coordinate obtained by the projection of the *training data* flowfield onto the POD mode 1 and η_2 is the reduced coordinate obtained by the projection of the *training data* flowfield onto the POD mode 2.

The reduced coordinates allow us to study the time evolution of an n-dimensional system by embedding into a lower, d=2 dimensional state. These reduced coordinates are then fitted individually by linear regression using both the reduced coordinates, as described in section 4.4.7. These create a set of differential equations which are used to predict the evolution of the reduced coordinates in time, and when paired up with the encoder function described in equation (4.10) produces a reduced order model, used to describe the time evolution of the various conservative variables of a flow field. This means that for each pair of reduced coordinates produced by projection of conservative variable components of a case of flowfield onto an orthonormal basis type a or basis type B, it creates a pair of ordinary differential equations (ODE), which describes the nature of evolution of the reduced coordinates in time. These ODE's produced can then be used to predict the evolution of the reduced coordinates for the same case of the flowfield, but for any initial condition.

Now for the generation of reduced order models, linear regression is to be performed for some cases whose embedding is done earlier to obtain the $\mathbf{V_1}$ and $\mathbf{V}$ matrices separately, for an optimum degree of fitting M. Here, the following cases were considered for the evaluation of linear regression of the reduced coordinates,

- Case 1: A flow condition of Ma = 0.69 at $\alpha = 5°$, where the reduced variables constructed out of flowfield projected onto basis type A and basis type B are considered.
- Case 2: A flow condition of Ma = 0.69 at $\alpha = 7.25°$, where the reduced variables constructed out of flowfield projected onto basis type A and basis type B are considered.
- Case 3: A flow condition of Ma = 0.71 at $\alpha = 4.45°$, where the reduced variables constructed out of flowfield projected onto basis type A and basis type B are considered.
- Case 4: A flow condition of Ma = 0.71 at $\alpha = 5.25°$, where the reduced variables constructed out of flowfield projected onto basis type A and basis type B are considered.

As discussed, the optimum degree of fitting of M is evaluated, for each of the cases and then the $\mathbf{V_1}$ and $\mathbf{V}$ matrices are stored for the sake of validation purpose, by reconstructing the flowfield. The degree of fitting M obtained for all the cases considered for both basis type A and basis type B are represented in table 5.6.

Now, consider case 1, which can be seen in figure 5.18a and figure 5.18c, where the flowfield is projected onto the basis type A and basis type B respectively, both excluding the shift mode. For the reduced coordinates thus obtained, η_1 and η_2, as discussed in section 4.4.7, the time derivatives are evaluated by

	Degree of fitting chosen for basis type A	Degree of fitting chosen for basis type A
Case 1	5	5
Case 2	5	5
Case 3	5	5
Case 4	5	5

Table 5.6: Degree of fitting chosen for basis type A and basis type B for the cases considered. For all cases, it was observed that a degree of fitting, M = 5, provided the best fit of the manifold.

forward Euler method to obtain $\frac{d\eta_1}{dt}$ and $\frac{d\eta_2}{dt}$, described as,

$$\frac{d\boldsymbol{\eta}}{dt} = \frac{\boldsymbol{\eta}_{t+1} - \boldsymbol{\eta}_t}{\Delta t} \tag{5.2}$$

where, Δt is the time step considered for the URANS simulation.

These are then separately fit by $\boldsymbol{\eta}_1$ and $\boldsymbol{\eta}_2$ obtained by the equation (4.10) for the receptive basis of choice, to obtain the governing ODE. The maximum order of the $\boldsymbol{\eta}_1$ and $\boldsymbol{\eta}_2$, used for fitting here is fixed at an order of 3. In this case, for the basis type A, seen in figure 5.18a the governing ODE are,

$$\begin{aligned}\frac{d\eta_1}{dt} = & -2.4875\times10^{-6}\,\eta_1^3 - 2.3570\times10^{-7}\,\eta_1^2\eta_2 - 7.5341\times10^{-5}\,\eta_1^2 - 2.5358\times10^{-6}\,\eta_1\eta_2^2 \\ & -4.9748\times10^{-5}\,\eta_1\eta_2 + 0.9854\,\eta_1 - 2.3078\times10^{-7}\,\eta_2^3 + 6.5812\times10^{-5}\,\eta_2^2 + 96.812\,\eta_2\end{aligned} \tag{5.3}$$

$$\begin{aligned}\frac{d\eta_2}{dt} = & -6.0634\times10^{-8}\,\eta_1^3 - 2.4694\times10^{-6}\,\eta_1^2\eta_2 + 8.4718\times10^{-6}\,\eta_1^2 - 8.6647\times10^{-8}\,\eta_1\eta_2^2 \\ & -1.9036\times10^{-4}\,\eta_1\eta_2 - 95.3303\,\eta_1 - 2.5237\times10^{-6}\,\eta_2^3 + 3.8496\times10^{-6}\,\eta_2^2 + 1.2249\,\eta_2\end{aligned} \tag{5.4}$$

and for basis type B, seen in figure 5.18c the governing ODE are,

$$\begin{aligned}\frac{d\eta_1}{dt} = & -2.0366\times10^{-5}\,\eta_1^3 - 1.6792\times10^{-7}\,\eta_1^2\eta_2 + 1.5349\times10^{-4}\,\eta_1^2 - 1.0756\times10^{-5}\,\eta_1\eta_2^2 \\ & -2.1184\times10^{-4}\,\eta_1\eta_2 - 4.0958\times10^{-2}\,\eta_1 + 1.5129\times10^{-7}\,\eta_2^3 - 5.9081\times10^{-5}\,\eta_2^2 - 69.469\,\eta_2\end{aligned} \tag{5.5}$$

$$\begin{aligned}\frac{d\eta_2}{dt} = & -1.1158\times10^{-6}\,\eta_1^3 - 2.2704\times10^{-5}\,\eta_1^2\eta_2 + 2.9947\times10^{-4}\,\eta_1^2 - 1.1333\times10^{-6}\,\eta_1\eta_2^2 \\ & +1.0595\times10^{-4}\,\eta_1\eta_2 + 1.3283\times10^{2}\,\eta_1 - 1.1892\times10^{-5}\,\eta_2^3 - 1.7413\times10^{-4}\,\eta_2^2 + 2.2530\,\eta_2\end{aligned} \tag{5.6}$$

For cases 1, 2 and 4 constructed over both basis type A and basis type B, there exists the governing equations which are described in Table 5.7. These ODE obtained for the reduced coordinate evolution are stored for validation purposes, where the time evolution of the reduced coordinates obtained from the projection of *validation data* on to the basis considered will be predicted from some time t_0. This prediction of reduced coordinates and the eventual conversion of the predicted reduced coordinates to the full flowfield using the decoder equation equation (4.13), is discussed in detail in the next section.

Case	Basis type A	Basis type B
1	$\begin{aligned}\frac{d\eta_1}{dt} =& -1.4924\times10^{-6}\,\eta_1^3 + 2.6431\times10^{-8}\,\eta_1^2\eta_2 \\ &+ 8.3735\times10^{-5}\,\eta_1^2 - 1.4926\times10^{-6}\,\eta_1\eta_2^2 \\ &+ 2.9177\times10^{-4}\,\eta_1\eta_2 + 2.4495\,\eta_1 \\ &- 6.3972\times10^{-9}\,\eta_2^3 - 9.5873\times10^{-5}\,\eta_2^2 \\ &+ 8.3367\times10^{1}\,\eta_2\end{aligned}$ (5.7) $\begin{aligned}\frac{d\eta_2}{dt} =& \ 1.2206\times10^{-7}\,\eta_1^3 - 1.6224\times10^{-6}\,\eta_1^2\eta_2 \\ &- 1.3794\times10^{-4}\,\eta_1^2 + 1.3623\times10^{-7}\,\eta_1\eta_2^2 \\ &+ 1.3243\times10^{-4}\,\eta_1\eta_2 - 8.3510\times10^{1}\,\eta_1 \\ &- 1.6244\times10^{-6}\,\eta_2^3 + 9.9702\times10^{-5}\,\eta_2^2 \\ &+ 2.3780\,\eta_2\end{aligned}$ (5.8)	$\begin{aligned}\frac{d\eta_1}{dt} =& -1.1135\times10^{-5}\,\eta_1^3 - 6.5852\times10^{-7}\,\eta_1^2\eta_2 \\ &- 9.9207\times10^{-5}\,\eta_1^2 - 1.1398\times10^{-5}\,\eta_1\eta_2^2 \\ &+ 6.7728\times10^{-4}\,\eta_1\eta_2 + 4.8955\,\eta_1 \\ &- 1.8929\times10^{-7}\,\eta_2^3 + 5.4052\times10^{-5}\,\eta_2^2 \\ &+ 8.4764\times10^{1}\,\eta_2\end{aligned}$ (5.9) $\begin{aligned}\frac{d\eta_2}{dt} =& \ 5.4821\times10^{-7}\,\eta_1^3 - 1.2154\times10^{-5}\,\eta_1^2\eta_2 \\ &- 1.7971\times10^{-4}\,\eta_1^2 + 5.6606\times10^{-8}\,\eta_1\eta_2^2 \\ &+ 1.5082\times10^{-3}\,\eta_1\eta_2 - 8.2145\times10^{1}\,\eta_1 \\ &- 1.2764\times10^{-5}\,\eta_2^3 + 1.0654\times10^{-4}\,\eta_2^2 \\ &- 5.9707\times10^{-2}\,\eta_2\end{aligned}$ (5.10)
2	$\begin{aligned}\frac{d\eta_1}{dt} =& -8.5283\times10^{-7}\,\eta_1^3 + 4.9441\times10^{-7}\,\eta_1^2\eta_2 \\ &- 2.1739\times10^{-5}\,\eta_1^2 - 7.8074\times10^{-7}\,\eta_1\eta_2^2 \\ &+ 1.9704\times10^{-4}\,\eta_1\eta_2 + 8.2320\,\eta_1 \\ &+ 5.3249\times10^{-7}\,\eta_2^3 + 2.6205\times10^{-5}\,\eta_2^2 \\ &+ 1.0986\times10^{2}\,\eta_2\end{aligned}$ (5.11) $\begin{aligned}\frac{d\eta_2}{dt} =& -6.4863\times10^{-7}\,\eta_1^3 - 7.5880\times10^{-7}\,\eta_1^2\eta_2 \\ &- 1.0588\times10^{-4}\,\eta_1^2 - 6.9886\times10^{-7}\,\eta_1\eta_2^2 \\ &+ 3.9530\times10^{-5}\,\eta_1\eta_2 - 1.0797\times10^{2}\,\eta_1 \\ &- 7.1263\times10^{-7}\,\eta_2^3 + 1.1377\times10^{-4}\,\eta_2^2 \\ &+ 4.3664\,\eta_2\end{aligned}$ (5.12)	$\begin{aligned}\frac{d\eta_1}{dt} =& -4.4048\times10^{-6}\,\eta_1^3 + 2.0275\times10^{-6}\,\eta_1^2\eta_2 \\ &- 1.7163\times10^{-4}\,\eta_1^2 - 2.5471\times10^{-6}\,\eta_1\eta_2^2 \\ &+ 3.0939\times10^{-4}\,\eta_1\eta_2 + 1.2185\times10^{1}\,\eta_1 \\ &+ 1.6233\times10^{-6}\,\eta_2^3 + 4.9135\times10^{-5}\,\eta_2^2 \\ &+ 8.9687\times10^{1}\,\eta_2\end{aligned}$ (5.13) $\begin{aligned}\frac{d\eta_2}{dt} =& -4.2933\times10^{-6}\,\eta_1^3 - 4.3642\times10^{-6}\,\eta_1^2\eta_2 \\ &- 4.1378\times10^{-4}\,\eta_1^2 - 3.1876\times10^{-6}\,\eta_1\eta_2^2 \\ &+ 4.2400\times10^{-4}\,\eta_1\eta_2 - 1.3182\times10^{2}\,\eta_1 \\ &- 2.6064\times10^{-6}\,\eta_2^3 + 1.7453\times10^{-4}\,\eta_2^2 \\ &+ 4.9012\times10^{-1}\,\eta_2\end{aligned}$ (5.14)
4	$\begin{aligned}\frac{d\eta_1}{dt} =& -1.0635\times10^{-6}\,\eta_1^3 - 4.7361\times10^{-8}\,\eta_1^2\eta_2 \\ &- 4.1203\times10^{-6}\,\eta_1^2 - 1.0900\times10^{-6}\,\eta_1\eta_2^2 \\ &- 3.9657\times10^{-5}\,\eta_1\eta_2 + 6.5708\,\eta_1 \\ &- 2.3423\times10^{-8}\,\eta_2^3 + 3.1921\times10^{-5}\,\eta_2^2 \\ &+ 9.8696\times10^{1}\,\eta_2\end{aligned}$ (5.15) $\begin{aligned}\frac{d\eta_2}{dt} =& -2.9893\times10^{-8}\,\eta_1^3 - 9.4534\times10^{-7}\,\eta_1^2\eta_2 \\ &- 3.8803\times10^{-6}\,\eta_1^2 - 5.8055\times10^{-8}\,\eta_1\eta_2^2 \\ &- 4.5179\times10^{-5}\,\eta_1\eta_2 - 9.7006\times10^{1}\,\eta_1 \\ &- 9.5793\times10^{-7}\,\eta_2^3 - 3.0826\times10^{-5}\,\eta_2^2 \\ &+ 4.6725\,\eta_2\end{aligned}$ (5.16)	$\begin{aligned}\frac{d\eta_1}{dt} =& -5.9776\times10^{-6}\,\eta_1^3 + 5.9774\times10^{-8}\,\eta_1^2\eta_2 \\ &+ 6.4598\times10^{-5}\,\eta_1^2 - 3.6159\times10^{-6}\,\eta_1\eta_2^2 \\ &- 7.1756\times10^{-5}\,\eta_1\eta_2 + 5.0202\,\eta_1 \\ &- 1.0937\times10^{-8}\,\eta_2^3 + 3.8870\times10^{-5}\,\eta_2^2 \\ &+ 7.5827\times10^{1}\,\eta_2\end{aligned}$ (5.17) $\begin{aligned}\frac{d\eta_2}{dt} =& -4.0494\times10^{-7}\,\eta_1^3 - 6.7059\times10^{-6}\,\eta_1^2\eta_2 \\ &+ 9.8836\times10^{-5}\,\eta_1^2 - 1.3199\times10^{-7}\,\eta_1\eta_2^2 \\ &+ 3.9758\times10^{-5}\,\eta_1\eta_2 - 1.2587\times10^{2}\,\eta_1 \\ &- 4.0322\times10^{-6}\,\eta_2^3 - 2.6350\times10^{-5}\,\eta_2^2 \\ &+ 6.2665\,\eta_2\end{aligned}$ (5.18)

Table 5.7: ODE for basis types A and B for cases 1, 2 and 4. The ODE obtained through linear regression for all the cases, for basis type A is tabulated in the left column of the table, while the right column tabulates the cases of ODE obtained for basis type B.

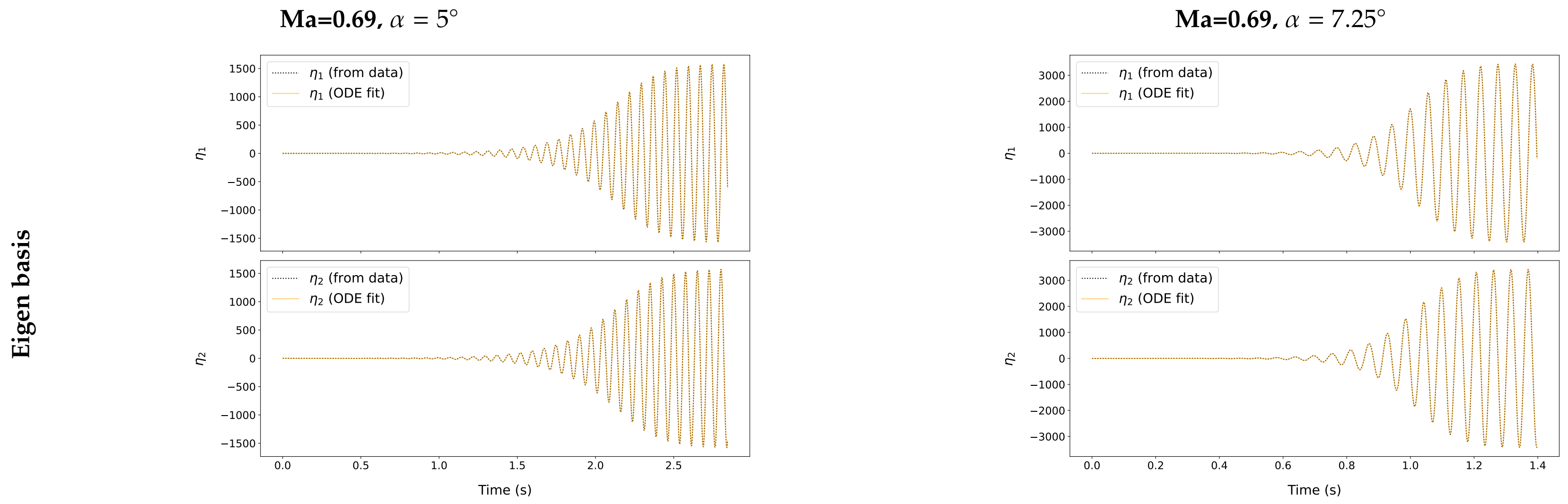

(a) ODE fitted for the *training data* in η_1 and η_2 for: Ma=0.69, α = 5° in the eigen basis

(b) ODE fitted for the *training data* in η_1 and η_2 for: Ma=0.69, α = 7.25° in the eigen basis

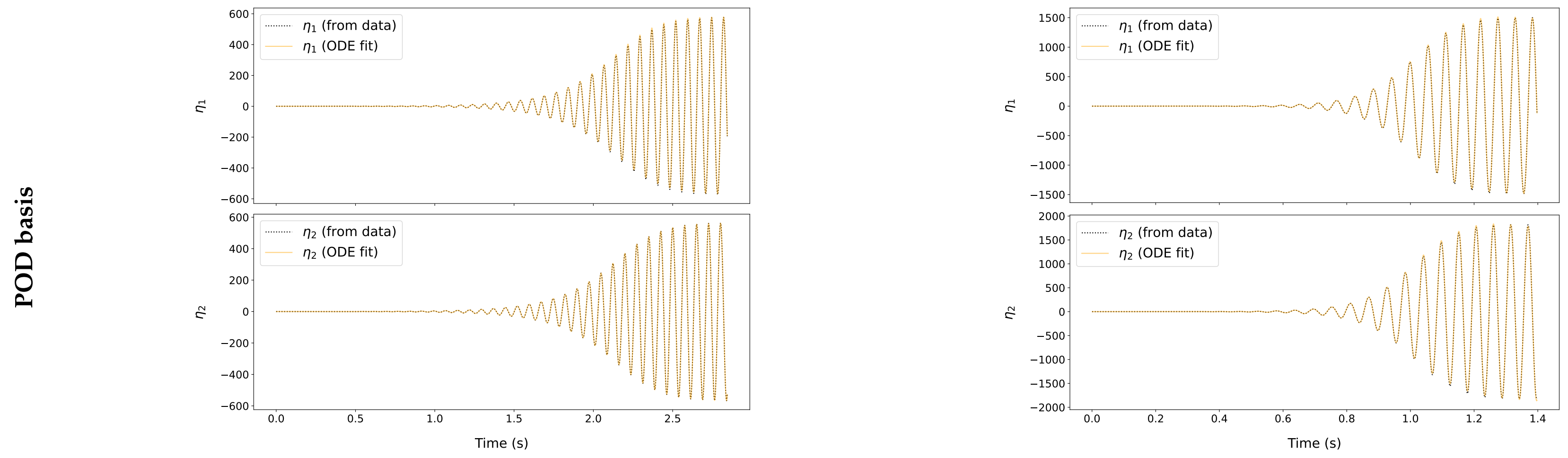

(c) ODE fitted for the *training data* in η_1 and η_2 for: Ma=0.69, α = 5° in the POD basis

(d) ODE fitted for the *training data* in η_1 and η_2 for: Ma=0.69, α = 7.25° in the POD basis

Figure 5.18: Images depicting ODE fitting for the *training data* in the reduced coordinates, for cases 1 and 2. Columns are Ma-AOA combinations, rows are basis type.

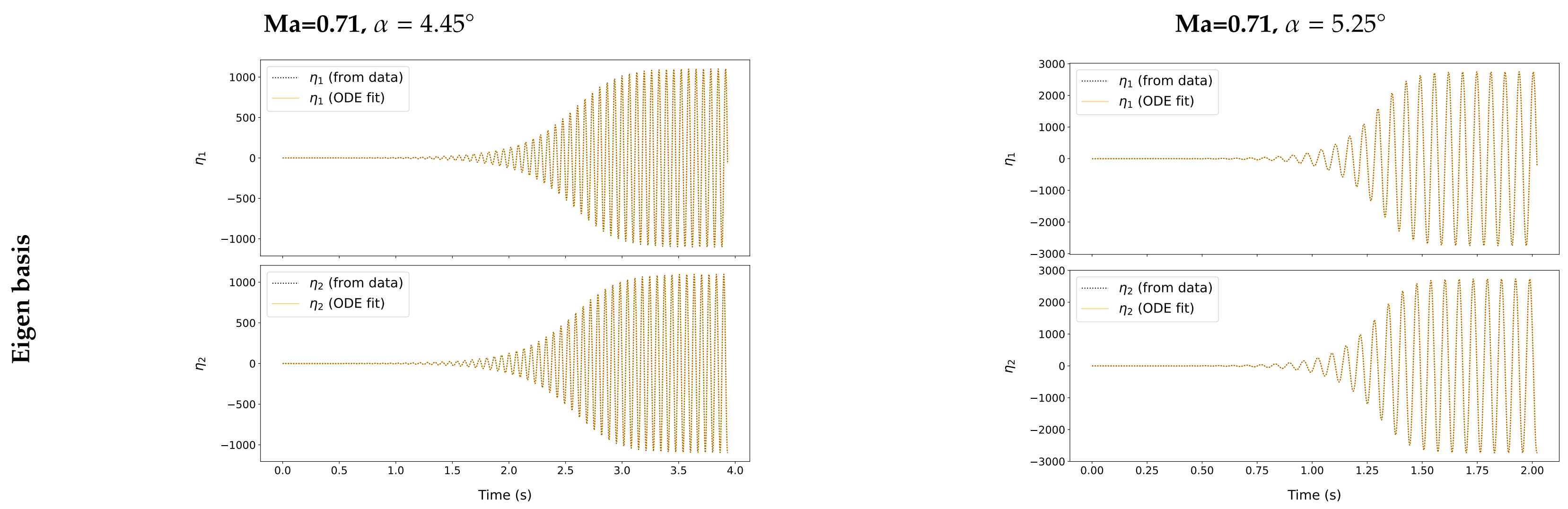

(a) ODE fitted for the *training data* in η_1 and η_2 for: Ma=0.71, α = 4.45° in the eigen basis

(b) ODE fitted for the *training data* in η_1 and η_2 for: Ma=0.71, α = 5.25° in the eigen basis

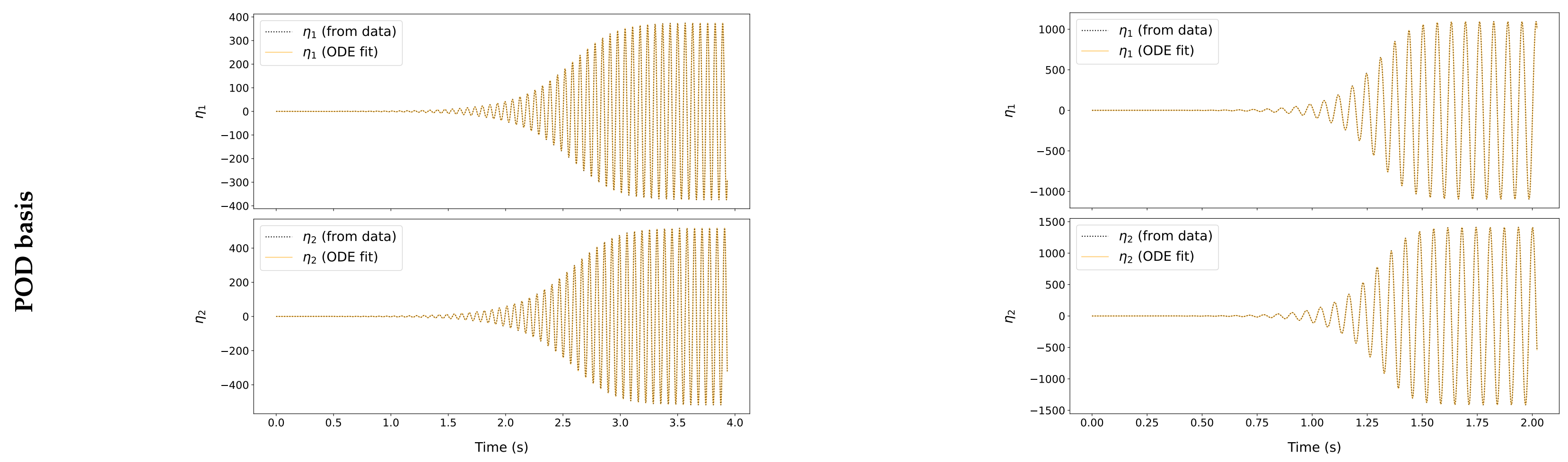

(c) ODE fitted for the *training data* in η_1 and η_2 for: Ma=0.71, α = 4.45° in the POD basis

(d) ODE fitted for the *training data* in η_1 and η_2 for: Ma=0.71, α = 5.25° in the POD basis

Figure 5.19: Images depicting ODE fitting for the *training data* in the reduced coordinates, for cases 3 and 4. Columns are Ma-AOA combinations, rows are basis type

5.2.3. Application of the reduced order model for prediction

Using the ordinary differential equations (ODE) for the reduced coordinates obtained through linear regression as seen in section 5.2.2, evolution of the same reduced coordinates for a different set of flow field data, say, the *validation data* which was recorded, can be carried out. Using reduced coordinates produced by the *validation data* for/at a time t_0 as initial conditions, predictions of the variations of the reduced coordinates of the *validation data* can be carried out using the ODE's obtained with the forward Euler method as,

$$\eta_{t+1} = \eta_t + \Delta t \cdot \left.\frac{d\eta}{dt}\right|_t \tag{5.19}$$

where, Δt is the time step considered for the URANS simulation and the $\left.\frac{d\eta}{dt}\right|_{t_n}$ considers the value of the ODE at η_t.

The 4 cases discussed in section 5.2.2, are used along with their ODE's for the reduced coordinate evolution prediction for the *validation data*. The t_0 considered for start of prediction for each of the cases are different to show the robustness of this method. The various starting times of predictions t_o for both $\boldsymbol{\eta}_1$ and $\boldsymbol{\eta}_2$ are represented as $t_0^{(\eta_1)}$ and $t_0^{(\eta_2)}$ for all the cases considered in table 5.8

Case	Basis type A	Basis type B
1	$t_0^{(\eta_1)} = 0.1284$ s $t_0^{(\eta_2)} = 0.1284$ s	$t_0^{(\eta_1)} = 0.1284$ s $t_0^{(\eta_2)} = 0.1284$ s
2	$t_0^{(\eta_1)} = 0.3865$ s $t_0^{(\eta_2)} = 0.3865$ s	$t_0^{(\eta_1)} = 0.3865$ s $t_0^{(\eta_2)} = 0.3865$ s
3	$t_0^{(\eta_1)} = 0.4174$ s $t_0^{(\eta_2)} = 0.4174$ s	$t_0^{(\eta_1)} = 0.4174$ s $t_0^{(\eta_2)} = 0.4174$ s
4	$t_0^{(\eta_1)} = 0.2087$ s $t_0^{(\eta_2)} = 0.2087$ s	$t_0^{(\eta_1)} = 0.2087$ s $t_0^{(\eta_2)} = 0.2087$ s

Table 5.8: Prediction start times, t_0, for η_1 and η_2 in each case and basis type.

Case 1 predictions for basis type A and basis type B are represented in figure 5.20a and figure 5.20c respectively. Case 2, 3 and 4 are also represented in similar fashion in figure 5.20 and figure 5.21. To investigate the error between the actual reduced coordinates produced by the projection of the *validation data* onto basis type A or basis type B, against the predicted reduced coordinate, NMTE is used, which was discussed and used in section 5.2.1. The NMTE errors observed for each case is represented in table 5.9.

Case	Basis type A	Basis type B
1	NMTE $\eta_1 = 0.12462$ NMTE $\eta_2 = 0.12405$	NMTE $\eta_1 = 0.13599$ NMTE $\eta_2 = 0.1395$
2	NMTE $\eta_1 = 0.2085$ NMTE $\eta_2 = 0.20845$	NMTE $\eta_1 = 0.30922$ NMTE $\eta_2 = 0.30123$
3	NMTE $\eta_1 = 0.13908$ NMTE $\eta_2 = 0.13.861$	NMTE $\eta_1 = 0.12179$ NMTE $\eta_2 = 0.12378$
4	NMTE $\eta_1 = 0.044762$ NMTE $\eta_2 = 0.04698$	NMTE $\eta_1 = 0.11805$ NMTE $\eta_2 = 0.13772$

Table 5.9: NMTE values for η_1 (first row) and η_2 (second row) between the predicted values of the reduced coordinates of the *validation data* using the ODE's obtained from *training data* and the actual reduced coordinates obtained from the *validation data* for each case and basis type.

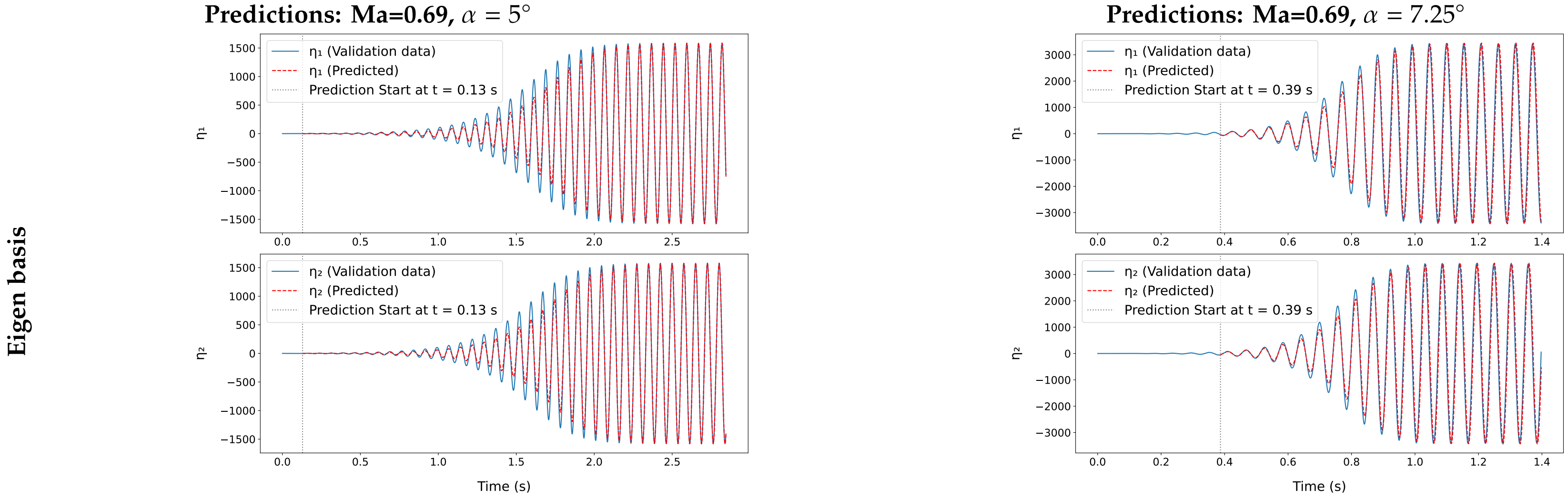

(a) Prediction for the *validation data* in η_1 and η_2 for: Ma=0.69, $\alpha = 5°$ in the eigen basis, from $t_0 = 0.13s$.

(b) Prediction for the *validation data* in in η_1 and η_2 for: Ma=0.69, $\alpha = 7.25°$ in the eigen basis , from $t_0 = 0.39s$.

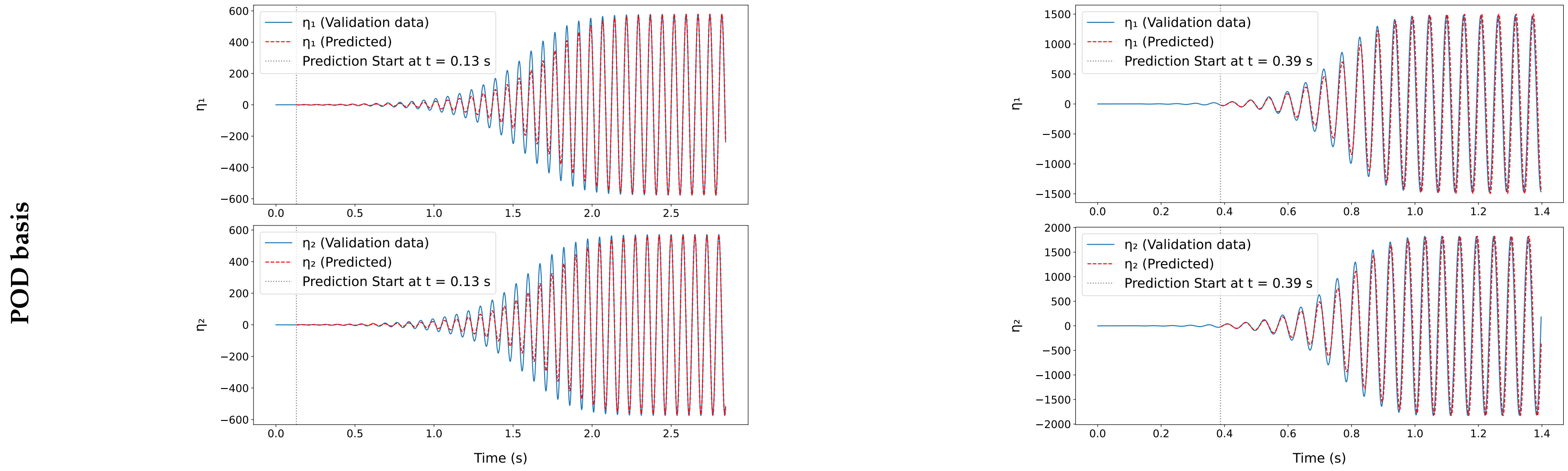

(c) Prediction for the *validation data* in in η_1 and η_2 for: Ma=0.69, $\alpha = 5°$ in the POD basis, from $t_0 = 0.13s$.

(d) Prediction for the *validation data* in in η_1 and η_2 for: Ma=0.69, $\alpha = 7.25°$ in the POD basis, from $t_0 = 0.39s$.

Figure 5.20: Images depicting ODE prediction for the *training data* in the reduced coordinates, for cases 1 and 2. Columns are Ma-AOA combinations, rows are basis type from a time t_0

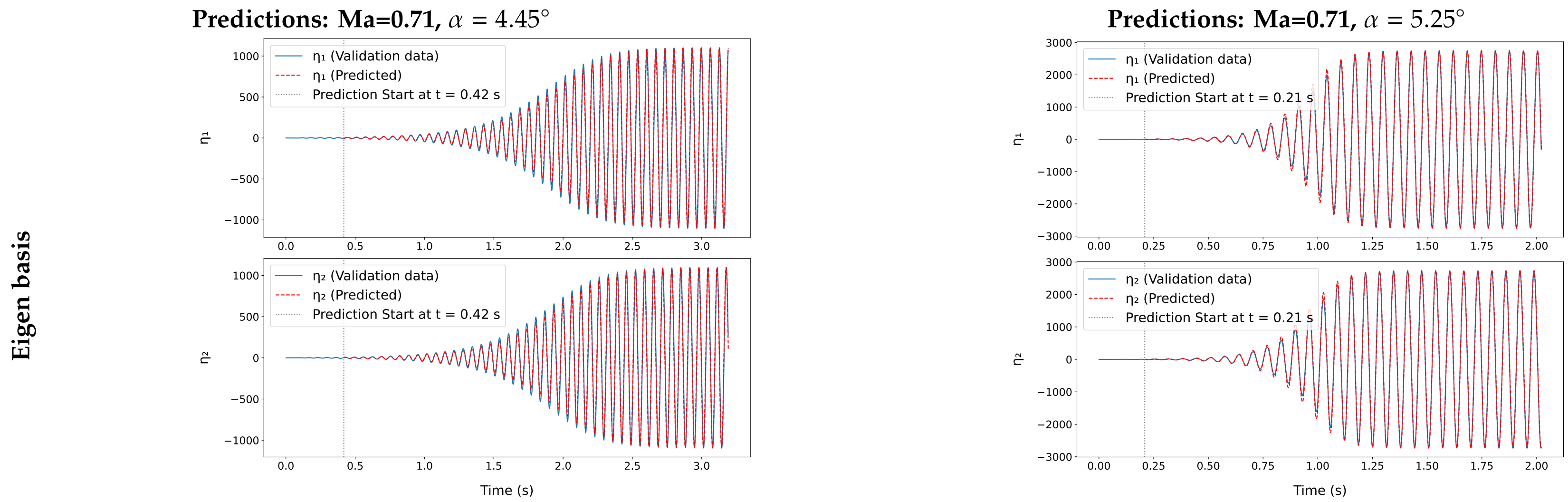

(a) Prediction for the *validation data* in η_1 and η_2 for: Ma=0.71, α = 4.45° in the eigen basis, from $t_0 = 0.47s$.

(b) Prediction for the *validation data* in η_1 and η_2 for: Ma=0.71, α = 5.25° in the eigen basis, from $t_0 = 0.21s$.

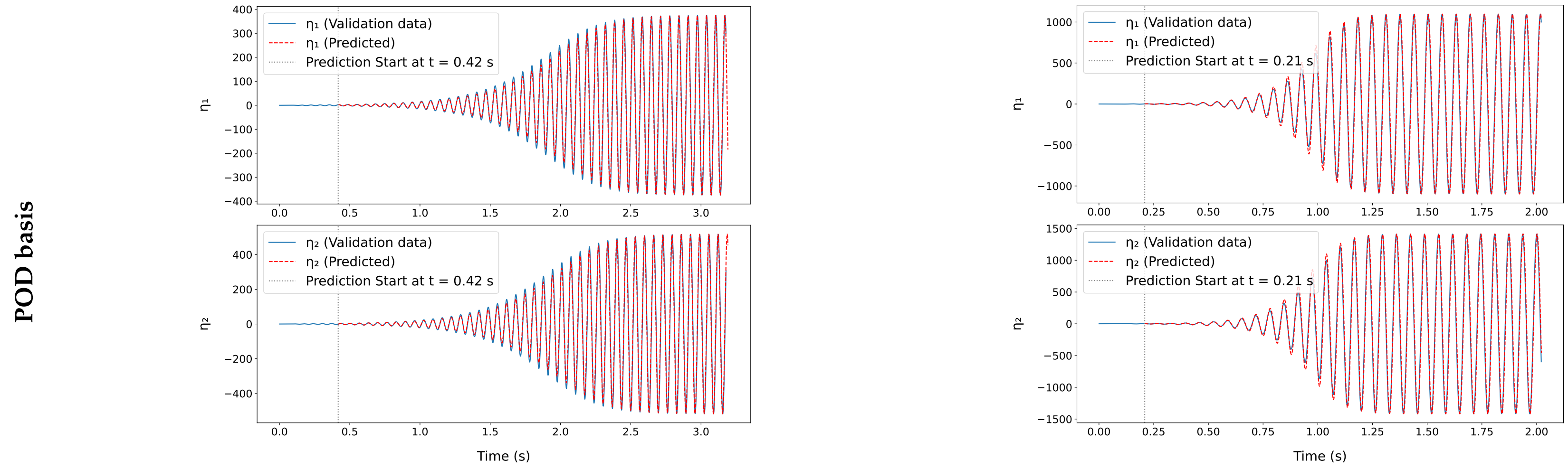

(c) Prediction for the *validation data* in η_1 and η_2 for: Ma=0.71, α = 4.45° in the POD basis, from $t_0 = 0.47s$.

(d) Prediction for the *validation data* in η_1 and η_2 for: Ma=0.71, α = 5.25° in the POD basis, from $t_0 = 0.21s$.

Figure 5.21: Images depicting ODE prediction for the *training data* in the reduced coordinates, for cases 3 and 4. Columns are Ma-AOA combinations, rows are basis type, from a time t_0.

These new predicted reduced coordinates, combined with the linear and non-linear coefficients $\mathbf{V_1}$ and $\mathbf{V}$ respectively, obtained for the training data of the same case, after appropriate fitting as discussed in section 5.2.1, can be used with the decoder function defined in equation (4.13). The decoder function, would thus reconstruct the flowfield based on the predicted reduced coordinates. Thus, flow field predictions for each of the conservative variables at any point in time can be obtained. For the cases 1, 2 3, and 4, the reconstructed flowfield is investigated, where the predicted reduced coordinates are based on basis type A and basis type B, and compare it with the actual URANS conservative variable flowfield chosen for the case.

Here initially, case 3 is considered. The prediction time of case 1 for both $\boldsymbol{\eta_1}$ and $\boldsymbol{\eta_2}$ coordinates i.e. $t_0^{(\eta_1)}$ and $t_0^{(\eta_2)}$, start at 0.1284 s. On reconstructing the flows based on predicted $\boldsymbol{\eta}$ from this $t_0^{(\eta_1)}$ and $t_0^{(\eta_2)}$, the predicted flow fields obtained via reduced coordinates using basis type A and basis type B at points in time t = 1s, 2s and 3s, are compared. As seen in the reduced coordinate prediction plot figure 5.21a and figure 5.21c,

- t = 1s, marks the time at which the evolution into limit cycle oscillation has started,
- t = 2s, marks the time at which the evolution into limit cycle oscillation is has almost ended,
- t = 3s, marks the time at which the flow has reached the state of limit cycle oscillation.

These time points are represented as red, blue and green circles respectively in figure 5.22, for the actual *validation data* $\boldsymbol{\eta}$ evolution. figure 5.22a represents these points in time for the *validation data* projected onto the basis type A and figure 5.22b represents these points in time for the *validation data* projected onto the basis type B.

The comparison of the predicted-reconstructed flowfield made with reduced coordinates obtained from basis type A and basis type B for case 3 is represented in figure 5.23. Here the conservative variable chosen to be reconstructed is the Z-momentum component. The figures with red circles indicate the time of evaluation to be at $t = 1$s, the blue circles to be at $t = 2$s and the green circles at $t = 3$s.

To evaluate the error of the reconstructed flowfield for case 3, two methods were undertaken

- Method 1: Evaluate the error of the flowfield by subtracting the predicted flowfields at points in time, with the actual URANS flowfield obtained at the same points in time. This error is evaluated and plotted for the predictions obtained through using both basis type A and basis type B. For case 3, at the points in time t = 1s, 2s and 3s, where the prediction was evaluated, the error plotted for the predictions for both basis type A and basis type B show a high degree of error to be present around the location of the shock, especially towards the foot of the shock.
- Method 2: Evaluate the L_2 norm of the difference in prediction at each time step to the URANS flowfield at the same point in time. This comparison resulting in an L_2 norm error trend for the entire time period of prediction for both basis type A predictions and basis type B predictions are represented in figure 5.24c and figure 5.24d. This method has been implemented to understand and quantify the difference between the full predicted flowfield and the full URANS flowfield, consisting of the full range of the field (i.e. including farfield). The L_2 error norm trend for a time series prediction would give an indication into which regions of flow does the predictions work best. For case 3, it can be seen that the predictions produced by basis type B are relatively better for the time period of prediction compared to basis type A.

On further investigating the method 2 for evaluating the L_2 norm error between the basis type A based projections and basis type B based projections, as seen in figure 5.24a and figure 5.24b respectively, the minimum and maximum error range observed at various points in time from the t_0 can be seen. Reconstruction of the *training data* flowfield using basis type A or the eigen basis results in a smaller of L_2 norm error for a time t≤1.5s, compared to the reconstruction made using basis type B. This follows the theory that the eigen basis used to reconstruct the flowfield can reconstruct the flow with lesser error when the reconstruction is region is closer to the base flow, i.e. when unsteadiness is lower. On the other hand the POD modes making up basis type B reconstruct the region of LCO seen at time t≥2.5s with lesser error compared to the what basis type A does. This is validated by the fact that the POD modes used for defining basis type B were extracted from the LCO region of the *training data*.

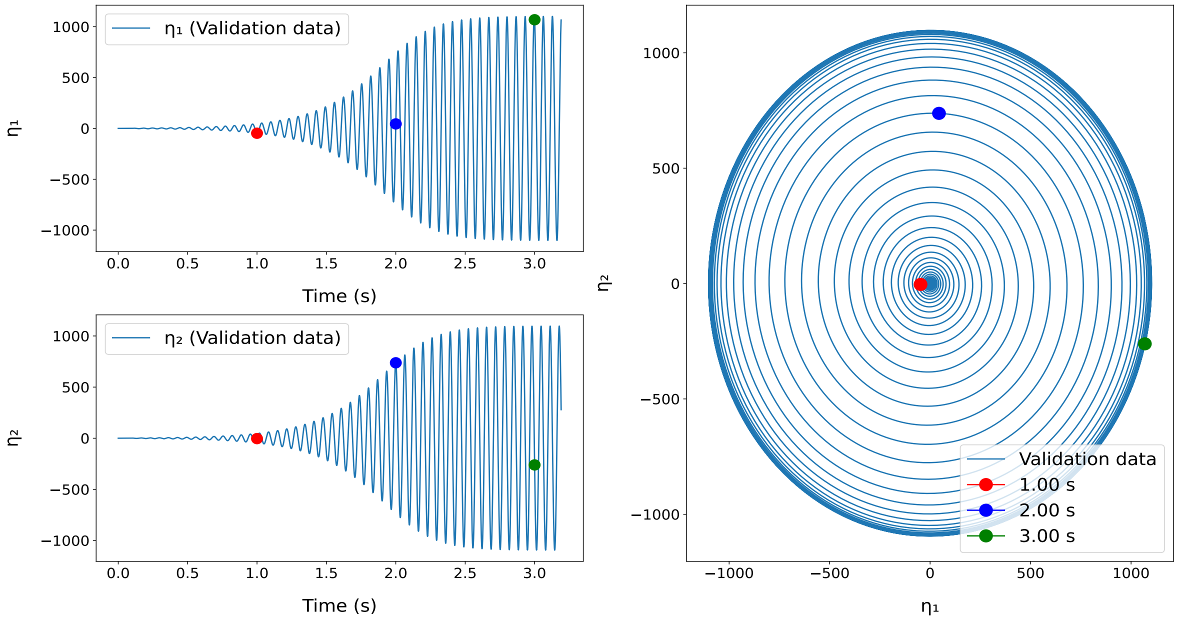

(a) Points in time t = 1s, 2s and 3s considered for Ma 0.71, α = 4.45° flowfield reconstruction, marked on the reduced coordinate plots on basis type A for the *validation data*

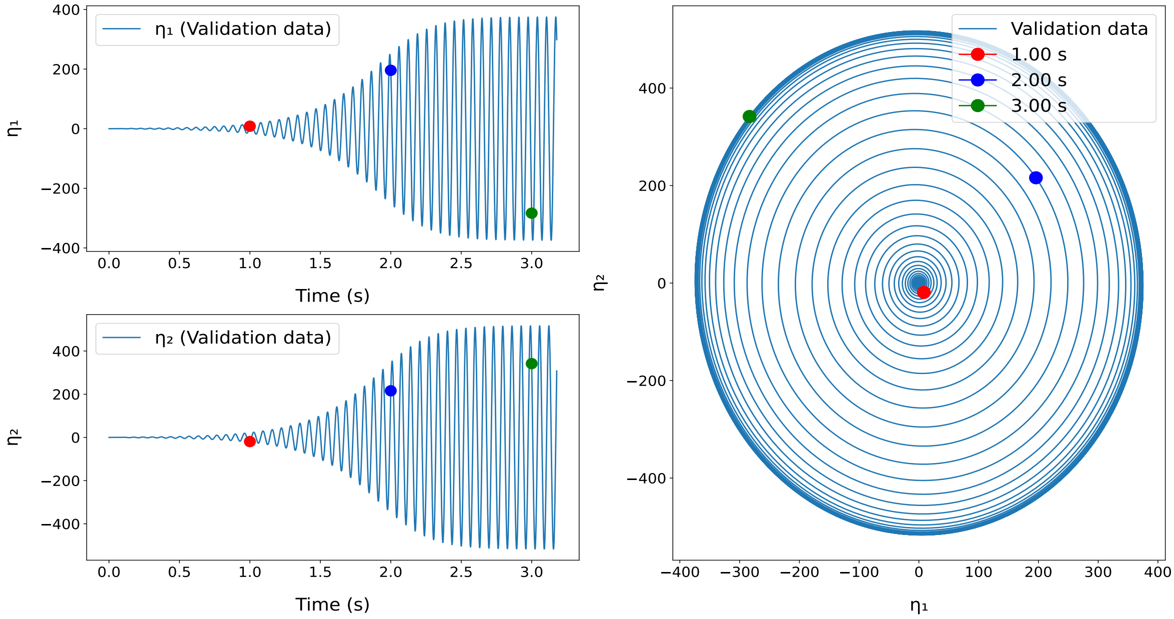

(b) Points in time t = 1s, 2s and 3s considered for Ma 0.71, α = 4.45° flowfield reconstruction, marked on the reduced coordinate plots on basis type B for the *validation data*

Figure 5.22: Points in time t = 1s, 2s and 3s considered for Ma 0.71, α = 4.45° flowfield reconstruction, marked on the reduced coordinate plots on basis type A and basis type B, for the *validation data*

For cases 1, 2, and 4, the predicted-reconstructed flowfield with basis type A and basis type B are compared, as done for case 3. As seen in figure 5.20a and figure 5.20c, the prediction done for the reduced coordinates of case 1 for both basis type A and basis type B are significantly deviating from the actual *validation data* reduced coordinate trend in the non-linear growth range of eta between 0.75 - 2 s. This could be due to the the stat time t_0 chosen for the prediction is close to the region where the effect of the initial perturbation given for initialization is still lingering. Thus, the starting assumption of η at t_0 for case 1 would not be a good initial point for the the prediction using ODE. The flowfield conservative variables represented here are X momentum, density and RhoE respectively. The results of the same are discussed in the appendix A in detail for various points in time similar to what was done for in case 3. A sample at one instance in time for cases 1, 2 and 4 are represented in Figure 5.25, to show the validity of prediction done by through the methods suggested. The evaluation of the errors between the predicted flowfield, using basis type A and basis type B, and the actual URANS flowfield obtained at the same points in time are also evaluated, following method 1 described above.

Using the same methodology, all the conservative variable components of the cases of Ma-α considered can be evaluated. The reconstructed flowfield variables can be then post processed to evaluate parameters like the coefficient of lift (C_L) from the Z momentum component and coefficient of pressure (C_p) from the energy density components. Using the density component of the flowfield, the flow over the aerofoil can be evaluated to predict the shock location motion for the period of prediction, by utilizing the aerodynamic property which ensures of the presence of a sharp density gradient present across the shock location. Locating the position of the density gradient through out different points in time over the suction side of the aerofoil helps us predict the location of the shock too in x/c or chord coordinates. One such example is represented in figure 5.26, where the shock location obtained from the density predictions out of basis type A and basis type b are compared, for a case of Ma=0.71 and α=4.45°. The shock locations are compared or the LCO region of the *validation data*, between 2.93 s - 3.05 s, comprising of 2 cycles of LCO in it. The shock location oscillation appears step-wise in figure 5.26, due the difficultly in resolving very close shock location values taken from density component of the flowfield in neighbouring time steps, owing to the numerical resolution of the density variation over the aerofoil. The NMTE errors for prediction of shock location done by basis type A and basis type B compared to the URANS shock location is represented in table 5.10, indicating a high degree of accuracy of shock prediction.

	NMTE
Basis type A prediction vs URANS	0.013872
Basis type B prediction vs URANS	0.011238

Table 5.10: NMTE values for predictions of shock locations using different basis types compared to the actual locations obtained from the URANS *validation data*

Prediction of Z momentum done at t = 1s for Ma=0.71 at $\alpha = 4.45°$

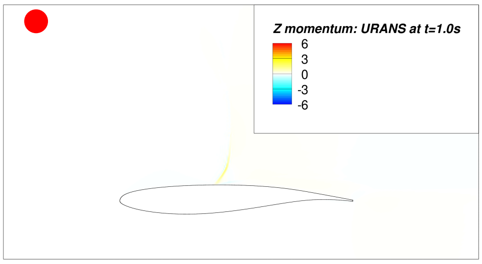

(a) URANS result at t = 1s

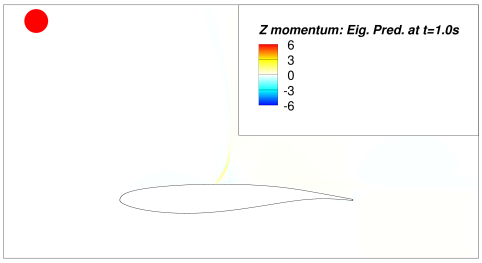

(b) Predicted flowfield using eigen basis, at t = 1s

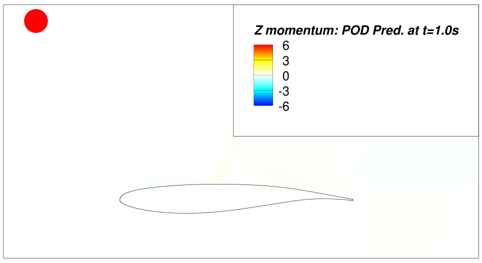

(c) Predicted flowfield using POD basis, at t = 1s

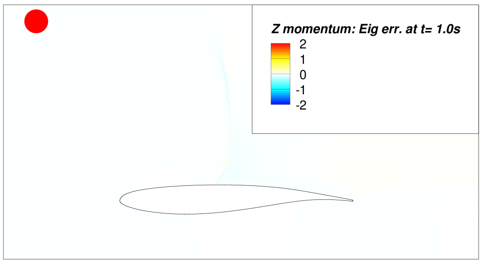

(d) Error between the predicted flowfield using eigen basis and URANS flowfield, at t = 1s

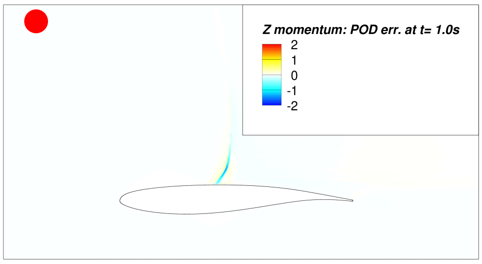

(e) Error between the predicted flowfield using POD basis and URANS flowfield, at t = 1s

Prediction of Z momentum done at t = 2s for Ma=0.71 at $\alpha = 4.45°$

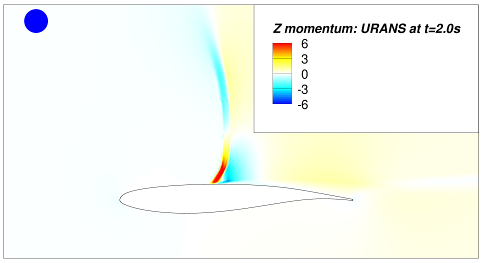

(f) URANS result at t = 2s

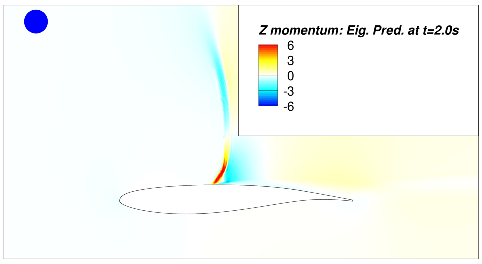

(g) Predicted flowfield using eigen basis, at t = 2s

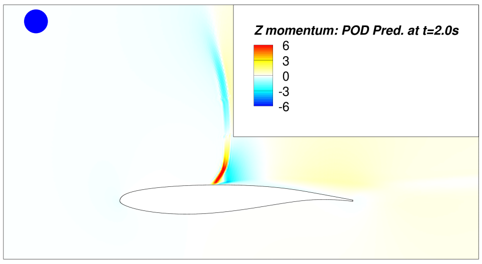

(h) Predicted flowfield using POD basis, at t = 2s

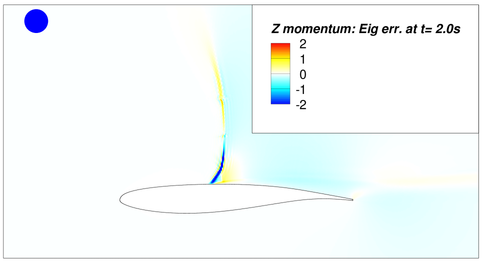

(i) Error between the predicted flowfield using eigen basis and URANS flowfield, at t = 2s

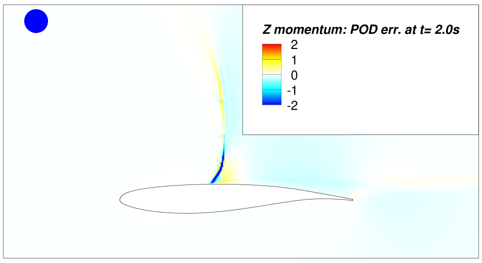

(j) Error between the predicted flowfield using POD basis and URANS flowfield, at t = 2s

Prediction of Z momentum done at t = 3s for Ma=0.71 at $\alpha = 4.45°$

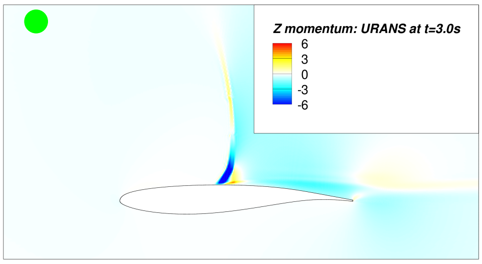

(k) URANS result at t = 3s

(l) Predicted flowfield using eigen basis, at t = 3s

(m) Predicted flowfield using POD basis, at t = 3s

(n) Error between the predicted flowfield using eigen basis and URANS flowfield, at t = 3s

(o) Error between the predicted flowfield using POD basis and URANS flowfield, at t = 3s

Figure 5.23: Predicted Z momentum flowfield done based on ODE for the eigen and POD basis, compared to the actual URANS flowfield at t = 1s, 2s and 3s. The comparison between the URANS flowfield to the predicted flowfields are carried out by the error plots.

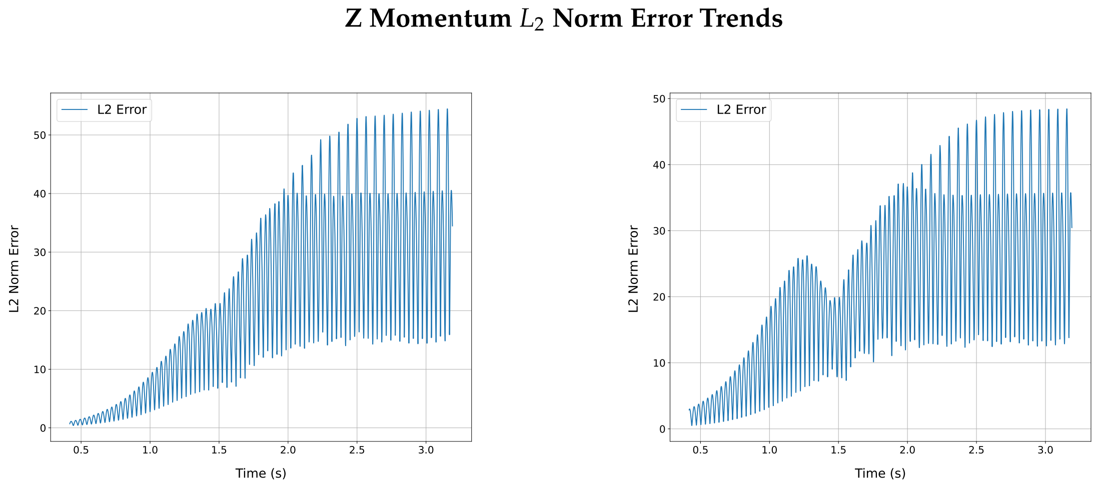

(a) L_2 norm error trend between the predictions based on the eigen basis and the URANS flowfield, of Z momentum. The norm is considered from prediction start point $t = 0.41739$ s, for the case of $Ma = 0.71$, $\alpha = 4.45°$.

(b) L_2 norm error trend between the predictions based on the POD basis and the URANS flowfield, of Z momentum. The norm is considered from prediction start point $t = 0.41739$ s, for the case of $Ma = 0.71$, $\alpha = 4.45°$.

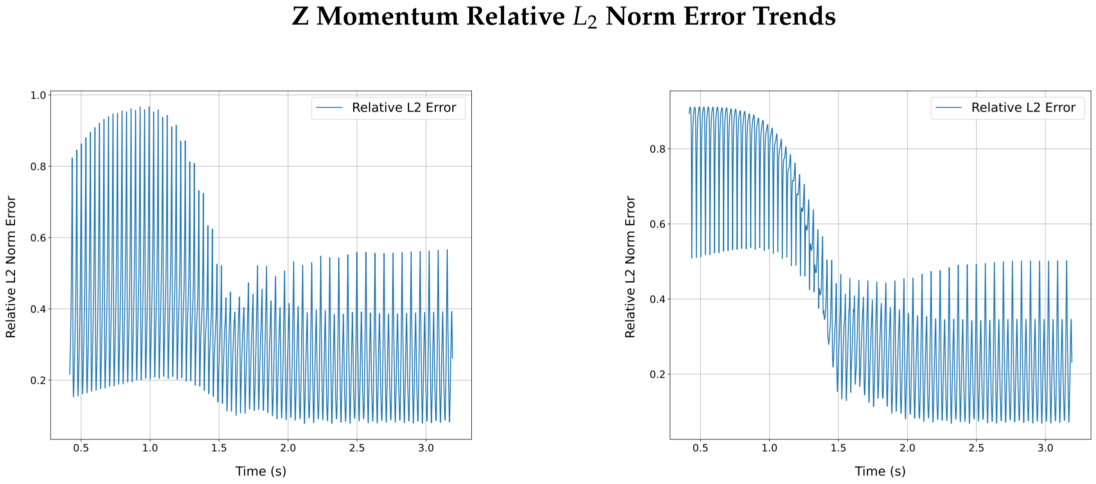

(c) Relative L_2 norm error trend between the predictions based on the eigen basis and the URANS flowfield, of Z momentum. The norm is considered from prediction start point $t = 0.41739$ s, for the case of $Ma = 0.71$, $\alpha = 4.45°$.

(d) Relative L_2 norm error trend between the predictions based on the POD basis and the URANS flowfield, of Z momentum. The norm is considered from prediction start point $t = 0.41739$ s, for the case of $Ma = 0.71$, $\alpha = 4.45°$.

Figure 5.24: Comparison of relative L_2 norm error trends for Z momentum using different bases and methods.

Prediction of RhoE done at t = 2s for Ma=0.71 at $\alpha = 5.25^\circ$

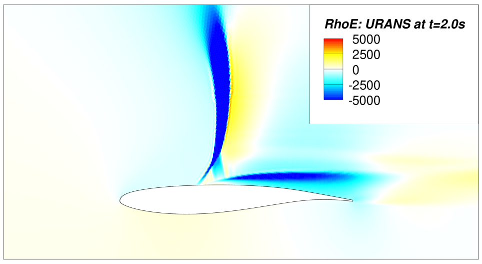

(a) URANS result at t = 2s

(b) Predicted flowfield using eigen basis, at t = 2s

(c) Predicted flowfield using POD basis, at t = 2s

(d) Error between the predicted flowfield using eigen basis and URANS flowfield, at t = 2s

(e) Error between the predicted flowfield using POD basis and URANS flowfield, at t = 2s

Prediction of X momentum done at t = 2.5s for Ma=0.69 at $\alpha = 5^\circ$

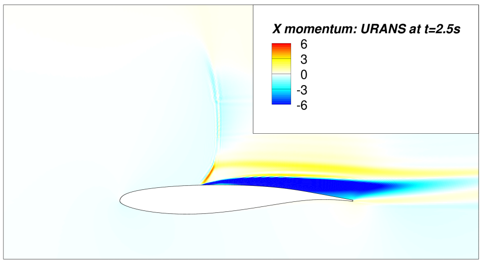

(f) URANS result at t = 2.5s

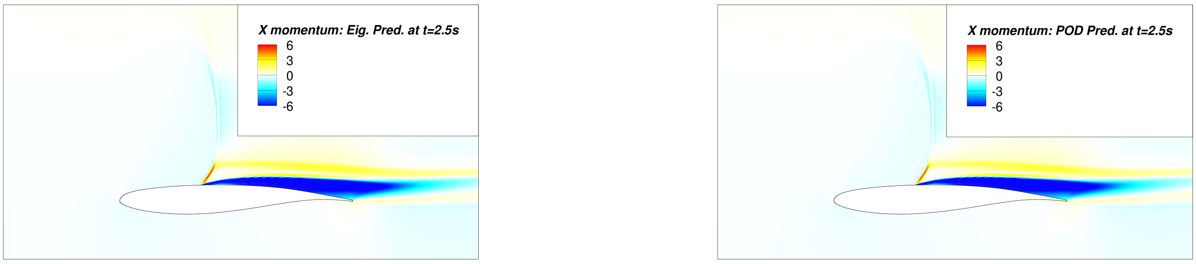

(g) Predicted flowfield using eigen basis, at t = 2.5s

(h) Predicted flowfield using POD basis, at t = 2.5s

(i) Error between the predicted flowfield using eigen basis and URANS flowfield, at t = 2.5s

(j) Error between the predicted flowfield using POD basis and URANS flowfield, at t = 2.5s

Prediction of density done at t = 1.55s for Ma=0.69 at α = 7.25°

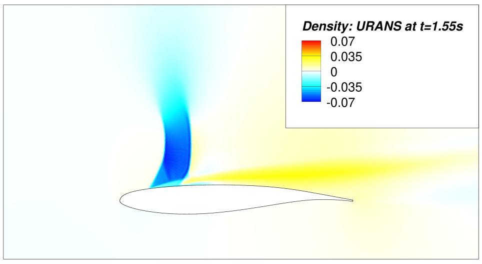

(k) URANS result at t = 1.55s

(l) Predicted flowfield using eigen basis, at t = 1.55s

(m) Predicted flowfield using POD basis, at t = 1.55s

(n) Error between the predicted flowfield using eigen basis and URANS flowfield, at t = 1.55s

(o) Error between the predicted flowfield using POD basis and URANS flowfield, at t = 1.55s

Figure 5.25: Predicted rhoE, X momentum and density flowfield done based on ODE for the eigen and POD basis, compared to the actual URANS flowfield at t = 2s, 2.5s and 1.55s for Ma-α combinations of 0.71 – 4.45°, 0.69 – 5° and 0.69 – 7.25° respectively. The comparison between the URANS flowfield to the predicted flowfields are carried out by the error plots.

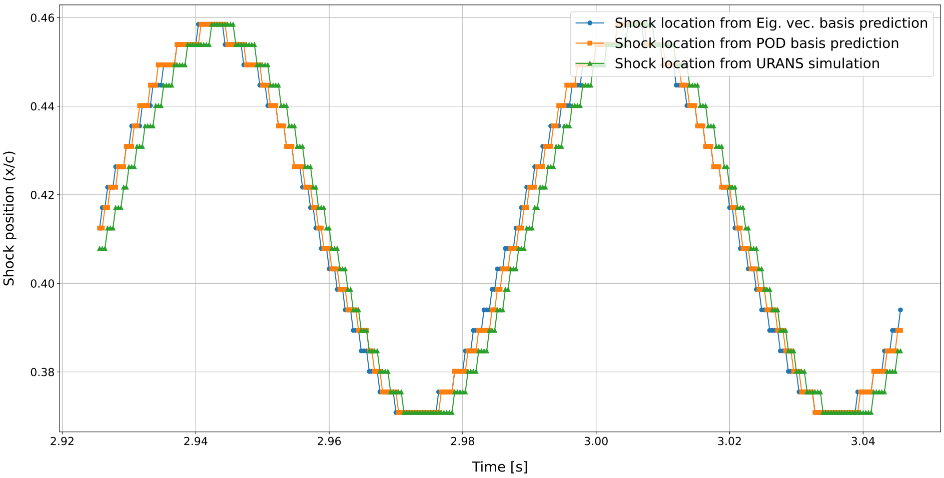

Figure 5.26: The comparison of the predicted shock location through the density flowfield data, reconstructed out of the predicted eta variables with the help of the ODE obtained through linear regression for both basis type A and basis type B, against the density data obtained from the URANS *validation data*. The case considered is case 3: Ma=0.71 and α = 4.45°. The shock location prediction is done between t = 2.93s and t = 3.05s, which are in the LCO region for the case considered. The shock location is obtained through finding the location of the sharpest density gradient along the surface of the aerofoil, which indicates the location of the shock.

5.2.4. Evaluation of the error of prediction and its minimization

During the evaluation of flow reconstruction results obtained in section 5.2.3, it was observed that all reconstructed flowfields exhibited a deviation from the original URANS/unsteady flowfield. This deviation was consistently observed in both the error plots for the flowfield components shown in Figure 5.23 and Figure 5.25, as well as through the evaluation of the absolute and relative L_2 norms between the unsteady URANS and the predicted/reconstructed flowfields for both basis type A and basis type B, as summarized in figure 5.24. The deviation of the predicted flowfields from the URANS unsteady flowfield can be attributed primarily to two sources:

1. Incomplete and improper capture of the dynamics in the $\mathbf{V_1}$ and $\mathbf{V}$ matrices constructed using the SSM embedding methodology described in section 4.4.6, leading to deviations from the actual flowfield.
2. Inaccurate prediction of reduced dynamics in the η coordinates due to limitations in the linear regression and ODE-based approaches.

Evaluation of the manifold using L_2 norm of normal component and remaking the tangent space

To assess the accuracy of capture of dynamics, a representative case with Ma = 0.71 and $\alpha = 4.45°$ was analyzed. For this case, a manifold was constructed by plotting the URANS reduced coordinates of *training data* and *validation data* against the L_2 norm of the normal component of the flow ($\|\mathbf{w}^{\perp}\|$), as discussed in section 4.4.6. This manifold was then compared with the manifold obtained from plotting the URANS reduced coordinates against the L_2 norm of the reconstructed normal component ($\|\mathbf{w_{recon}}\| = \|\mathbf{V}\eta^{\mathbf{2:M}}\|$). Comparisons were performed for both basis type A and basis type B, excluding the shift mode, as illustrated in figure 5.27. For both basis types, the reduced coordinates (η) in conjunction with the normal component of the flow yield a conical manifold. According to the theory of SSM embedding [14, 32], such a manifold should exhibit tangency to $\mathcal{T}_\mathbf{0}\mathcal{M}_\mathbf{0}$. However, the manifolds constructed using the URANS reduced coordinates for both basis types do not exhibit this tangency, whereas the manifolds using the reconstructed normal component, $\mathbf{V}\eta^{\mathbf{2:M}}$, do. This difference is further highlighted in the cross-sections at $\eta_2 = 0$ shown in figure 5.27b and figure 5.27d.

The absence of tangency in the URANS-$\|\mathbf{w}^{\perp}\|$ manifold is attributed to improper splitting of the total unsteady URANS flowfield ($\mathbf{w}'$) into tangential and normal components. The principal cause is the inaccuracy of the extracted eigenmodes for basis type A and POD modes for basis type B, which are used to define the tangent space $\mathcal{T}_\mathbf{0}\mathcal{M}_\mathbf{0}$. The extracted modes do not perfectly span the tangent plane, resulting in improper decomposition when constructing reduced coordinates and splitting the flowfield. To address this, the current tangent plane for both basis types is corrected as follows:

Step 1: Redefine the reduced coordinates as $\eta \in \mathbb{R}^2$ for a point $\mathbf{w}' \in \mathcal{M}_0$ using the orthogonal projection:

$$\eta = \mathbf{U}_1^T \mathbf{w}' \tag{5.20}$$

where $\mathbf{U}_1$ comprises the orthonormalized real and imaginary components of the global mode (for basis type A) or orthonormalized POD modes (for basis type B).

Step 2: Redefine the unsteady flowfield as

$$\mathbf{w}' = \mathbf{U}_1\eta + \mathbf{V}\eta^{1:M} \tag{5.21}$$

with the constraint $\mathbf{V}^T\mathbf{U}_1 = \mathbf{0}$, where $\mathbf{V} = \mathbf{U}_1$. The second term in equation (5.21) models the manifold's component normal to the $\mathbf{U}_1$ plane, with $\mathbf{V}$ containing coefficients for both linear and non-linear monomials. This approach allows for linear parts in the normal component, implying the plane may not be a perfect tangent plane.

Step 3: Solve for $\mathbf{V}$ by minimizing the residual, as previously described in section 4.4.6:

$$\mathbf{V}^* = \mathrm{argmin}_{\mathbf{V}} \sum_{j=1}^{P} ||\mathbf{w}'^{\perp}_j - \mathbf{V}\eta_j^{1:M}||^2 \tag{5.22}$$

where $\mathbf{w}'^{\perp}_j = \mathbf{w}'_j - \mathbf{U}_1\mathbf{U}_1^T\mathbf{w}'_j$ and $\eta_j^{1:M} = \mathbf{U}_1^T\mathbf{w}_j^{1:M}$.

Step 4: Update the tangent plane by constructing $\mathbf{U}_{1new} = \mathbf{U}_1 + [\mathbf{V}^{10}, \mathbf{V}^{01}]$, where $\mathbf{V}^{10}, \mathbf{V}^{01}$ are the first two columns of $\mathbf{V}$ representing the linear coefficients of η_1 and η_2. Orthonormalize the columns of $\mathbf{U}_{1new}$ and set as the new $\mathbf{U}_1$ for the next iteration.

Step 5: Repeat steps 1–4 until the L_2 norms of the first two columns of $\mathbf{V}$ $(\mathbf{V}^{10}, \mathbf{V}^{01})$ converge below a specified threshold, or a maximum number of iterations is reached.

Step 6: Upon convergence, the final $\mathbf{U}_1$ vector, denoted as $\mathbf{U}_1^f$, is used to construct the final $\mathbf{V}$ containing only the coefficients of the non-linear terms, following the methodology in section 4.4.6. The resulting $\mathbf{U}_1$ vectors are referred to as the initial remade basis type A and initial remade basis type B, respectively.

With the new set of reduced coordinates obtained by projecting the URANS *training* and *validation data* onto $\mathbf{U}_1^f$, the URANS-$\|\mathbf{w}^{\perp}\|$ and URANS-$\|\mathbf{w_{recon}}\|$ manifolds can be compared again in terms of tangency to the new tangent space $\mathcal{T}_0'\mathcal{M}_0'$ defined by $\mathbf{U}_1^{final}$. As shown in figure 5.28, both manifolds for initial remade basis type A and B exhibit strong overlap and tangency to the new tangent space, indicating that $\mathcal{T}_0'\mathcal{M}_0'$ is appropriately defined.

Examination of the cross-sections in figure 5.28c and figure 5.28d, particularly in the region near the base flow $(-150 < \eta < 150)$, reveals a pulse-shaped bulge at the bottom of the URANS-$\|\mathbf{w}^{\perp}\|$ manifold. This feature results from the initial perturbation applied in the URANS *training* and *validation* data, causing a lack of overlap between the URANS-$\|\mathbf{w}^{\perp}\|$ and URANS-$\|\mathbf{w_{recon}}\|$ manifolds within the range $-100 < \eta < 100$. Because the initial remade basis types are constructed from the complete URANS flow, including the base flow, this pulse effect hinders perfect overlap and thus limits the ability to accurately capture the linear and non-linear dynamics coefficients in $\mathbf{V}_1$ and $\mathbf{V}$.

Ma = 0.71, $\alpha = 4.45°$	for all η	for $\lvert\eta\rvert > 100$
NMTE for reconstructed **Basis type A**	0.0255	0.019671
NMTE for reconstructed **Basis type B**	0.02734	0.01984

Table 5.11: NMTE values between the cross section of the manifolds made through URANS projections and remade flowfield projections onto different remade basis types for Ma = 0.71, $\alpha = 4.45°$.

To address this issue, the remaking process is repeated for three additional iterations, starting from $\mathbf{U}_1^f$, but restricted to flowfields with $|\eta| > 100$ to exclude the base flow region affected by the pulse. The final remade vector obtained from this process is denoted as $\mathbf{U}_1 = \mathbf{U}_1^{final}$. The resulting $\mathbf{U}_1$ vectors are referred to as the final remade basis type A and final remade basis type B, respectively. Using this new basis definition for both basis types, the reduced coordinates (η), $\mathbf{V}_1$, and $\mathbf{V}$ are reconstructed according to the methodology in section 4.4.6. The intention is that the new $\mathbf{V}_1$ and $\mathbf{V}$ will enable accurate reconstruction of all flowfields of $|\eta| > 100$ for the *validation data*, based on the assumption that the URANS-$\|\mathbf{w}^{\perp}\|$ manifold for $|\eta| > 100$ is smooth and extrapolation to $|\eta| < 100$ is expected to produce tangency at $\mathbf{w}' = \eta = 0$. The Taylor series expansion used for $\mathbf{V}$ supports this extrapolation, facilitating a better overlap between the URANS-$\|\mathbf{w_{recon}}\|$ and the trimmed URANS-$\|\mathbf{w}^{\perp}\|$ manifolds.

Finally, the URANS-$\|\mathbf{w}^{\perp}\|$ and URANS-$\|\mathbf{w_{recon}}\|$ manifolds are constructed again, with the URANS-$\|\mathbf{w}^{\perp}\|$ manifold built for $|\eta| > 100$ (*training data*) and the URANS-$\|\mathbf{w_{recon}}\|$ manifold made for the full η range (*validation data*). These η-trimmed manifolds are compared in figure 5.29. As indicated by the NMTE values in Table 5.11, the manifolds made for $|\eta| > 100$ exhibit improved overlap after remaking of the basis, compared to manifolds that include all η values. Consequently, all further predictions are based on the $|\eta| > 100$ range.

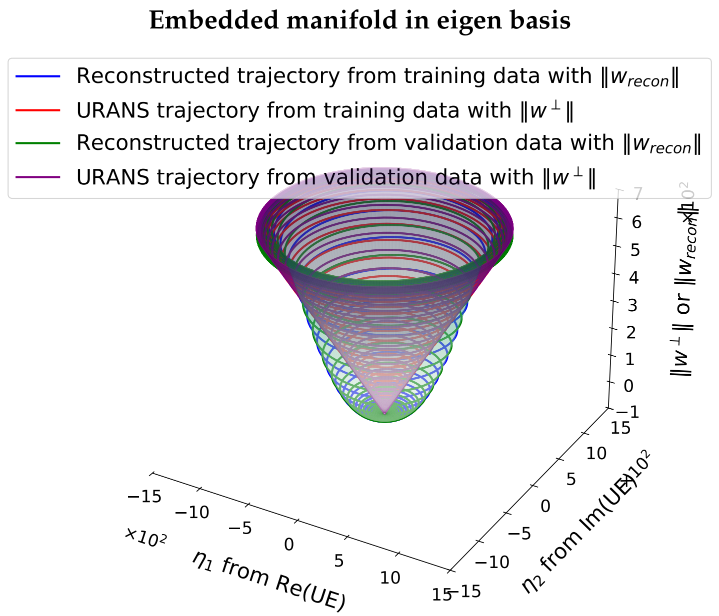

(a) 3D embedded manifold of the URANS *training data* and *validation data* for Ma=0.71 - α = 4.45° constructed with the eigen basis compared with the , manifold obtained through trajectories from projection of the reconstructed flowfield data onto the eigen basis without the shift mode, plotted against the L_2 norm of the normal component of the URANS field and the reconstructed flowfield.

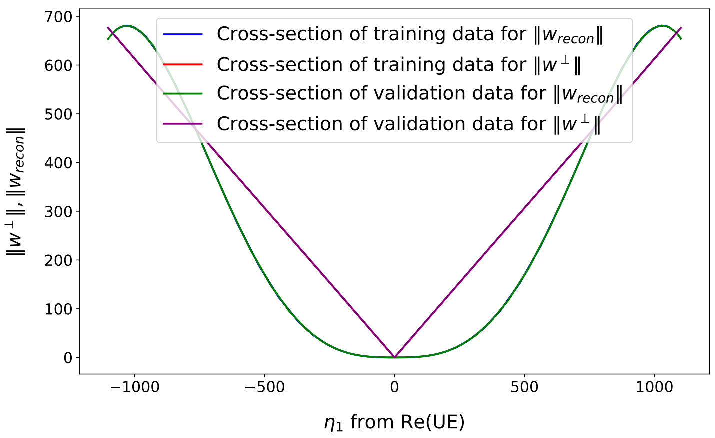

(b) Cross section of the 3D embedded manifold of the URANS *training data* and *validation data* and their reconstructed flowfields, for Ma=0.71 - α = 4.45° constructed with the eigen basis without the shift mode and the L_2 norm of the normal component of the URANS field and the reconstructed flowfield.

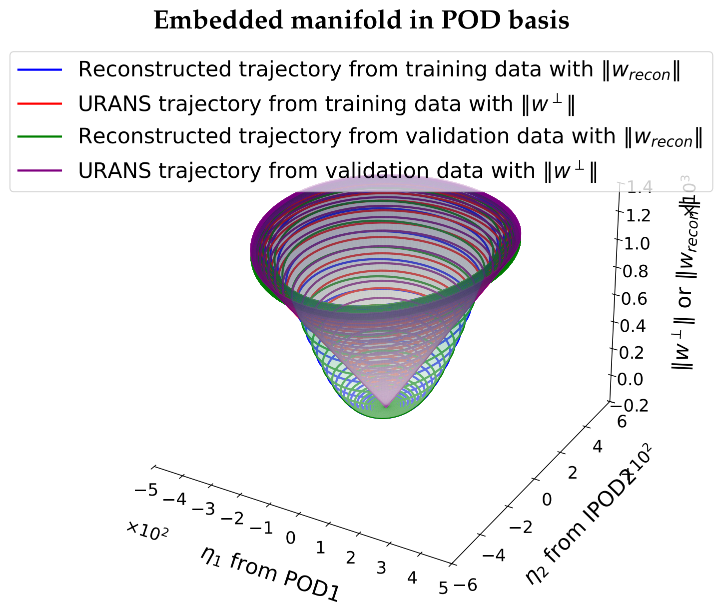

(c) 3D embedded manifold of the URANS *training data* and *validation data* for Ma=0.71 - α = 4.45° constructed with the POD basis compared with the , manifold obtained through trajectories from projection of the reconstructed flowfield data onto the POD basis without the shift mode, plotted against the L_2 norm of the normal component of the URANS field and the reconstructed flowfield.

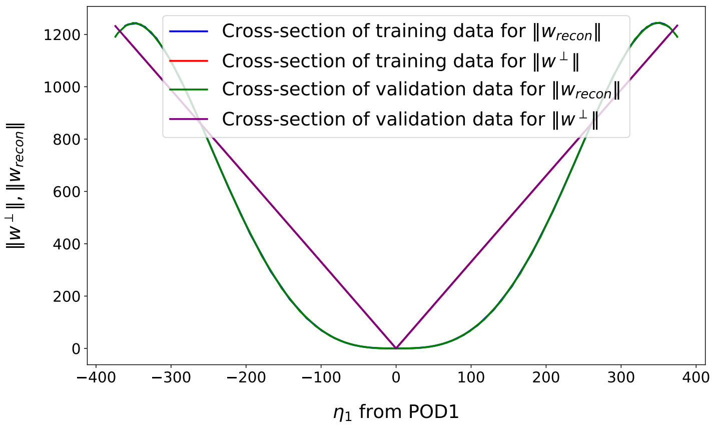

(d) Cross section of the 3D embedded manifold of the URANS *training data* and *validation data* and their reconstructed flowfields, for Ma=0.71 - α = 4.45° constructed with the POD basis without the shift mode and the L_2 norm of the normal component of the URANS field and the reconstructed flowfield.

Figure 5.27: Embedded manifolds of the URANS *training data* and *validation data* and the trajectories and manifolds of the reconstructed data constructed using eigen and POD basis without the shift mode plotted against the L_2 norm of the normal component of the URANS field and the reconstructed flowfield, along with comparison of the cross section of their manifolds: $Ma = 0.71$ at $\alpha = 4.45°$

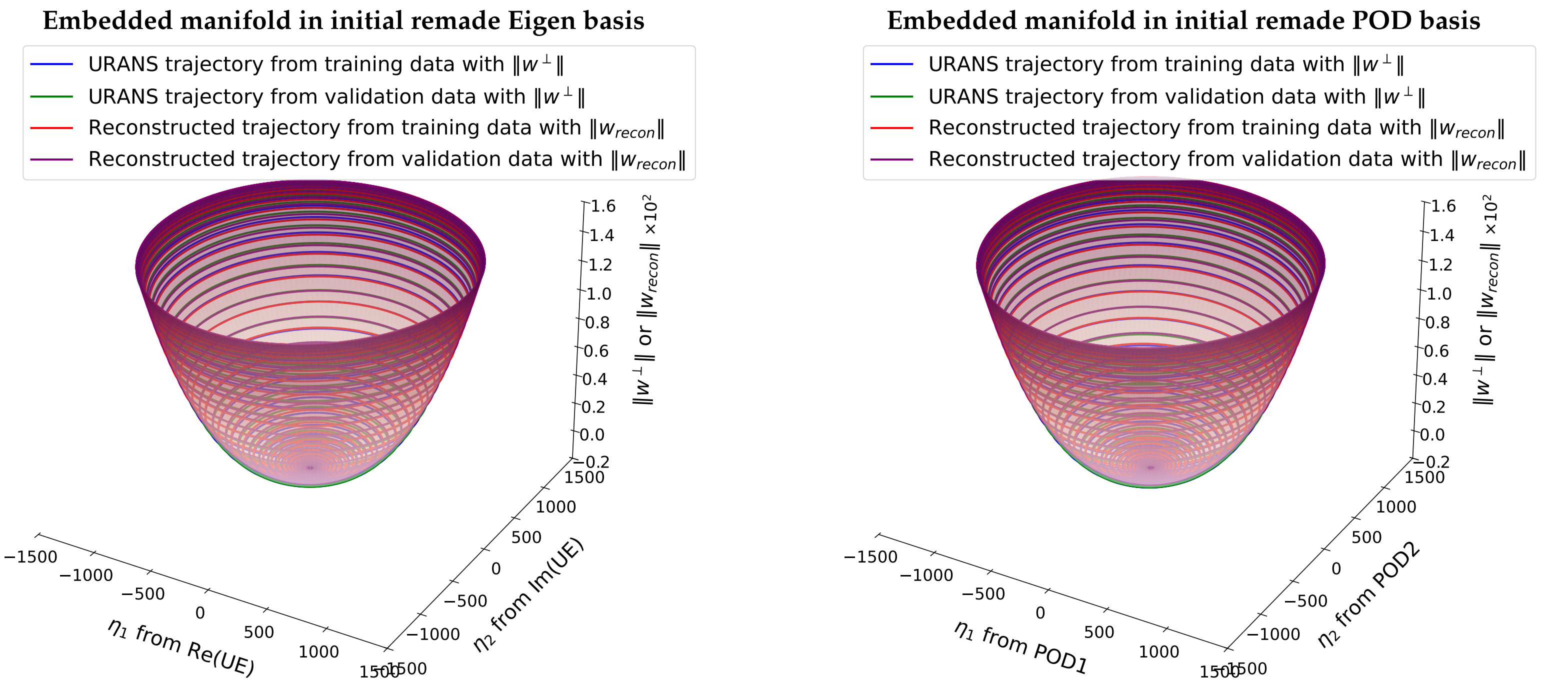

(a) 3D embedded manifold of the URANS *training data* and *validation data* for Ma=0.71 - α = 4.45° constructed with the initial remade eigen basis/basis type A compared with the, manifold obtained through trajectories from projection of the reconstructed flowfield data onto the remade eigen basis/basis type A, plotted against the L_2 norm of the normal component of the URANS field and the reconstructed flowfield.

(b) 3D embedded manifold of the URANS *training data* and *validation data* for Ma=0.71 - α = 4.45° constructed with the initial remade POD basis/basis type B compared with the, manifold obtained through trajectories from projection of the reconstructed flowfield data onto the remade POD basis/basis type B, plotted against the L_2 norm of the normal component of the URANS field and the reconstructed flowfield.

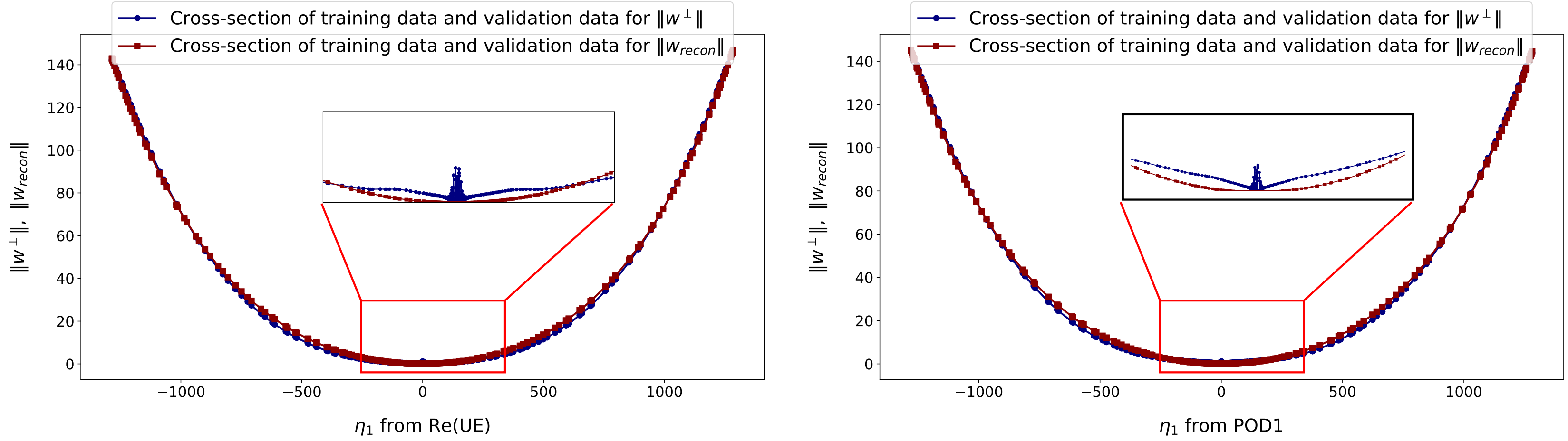

(c) Cross section of the 3D embedded manifold of the URANS *training data* and *validation data* and their reconstructed flowfields, for Ma=0.71 - α = 4.45° constructed with the initial remade eigen basis/basis type A and the L_2 norm of the normal component of the URANS field and the reconstructed flowfield. A zoomed in region close to the base flow between -100<η<100 is shown as an internal image.

(d) Cross section of the 3D embedded manifold of the URANS *training data* and *validation data* and their reconstructed flowfields, for Ma=0.71 - α = 4.45° constructed with the initial remade POD basis/basis type B and the L_2 norm of the normal component of the URANS field and the reconstructed flowfield. A zoomed in region close to the base flow between -100<η<100 is shown as an internal image.

Figure 5.28: Comparison of embedded manifolds of the URANS data against the L_2 norm of the normal component of the URANS field and the reconstructed flowfield and their cross-sections (with zoomed-in regions) for Ma=0.71, α = 4.45° using initial remade eigen and POD bases.

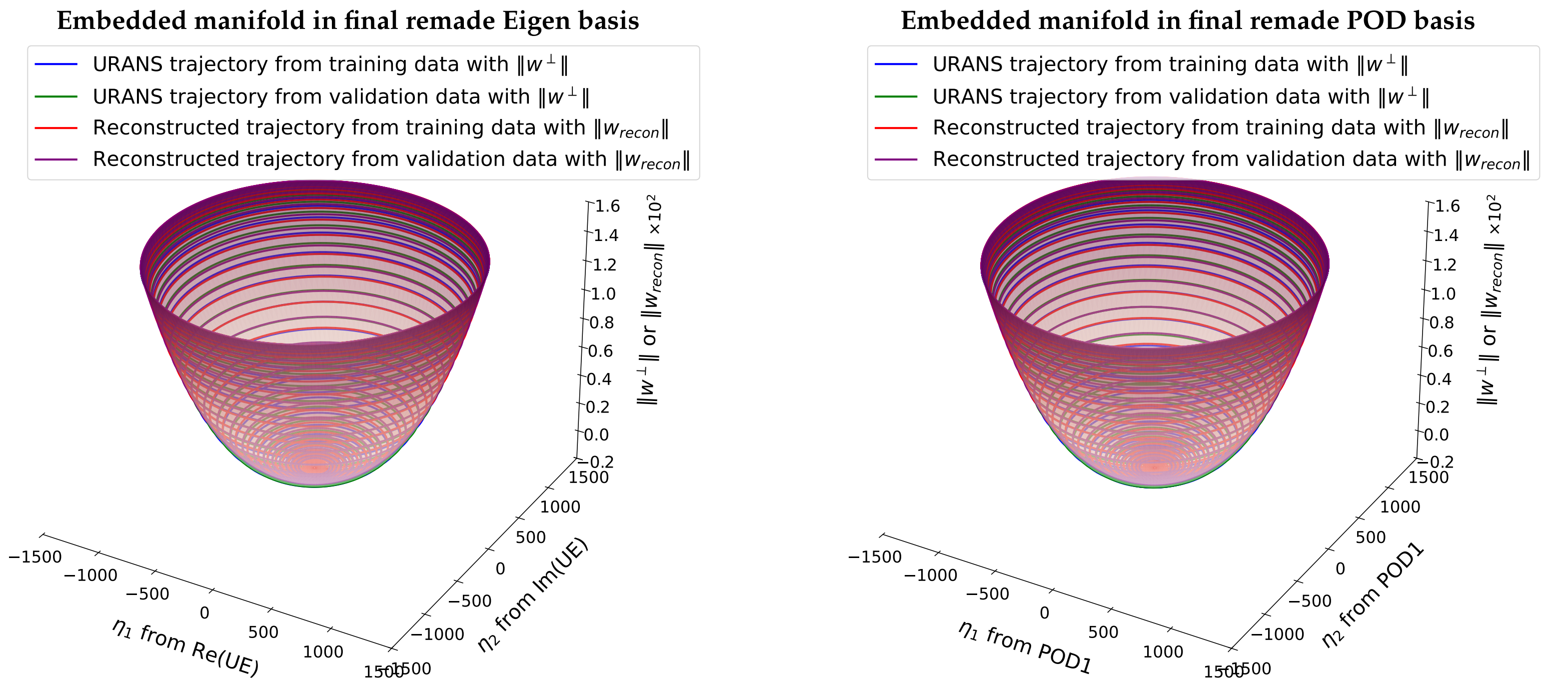

(a) 3D embedded manifold of the URANS *training data* and *validation data* for Ma=0.71 - α = 4.45° constructed with the final remade eigen basis/basis type A beyond $\eta > 100$, compared with the manifold obtained through trajectories from projection of the reconstructed flowfield data onto the remade eigen basis/basis type A, plotted against the L_2 norm of the normal component of the URANS field and the reconstructed flowfield.

(b) 3D embedded manifold of the URANS *training data* and *validation data* for Ma=0.71 - α = 4.45° constructed with the final remade POD basis/basis type B beyond $\eta > 100$, compared with the manifold obtained through trajectories from projection of the reconstructed flowfield data onto the remade POD basis/basis type B, plotted against the L_2 norm of the normal component of the URANS field and the reconstructed flowfield.

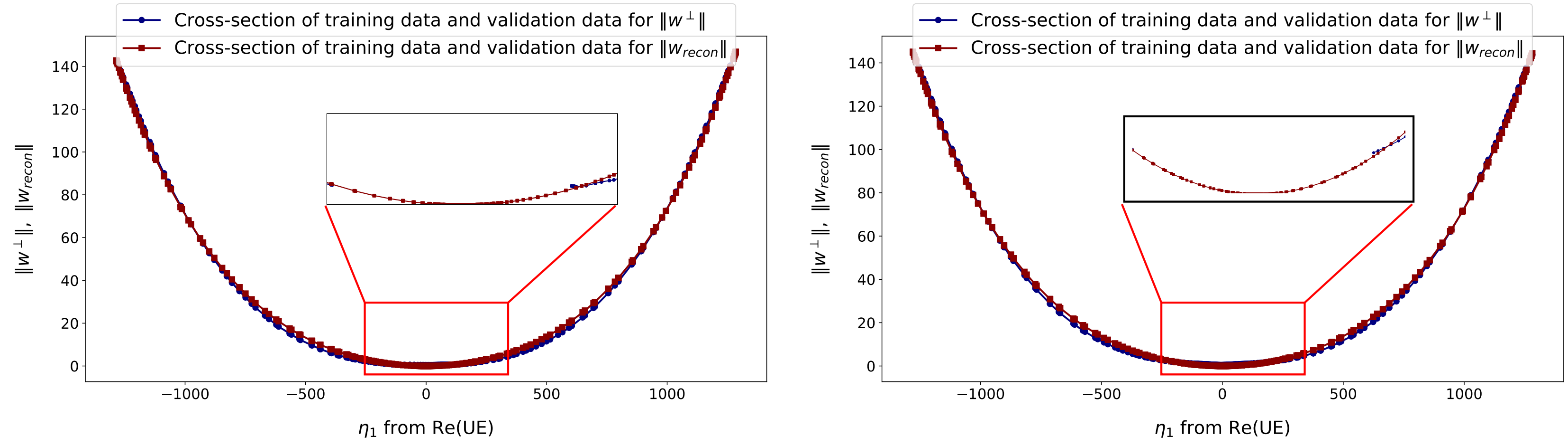

(c) Cross section of the 3D embedded manifold of the URANS *training data* and *validation data* and their reconstructed flowfields, for Ma=0.71 - α = 4.45° constructed with the final remade eigen basis/basis type A beyond $\eta > 100$, and the L_2 norm of the normal component of the URANS field and the reconstructed flowfield. A zoomed in region close to the base flow between -100<η<100 is shown as an internal image.

(d) Cross section of the 3D embedded manifold of the URANS *training data* and *validation data* and their reconstructed flowfields, for Ma=0.71 - α = 4.45° constructed with the final remade POD basis/basis type B beyond $\eta > 100$, and the L_2 norm of the normal component of the URANS field and the reconstructed flowfield. A zoomed in region close to the base flow between -100<η<100 is shown as an internal image.

Figure 5.29: Comparison of embedded manifolds of the URANS data against the L_2 norm of the normal component of the URANS field beyond $\eta > 100$, and the reconstructed flowfield and their cross-sections (with zoomed-in regions) for Ma=0.71, α = 4.45° using final remade eigen and POD bases.

New ODE constructed and used for prediction of validation data

After the definition of the final remade basis vector $\mathbf{U}_1 = \mathbf{U}_1^{final}$ for both the basis types, reduced coordinates (η) of the *training data* can be made through its projection of the flowfield onto $\mathbf{U}_1$. This results in the time varying $\eta = [\eta_1, \eta_2]$, which can be described by an ODE using linear regression as defined in section 4.4.7. This results in the new ODE for the final remade basis. Here for the final remade basis type A where $|\eta| > 100$ was considered the ODE defined are,

$$\begin{aligned}\frac{d\eta_1}{dt} = & -1.8515\times10^{-6}\,\eta_1^3 - 9.1928\times10^{-8}\,\eta_1^2\eta_2 - 5.3973\times10^{-5}\,\eta_1^2 - 1.8873\times10^{-6}\,\eta_1\eta_2^2 \\ & - 5.1953\times10^{-5}\,\eta_1\eta_2 + 3.1336\,\eta_1 - 7.9531\times10^{-8}\,\eta_2^3 + 4.7125\times10^{-5}\,\eta_2^2 + 96.6479\,\eta_2\end{aligned} \tag{5.23}$$

$$\begin{aligned}\frac{d\eta_2}{dt} = & -1.17699\times10^{-7}\,\eta_1^3 - 1.7936\times10^{-6}\,\eta_1^2\eta_2 + 7.5263\times10^{-6}\,\eta_1^2 - 1.4537\times10^{-7}\,\eta_1\eta_2^2 \\ & - 1.4062\times10^{-4}\,\eta_1\eta_2 - 95.2275\,\eta_1 - 1.8264\times10^{-6}\,\eta_2^3 - 6.9892\times10^{-6}\,\eta_2^2 + 2.9165\,\eta_2\end{aligned} \tag{5.24}$$

and for the final reconstructed basis type B, seen in figure 5.18c the governing ODE are,

$$\begin{aligned}\frac{d\eta_1}{dt} = & -1.7317\times10^{-6}\,\eta_1^3 - 5.8785\times10^{-8}\,\eta_1^2\eta_2 + 3.0588\times10^{-5}\,\eta_1^2 - 1.7430\times10^{-6}\,\eta_1\eta_2^2 \\ & - 9.4123\times10^{-5}\,\eta_1\eta_2 + 2.3182\,\eta_1 - 2.6730\times10^{-8}\,\eta_2^3 - 2.6174\times10^{-5}\,\eta_2^2 - 95.8094\,\eta_2\end{aligned} \tag{5.25}$$

$$\begin{aligned}\frac{d\eta_2}{dt} = & \,1.8722\times10^{-8}\,\eta_1^3 - 1.9410\times10^{-6}\,\eta_1^2\eta_2 + 6.7995\times10^{-5}\,\eta_1^2 - 2.7196\times10^{-8}\,\eta_1\eta_2^2 \\ & + 2.9517\times10^{-5}\,\eta_1\eta_2 + 96.0661\,\eta_1 - 1.9453\times10^{-6}\,\eta_2^3 - 7.3257\times10^{-5}\,\eta_2^2 + 3.7319\,\eta_2\end{aligned} \tag{5.26}$$

These ODE made for the *training data* for the final remade basis are represented in figure 5.30a and figure 5.30b. These ODE's are then used with forward Euler integration as discussed previously in section 5.2.3 to give the prediction of the *validation data* from a point $\eta = 100$, which here for the case of Ma=0.71, $\alpha = 4.45°$ correspond to a point at $t = 1.23$s from the start of *validation data*. Now for the predicted values of η for the *validation data*, the reconstruction of the flowfield using equation (4.13) with the $\mathbf{V_1}$ and $\mathbf{V}$ matrices obtained after the final reconstruction. The points at which the predicted flowfield obtained from the use of the final remade basis type A and final remade basis type B are represented in figure 5.31, where the points in time $t = 1.23$s, 2s and 3s were considered, represented as red, blue and green circles on the plot.

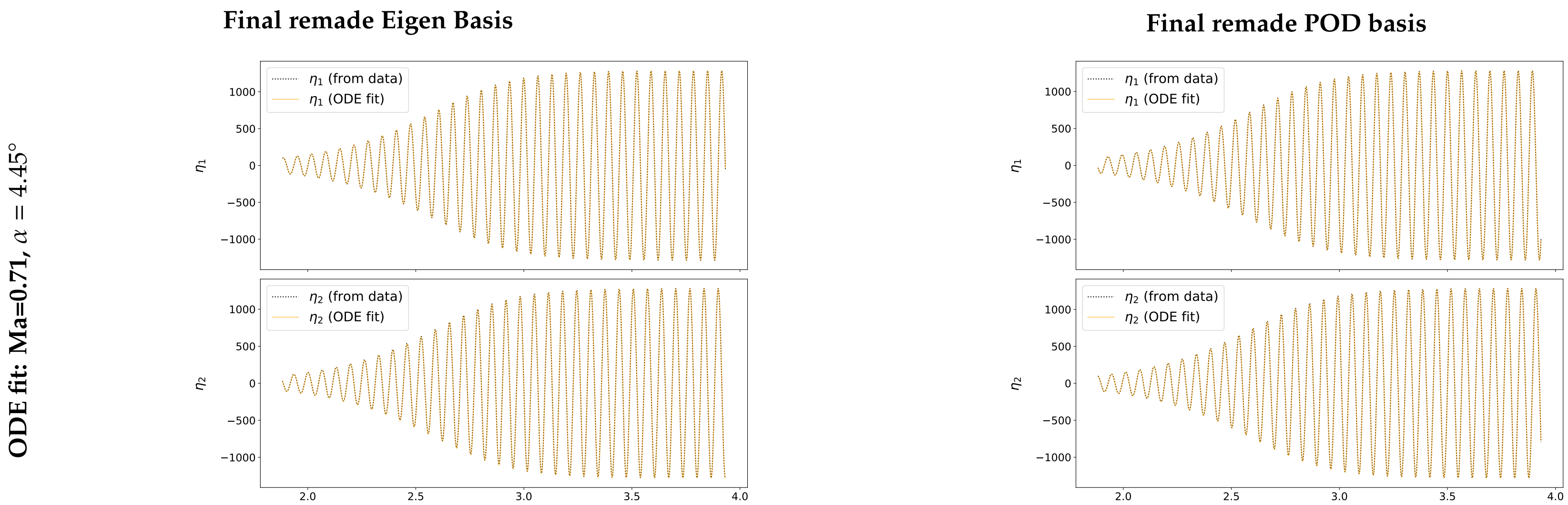

(a) ODE fit for the *training data* in η_1 and η_2 for: Ma=0.71, $\alpha = 4.45°$ in the final remade eigen basis/ final remade basis type A, from $t_0 = 1.23s$.

(b) ODE fit for the *training data* in η_1 and η_2 for: Ma=0.71, $\alpha = 4.45°$ in the final remade POD basis/ final remade basis type B, from $t_0 = 1.23s$.

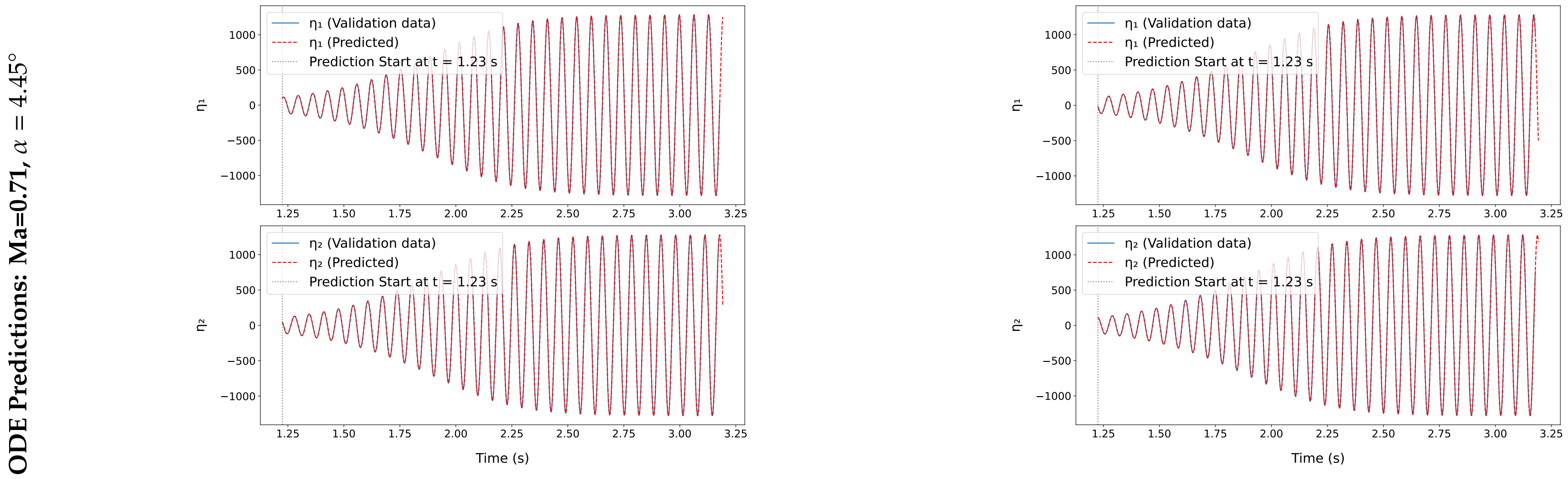

(c) Prediction for the *validation data* in η_1 and η_2 for: Ma=0.71, $\alpha = 4.45°$ in the final remade eigen basis/ final remade basis type A, from $t_0 = 1.23s$.

(d) Prediction for the *validation data* in η_1 and η_2 for: Ma=0.71, $\alpha = 5.25°$ in the final remade POD basis/ final remade basis type B, from $t_0 = 1.23s$.

Figure 5.30: Images depicting ODE fit and prediction for the *training data* in the reduced coordinates, for Ma=0.71 $\alpha = 4.45°$ for the final remade basis's for $|\eta| > 100$. Columns are remade basis type, and rows are the ODE fit for *training data* and prediction of *validation data* from a time t_0.

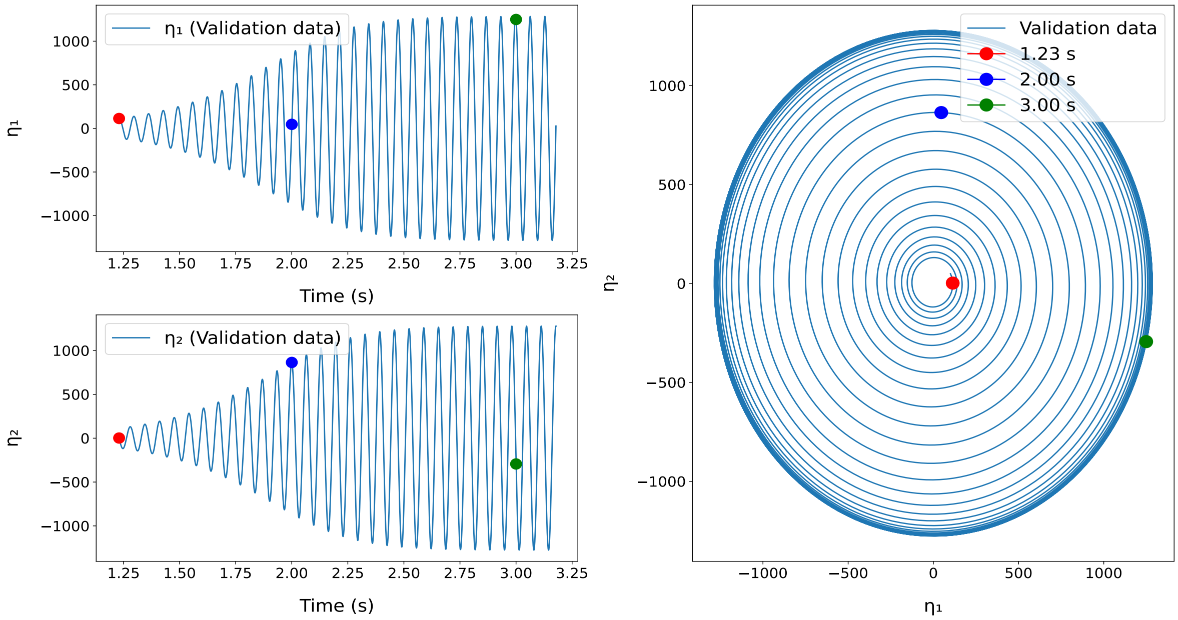

(a) Points in time t = 1.23s, 2s and 3s considered for Ma 0.71, α = 4.45° flowfield reconstruction, marked on the reduced coordinate plots on final remade basis type A for the *validation data*

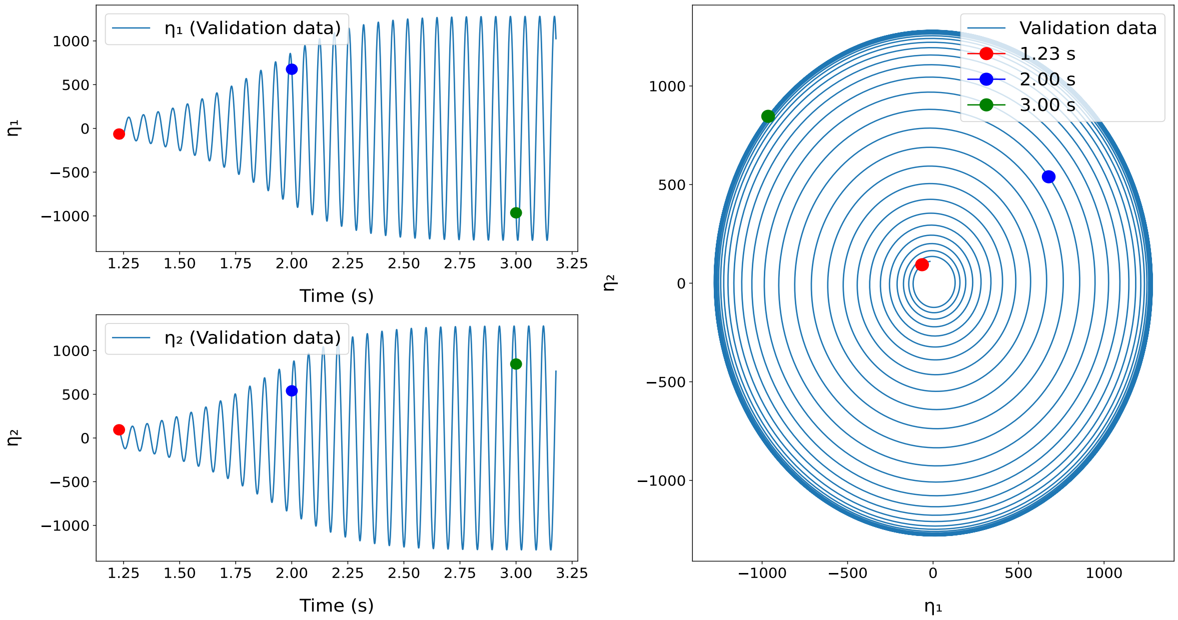

(b) Points in time t = 1.23s, 2s and 3s considered for Ma 0.71, α = 4.45° flowfield reconstruction, marked on the reduced coordinate plots on final remade basis type B for the *validation data*

Figure 5.31: Points in time t = 1.23s, 2s and 3s considered for Ma 0.71, α = 4.45° flowfield reconstruction, marked on the reduced coordinate plots on final remade basis type A and final remade basis type B, for the *validation data*

Prediction of validation data flowfields using the final remade basis vectors

Using the predicted reduced coordinates η obtained, denoted in figure 5.30c and figure 5.30d, the Z momentum component of the flowfields are reconstructed at times t = 1.23s, 2s and 3s. The predicted Z momentum component of the flowfield using the final remade basis type A and final reconstructed basis type B are compared against the actual unsteady URANS flowfield of the *validation data* for each point in time considered. An error flowfield plot previously discussed as method 1 of error evaluation, in section 5.2.3, is considered and are also plotted to visualize the location of error for the flowfield reconstruction. The times t = 1.23s, 2s and 3s are represented as red, blue and green circles on the flowfield plots as depicted in figure 5.32.

Compared to the error of prediction obtained in section 5.2.3 for the same case (case 3), it can be seen that the error of prediction has become significantly better, indicated by the maxima and minima of the error in the error plots in figure 5.32 compared to the error plots in figure 5.23. These comparisons can be carried out only for the prediction times of t = 2s and 3s as due to the start time being different in the case of the predictions done for the final remade basis (t = 1.23s). The shock foot still appears to be the region where error of reconstruction in concentrated for all the time points considered.

Using the method 2 of error evaluation discussed in section 5.2.3, absolute and relative L_2 norm of the difference of the predicted flowfield and URANS flowfield is found for both the final remade basis and is represented in figure 5.33. Comparing from $t = 1.23s$ time mark in the result previously obtained in figure 5.24, it can be clearly seen that in figure 5.33 are lower by a factor of 1-10 for the absolute L_2 norm and 0.55-0.7 points lower for the relative L_2 norm. It is also interesting to see that in contrast to an increasing trend of absolute L_2 norm as observed in the case of both basis type A and basis type B in figure 5.24, for the final remade basis's an almost generally decreasing trend is observed. This indicates a very good prediction and reconstruction of the flowfield close to the LCO region relative to the region of start of prediction.

As previously stated in section 5.2.3, the predicted flowfield components can further be post processed into non-dimensional components like coefficient of lift (C_L) from the Z momentum component or coefficient of pressure (C_p) from the energy density component. Similar to what was depicted in figure 5.26, the shock location can be predicted using the new density component of the flowfield projections obtained from the use of final remade basis's. The shock location, is evaluated as the position of sharpest density gradient along the surface of the aerofoil and the comparison between the shock location obtained from the density component of the unsteady URANS *validation data*, against the final remade basis type A prediction and the final remade basis type B are represented in figure 5.34. This comparison, similar to the one indicated in figure 5.26, is evaluated in the LCO region, between 2.93 s - 3.05 s, comprising of 2 cycles of LCO in it. The NMTE errors for the predicted shock location path from the final remade basis type A and B are compared to the URANS shock location are represented in table 5.12. Compared to the predictions done in section 5.2.3, represented in table 5.10, this new shock location prediction is even more accurate, with a better match in the phase of oscillation compared to the previous prediction, where an offset could be visibly observed.

	NMTE
Remade Basis type A prediction vs URANS	0.005637
Remade Basis type B prediction vs URANS	0.005634

Table 5.12: NMTE values for predictions of shock locations using different final remade basis types compared to the actual locations obtained from the URANS *validation data*

Prediction of Z momentum done at t = 1.23s for Ma=0.71 at α = 4.45°

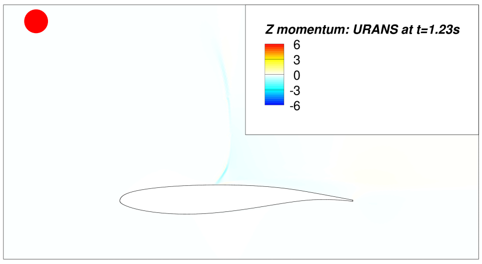

(a) URANS result at t = 1.23s

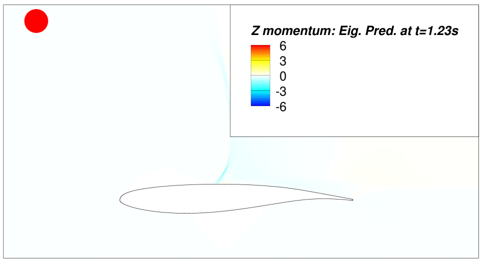

(b) Predicted flowfield using final remade eigen basis, at t = 1.23s

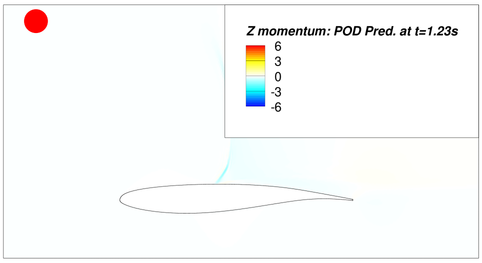

(c) Predicted flowfield using final remade POD basis, at t = 1s

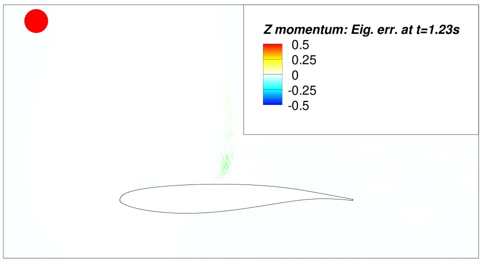

(d) Error between the predicted flowfield using final remade eigen basis and URANS flowfield, at t = 1s

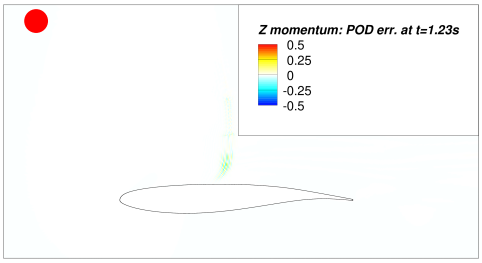

(e) Error between the predicted flowfield using final remade POD basis and URANS flowfield, at t = 1s

Prediction of Z momentum done at t = 2s for Ma=0.71 at α = 4.45°

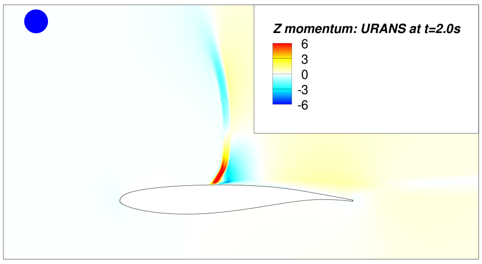

(f) URANS result at t = 2s

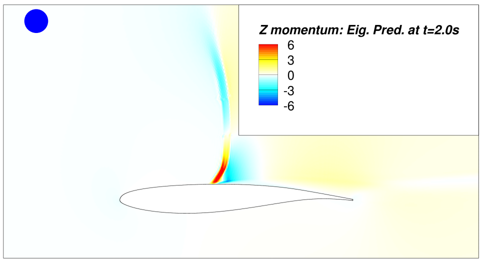

(g) Predicted flowfield using final remade eigen basis, at t = 2s

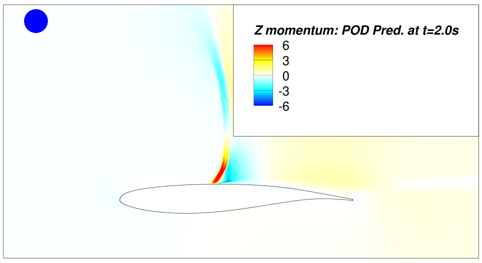

(h) Predicted flowfield using final remade POD basis, at t = 2s

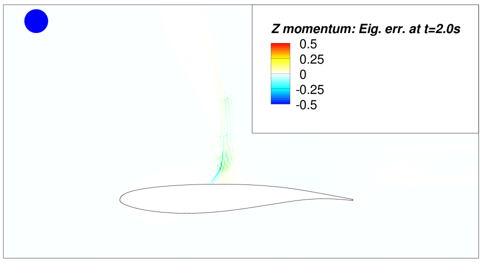

(i) Error between the predicted flowfield using final remade eigen basis and URANS flowfield, at t = 2s

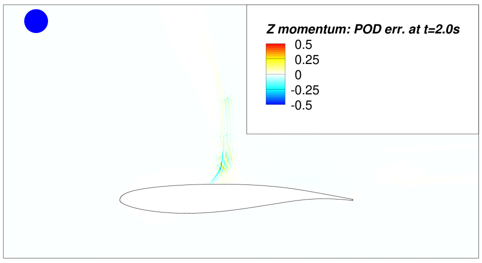

(j) Error between the predicted flowfield using final remade POD basis and URANS flowfield, at t = 2s

Prediction of Z momentum done at t = 3s for Ma=0.71 at $\alpha = 4.45°$

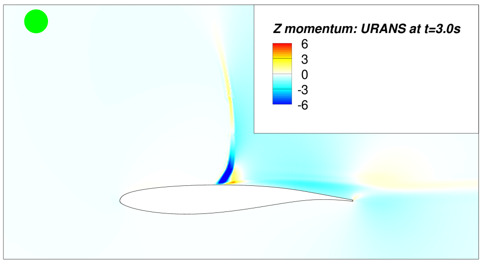

(k) URANS result at t = 3s

(l) Predicted flowfield using final remade eigen basis, at t = 3s

(m) Predicted flowfield using final remade POD basis, at t = 3s

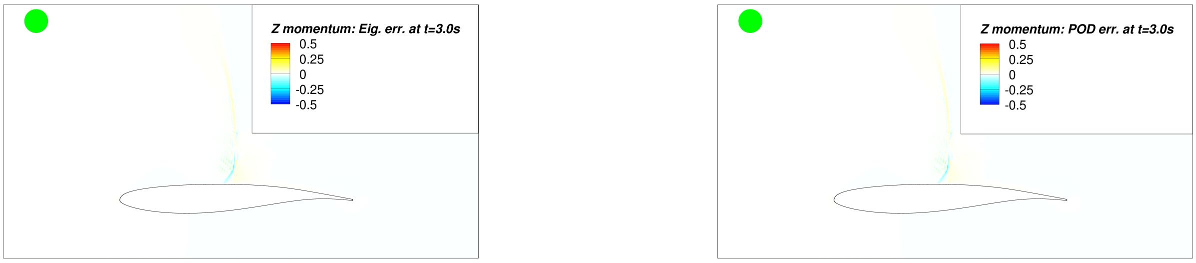

(n) Error between the predicted flowfield using final remade eigen basis and URANS flowfield, at t = 3s

(o) Error between the predicted flowfield using final remade POD basis and URANS flowfield, at t = 3s

Figure 5.32: Predicted Z momentum flowfield done based on ODE for the final remade eigen and final remade POD basis, compared to the actual URANS flowfield at t = 1.23s, 2s and 3s. The comparison between the URANS flowfield to the predicted flowfields are carried out by the error plots.

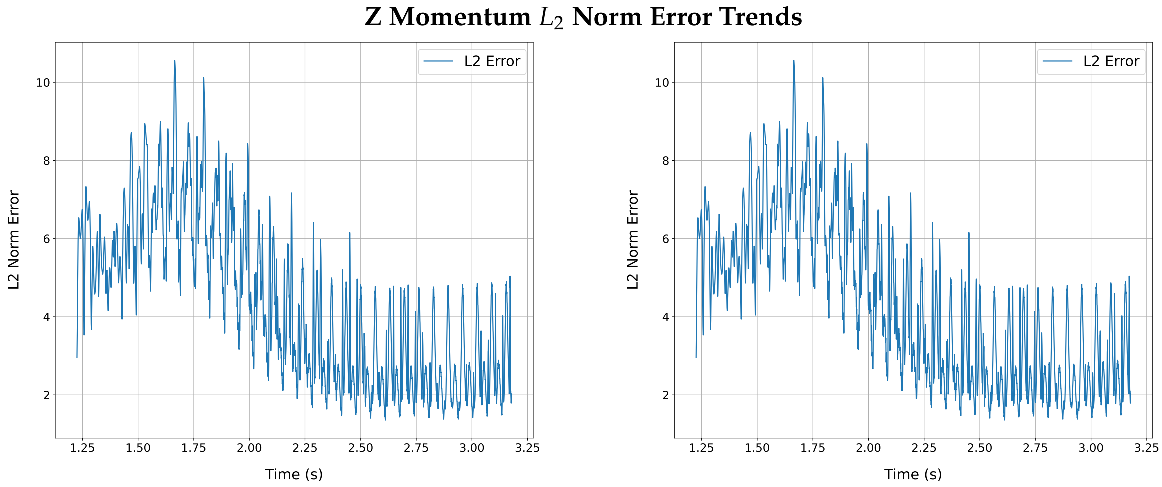

(a) L_2 norm error trend between the predictions based on the final remade eigen basis and the URANS flowfield, of Z momentum. The norm is considered from prediction start point $t = 1.23$ s, for the case of $Ma = 0.71$, $\alpha = 4.45°$.

(b) L_2 norm error trend between the predictions based on the final remade POD basis and the URANS flowfield, of Z momentum. The norm is considered from prediction start point $t = 1.23$ s, for the case of $Ma = 0.71$, $\alpha = 4.45°$.

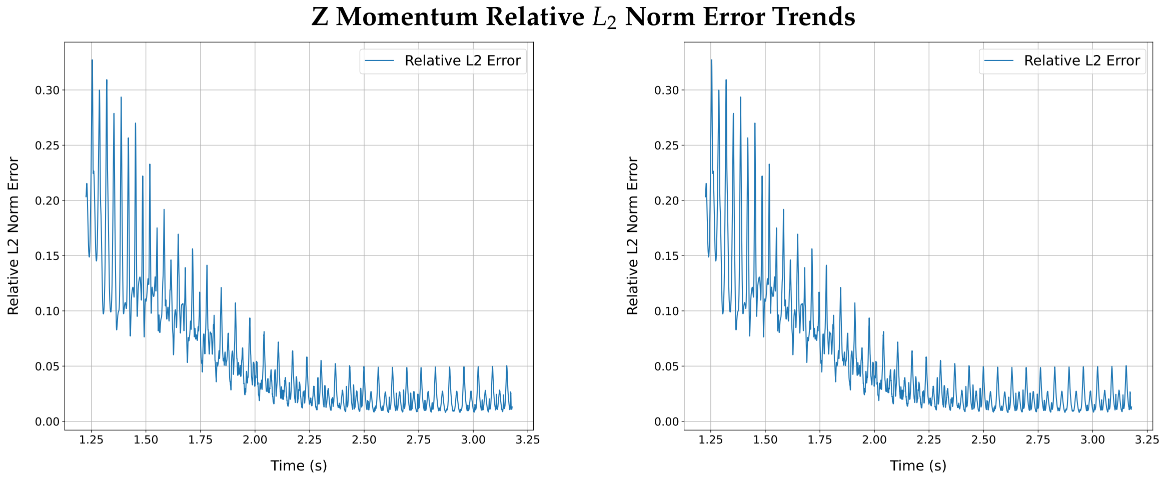

(c) Relative L_2 norm error trend between the predictions based on the final remade eigen basis and the URANS flowfield, of Z momentum. The norm is considered from prediction start point $t = 1.23$ s, for the case of $Ma = 0.71$, $\alpha = 4.45°$.

(d) Relative L_2 norm error trend between the predictions based on the final remade POD basis and the URANS flowfield, of Z momentum. The norm is considered from prediction start point $t = 1.23$ s, for the case of $Ma = 0.71$, $\alpha = 4.45°$.

Figure 5.33: Comparison of relative L_2 norm error trends for Z momentum using different final remade bases and methods.

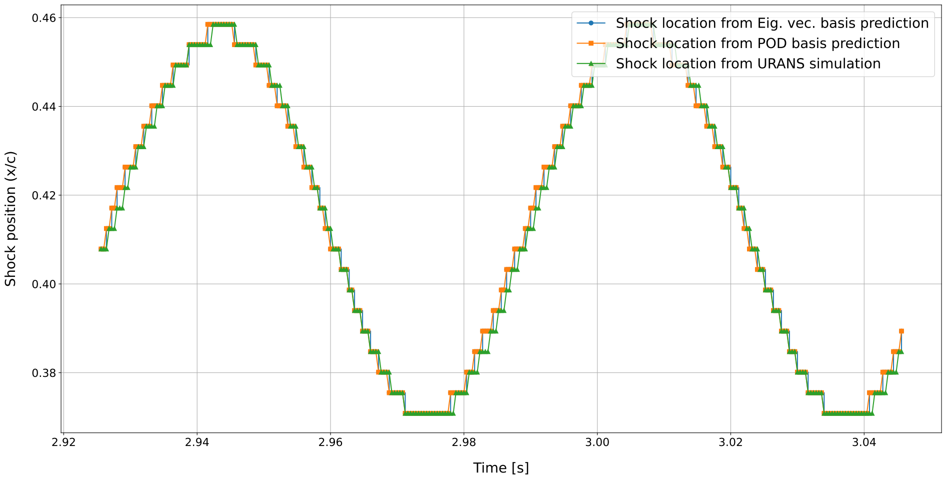

Figure 5.34: The comparison of the predicted shock location through the density flowfield data, reconstructed out of the predicted eta variables with the help of the ODE obtained through linear regression for both the final remade basis type A and basis type B, against the density data obtained from the URANS *validation data*. The case considered is case 3: Ma=0.71 and $\alpha = 4.45°$. The shock location prediction is done between t = 2.93s and t = 3.05s, which are in the LCO region for the case considered. The shock location is obtained through finding the location of the sharpest density gradient along the surface of the aerofoil, which indicates the location of the shock.

6

Conclusion

This thesis presented a comprehensive study on the development of a non-linear reduced order model (ROM) for transonic buffet phenomena, based on Spectral Submanifold (SSM) embedding. Transonic buffet, characterized by self-sustained shock oscillations and shock wave-boundary layer interactions (SWBLI), poses a serious threat to the structural integrity of aircraft wings, limiting the operational flight envelope and potentially leading to fatigue failure. Traditional modelling approaches, particularly those based on linearized reduced order models, have been shown to be inadequate in capturing the essential non-linear features of buffet dynamics, throughout the growth of the instability stemming from a Hopf bifurcation from close to the base flow to limit cycle oscillation (LCO) behaviour. This inadequacy motivated the need for an advanced modelling approach that can faithfully represent the non-linear evolution of perturbations and the limit-cycle behaviour of transonic flows.

To address this, the thesis adopts and applies a data-driven methodology utilizing the mathematical framework of Spectral Submanifolds (SSM). SSM's are low-dimensional invariant manifolds that act as non-linear extensions of linear subspaces. Unlike linear subspaces, SSM's remain invariant under the full non-linear dynamics and, therefore, provide an ideal setting for constructing reduced-order models that preserve the essential physics of growing oscillatory instabilities. The key advantage of using SSM embedding lies in its ability to systematically reduce the high-dimensional flow dynamics onto a non-linear manifold, parametrized by a few dominant modal coordinates, and then reconstruct the full-state dynamics from this reduced representation. The implementation of this technique involved multiple steps. First, steady RANS and unsteady URANS simulations were performed for a supercritical aerofoil configuration (OAT15A) to obtain the base flows and time-dependent flow fields, respectively. The URANS fields are recorded with two initializations, set by varying perturbations, resulting in two set of flow data for each case of Ma-α considered; *training data* and *validation data*. Then, a global linear stability analysis was carried out on the steady base flow to extract the eigenmodes and identify the unstable modes responsible for the onset of buffet, confirming the presence of a supercritical Hopf bifurcation. Proper Orthogonal Decomposition (POD) was used to extract the most energetic/dominant structures from the unsteady flow field. The real and imaginary components of the eigenvectors and first and second POD modes extracted were used to construct two basis's for the construction of non-linear manifold. The shift mode combined with these basis separately were used to visualize a local embedding space, onto which the high-dimensional flow states were projected to obtain a three dimensional representation of the n-dimensional manifold $\mathcal{M}_0$. The linearity and the nonlinearity of the transient flow are captured with the help of coefficient matrices $\mathbf{V_1}$ and $\mathbf{V}$, which when paired with monomials constructed out of the reduced coordinates obtained through projection of the unsteady flowfield onto the two basis components, can be used to reconstruct the flowfields back again. The production of the reduced coordinates act as an encoder function while the function used for the reconstruction of flowfields act as a decoder function. The reduced coordinates which lie on the tangent plane $\mathcal{T}_0\mathcal{M}_0$, tangential to the manifold, captures the evolution of the dynamics of the higher dimensional system in 2 dimensions, as reduced coordinates, which is an image of the trajectories lying on the manifold. Building an ODE using linear regression for the reduced coordinates, gives the means of capturing the evolution of the reduced dynamics. Pairing the encoder and ODE function, a reduced order model is obtained.

The results obtained from this methodology as the reconstructed flow fields demonstrated strong agreement when compared to the original URANS simulations. An optimum degree of fit M, for the monomials is investigated first for each case of Ma-α considered, using the corresponding *training data*. This would result in pairs of coefficient matrices $\mathbf{V_1}$ and $\mathbf{V}$, which are used to reconstruct the unsteady URANS flowfield. The manifolds obtained through the projection of the unsteady URANS *training data* data and the reconstructed flowfields are compared, as well as the three dimensional trajectories obtained through the projection of the URANS *training data* flowfield and the reconstructed flowfield over the basis considered combined with the shift mode. It was seen that there exists a deviation between the three dimensional trajectories and hence, the manifolds for both the projections. This points to the error present due to the use of Taylor expansion using the monomials of the reduced coordinates, to capture the non-linearities of the unsteady flow. After obtaining an optimum degree of fit M, for the monomials used for fitting the reconstructed trajectories for each case investigated, the image of the trajectories over the tangent plane $\mathcal{T}_0\mathcal{M}_0$ i.e. evolution of the reduced coordinates are considered. The evolution of the reduced coordinates on the tangent plane $\mathcal{T}_0\mathcal{M}_0$ are captured through ODE equations, using linear regression. The pair of ODE equations obtained for the reduced coordinates, combined with the encoder equation results in a reduced order model (ROM). The reduced order model obtained thus was able to reproduce (to a certain accuracy) and predict the time evolution of key flow variables for the cases considered, but for the *validation data* from various points in time, demonstrating robustness of the method. The prediction of *validation data* in reduced coordinates from some time point t_0, has been observed to have errors compared to the actual evolution of the reduced coordinates of *validation data*, mainly owing to the fact that the use of linear regression for creating ODE's for one data set would not truly predict the evolution of another data set of same condition. The error in prediction and error of reconstruction are the two main factors that cause a deviation of the predicted and reconstructed flowfield, from the true flowfield. The error of reconstructed flowfield is observed to be more dominant close to the location where the shock is present, concentrated towards the region of the foot of the shock. Comparing between the basis chosen for the investigation, there is no particular trend of obtaining a better flowfield prediction or reduced order model using the basis type A or basis type B, although looking at the error of norm for the predicted and actual URANS data, it could be seen that the basis type A produced better results close to the base flow and the basis type B produced better results near the LCO region. The model though was successful in capturing the nonlinearity seen in the evolution of the unsteadiness into an LCO behaviour seen in transonic buffeting, validating its ability to model post-bifurcation dynamics. Importantly, the model maintained accuracy across different operating conditions, including variations in Mach number and angle of attack, suggesting its robustness and generalizability. The model was also able to predict the shock location with a good degree of accuracy in the LCO region of the dynamics. Further post processing of the reconstructed flowfields to non-dimensional parameters like the coefficient of lift (C_L), coefficient of pressure (C_p) etc, are possible for the sake of comparison with the original URANS flowfield considered.

On evaluation of the error observed between the URANS data and the predicted data, a comparison of the 3D embedded manifold constructed using the reduced coordinates against the L_2 norm of the normal component ($\|\mathbf{w}^{\perp}\|$) of the URANS data and the 3D manifold constructed using the reduced coordinates against the L_2 norm of the reconstructed normal component ($\|\mathbf{w_{recon}}\|$) is done. The lack of tangency of the the URANS-$\|\mathbf{w}^{\perp}\|$ manifold, indicated an incorrect tangent space $\mathcal{T}_0\mathcal{M}_0$ used for the reduction of the n-dimensional dynamics with the encoder function. This pointed to an inaccuracy in the extracted eigen modes and POD modes, which failed to capture the complete linear nature of the system and hence fail to span the real tangent plane. The basis vectors for both basis types are then remade by extracting the linear components remaining in the normal component of the flow, and a new set of initial remade basis are defined. The 3D manifolds of URANS-$\|\mathbf{w}^{\perp}\|$ and URANS-$\|\mathbf{w_{recon}}\|$ are constructed again, which now indicates tangency and hence a proper and correct tangent space $\mathcal{T}_0'\mathcal{M}_0'$. Evaluating near the base flow, it was observed that the presence of the initializing pulse in the URANS data, caused a deviation in the URANS-$\|\mathbf{w}^{\perp}\|$ manifold from the URANS-$\|\mathbf{w_{recon}}\|$ manifold. For the case evaluated (Ma=0.71, $\alpha = 4.45°$), the manifold region distorted by the presence of the pulse is ignored and the process of remaking is carried out again over the initial remade basis, for a region of flow outside the influence of the pulse. This results in a final remade basis which is then used to create reduced coordinates (η) for *training data*. ODE's defining the nature of the new reduced coordinates are then defined using linear regression and a prediction of evolution of the reduced coordinates using these new ODE's for the *validation data* is then carried out. The resultant predicted flowfield obtained through the reconstruction seem to show a better match to the actual URANS flowfield, than the one with the non remade/original basis, as well showing a better prediction of the shock location through post processing.

The use of spectral submanifold embedding proved to be a powerful approach for reduced order modelling of non-linear flow phenomena. It successfully addressed the limitations of linear models by incorporating the weakly non-linear dynamics characteristic of Hopf bifurcations and limit cycles. Unlike input-output black box models, this approach maintained a clear connection to the underlying physics through the use of eigenspace/POD space-based projection and invariant manifold theory, all the while using only two dominant modes, without the use/need of additional modes to capture the non-linear behaviour, as seen in methods like DMD. Moreover, the low dimensionality of the reduced model makes it particularly well-suited for real-time control applications, including the development of model-based controllers for buffet suppression.

This thesis has demonstrated that SSM-based reduced order models provide a physically interpretable, mathematically rigorous, and computationally efficient framework for modelling transonic buffet. The success of this approach opens new avenues for its application not only in aerodynamic instability modelling but also in real-time control system design for high-speed aerospace vehicles. Future work could involve extending the methodology to three-dimensional wings, incorporating actuation models for control design, and exploring approaches for identification of the spectral submanifold from experimental data.

References

[1] Alessandro Accorinti et al. “Experimental Investigation of Transonic Shock Buffet on an OAT15A Profile”. In: *AIAA Journal* 60.11 (2022), pp. 6289–6300. DOI: `10.2514/1.J061135`.

[2] Steven Allmaras, Forrester Johnson, and Philippe Spalart. “Modifications and clarifications for the implementation of the Spalart-Allmaras turbulence model”. In: *Seventh International Conference on Computational Fluid Dynamics (ICCFD7)* (Jan. 2012), pp. 1–11.

[3] A. M. LYAPUNOV and. “The general problem of the stability of motion”. In: *International Journal of Control* 55.3 (1992), pp. 531–534. DOI: `10.1080/00207179208934253`.

[4] Jan Awrejcewicz, Vadim A. Krys’ko, and Alexander F. Vakakis. “Order Reduction by Proper Orthogonal Decomposition (POD) Analysis”. In: *Nonlinear Dynamics of Continuous Elastic Systems*. Berlin, Heidelberg: Springer Berlin Heidelberg, 2004, pp. 177–238. DOI: `10.1007/978-3-662-08992-7_3`.

[5] Shervin Bagheri. “Koopman-mode decomposition of the cylinder wake”. In: *Journal of Fluid Mechanics* 726 (2013), pp. 596–623. DOI: `10.1017/jfm.2013.249`.

[6] Thomas Breunung and George Haller. “Explicit backbone curves from spectral submanifolds of forced-damped nonlinear mechanical systems”. In: *Proceedings of the Royal Society A: Mathematical, Physical and Engineering Sciences* 474.2213 (2018), p. 20180083. DOI: `10.1098/rspa.2018.0083`.

[7] Steven L. Brunton, Joshua L. Proctor, and J. Nathan Kutz. “Discovering governing equations from data by sparse identification of nonlinear dynamical systems”. In: *Proceedings of the National Academy of Sciences* 113.15 (2016), pp. 3932–3937. DOI: `10.1073/pnas.1517384113`.

[8] Steven L. Brunton et al. “Koopman Invariant Subspaces and Finite Linear Representations of Nonlinear Dynamical Systems for Control”. In: *PLOS ONE* 11.2 (Feb. 2016), pp. 1–19. DOI: `10.1371/journal.pone.0150171`.

[9] “Buffet boundary prediction using RANS-based criteria and adjoint methods”. In: *Aerospace Science and Technology* 126 (2022), p. 107664. ISSN: 1270-9638. DOI: `https://doi.org/10.1016/j.ast.2022.107664`.

[10] Gergely Buza. “Spectral Submanifolds of the Navier–Stokes Equations”. In: *SIAM Journal on Applied Dynamical Systems* 23.2 (2024), pp. 1052–1089. DOI: `10.1137/23M154858X`.

[11] Xavier Cabre, Ernest Fontich, and Rafael De la Llave. “The parameterization method for invariant manifolds II: Regularity with respect to parameters”. In: *Indiana University Mathematics Journal* 52 (Jan. 2003). DOI: `10.1512/iumj.2003.52.2407`.

[12] Xavier Cabré, Ernest Fontich, and Rafael de la Llave. “The parameterization method for invariant manifolds III: overview and applications”. In: *Journal of Differential Equations* 218.2 (2005), pp. 444–515. ISSN: 0022-0396. DOI: `https://doi.org/10.1016/j.jde.2004.12.003`.

[13] Xavier Cabré, Ernest Fontich, and Rafael de la Llave. “The parameterization method for invariant manifolds. I: Manifolds associated to non-resonant subspaces”. In: *Indiana University Mathematics Journal* 52 (2003), pp. 283–328. URL: `https://api.semanticscholar.org/CorpusID:119754020`.

[14] Mattia Cenedese et al. “Data-driven modeling and prediction of non-linearizable dynamics via spectral submanifolds”. In: *Nature Communications* 13.1 (Feb. 2022), p. 872. ISSN: 2041-1723. URL: `https://doi.org/10.1038/s41467-022-28518-y`.

[15] J. D. Crouch et al. “Global Structure of Buffeting Flow on Transonic Airfoils”. In: *IUTAM Symposium on Unsteady Separated Flows and their Control*. Ed. by Marianna Braza and Kerry Hourigan. Dordrecht: Springer Netherlands, 2009, pp. 297–306.

[16] J.D. Crouch, B.R. Ahrabi, and D.S. Kamenetskiy. “Weakly nonlinear behaviour of transonic buffet on airfoils”. In: *Journal of Fluid Mechanics* 999 (2024), A8. DOI: `10.1017/jfm.2024.499`.

[17] J.D. Crouch, A. Garbaruk, and D. Magidov. “Predicting the onset of flow unsteadiness based on global instability”. In: *Journal of Computational Physics* 224.2 (2007), pp. 924–940. ISSN: 0021-9991. DOI: `https://doi.org/10.1016/j.jcp.2006.10.035`.

[18] Jeffrey D. Crouch et al. “Origin of transonic buffet on aerofoils”. In: *Journal of Fluid Mechanics* 628 (2009), pp. 357–369.

[19] A D’Aguanno, F. F. J. Schrijer, and B. W. van Oudheusden. “Experimental investigation of the transonic buffet cycle on a supercritical airfoil”. In: *Experiments in Fluids* 32 (2021). DOI: `10.1007/s00348-021-03319-z`.

[20] Julien Dandois et al. “Buffet Control by Means of Mechanical and Fluidic Vortex Generators”. In: *5th Flow Control Conference*. DOI: `10.2514/6.2010-4975`.

[21] Thomas Daniel et al. “Model order reduction assisted by deep neural networks (ROM-net)”. In: *Advanced Modeling and Simulation in Engineering Sciences* 7.1 (Apr. 2020), p. 16. DOI: `10.1186/s40323-020-00153-6`.

[22] E. Brian Davies. *Spectral Theory and Differential Operators*. Cambridge Studies in Advanced Mathematics. Cambridge University Press, 1995.

[23] Haller G. and Jain S. “How to compute invariant manifolds and their reduced dynamics in high-dimensional finite element models.” In: *Nonlinear Dynamics 107* (2022).

[24] Chuanqiang Gao, Weiwei Zhang, and Zhengyin Ye. “A new viewpoint on the mechanism of transonic single-degree-of-freedom flutter”. In: *Aerospace Science and Technology* 52 (2016), pp. 144–156. ISSN: 1270-9638. DOI: `https://doi.org/10.1016/j.ast.2016.02.029`.

[25] Chuanqiang Gao, Weiwei Zhang, and Zhengyin Ye. “Numerical study on closed-loop control of transonic buffet suppression by trailing edge flap”. In: *Computers Fluids* 132 (2016), pp. 32–45. ISSN: 0045-7930. DOI: `https://doi.org/10.1016/j.compfluid.2016.03.031`.

[26] Chuanqiang Gao et al. “Active control of transonic buffet flow”. In: *Journal of Fluid Mechanics* 824 (2017), pp. 312–351. DOI: `10.1017/jfm.2017.344`.

[27] Chuanqiang Gao et al. “Mechanism of frequency lock-in in transonic buffeting flow”. In: *Journal of Fluid Mechanics* 818 (2017), pp. 528–561. DOI: `10.1017/jfm.2017.120`.

[28] E. Garnier and S. Deck. “Large-Eddy Simulation of Transonic Buffet over a Supercritical Airfoil”. In: *Direct and Large-Eddy Simulation VII*. Ed. by Vincenzo Armenio, Bernard Geurts, and Jochen Fröhlich. Dordrecht: Springer Netherlands, 2010, pp. 549–554. ISBN: 978-90-481-3652-0.

[29] Nicholas F. Giannelis, Gareth A. Vio, and Oleg Levinski. “A review of recent developments in the understanding of transonic shock buffet”. In: *Progress in Aerospace Sciences* 92 (2017), pp. 39–84. DOI: `https://doi.org/10.1016/j.paerosci.2017.05.004`.

[30] J Gibb. “THE CAUSE AND CURE OF PERIODIC FLOWS AT TRANSONIC SPEEDS.” In: (1990). URL: `https://books.google.de/books?id=_25RnQEACAAJ`.

[31] AB HAINES, J Osborne, and HH PEARCEY. “The interaction between local effects at the shock and rear separation- A source of significant scale effects in wind-tunnel tests on aerofoils and wings(Shock-induced boundary layer separation and scale effects in wind tunnel tests on airfoils and wings)”. In: (1968).

[32] George Haller and Sten Ponsioen. “Nonlinear normal modes and spectral submanifolds: Existence, uniqueness and use in model reduction”. In: *Nonlinear Dynamics* 86 (Nov. 2016). DOI: `10.1007/s11071-016-2974-z`.

[33] A. Haro and R. de la Llave. “A parameterization method for the computation of invariant tori and their whiskers in quasi-periodic maps: Rigorous results”. In: *Journal of Differential Equations* 228.2 (2006), pp. 530–579. ISSN: 0022-0396. DOI: `https://doi.org/10.1016/j.jde.2005.10.005`.

[34] Eugene Izhikevich. *Dynamical Systems in Neuroscience: The Geometry of Excitability and Bursting*. Vol. 25. Jan. 2007. DOI: `10.7551/mitpress/2526.001.0001`.

[35] L. Jacquin et al. “Experimental Study of Shock Oscillation over a Transonic Supercritical Profile”. In: *AIAA Journal* 47.9 (2009), pp. 1985–1994. DOI: `10.2514/1.30190`.

[36] Laurent Jacquin et al. "An Experimental Study of Shock Oscillation over a Transonic Supercritical Profile". In: *35th AIAA Fluid Dynamics Conference and Exhibit*. DOI: `10.2514/6.2005-4902`. URL: `https://arc.aiaa.org/doi/abs/10.2514/6.2005-4902`.

[37] Al Kelley. "On the Liapounov subcenter manifold". In: *Journal of Mathematical Analysis and Applications* 18.3 (1967), pp. 472–478. ISSN: 0022-247X. DOI: `https://doi.org/10.1016/0022-247X(67)90039-X`.

[38] Gaëtan Kerschen et al. "The Method of Proper Orthogonal Decomposition for Dynamical Characterization and Order Reduction of Mechanical Systems: An Overview". In: *Nonlinear Dynamics* 41 (Aug. 2005), pp. 147–169. DOI: `10.1007/s11071-005-2803-2`.

[39] Florian Kogelbauer and George Haller. "Rigorous Model Reduction for a Damped-Forced Nonlinear Beam Model: An Infinite-Dimensional Analysis". In: *Journal of Nonlinear Science* 28.3 (2018-06), pp. 1109–1150. ISSN: 1432-1467. DOI: `10.3929/ethz-b-000237895`.

[40] Yuri A. Kuznetsov. *Elements of applied bifurcation theory (4th ed.)* Springer-Verlag, 2023. ISBN: 0387983821. DOI: `doi.org/10.1007/978-3-031-22007-4`.

[41] D.A. Lawrence, J.H. Myatt, and R.C. Camphouse. "On model reduction via empirical balanced truncation". In: *Proceedings of the 2005, American Control Conference, 2005.* 2005, 3139–3144 vol. 5. DOI: `10.1109/ACC.2005.1470454`.

[42] B. H. K. Lee. "Oscillatory shock motion caused by transonic shock boundary-layer interaction". In: *AIAA Journal* 28.5 (1990), pp. 942–944.

[43] B.H.K. Lee. "Self-sustained shock oscillations on airfoils at transonic speeds". In: *Progress in Aerospace Sciences* 37.2 (2001), pp. 147–196. ISSN: 0376-0421. DOI: `https://doi.org/10.1016/S0376-0421(01)00003-3`. URL: `https://www.sciencedirect.com/science/article/pii/S0376042101000033`.

[44] Kuan Lu et al. "Review for order reduction based on proper orthogonal decomposition and outlooks of applications in mechanical systems". In: *Mechanical Systems and Signal Processing* 123 (2019), pp. 264–297. ISSN: 0888-3270. DOI: `https://doi.org/10.1016/j.ymssp.2019.01.018`.

[45] DG Mabey. "Oscillatory flows from shock induced separations on biconvex aerofoils of varying thickness in ventilated wind tunnels". In: *1981. 14* (1981).

[46] Matthias Maier. *Transonic 2D flow around Onera OAT15a airfoil at Mach 0.73*. Youtube. 2021. URL: `https://www.youtube.com/watch?v=yM2rT3teakE`.

[47] John B McDevitt and Arthur F Okuno. *Static and dynamic pressure measurements on a NACA 0012 airfoil in the Ames high Reynolds number facility*. Tech. rep. 1985.

[48] Jens Nitzsche. "A numerical study on aerodynamic resonance in transonic separated flow". In: (2009).

[49] Jens Nitzsche et al. "Fluid-mode flutter in plane transonic flows". In: *International Forum on Aeroelasticity and Structural Dynamics 2019, IFASD 2019*. June 2019. URL: `https://elib.dlr.de/127989/`.

[50] Jens Nitzsche et al. "The Effect of Shock Control Bumps on the Transonic Flutter and Buffeting Characteristics of a Typical Wing Section". In: *19th International Forum on Aeroelasticity and Structural Dynamics, IFASD 2022*. June 2022.

[51] BERND R. NOACK et al. "A hierarchy of low-dimensional models for the transient and post-transient cylinder wake". In: *Journal of Fluid Mechanics* 497 (2003), pp. 335–363. DOI: `10.1017/S0022112003006694`.

[52] Andrea Opreni et al. "Model order reduction based on direct normal form: application to large finite element MEMS structures featuring internal resonance". In: *Nonlinear Dynamics* 105.2 (July 2021), pp. 1237–1272. ISSN: 1573-269X. DOI: `10.1007/s11071-021-06641-7`.

[53] Edoardo Paladini et al. "Analysis and comparison of transonic buffet phenomenon over several 3D wings". In: *AIAA Journal* (2018), pp. 1–18. DOI: `10.2514/1.J056473`.

[54] HH Pearcey. *A Method for the Prediction of the Onset of Buffeting and Other Separation Effects from Wind Tunnel Tests on Rigid Models: This Report was Presented at the Fourteenth Meeting of the Wind Tunnel and Model Testing Panel, Held from 20th to 21st October, 1958, in Copenhagen, Denmark*. North Atlantic Treaty Organization, Advisory Group for Aeronautical Research, 1958.

[55] HH Pearcey. "Some effects of shock-induced separation of turbulent boundary layers in transonic flow past aerofoils". In: (1955).

[56] HH Pearcey and DW Holder. *Simple methods for the prediction of wing buffeting resulting from bubble type separation*. NPL, 1962.

[57] Sten Ponsioen, Tiemo Pedergnana, and George Haller. "Automated computation of autonomous spectral submanifolds for nonlinear modal analysis". In: *Journal of Sound and Vibration* 420 (2018), pp. 269–295. ISSN: 0022-460X. DOI: `https://doi.org/10.1016/j.jsv.2018.01.048`.

[58] S. Raghunathan, R.D. Mitchell, and M.A. Gillan. "Transonic shock oscillations on NACA0012 aerofoil". In: *Shock Waves* 8.4 (1998), pp. 191–202. DOI: `10.1007/s001930050113`.

[59] R.M. Rosenberg. "On Nonlinear Vibrations of Systems with Many Degrees of Freedom". In: ed. by G.G. Chernyi et al. Vol. 9. Advances in Applied Mechanics. Elsevier, 1966, pp. 155–242. DOI: `https://doi.org/10.1016/S0065-2156(08)70008-5`. URL: `https://www.sciencedirect.com/science/article/pii/S0065215608700085`.

[60] Andrea Sansica et al. "System Identification of Two-Dimensional Transonic Buffet". In: *AIAA Journal* 60.5 (2022), pp. 3090–3106. DOI: `10.2514/1.J061001`.

[61] Fulvio Sartor, Clément Mettot, and Denis Sipp. "Stability, receptivity, and sensitivity analyses of buffeting transonic flow over a profile". In: *Aiaa Journal* 53.7 (2015), pp. 1980–1993.

[62] Sven Scharnowski et al. "Comparison of shock-buffet dynamics on a supercritical airfoil with and without a pitching degree of freedom". In: *CEAS Aeronautical Journal* 15 (2024). DOI: `https://doi.org/10.1007/s13272-023-00692-9`.

[63] S.W. Shaw and C. Pierre. "Normal Modes for Non-Linear Vibratory Systems". In: *Journal of Sound and Vibration* 164.1 (1993), pp. 85–124. ISSN: 0022-460X. DOI: `https://doi.org/10.1006/jsvi.1993.1198`. URL: `https://www.sciencedirect.com/science/article/pii/S0022460X83711983`.

[64] Denis Sipp and Anton Lebedev. "Global stability of base and mean flows: a general approach and its applications to cylinder and open cavity flows". In: *Journal of Fluid Mechanics* 593 (2007), pp. 333–358.

[65] Steven H. Strogatz. *Nonlinear Dynamics and Chaos With Applications to Physics, Biology, Chemistry, and Engineering*. CRC Press, 2015.

[66] Robert Szalai. "Data-Driven Reduced Order Models Using Invariant Foliations, Manifolds and Autoencoders". In: *Journal of Nonlinear Science* 33.5 (June 2023), p. 75. ISSN: 1432-1467. URL: `https://doi.org/10.1007/s00332-023-09932-y`.

[67] Robert Szalai, David Ehrhardt, and George Haller. "Nonlinear model identification and spectral submanifolds for multi-degree-of-freedom mechanical vibrations". In: *Proceedings of the Royal Society A: Mathematical, Physical and Engineering Sciences* 473.2202 (2017), p. 20160759. DOI: `10.1098/rspa.2016.0759`.

[68] Floris Takens. "Detecting strange attractors in turbulence". In: *Dynamical Systems and Turbulence, Warwick 1980*. Ed. by David Rand and Lai-Sang Young. Berlin, Heidelberg: Springer Berlin Heidelberg, 1981, pp. 366–381. ISBN: 978-3-540-38945-3.

[69] Mark C. Thompson and Patrice Le Gal. "The Stuart–Landau model applied to wake transition revisited". In: *European Journal of Mechanics - B/Fluids* 23.1 (2004). Bluff Body Wakes and Vortex-Induced Vibrations, pp. 219–228. ISSN: 0997-7546. DOI: `https://doi.org/10.1016/j.euromechflu.2003.09.012`.

[70] Reik Thormann and Markus Widhalm. "Linear-Frequency-Domain Predictions of Dynamic-Response Data for Viscous Transonic Flows". In: *AIAA Journal* 51.11 (2013), pp. 2540–2557. DOI: `10.2514/1.J051896`.

[71] Hendrik Tijdeman. "Investigation of the transonic flow around oscillating airfoils". In: *NLR-TR-77090* (1977).

[72] Alessandra Vizzaccaro et al. "Direct computation of nonlinear mapping via normal form for reduced-order models of finite element nonlinear structures". In: *Computer Methods in Applied Mechanics and Engineering* 384 (2021), p. 113957. ISSN: 0045-7825. DOI: `https://doi.org/10.1016/j.cma.2021.113957`.

[73] Tea Vojković, Dimitris Boskos, and Abel-John Buchner. *Reduced-Order Modelling and Closed-Loop Control of the Cylinder Wake*. 2024. arXiv: `2410.03330 [physics.flu-dyn]`.

[74] Andre Weiner and Richard Semaan. “flowTorch - a Python library for analysis and reduced-order modeling of fluid flows”. In: *Journal of Open Source Software* 6.68 (2021), p. 3860. DOI: `10.21105/joss.03860`. URL: `https://doi.org/10.21105/joss.03860`.

A

Appendix

For cases 1, 2 and 4 discussed in subsection 5.2.2, we investigate various positions in the evolution of the reduced coordinates, such that the prediction carried out using basis type A and basis type B can be made into flowfields at those points in time using Equation 4.13, as previously done for case 3 in subsection 5.2.3. Here the points in time used for evaluation for the remaining cases are described in Table A.1,

	Time point 1 (s)	**Time point 2 (s)**	**Time point 3 (s)**
Case 1	0.5	1.5	2.5
Case 2	0.5	0.77	1.55
Case 4	0.4	0.75	2

Table A.1: Selected time points for different cases 1, 2 and 4

The time points considered, for each of the cases are represented as red, blue and green dots denoting the points of time chosen.The red, blue and green dotes represent the first time point, the second time point and the third time point respectively. The reduced coordinate variation plots for the URANS *validation data* on both basis type A and basis type B are represented as,

- For case 1: Figure A.1,
- For case 2: Figure A.4,
- For case 4: Figure A.7.

For each of the time points chose, we reconstruct the flowfield with Equation 4.13, using the predicted reduced coordinates obtained using basis type A and basis type B. For each case, we split and depict the predicted flowfield using both the basis types and compare it to the original URANS flowfield at that point in time. The error plots obtained by subtracting the predicted flowfield obtained for a particular basis from the URANS flowfield at the same point in time. We also compare the L_2 norm error for the predictions and reconstructions done from the start point of prediction for each case, as per Table 5.8.

A.1. Case 1: Prediction done for Ma=0.69 $\alpha = 5°$

The reduced coordinate evolution in time for the URANS *validation data* is plotted in Figure A.1, with the selected time points at which the predicted flowfields are compared to the actual URANS flowfield. The selected time points are 0.5s, 1.5s and 2s, which are represented by red, blue and green dots respectively, and are indicated for both basis type A and basis type B in Figure A.1. The flowfields predicted using the reduced coordinates made of the basis type A and basis type B are compared in Figure A.2, where for each time point, we have the actual URANS *validation data* flowfield at the center, the predicted flowfield from basis type A on the left column below the actual URANS *validation data* flowfield and the error between the prediction and the actual flowfield below it. Similarly, the predicted flowfield from basis type B is present on the right column below the actual URANS *validation data* flowfield and the error between the prediction and the actual flowfield below it.

As per the start times decided for each of the cases, as given in Table 5.8, we evaluate the L_2 norm error for the flowfield obtained for each of the time step predicted and the actual URANS data. This evaluation is done for both basis type A and basis type B, and are represented in Figure A.3. Here, it is evident that the L_2 norm error between the predicted flowfield of basis type A and the URANS flowfield seems to show a lower error compared to the prediction done by basis type B. The eigen basis describes the flowfield better than the POD basis for this case.

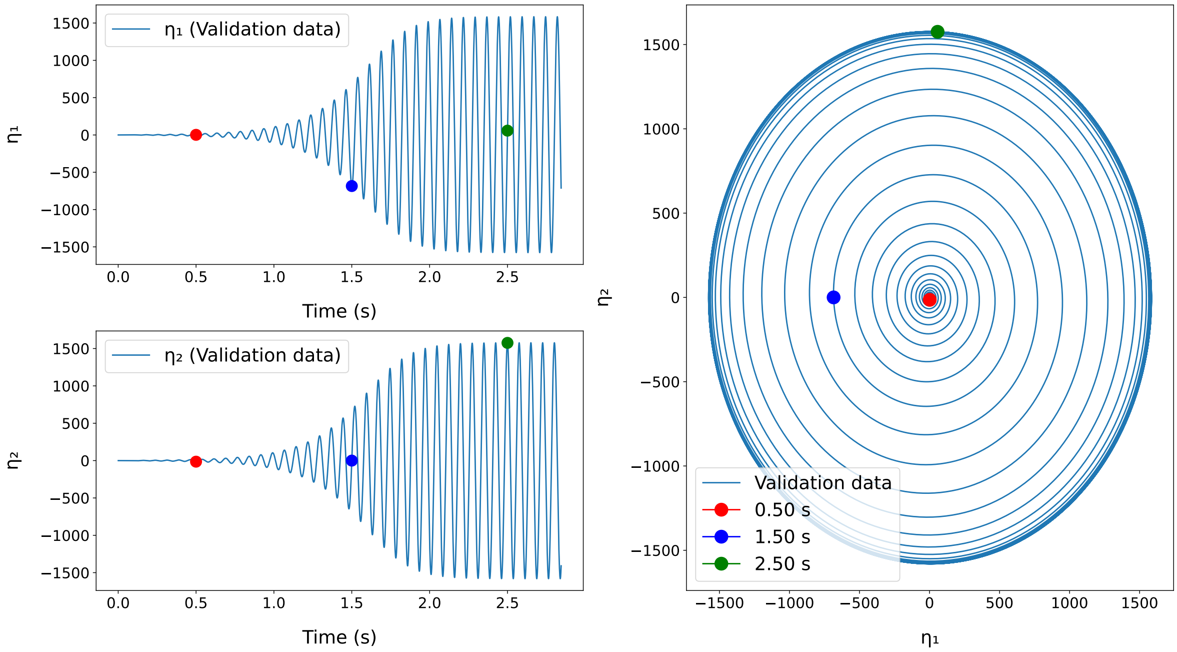

(a) Points in time t = 0.5s, 1.5s and 2.5s considered for Ma 0.69, $\alpha = 5°$ reconstruction, marked on the reduced coordinate plots on basis type A for the *validation data*

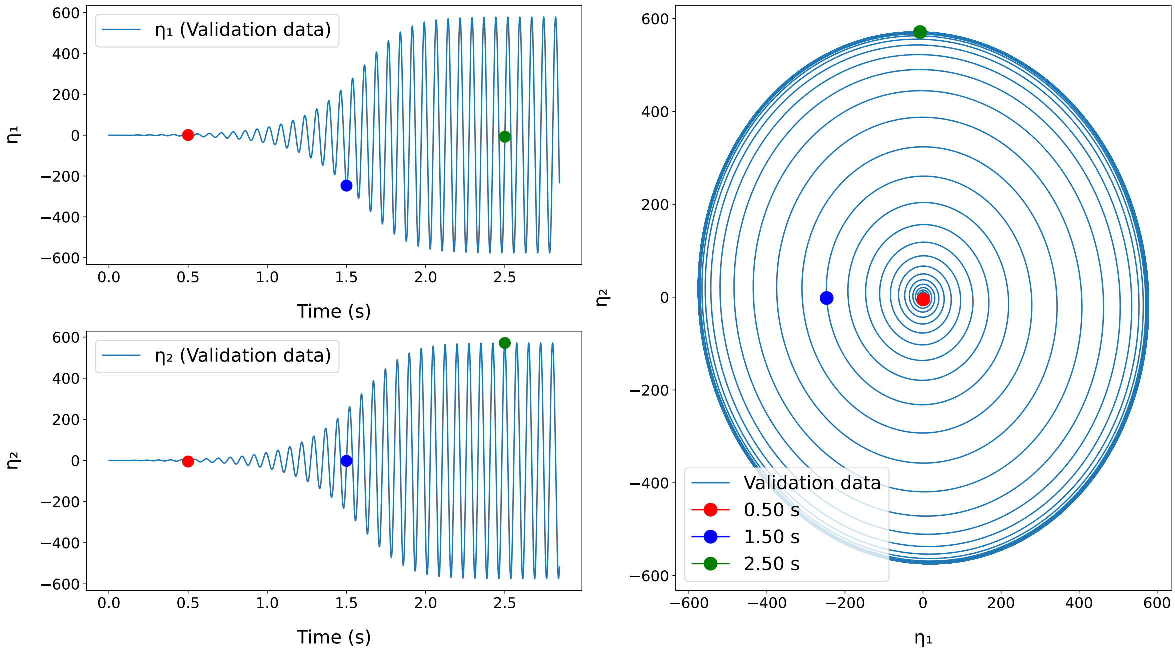

(b) Points in time t = 0.5s, 1.5s and 2.5s considered for Ma 0.69, $\alpha = 5°$reconstruction, marked on the reduced coordinate plots on basis type B for the *validation data*

Figure A.1: Points in time t = 0.5s, 1.5s and 2.5s considered for Ma 0.69, $\alpha = 5°$reconstruction, marked on the reduced coordinate plots on basis type A and basis type B, for the *validation data*

Prediction of X momentum done at t = 0.5s for Ma=0.69 at $\alpha = 5°$

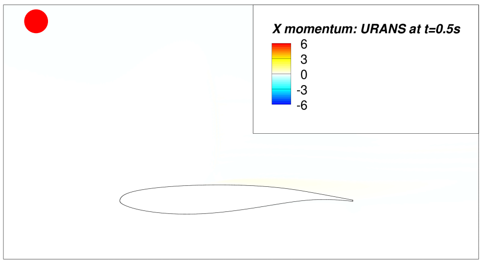

(a) URANS result at t = 0.5s

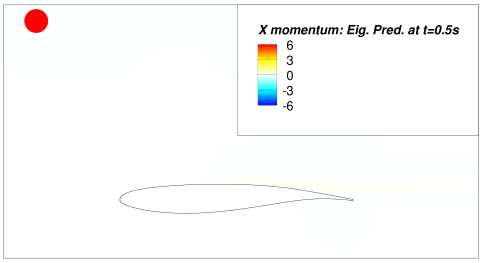

(b) Predicted flowfield using eigen basis, at t = 0.5s

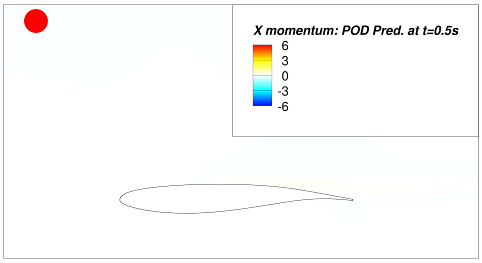

(c) Predicted flowfield using POD basis, at t = 0.5s

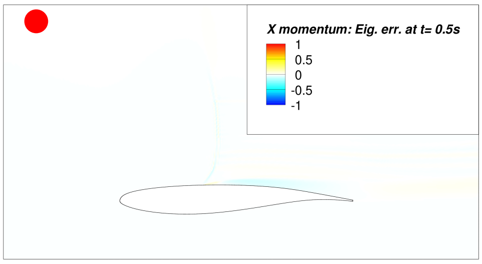

(d) Error between the predicted flowfield using eigen basis and URANS flowfield, at t = 0.5s

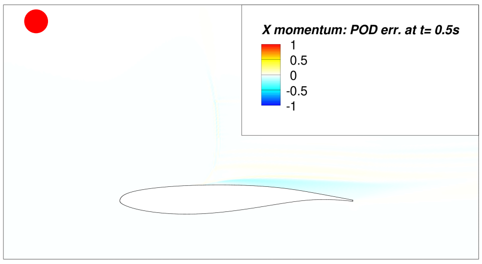

(e) Error between the predicted flowfield using POD basis and URANS flowfield, at t = 0.5s

Prediction of X momentum done at t = 1.5s for Ma=0.69 at $\alpha = 5°$

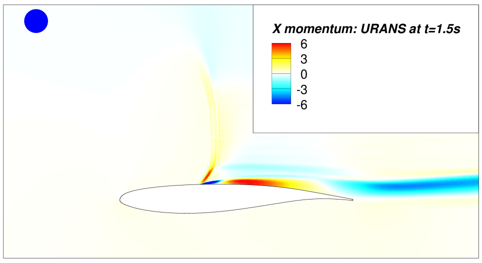

(f) URANS result at t = 1.5s

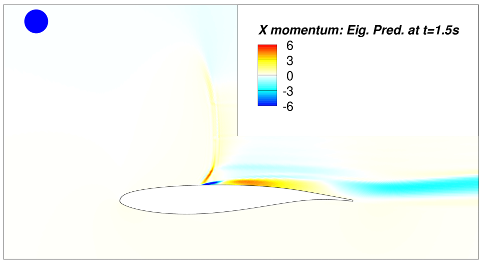

(g) Predicted flowfield using eigen basis, at t = 1.5s

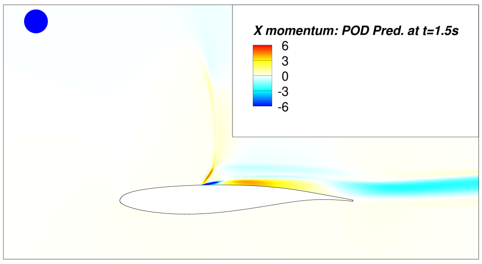

(h) Predicted flowfield using POD basis, at t = 1.5s

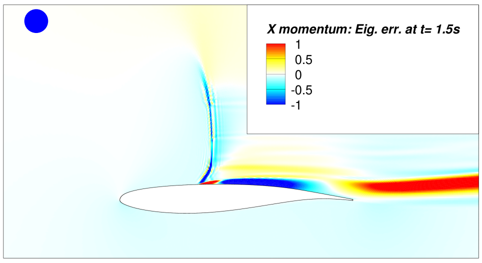

(i) Error between the predicted flowfield using eigen basis and URANS flowfield, at t = 1.5s

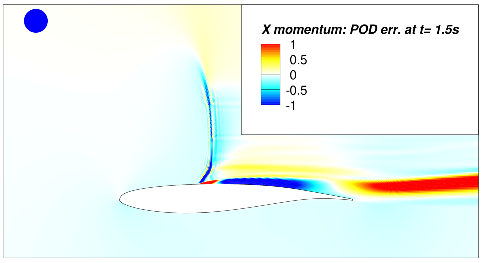

(j) Error between the predicted flowfield using POD basis and URANS flowfield, at t = 1.5s

Prediction of X momentum done at t = 2.5s for Ma=0.69 at $\alpha = 5°$

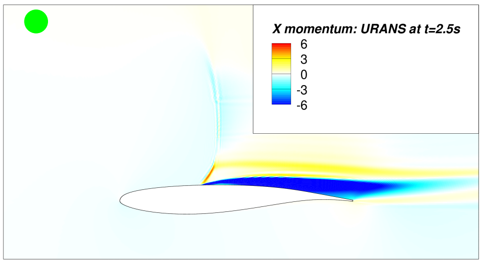

(k) URANS result at t = 2.5s

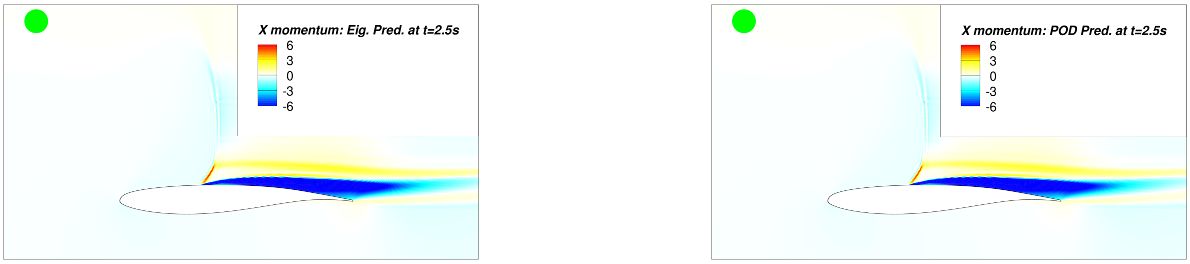

(l) Predicted flowfield using eigen basis, at t = 2.5s

(m) Predicted flowfield using POD basis, at t = 2.5s

(n) Error between the predicted flowfield using eigen basis and URANS flowfield, at t = 2.5s

(o) Error between the predicted flowfield using POD basis and URANS flowfield, at t = 2.5s

Figure A.2: Predicted X momentum flowfield done based on ODE for the eigen and POD basis, compared to the actual URANS flowfield at t = 0.5s, 1.5s and 2.5s. The comparison between the URANS flowfield to the predicted flowfields are carried out by the error plots.

X momentum L_2 Norm Error Trends

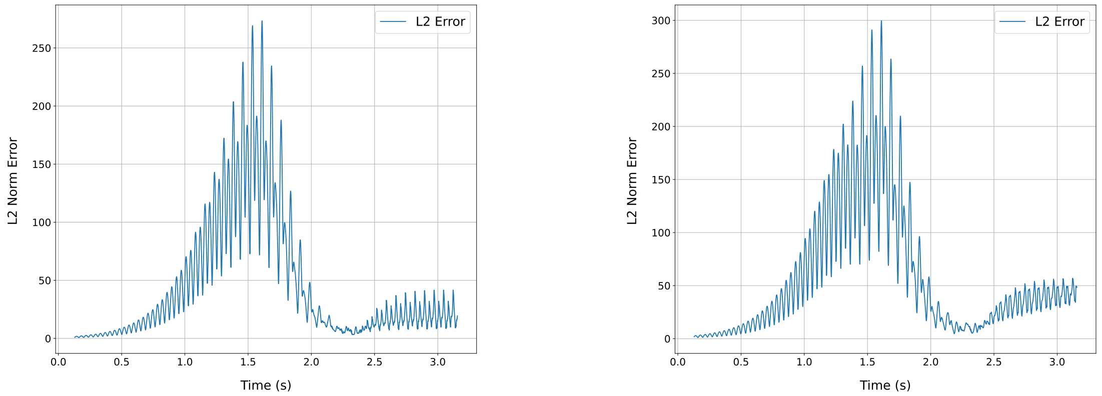

(a) L_2 norm error trend between the predictions based on the eigen basis and the URANS flowfield, of X momentum. The norm is considered from prediction start point $t = 0.125$ s, for the case of $Ma = 0.69$, $\alpha = 5°$.

(b) L_2 norm error trend between the predictions based on the POD basis and the URANS flowfield, of X momentum. The norm is considered from prediction start point $t = 0.125$ s, for the case of $Ma = 0.69$, $\alpha = 5°$.

X momentum Relative L_2 Norm Error Trends

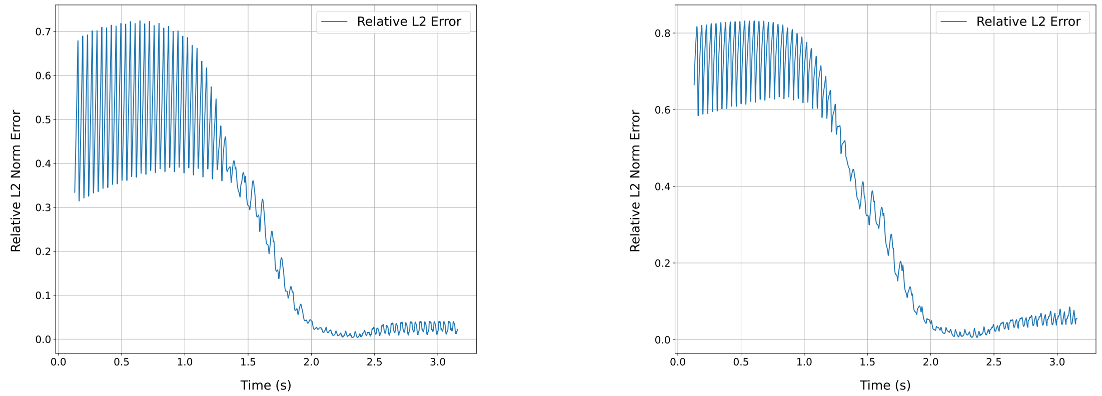

(c) Relative L_2 norm error trend between the predictions based on the eigen basis and the URANS flowfield, of X momentum. The norm is considered from prediction start point $t = 0.125$ s, for the case of $Ma = 0.69$, $\alpha = 5°$.

(d) Relative L_2 norm error trend between the predictions based on the POD basis and the URANS flowfield, of X momentum. The norm is considered from prediction start point $t = 0.125$ s, for the case of $Ma = 0.69$, $\alpha = 5°$.

Figure A.3: Comparison of relative L_2 norm error trends for X momentum using different bases and methods.

A.2. Case 2: Prediction done for Ma=0.69 $\alpha = 7.25°$

The reduced coordinate evolution in time for the URANS *validation data* is plotted in Figure A.4, with the selected time points at which the predicted flowfields are compared to the actual URANS flowfield. The selected time points are 0.5s, 0.77s and 1.55s, which are represented by red, blue and green dots respectively, and are indicated for both basis type A and basis type B in Figure A.4. The flowfields predicted using the reduced coordinates made of the basis type A and basis type B are compared in Figure A.5, where for each time point, we have the actual URANS *validation data* flowfield at the center, the predicted flowfield from basis type A on the left column below the actual URANS *validation data* flowfield and the error between the prediction and the actual flowfield below it. Similarly, the predicted flowfield from basis type B is present on the right column below the actual URANS *validation data* flowfield and the error between the prediction and the actual flowfield below it.

As per the start times decided for each of the cases, as given in Table 5.8, we evaluate the L_2 norm error for the flowfield obtained for each of the time step predicted and the actual URANS data. This evaluation is done for both basis type A and basis type B, and are represented in Figure A.6. Here, it is evident that the L_2 norm error between the predicted flowfield of basis type A and the URANS flowfield seems to show a lower error compared to the prediction done by basis type B. The eigen basis describes the flowfield better than the POD basis for this case.

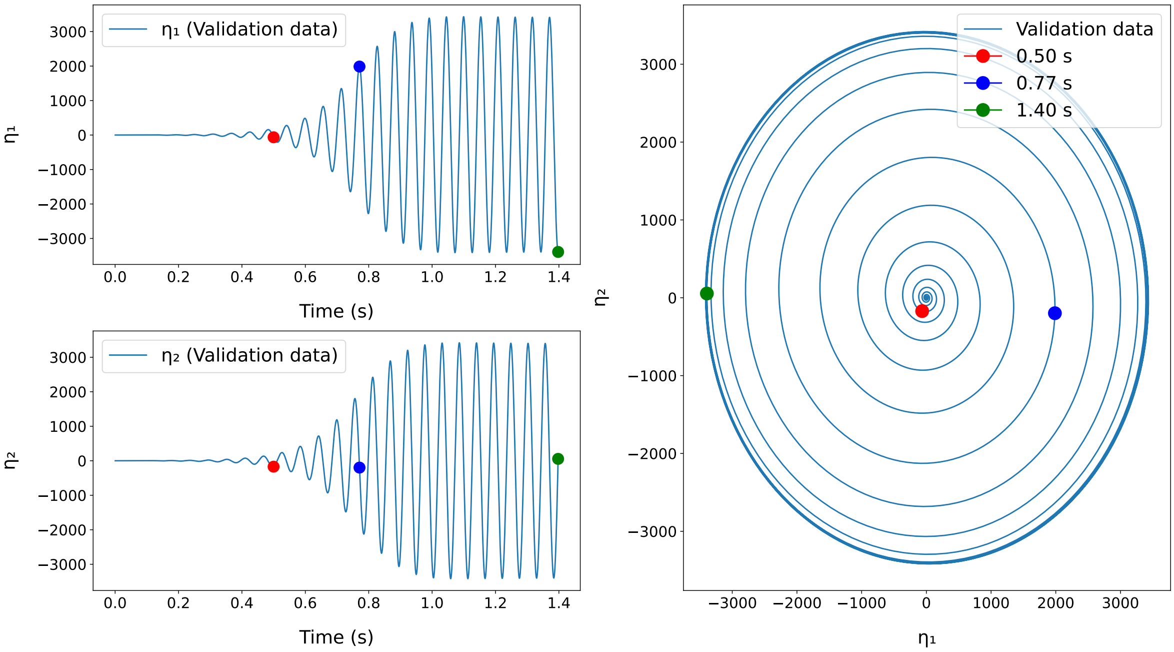

(a) Points in time t = 0.5s, 0.77s and 1.55s considered for Ma 0.69, $\alpha = 5°$ reconstruction, marked on the reduced coordinate plots on basis type A for the *validation data*

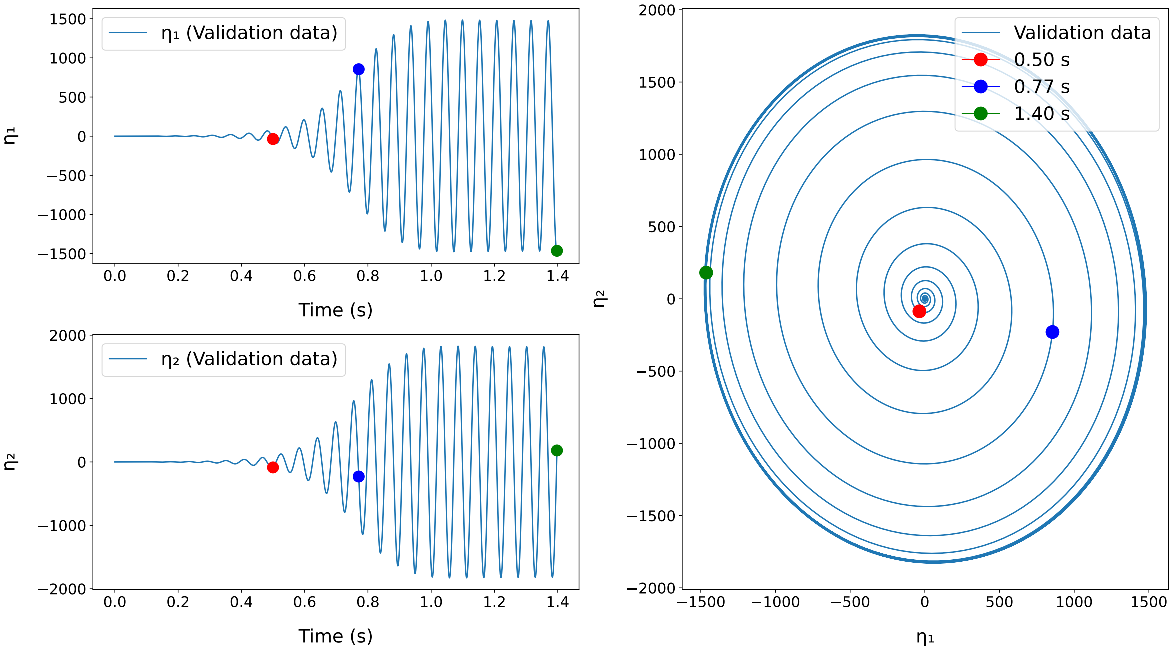

(b) Points in time t = 0.5s, 0.77s and 1.55s considered for Ma 0.69, $\alpha = 5°$ reconstruction, marked on the reduced coordinate plots on basis type B for the *validation data*

Figure A.4: Points in time t = 0.5s, 0.77s and 1.55s considered for Ma 0.69, $\alpha = 5°$ reconstruction, marked on the reduced coordinate plots on basis type A and basis type B, for the *validation data*

Prediction of density done at t = 0.5s for Ma=0.69 at $\alpha = 7.25°$

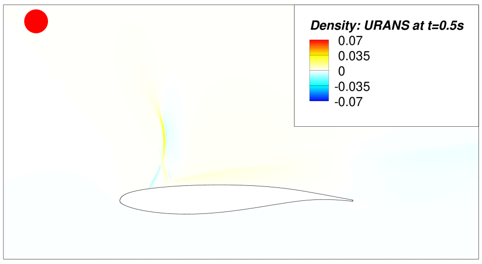

(a) URANS result at t = 0.5s

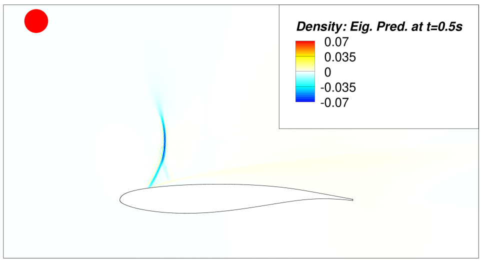

(b) Predicted flowfield using eigen basis, at t = 0.5s

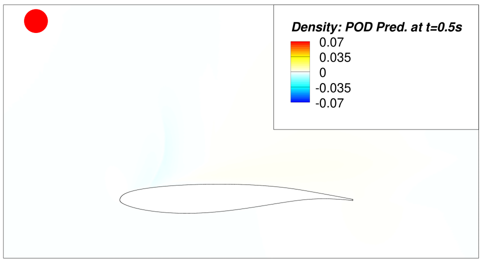

(c) Predicted flowfield using POD basis, at t = 0.5s

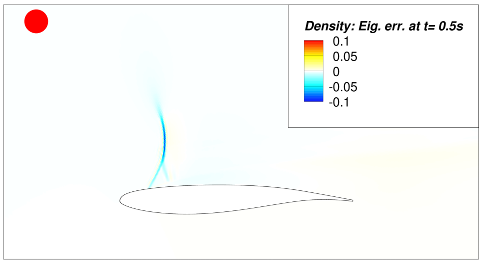

(d) Error between the predicted flowfield using eigen basis and URANS flowfield, at t = 0.5s

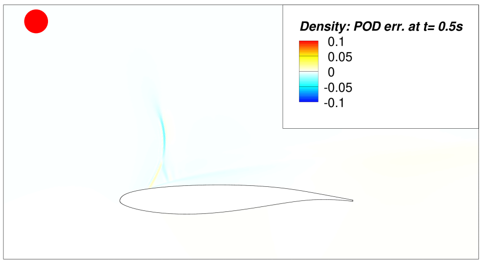

(e) Error between the predicted flowfield using POD basis and URANS flowfield, at t = 0.5s

Prediction of density done at t = 0.77s for Ma=0.69 at $\alpha = 7.25°$

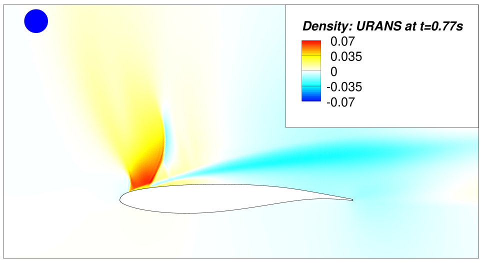

(f) URANS result at t = 1.5s

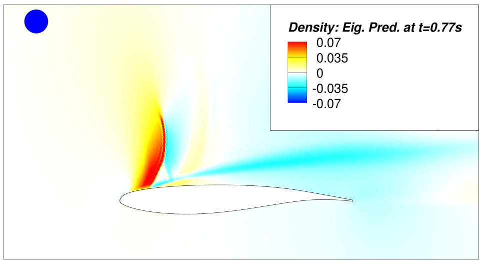

(g) Predicted flowfield using eigen basis, at t = 0.77s

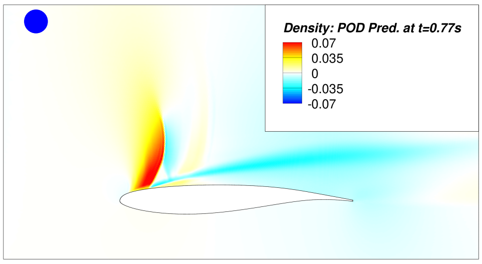

(h) Predicted flowfield using POD basis, at t = 0.77s

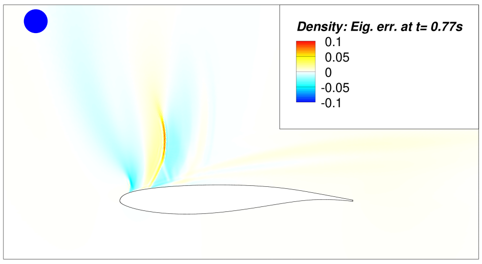

(i) Error between the predicted flowfield using eigen basis and URANS flowfield, at t = 0.77s

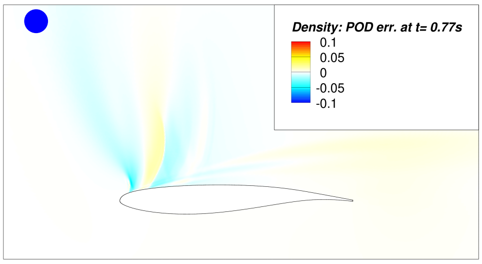

(j) Error between the predicted flowfield using POD basis and URANS flowfield, at t = 0.77s

Prediction of density done at t = 1.55s for Ma=0.69 at $\alpha = 7.25°$

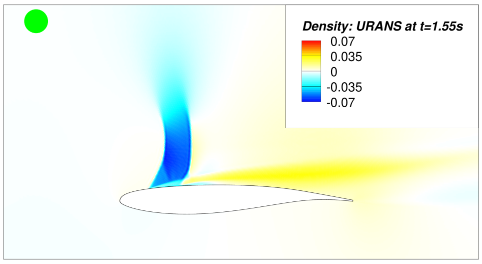

(k) URANS result at t = 1.55s

(l) Predicted flowfield using eigen basis, at t = 1.55s

(m) Predicted flowfield using POD basis, at t = 1.55s

(n) Error between the predicted flowfield using eigen basis and URANS flowfield, at t = 1.55s

(o) Error between the predicted flowfield using POD basis and URANS flowfield, at t = 1.55s

Figure A.5: Predicted density flowfield done based on ODE for the eigen and POD basis, compared to the actual URANS flowfield at t = 0.5s, 0.77s and 1.55s. The comparison between the URANS flowfield to the predicted flowfields are carried out by the error plots.

Density L_2 Norm Error Trends

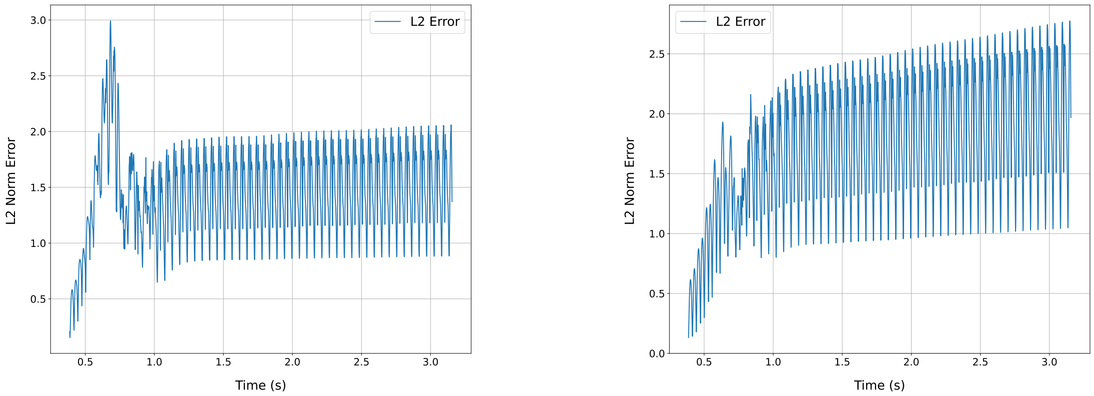

(a) L_2 norm error trend between the predictions based on the eigen basis and the URANS flowfield, of Density. The norm is considered from prediction start point $t = 0.375$ s, for the case of $Ma = 0.69$, $\alpha = 7.25°$.

(b) L_2 norm error trend between the predictions based on the POD basis and the URANS flowfield, of Density. The norm is considered from prediction start point $t = 0.375$ s, for the case of $Ma = 0.69$, $\alpha = 7.25°$.

Density Relative L_2 Norm Error Trends

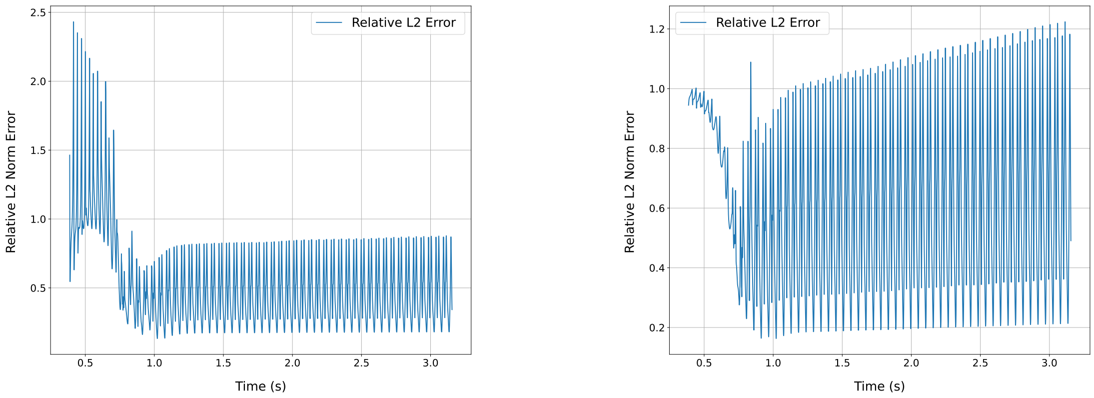

(c) Relative L_2 norm error trend between the predictions based on the eigen basis and the URANS flowfield, of Density. The norm is considered from prediction start point $t = 0.375$ s, for the case of $Ma = 0.69$, $\alpha = 7.25°$.

(d) Relative L_2 norm error trend between the predictions based on the POD basis and the URANS flowfield, of Density. The norm is considered from prediction start point $t = 0.375$ s, for the case of $Ma = 0.69$, $\alpha = 7.25°$.

Figure A.6: Comparison of relative L_2 norm error trends for Density using different bases and methods.

A.3. Case 4: Prediction done for Ma=0.71 $\alpha = 5.25°$

The reduced coordinate evolution in time for the URANS *validation data* is plotted in Figure A.7, with the selected time points at which the predicted flowfields are compared to the actual URANS flowfield. The selected time points are 0.4s, 0.75s and 2s, which are represented by red, blue and green dots respectively, and are indicated for both basis type A and basis type B in Figure A.7. The flowfields predicted using the reduced coordinates made of the basis type A and basis type B are compared in Figure A.8, where for each time point, we have the actual URANS *validation data* flowfield at the center, the predicted flowfield from basis type A on the left column below the actual URANS *validation data* flowfield and the error between the prediction and the actual flowfield below it. Similarly, the predicted flowfield from basis type B is present on the right column below the actual URANS *validation data* flowfield and the error between the prediction and the actual flowfield below it.

As per the start times decided for each of the cases, as given in Table 5.8, we evaluate the L_2 norm error for the flowfield obtained for each of the time step predicted and the actual URANS data. This evaluation is done for both basis type A and basis type B, and are represented in Figure A.9. Here, it is evident that the L_2 norm error between the predicted flowfield of basis type A and the URANS flowfield seems to show a lower error compared to the prediction done by basis type B. The eigen basis describes the flowfield better than the POD basis for this case.

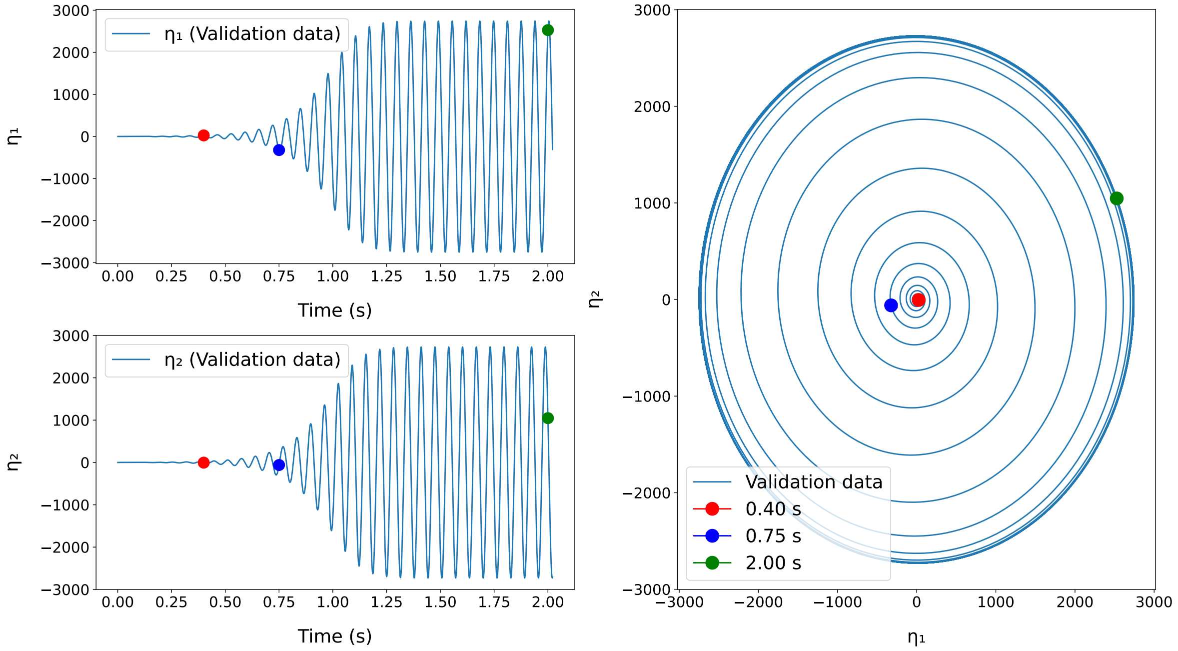

(a) Points in time t = 0.4s, 0.75s and 2s considered for Ma 0.71, α = 5.25° reconstruction, marked on the reduced coordinate plots on basis type A for the *validation data*

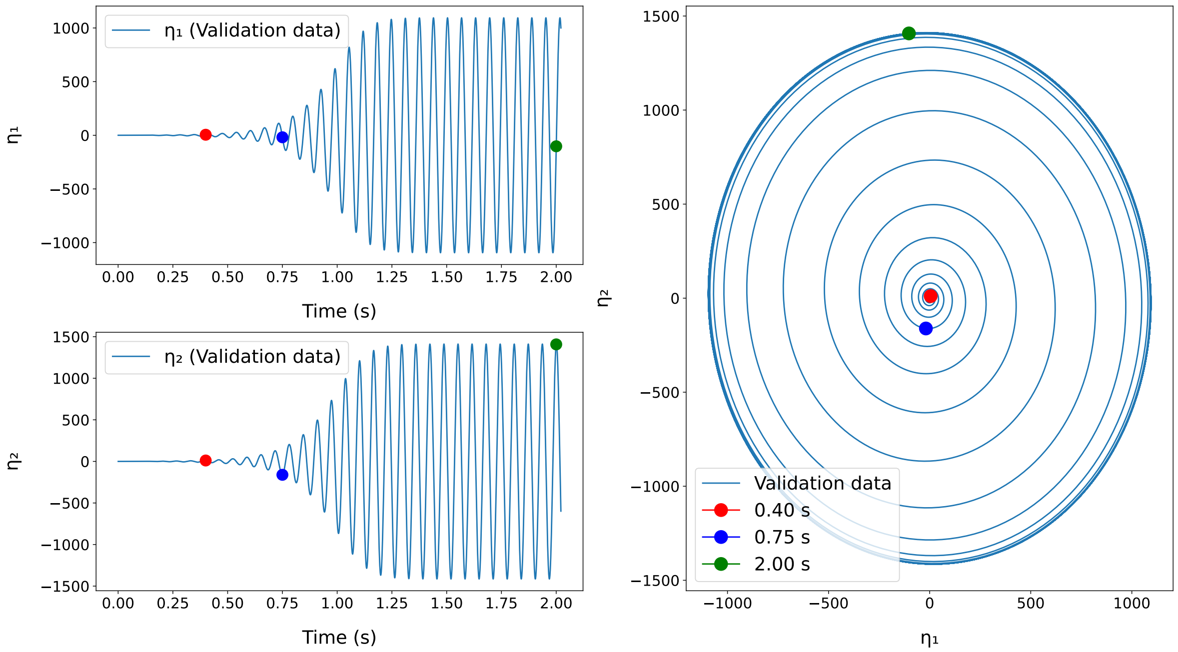

(b) Points in time t = 0.4s, 0.75s and 2s considered for Ma 0.71, α = 5.25° reconstruction, marked on the reduced coordinate plots on basis type B for the *validation data*

Figure A.7: Points in time t = 0.4s, 0.75s and 2s considered for Ma 0.71, α = 5.25° reconstruction, marked on the reduced coordinate plots on basis type A and basis type B, for the *validation data*

Prediction of RhoE done at t = 0.4s for Ma=0.71 at α = 5.25°

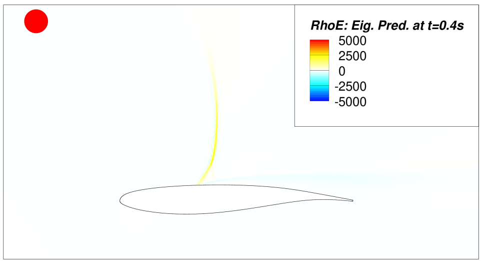

(a) URANS result at t = 0.4s

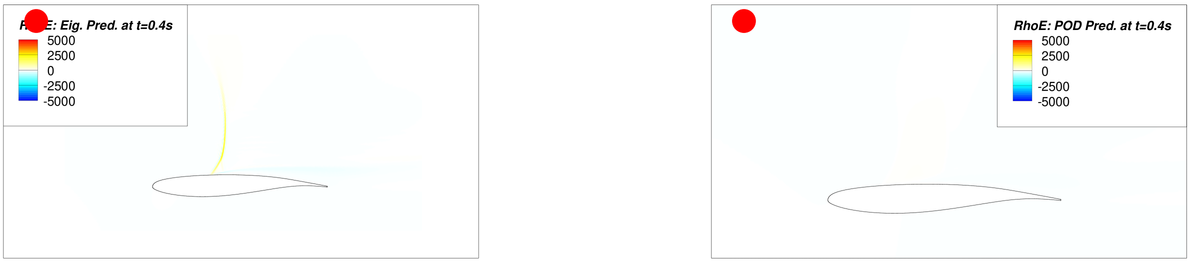

(b) Predicted flowfield using eigen basis, at t = 0.4s

(c) Predicted flowfield using POD basis, at t = 0.4s

(d) Error between the predicted flowfield using eigen basis and URANS flowfield, at t = 0.4s

(e) Error between the predicted flowfield using POD basis and URANS flowfield, at t = 0.4s

Prediction of RhoE done at t = 0.75s for Ma=0.71 at α = 5.25°

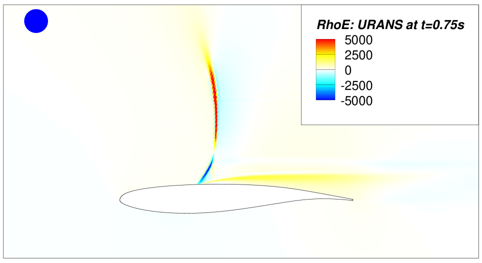

(f) URANS result at t = 2s

(g) Predicted flowfield using eigen basis, at t = 0.75s

(h) Predicted flowfield using POD basis, at t = 0.75s

(i) Error between the predicted flowfield using eigen basis and URANS flowfield, at t = 0.75s

(j) Error between the predicted flowfield using POD basis and URANS flowfield, at t = 0.75s

Prediction of rhoE done at t = 2s for Ma=0.71 at $\alpha = 5.25°$

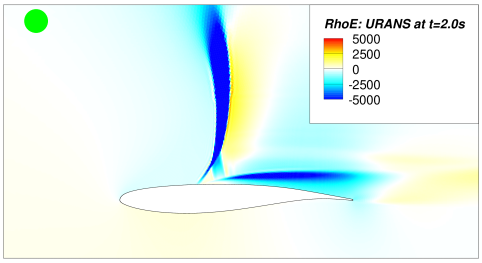

(k) URANS result at t = 3s

(l) Predicted flowfield using eigen basis, at t = 2s

(m) Predicted flowfield using POD basis, at t = 2s

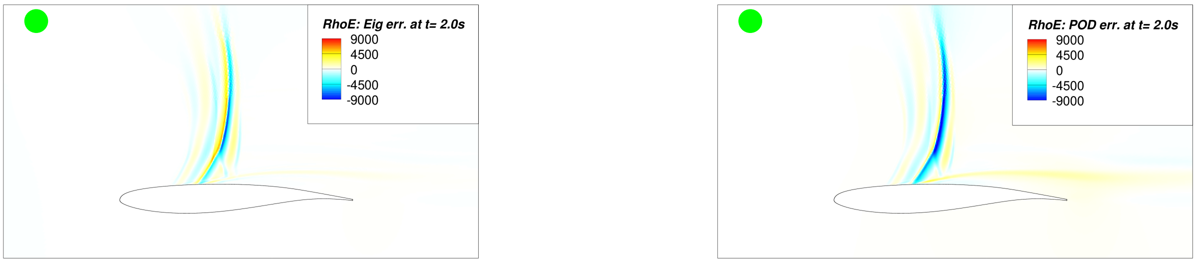

(n) Error between the predicted flowfield using eigen basis and URANS flowfield, at t = 2s

(o) Error between the predicted flowfield using POD basis and URANS flowfield, at t = 2s

Figure A.8: Predicted rhoE flowfield done based on ODE for the eigen and POD basis, compared to the actual URANS flowfield at t = 0.4s, 0.75s and 2s. The comparison between the URANS flowfield to the predicted flowfields are carried out by the error plots.

RhoE L_2 Norm Error Trends

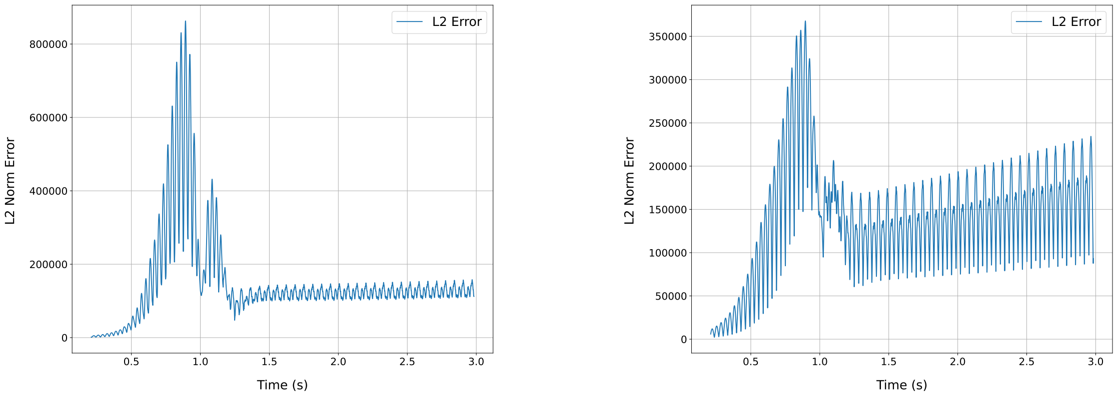

(a) L_2 norm error trend between the predictions based on the eigen basis and the URANS flowfield, of RhoE. The norm is considered from prediction start point $t = 0.208$ s, for the case of $Ma = 0.71$, $\alpha = 5.25°$.

(b) L_2 norm error trend between the predictions based on the POD basis and the URANS flowfield, of RhoE. The norm is considered from prediction start point $t = 0.208$ s, for the case of $Ma = 0.71$, $\alpha = 5.25°$.

RhoE Relative L_2 Norm Error Trends

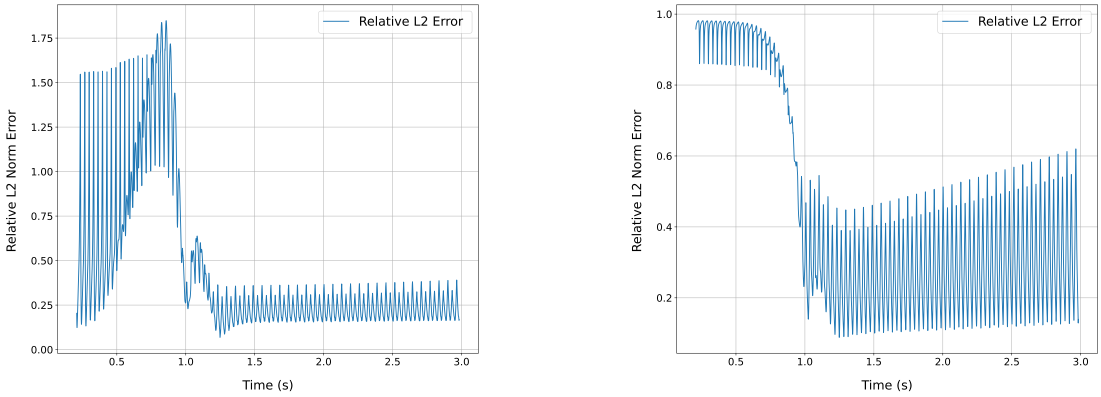

(c) Relative L_2 norm error trend between the predictions based on the eigen basis and the URANS flowfield, of RhoE. The norm is considered from prediction start point $t = 0.208$ s, for the case of $Ma = 0.71$, $\alpha = 5.25°$.

(d) Relative L_2 norm error trend between the predictions based on the POD basis and the URANS flowfield, of RhoE. The norm is considered from prediction start point $t = 0.208$ s, for the case of $Ma = 0.71$, $\alpha = 5.25°$.

Figure A.9: Comparison of relative L_2 norm error trends for RhoE using different bases and methods.